Mapping Myocardial Elasticity with Intracardiac Acoustic Radiation Force Impulse Methods

by

Peter J. Hollender

Department of Biomedical Engineering
Duke University

Date: _____

Approved:

_____
Gregg E. Trahey, Supervisor

_____
Sina Farsiu

_____
Jason Koontz

_____
Mark Palmeri

_____
Patrick Wolf

Dissertation submitted in partial fulfillment of the requirements for the degree of
Doctor of Philosophy in the Department of Biomedical Engineering
in the Graduate School of Duke University
2014

Abstract

Mapping Myocardial Elasticity with Intracardiac Acoustic Radiation Force Impulse Methods

by

Peter J. Hollender

Department of Biomedical Engineering
Duke University

Date: _____

Approved:

_____
Gregg E. Trahey, Supervisor

_____
Sina Farsiu

_____
Jason Koontz

_____
Mark Palmeri

_____
Patrick Wolf

An abstract of a dissertation submitted in partial fulfillment of the requirements for the degree of Doctor of Philosophy in the Department of Biomedical Engineering in the Graduate School of Duke University
2014

Abstract

Implemented on an intracardiac echocardiography transducer, acoustic radiation force methods may provide a useful means of characterizing the heart's elastic properties. Elasticity imaging may be of benefit for diagnosis and characterization of infarction and heart failure, as well as for guidance of ablation therapy for the treatment of arrhythmias. This thesis tests the hypothesis that with appropriately designed imaging sequences, intracardiac acoustic radiation force impulse (ARFI) imaging and shear wave elasticity imaging (SWEI) are viable tools for quantification of myocardial elasticity, both temporally and spatially. Multiple track location SWEI (MTL-SWEI) is used to show that, in healthy *in vivo* porcine ventricles, shear wave speeds follow the elasticity changes with contraction and relaxation of the myocardium, varying between 0.9 and 2.2 m/s in diastole and 2.6 and 5.1 m/s in systole. Infarcted tissue is less contractile following infarction, though not unilaterally stiffer. Single-track-location SWEI (STL-SWEI) is proven to provide suppression of speckle noise and enable improved resolution of structures smaller than 2 mm in diameter compared to ARFI and MTL-SWEI. Contrast to noise ratio and lateral edge resolution are shown to vary with selection of time step for ARFI and arrival time regression filter size for STL-SWEI and MTL-SWEI. In 1.5 mm targets, STL-SWEI achieves alternately the tightest resolution (0.3 mm at CNR = 3.5 for a 0.17 mm filter) and highest CNR (8.5 with edge width = 0.7 mm for a 0.66 mm filter) of the modalities, followed by ARFI and then MTL-SWEI. In larger, 6 mm targets,

the CNR-resolution tradeoff curves for ARFI and STL-SWEI overlap for ARFI time steps up to 0.5 ms and kernels $\leq$1 mm for STL-SWEI. STL-SWEI can operate either with a 25 dB improvement over MTL-SWEI in CNR at the same resolution, or with edge widths 5$\times$ as narrow at equivalent CNR values, depending on the selection of regression filter size. *Ex vivo* ablations are used to demonstrate that ARFI, STL-SWEI and MTL-SWEI each resolve ablation lesions between 0.5 and 1 cm in diameter and gaps between lesions smaller than 5 mm in 3-D scans. Differences in contrast, noise, and resolution between the modalities are discussed. All three modalities are also shown to resolve "x"-shaped ablations up to 22 mm in depth with good visual fidelity and correspondence to surface photographs, with STL-SWEI providing the highest quality images. Series of each type of image, registered using 3-D data from an electroanatomical mapping system, are used to build volumes that show ablations in *in vivo* canine atria. *In vivo* images are shown to be subject to increased noise due to tissue and transducer motion, and the challenges facing the proposed system are discussed. Ultimately, intracardiac acoustic radiation force methods are demonstrated to be promising tools for characterizing dynamic myocardial elasticity and imaging radiofrequency ablation lesions.

Contents

List of Tables

List of Figures

List of Abbreviations and Symbols

Symbols

G or μ	Shear Modulus (kPa)
E	Young's Modulus (kPa)
ν	Poisson's Ratio
ρ	Density (g/cm^3)
SWS or c_T	Transverse (shear) wave velocity (m/s)
c	Speed of sound (m/s)
f	Frequency (Hz)
λ	wavelength (m)
T	Shear wave arrival time (s)
t	Tracking time ("slow time") (s)
z	Axial depth (m)
x_t	Lateral tracking location (m)
x_p	Lateral push location (m)

Abbreviations

AF	Atrial Fibrillation
AMI	Acute Myocardial Infarction
ARFI	Acoustic Radiation Force Impulse or Acoustic Radiation Force Impulse Imaging. Both the type of ultrasonic pulse and the imaging modality use this notation.

AV	Atrioventricular
BPM	Beats per minute
CNR	Contrast-to-Noise Ratio
DOF	Depth of Field
EAM	Electroanatomical Mapping
ECG	Electrocardiogram
FOV	Field of View
FPS	Frames per second
HR	Heart Rate
ICE	Intracardiac Echocardiography
IVS	Interventricular Septum
LA	Left Atrium
LV	Left Ventricle
LVFW	Left Ventricular Free Wall
MRI	Magnetic Resonance Imaging
MTL-SWEI	Multiple Track Location Shear Wave Elasticity Imaging
PRF	Pulse Repetition Frequency
PRI	Pulse Repetition Interval
RA	Right Atrium
RFA	Radiofrequency Ablation
ROI	Region of Interest
RV	Right Ventricle
RVFW	Right Ventricular Free Wall
SA	Sinoatrial
SNR	Signal-to-Noise Ratio
STL-SWEI	Single Track Location Shear Wave Elasticity Imaging

SWEI	Shear Wave Elasticity Imaging
SWS	Shear Wave Speed

Acknowledgements

I would like to thank first and foremost the other members of the Trahey lab, and all of the graduate students and professors across the Duke ultrasound community. Without the years and years of research and innovation that they put in prior to my time, none of this would have been possible. Their advice, explanations, and assistance were critical to my success, both in and out of the lab. I would like to especially thank Drs. Richard Bouchard, David Bradway, and Veronica Rotemberg, who helped convince me that Duke was a great place to complete my Ph.D, and with whom I have become lifelong friends. I would also like to specifically thank Dr. Brett Byram, Dr. Mark Palmeri, MD, Dr. Stephen Rosenzweig, and Nick Bottenus for their patience in discussing ultrasound theory with me, both for practical research-related applications and for off-the-wall ideas. A very special thanks goes out to Lily Kuo, MS, who as a masters student and researcher, was indispensable for running many of the experiments. I also want to thank the principal investigators of the three ultrasound labs, Drs. Gregg Trahey, Kathy Nightingale, and Patrick Wolf, not only for obtaining the funding for this work, but for their ideas, feedback and encouragement that kept me moving forward even when the science seemed at times hopeless. I want to especially thank Gregg for his incredible combination of passion, vision, and support, for helping me grow as a scientist, and encouraging me to have a rich and fulfilling life outside of the lab. I would like to thank Ellen Dixon-Tulloch for her expert assistance with the animal studies, as well as Matt Brown and Ned

Danieley for their seemingly unlimited expertise with computers, system design, and practical engineering. I would like to thank Siemens Medical Systems for their in-kind and technical support, as well as for the opportunity to co-op with them during my second year. I would like to thank the National Institute of Health for providing the funding for this research in the form of medical imaging training grant EB001040, and grants R37HL096023 and R01EB01248. Finally, I would like to thank my parents for supporting my choice of career and enabling me to attend Duke.

1

Introduction

This dissertation is organized to follow the development and application of advanced ultrasound imaging methods for assessing myocardial elasticity using an intracardiac echocardiography (ICE) transducer. Two intracardiac imaging tasks are addressed. The first is the assessment of dynamic myocardial stiffness through the cardiac cycle and variations in the presence of acute myocardial infarct. The second is imaging lesions formed through radiofrequency ablation in three dimensions. The chapters are organized from the most-controlled, most-quantifiable theory and phantom experiments to the least-controlled, most-qualitative *in vivo* case studies.

Chapter 2 provides a review of the clinical problem(s) and a background on acoustic radiation force-based elasticity imaging.

Chapter 3 is a published paper that describes a sequence for high frame rate shear wave elasticity imaging (SWEI) and tests its ability image dynamically contracting myocardium in an *in vivo* setting.

Chapter 4 is another published paper that expands on the work from chapter 3 to introduce a method for building high frame rate 2-D movies of myocardial elasticity by using ECG triggering and multi-beat synthesis. Chapter 4 also follows a longi-

tudinal infarct animal study, using ARFI and SWEI to characterize the contractile properties of normal, spared, and infarcted myocardium.

Chapter 5 introduces a speckle-free variant of SWEI imaging called single track location SWEI (STL-SWEI) and compares it to ARFI imaging and traditional MTL-SWEI imaging in a phantom study. This paper is in review.

Chapter 6 applies ARFI, MTL-SWEI, and STL-SWEI imaging to the task to three-dimensional radiofrequency ablation lesion assessment in a series of controlled *ex vivo* experiments using an ICE transducer.

Chapter 7 describes the fusion of an electro-anatomical mapping system to the proposed ICE elasticity imaging system, and presents reconstructions of 3-D sections of healthy and ablated myocardium from *in vivo* experiments.

Chapter 8 provides insights on the implications of this work and offers future directions for this line of research.

The first appendix details very high frame rate shear wave imaging, which was developed to improve on the sequences used in chapters 3 and 4, but never used in a longitudinal study.

The second two appendices cover specific signal processing techniques, which enrich the work presented elsewhere in the thesis. Appendix B studies an artifact present in STL-SWEI and proposes methods for correcting it, and Appendix C presents an advanced method for shear wave speed reconstruction.

2

Background

2.1 Clinical Motivation

The heart is one of the most mechanically complex organs in the body. It is an electromechanical muscular pump that remains in perpetual motion from weeks after conception until death, moving blood through the body with a rhythmic sequence of contraction and relaxation of its four chambers. The heart's primary function is sending deoxygenated blood through the pulmonary circuit, and then pumping the freshly-oxygenated blood throughout the body. Cardiovascular disease, the leading cause of death in the United States, is actually a class of diseases affecting the electrical and/or mechanical components of the cardiovascular system (Bonow et al., 2011). The heart needs a properly functioning conduction system, healthy cardiac muscle and vasculature, and an ample supply of oxygenated blood from the coronary arteries to maintain its normal rhythm. If any of these processes are disrupted, the resultant symptoms can range from mild discomfort to heart failure and death.

2.1.1 Acute Myocardial Infarct

Acute myocardial infarction occurs when blood flow to the heart is interrupted by occlusion of a coronary artery. Without an ample supply of oxygenated blood, a series of deleterious effects are set off, whose severity and permanence increase with the duration of blockage. It is thus of clinical imperative to restore oxygenated blood flow as quickly as possible, through pharmacological and/or surgical intervention. The flowchart in figure 2.1 depicts part of the complex progression of myocardial damage following infarction (Diamond and Forrester, 1972; Morales et al., 2002; Solomon and Pfeffer, 2007). Some effects happen almost instantaneously, as the oxygen-deprived myocytes switch to anaerobic glycolysis, and begin building up lactic acid. Even if reperfusion is performed within 30 minutes (the "reversible phase") by thrombolysis or Percutaneous Coronary Intervention (PCI), at least temporary dysfunction is seen over the following days and weeks in what is known as myocardial "stunning" (Bolli, 1990; Hare, 2007). Stunning is marked by a decreased oxygen demand and cardiac performance, but recovers over time. After approximately 30 minutes, irreversible damage begins to occur as cardiomyocytes in the endocardium normally supplied blood by the occluded artery undergo necrosis; they die first because they are farthest from the now-deficient supply (Saraste et al., 1997; Krijnen et al., 2002; Van de Werf et al., 2003). Over the next hours, the necrotic region grows until it is completely transmural. The necrotic tissue is unable to support wall stress, and distention of the tissue in response to cardiac pressure can cause the infarcted region to stretch and grow. This continues until the wall is stretched so thin that connective tissue bears the loads normally supported by the myocardium, or, in extreme cases, an aneurysm occurs. Over weeks and months after infarction, global remodeling begins to occur as the workload for maintaining function is driven onto the spared myocardium. Bogen et al. (1980) noted that myocardial infarction is characterized by a localized

increase in myocardial stiffness and decreased contractility that evolves over weeks after the infarction event. Increased wall stresses in the rest of the ventricle cause it to grow and thin, increasing dysfunction and the subsequent risk of heart failure. Over a similar time period, the necrotic tissue degrades and is replaced by collagen, forming a stiff, fibrous scar (McKay et al., 1986; Uusimaa et al., 1997). If reperfusion is performed within hours to weeks after infarction, some akinetic (non-moving) tissue may recover. This tissue is said to be hibernating, and maintains its viability throughout ischemia, potentially through a collateral blood supply (Solomon and Pfeffer, 2007; Bonow et al., 2011). When reperfusing the heart with drugs or surgery, an additional risk comes from a response called edema (Laine and Allen, 1991). Edema is swelling of the tissue with interstitial fluid which occurs with ischemia but spikes with reperfusion due to a gradient formed in sodium channels (Karolle et al., 1991). Edema can last for a few weeks and has risks of its own, but has been shown to be potentially reduced by ischemic post-conditioning during reperfusion (Thuny et al., 2012).

Because the progression of the disease following the initial insult is complicated, a means to readily distinguish necrotic, stunned, hibernating, edemic, and healthy tissues could greatly improve diagnoses and management (Pagley et al., 1997; Haas et al., 1997). Infarctions are currently detected by electrocardiogram (ECG) (Lee et al., 1987; Adams et al., 1993), and can be imaged with contrast-enhanced MRI (Lima et al., 1995; Kim et al., 1999, 2000; PG and J, 2012), PET (Matsunari et al., 2003), Computed Tomography (CT) (Mahnken et al., 2005), or most commonly, Echocardiography (Heger et al., 1979; Hauser et al., 1985; Gruseels et al., 1995). PET provides low resolution 3-D images of perfusion, and MRI provides high resolution functional maps, but these systems are costly and bulky. ECG is the first line of detection, as ST-segment elevation is a good indicator of infarction. Echocardiography is then used to determine which coronary arteries are involved, by examining

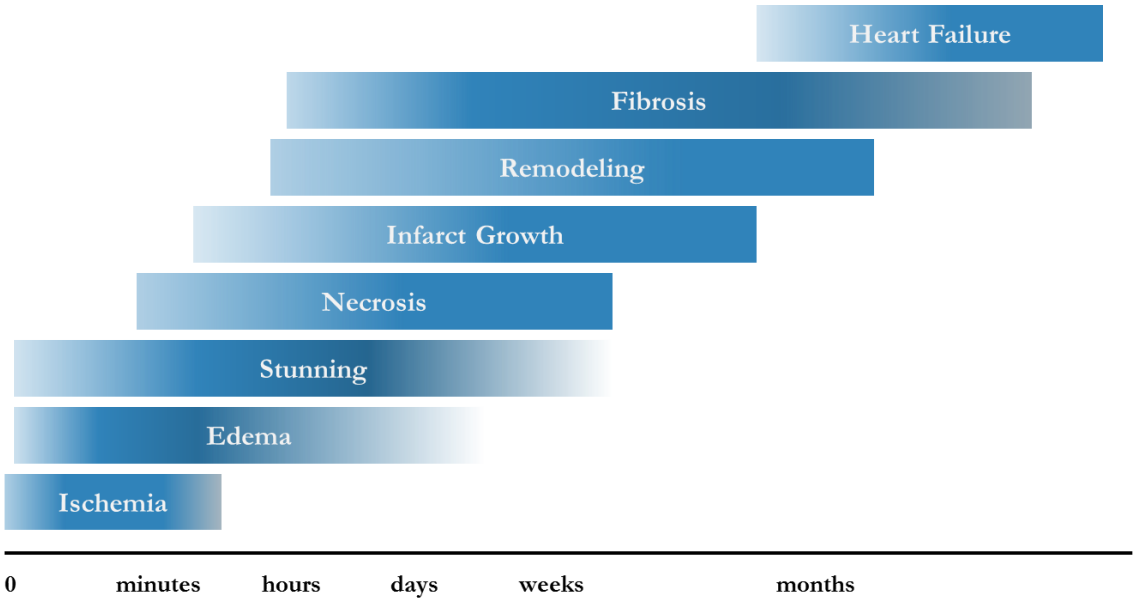

FIGURE 2.1: Basic progression of Acute Myocardial Ischemia. Irreversible damage occurs after 30-60 minutes.

the kinematics of the wall segments. Because infarction changes cardiac mechanics, it may be a good candidate for the elasticity imaging proposed in this work, which could provide high-resolution and precise characterization of myocardial structure.

2.1.2 Radiofrequency Ablation

Another potential target for elasticity imaging is in radiofrequency ablation (RFA) monitoring. RFA is used to treat arrhythmias by locally heating the tissue from a catheter (Calkins et al., 2007). This causes local protein denaturation in the tissue which creates stiff, nonconductive lesions. Lines or loops of individually-created lesions are generated to eliminate the re-entrant conductive pathways that cause arrhythmias. Melby et al. (2008) and Haissaguerre et al. (2005) noted that gaps in these lines can compromise the efficacy of the ablation procedure, and Calkins et al. (2012) identifies reconnection of the pulmonary veins as the primary source of AF recurrence. Forming a lesion extending through all layers from the endocardium through to the epicardium is critical for the ablation's success (Kowalski et al., 2012).

Ablating too much tissue, however, can cause unnecessary collateral damage to surrounding tissue, including the esophagus (figure 2.2). Electroanatomical mapping (EAM) systems are used to identify target regions to ablate and confirm electrical disruption due to ablation (Burkhardt and Natale, 2009), but myocardial "stunning" (Bolli, 1990; Sparks et al., 1998) may create a region of incomplete ablation which is electrically inactive at the end of the procedure but will become symptomatic in the future. A 2007 study found that 20% of patients receiving treatment for atrial fibrillation (AF, or A-Fib) were readmitted within one year, and 30% were re-admitted within two years (Berruezo et al., 2007). B-Mode echocardiography is often used to monitor ablation procedures (Marrouche et al., 2003; Daoud et al., 1999; Vaina et al., 2006; Chu et al., 1994), but beyond ensuring correct cather tip placement and contact, does not provide feedback on the extent or transmurality of the generated lesion (Fisher et al., 1997; Ren et al., 2001; Szili-Torok et al., 2003). The duration, power, and temperature of the ablation are used to predict lesion size, but actual feedback on the size and shape of the generated lesion is currently unavailable clinically (Melby et al., 2008; Kowalski et al., 2012). MRI systems have been developed to monitor RF ablations (Lardo et al., 2000), but the cost of performing ablations in an MRI may be prohibitive, all corresponding equipment must be nonmagnetic, and MRI is contraindicated by pacemakers and other implanted devices. A more accessible technique for monitoring the formation of ablation lesions could be of great benefit. Figure 2.3 outlines the current treatment method of treatment, including recurrence and repeat treatment, while figure 2.4 outlines how the intracardiac elasticity imaging system proposed in this work could improve outcomes by identifying "at risk" regions of incomplete ablation as candidates for additional preventative ablation. This may provide an alternative or more sensitive addition to adenosine infusion, which has been shown to promote reconduction at the time of the first ablation, but has not been a successful predictor of long term recurrence (Arentz et al.,

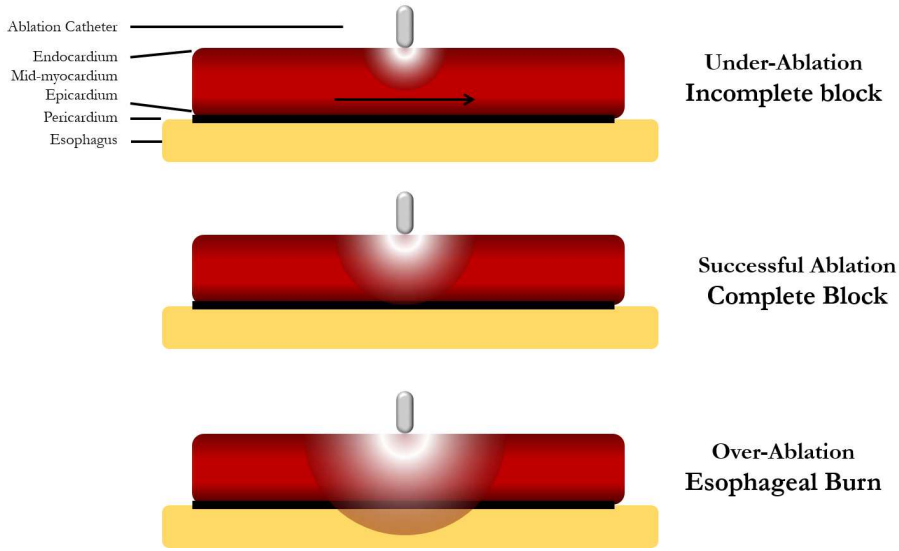

FIGURE 2.2: Lesion Transmurality. Under ablation (top) leads to incomplete block, and over ablation (bottom) leads to collateral damage.

2004).

2.1.3 Acoustic Radiation Force Impulse Imaging

Acoustic radiation force impulse (ARFI) images (Nightingale et al., 2002) provide information about relative differences in tissue stiffness, similar to those generated with compressive strain imaging methods. However, ARFI offers advantages resulting from the generation of the mechanical excitation within the structure of interest and limited susceptibility to out of plane motion artifacts. Acoustic radiation force is applied to all targets insonified by a pressure wave. Through absorption (and a significantly lesser extent, scattering), momentum is transferred from the wave into the medium, generating transient motion away from the source of the wave. The magnitude of the body force applied is given by (Nyborg, 1965; Torr, 1984; Nightingale et al., 2002):

$$F(\vec{r}) = \frac{2\alpha I(\vec{r})}{c}, \tag{2.1}$$

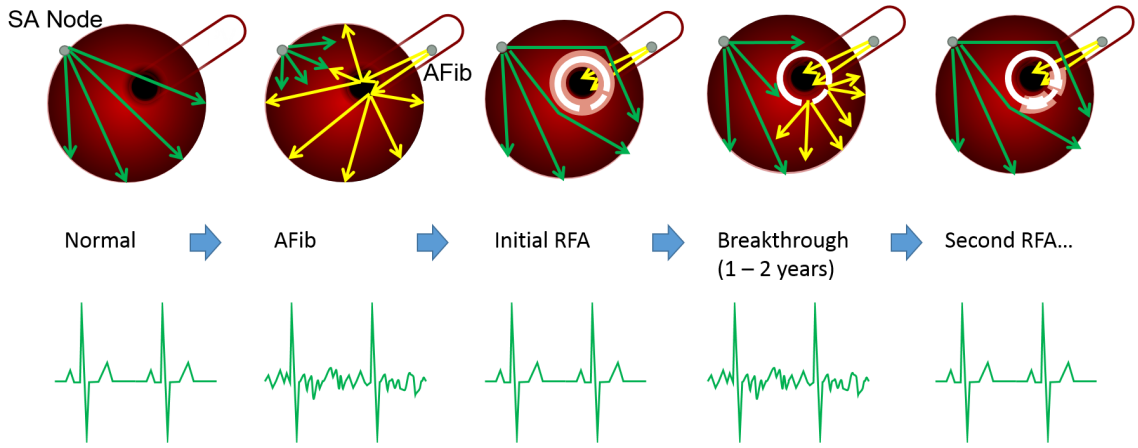

FIGURE 2.3: Current course of treatment and re-treatment for atrial fibrillation. 30% of patients are re-admitted within two years of the inital treatment (Berruezo et al., 2007). Green arrows indicate normal asymptomatic electrical propagation, and yellow arrows indicate asynchronous electrical signals associated with atrial fibrillation. The white region is permanently treated, and the pink area is temporarily treated and considered "at risk" for breakthrough.

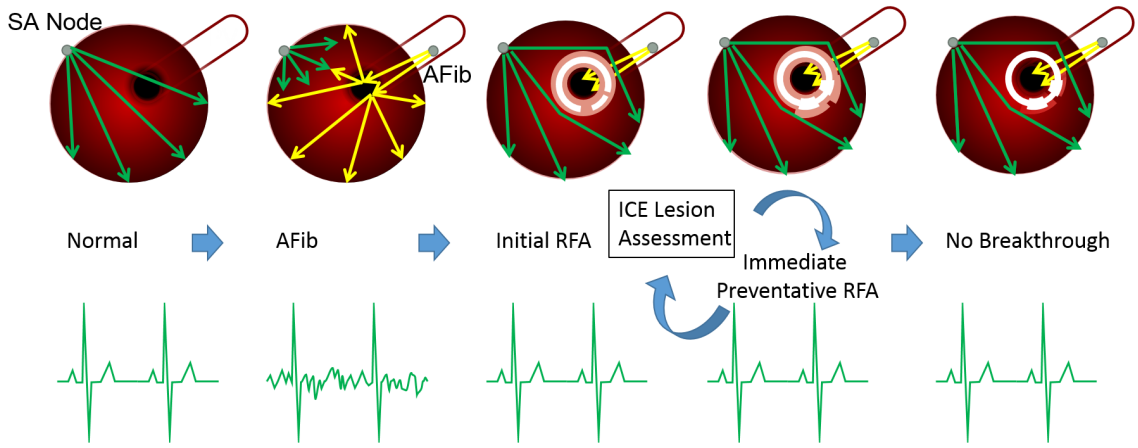

FIGURE 2.4: Proposed course of treatment for atrial fibrillation with integrated ICE elasticity imaging. Imaging of the ablated tissue at the time of the first treatment may guide preventative ablation to improve treatment permanence. Green arrows indicate normal asymptomatic electrical propagation, and yellow arrows indicate asynchronous electrical signals associated with atrial fibrillation. The white region is permanently treated, and the pink area is temporarily treated and considered "at risk" for breakthrough.

where $F(\vec{r})$ is the local body force in the direction of the beam (N/cm^3), $I(\vec{r})$ is the pulse-averaged intensity (W/cm^2) of the acoustic wave at spatial location $\vec{r}$, α is the local tissue attenuation (absorption) coefficient (Np/cm), and c is the speed of sound (m/s). A pulse at ultrasonic frequency generates a low frequency (100-1000 Hz) shear wave in an elastic medium, so even "push" pulses with many cycles (10-100μs) can be considered impulsive on the time scale of the shear response. The magnitude of the radiation force is dependent on both the beamforming of the excitation pulse ($I(\vec{r})$ and the properties of the imaged tissue, but when α and c are constant over the target region, the force profile is known and the relative displacement magnitude of a point in the field is inversely proportional to the shear modulus G at that point (Palmeri et al., 2006a). To generate a two-dimensional image, ARFI ensembles are translated across the imaging field of view (FOV), in the same way that a Color Doppler image is created. Images are generated of the tissue displacement magnitude within the excitation region, tracked for 1-2 ms after excitation with high speed ultrasound. ARFI images portray relative differences in the displacement response within each excited region, either as the displacement at a fixed time step, or as the maximum displacement. Although absolute elasticity estimates are possible with careful calibration, in most *in vivo* imaging scenarios, the 3D distribution of radiation force, variations in acoustic attenuation, and the transient nature of ARFI excitations complicate estimation of absolute elasticity, and therefore ARFI images normally provide qualitative maps of relative elasticity. Since lateral edges can be seen within a push beam (Dahl et al., 2007), the resolution in ARFI images is limited only by the mechanics of the tissue response and by the resolution of the tracking beams (Palmeri et al., 2006a). For imaging small structures, however, contrast-to-noise ratio (CNR) is often considered to be the limiting factor, and the contrast in ARFI images has been shown to be reduced when the size of the push beam exceeds the size of the structure being imaged (Nightingale et al.,

2006),(Palmeri et al., 2006a). These effects and others are explored in detail in chapter 5.

2.1.4 Shear Wave Elasticity Imaging

This section is adapted from the background section of the paper in review, "Matched Single- and Multiple- Track Location Shear Wave and Acoustic Radiation Force Impulse Imaging: Comparison of Suitability for Micro-Elasticity (μ-E) Imaging", which appears in its entirety in chapter 5

Shear Wave Elasticity Imaging (SWEI), originally described by Sarvazyan et. al. (Sarvazyan et al., 1998), and first demonstrated *in vivo* by our group (Nightingale et al., 2003), quantifies tissue stiffness by exciting the tissue with an ARFI push beam and monitoring the associated shear wave propagation through the region of interest. An example of shear wave propagation in response to focused acoustic radiation force is shown in figure 2.5.

Time-of-flight (TOF) based reconstruction algorithms are then used to estimate the shear wave speed (SWS) (Palmeri et al., 2008; Wang et al., 2010; Rouze et al., 2010; Muller et al., 2009; Tanter et al., 2008; McAleavey et al., 2009a; McLaughlin and Renzi, 2006b; Chen et al., 2004), which in linear elastic materials is proportional to the square root of the shear modulus G divided by the density ρ:

$$\text{SWS} = \sqrt{\frac{G}{\rho}} \tag{2.2}$$

SWS typically has units of m/s, G has units of kPa, and ρ has units of g/cm^3 and is generally assumed to be close of 1 g/cm^3 in tissue. We define a 2D spatial coordinate system with z being the axial direction in line with the ultrasound beam, and x being the lateral direction, transverse to the beam, in which shear wave will propagate. x_p and x_t will represent the push and track beam locations in the lateral

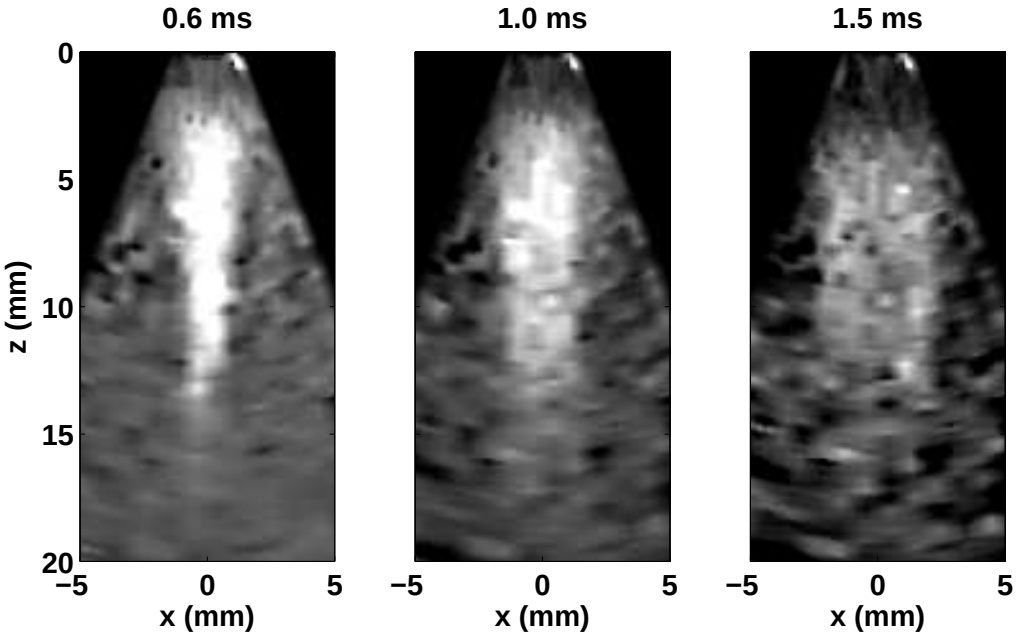

FIGURE 2.5: A shear wave propagates laterally from a focused "push" in a gelatin phantom. Brightness indicates the magnitude of the local axial displacement away from the transducer. Each frame shows a different time step after excitation. The wave travels away from the push location at the shear wave speed, and starts to dissipate due to geometric spreading.

dimension, respectively. We define the arrival time $T(z, x_t, x_p)$ as a characteristic of the shear wave generated at location (z, x_p) and tracked at location (z, x_t). T is typically chosen to be the time of peak axial velocity, displacement, or match-filtered velocity or displacement (i.e. the peak of the cross-correlation between a signal and a reference). When the track beam is aligned with the push beam, the initial arrival time is $T(z, x_p, x_p)$. Figure 2.6 shows a diagram of the most basic single push beam, two track beam configuration. T increases as x_t moves away from x_p, at a rate determined by the local shear wave speed $\mathrm{SWS}(z, x)$. For a push location x_p, we expect the arrival time T measured at location x_t to be

$$T(z, x_t, x_p) = T(z, x_p, x_p) + \mathrm{sgn}(x_t - x_p) \int_{x_p}^{x_t} \frac{1}{\mathrm{SWS}(z, x)} dx. \tag{2.3}$$

To make an estimate of shear wave speed, we hold x_p constant, and take the partial

derivative of equation 2.3 with respect to the tracking positions x_t, and invert $\partial T/\partial x_t$ to get the shear wave speed at each tracking location x_t:

$$\mathrm{SWS}\left(z, x_t, x_p\right) = \mathrm{sgn}(x_t - x_p)\left(\frac{\partial T\left(z, x_t, x_p\right)}{\partial x_t}\right)^{-1} \tag{2.4}$$

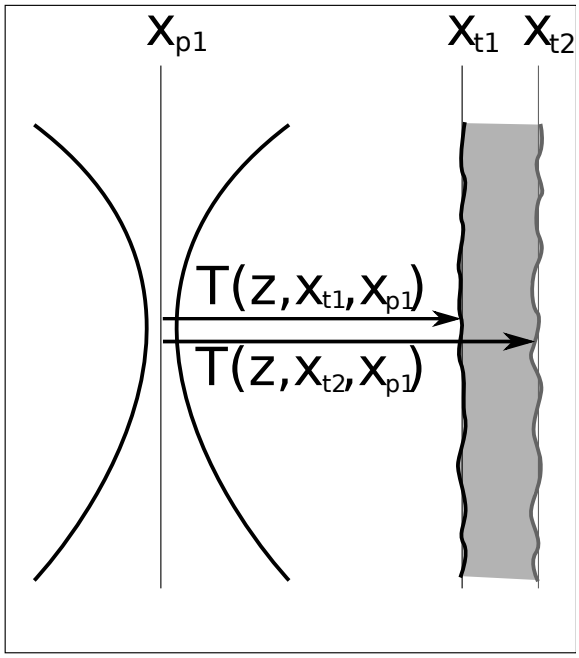

FIGURE 2.6: The simplest estimate of shear wave speed is calculated by dividing the known distance Δx by the difference in shear wave arrival time. The tracking beams illustrated show random speckle bias through depth, and the interrogated region is shaded. A single shear wave generated at x_{p_1} is tracked at multiple locations spaced laterally $\Delta x = x_{t_2} - x_{t_1}$ apart.

In practicality, a finite set of track locations $\mathbf{x_t} = \langle x_{t1}, x_{t2}, ..., x_{tN}\rangle$ are used to construct sampled estimates of the shear wave speed. In the example of figure 2.6, $\partial T/\partial x_t$ is estimated from two track beams, x_{t1} and x_{t2}, as the ratio of the beam separation $x_{t2} - x_{t1}$ to the finite difference between the estimated arrival times $\hat{T}$:

$$\hat{\mathrm{SWS}}_{\mathrm{MTL}}(z, x_t, x_{p1}) = \frac{x_{t2} - x_{t1}}{\hat{T}(z, x_{t2}, x_{p1}) - \hat{T}(z, x_{t1}, x_{p1})}, \tag{2.5}$$

for $x_{t1} < x_t < x_{t2}$.

With more than two track beams, linear regression or another estimator may be used to find the slope of the arrival times (Palmeri et al., 2008; Wang et al., 2010; Rouze et al., 2010). This is visualized in figure 2.7, which shows the time profile of displacement at a fixed depth, with one row for each track beam, and a single push in the center. The resulting estimate $\mathrm{SWS}_{\mathrm{MTL}}$ will then reflect the shear elasticity of the tissue region between the widest-spaced tracking beams used in the estimation. The selection of push location x_p theoretically does not affect the derivative estimate, provided that the separation between the push and track beams $|x_t - x_p|$ is neither too small (the tissue motion does not represent a propagating shear wave) nor too large (the shear wave amplitude is too small to detect). In MTL-SWEI, multiple push locations x_p can be used to extend the field of view and/or provide overlapping estimates of the same region (Tanter et al., 2008).

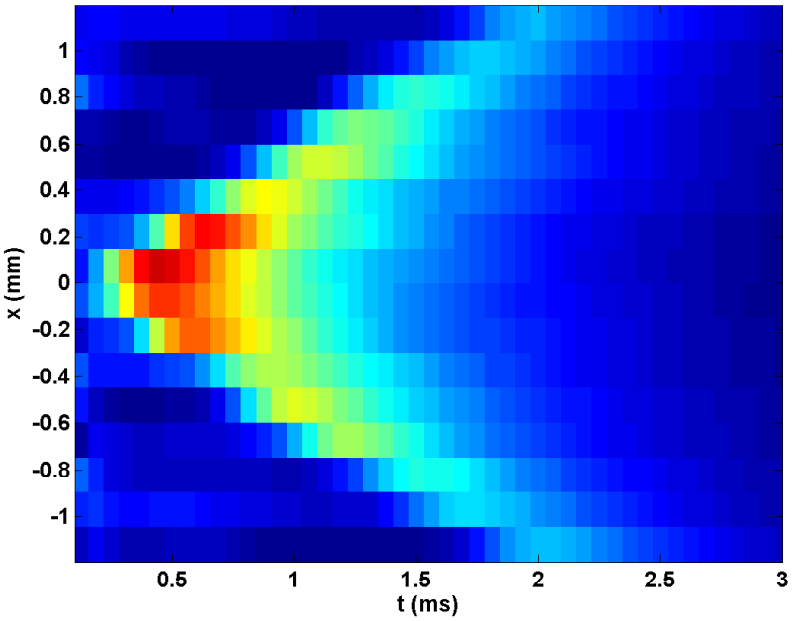

FIGURE 2.7: A shear wave generated in a uniform gelatin phantom and tracked with 16 parallel receive lines. The push is at $x_p = 0$ mm, and the tracking beams cover 1.2 mm to the left and right. The time delays at successive lateral locations indicate the shear wave speed, just under 1 m/s.

3

Intracardiac Echocardiography (ICE) Measurement of Dynamic Myocardial Stiffness with Shear Wave Velocimetry

This chapter was published in 2012 and is presented in its entirety (Hollender et al., 2012) with only minor notational revisions. This work represents the first implementation of SWEI on an ICE transducer, and demonstrates promise for characterizing myocardial contractility with high framerate SWEI. At the same time, it reveals many of the challenges of ICE ARFI and SWEI, which would go on to guide the development of advanced sequences (chapter 4) and motivate the development of a three dimensional registration system (chapter 7). The term "shear wave velocimetry" was chosen over SWEI to distinguish the fact that we were reporting model-free shear wave speeds, and not shear moduli. The field would go on to accept SWEI as describing shear wave speeds, as the term was already well known, and simply accepted that the assumptions necessary for reporting G rarely held for biological tissues due to geometry and dispersion.

3.1 Abstract

Acoustic Radiation Force (ARF)-based methods have been demonstrated to be a viable tool for noninvasively estimating tissue elastic properties, and shear wave velocimetry has been used to quantitatively measure the stiffening and relaxation of myocardial tissue in open-chest experiments. Dynamic stiffness metrics may prove to be indicators for certain cardiac diseases, but a clinically-viable means of remotely generating and tracking transverse wave propagation in myocardium is needed. Intracardiac echocardiography (ICE) catheter-tip transducers are demonstrated here as a viable tool for making this measurement. ICE probes achieve favorable proximity to the myocardium, enabling the use of shear wave velocimetry from within the right ventricle throughout the cardiac cycle. This work describes the techniques used to overcome the challenges of using a small probe to perform ARF-driven shear wave velocimetry, and presents *in vivo* porcine data showing the effectiveness of this method in the interventricular septum.

3.2 Introduction

Various methods have been developed to characterize the beating heart's dynamic elastic properties in the hopes of providing a key indicator of cardiac health and function. Ejection Fraction (EF), for example, is a measurement of the relative change in volume of a heart chamber as it beats; a low EF is often used as an indicator for risk of heart failure. While EF measurements can be made readily and noninvasively with conventional B-mode echocardiography, one study found that in approximately one-third of heart failure cases, EF was normal, though a passive stiffening of the left ventricle was present (Zile et al., 2004). Westermann et al. (2008) also found

abnormal relaxation in patients with heart failure and normal EF.

The clinical importance of dynamic myocardial stiffness has been extensively researched, in both the left ventricle (Zile et al., 2004; Westermann et al., 2008) and the right ventricle (Mebazaa et al., 2004; Bleeker et al., 2006; Haddad et al., 2008). Both the absolute stiffness of the myocardium at various points in the cardiac cycle, and contractility, the relative changes in stiffness between systole and diastole, are of interest. Magnetic resonance imaging (MRI) has recently been shown to be able to characterize the elasticity of the left ventricle (LV) through the cardiac cycle with a technique called magnetic resonance elastography (MRE) (Kolipaka et al., 2010). MRE measures the propagation velocity of acoustically-generated mechanical waves across the heart with MRI to determine its elastic properties. While MRE is able to measure global LV stiffness, MRI is expensive and relatively slow, and many patients have conditions or implants precluding them from undergoing MRI, while others may have regional defects that could be missed by these global metrics.

3.2.1 Ultrasonic Measurements of Myocardial Elasticity

Ultrasound may provide a readily available, real-time solution for dynamic cardiac elasticity imaging, as numerous echocardiographic techniques have been proposed to analyze myocardial stiffness and contractility. A quantitative measurement of the dynamic myocardial stiffness may have implications for diagnosing dysfunction as well as characterizing abnormal regions due to infarct or ischemia. Several such ultrasonic techniques are being explored vigorously, including strain and strain-rate imaging (Langeland et al., 2005; D'Hooge et al., 2000; Serri et al., 2006) Acoustic Radiation Force Impulse (ARFI) imaging techniques (Hsu et al., 2007b), and velocimetric methods (Bouchard et al., 2009b; Pislaru et al., 2009; Couade et al., 2011; Pernot et al., 2011; Kanai, 2005). Like MRE, ARFI and velocimetric methods measure the transient mechanical response of tissue to indicate elasticity, but use ultra-

sound to track and often generate the mechanical waves. Kanai (2005) first imaged the propagation of mechanical Lamb waves from aortic valve closure (AVC) in the interventricular septum (IVS) to estimate viscoelastic properties. Hsu et al. (2007b) first showed a cyclically-varying on-axis ARFI response in open-chest canine myocardium, coupling the transducer to the heart wall to control for motion. Bouchard *et al.* similarly demonstrated the feasibility of using ultrasound to track the velocity of ARF-induced transverse waves in an open-chest experiment for a quantitative measure of elasticity (Bouchard et al., 2009b, 2011), but also noted the challenge that remotely generating displacements in rapidly moving tissue would pose. Pislaru et al. (2009) estimated viscoelastic properties using Lamb wave propagation in the open-chest ovine free wall in response to a coupled mechanical shaker. Couade et al. (2011) also used open-chest preparations to achieve proximity in sheep, and was able to generate and track shear wave propagation in myocardial tissue throughout the cardiac cycle *in vivo* with supersonic shear imaging. Pernot et al. (2011) has recently achieved similar success with supersonic shear imaging, but with a Langendorff *ex vivo* preparation of rat hearts to study the effect of preload pressures on systolic stiffness.

3.2.2 Intracardiac Echocardiography

Pernot et al. (2011) suggest that to perform rapid shear wave velocimetry *in vivo* with clinical viability, a low frequency echocardiography probe would be needed for transthoracic imaging. To date, we have been unable to reliably generate and track transverse waves in myocardium transthoracically, and we propose here an alternative approach to move from open-chested experiments to closed-chested ones, towards clinical applicability. This work demonstrates the feasibility of using Intracardiac Echocardiography (ICE) catheter-tip ultrasonic linear arrays to obtain measures of dynamic myocardial stiffness using shear wave velocimetry. ICE catheters are com-

monly used echocardiographic tools, providing high-quality images of the heart from within the chambers for assessment of function and guidance of therapy (Mullen et al., 2003; Chu et al., 1994). While a catheterization can be considered at least minimally invasive, in patients with known conditions or those recovering from procedures, the additional information provided to clinicians by elasticity measurements may justify this method for cardiac function monitoring. ICE transducers have already been used for qualitative ARFI imaging *in vivo* (Eyerly et al., 2010; Wolf et al., 2011), though their small size presents a number of challenges, including reactive acoustic force and limited acoustic output, as characterized by Hsu et al. (2007a). By imaging from within the heart chambers, however, proximity to the target tissue is dramatically increased, and acoustic clutter observed in transthoracic echocardiography from the overlying tissue is markedly reduced. *In vivo* data presented here will demonstrate that ICE transducers are capable of making dynamic elasticity measurements similar to those made in open-chest preparations, but in the IVS with minimal invasiveness.

Shear Wave Elasticity Imaging

Shear Wave Elasticity Imaging (SWEI) is a quantitative way to measure tissue elasticity, first proposed by Sarvazyan et al. (1998). Sarvazyan observed that when shear waves are generated in a material, their lateral propagation velocity is determined by their elastic properties. The velocity of propagation of this wave (c_T) is governed under the assumptions of linear behavior in an isotropic, semi-infinite medium by

$$c_T = \sqrt{\frac{G}{\rho}}, \tag{3.1}$$

where G [kPa] is the shear modulus of elasticity (second Lamé constant) and ρ [g/cm^3] is the density. The assumptions of linearity, isotropy, and a semi-infinite medium

don't necessarily apply to myocardium, so we will report the shear velocities c_T directly, and use Shear Wave Velocimetry as its own measurement.[1]

Acoustic Radiation Force (ARF) provides a convenient solution for using a single transducer to excite a shear wave and track its propagation. In the focal region of the excitation beam, the body force is tightly focused laterally, and generates transverse waves that propagate away from the excitation beam (Palmeri et al., 2005). Because the wave displacements are orthogonal to the propagation direction, they are axial displacements relative to the transducer face, and can be tracked with high spatial resolution. Provided that enough stress is applied to shear the tissue and create a transverse wave in the field of view, a velocity estimate can be made, independent of amplitude. This provides an advantage over on-axis response methods, like those shown by Hsu et al. (2007b), where the target tissue would move around under the axial region of excitation if not mechanically coupled to the transducer.

3.3 Materials and Methods

3.3.1 Experimental Setup

All data presented here were acquired with Siemens AcuNav 10-French ICE catheters, running on a Siemens S2000 scanner. The AcuNav is an FDA-approved, 64-element, 7.25 MHz linear phased array ultrasound transducer, with a 7 mm aperture in azimuth. The small array size is necessary for intracardiac application.

We developed custom pulse sequences to record *in vivo* IQ ultrasound and matched ECG data from six healthy porcine subjects in compliance with protocols from Duke

[1] While myocardial displacement propagation has often been assumed to be a shear wave (Bouchard et al., 2009a; Couade et al., 2011; Pernot et al., 2011), a number of groups have suggested that an antisymmetric Lamb wave model is more appropriate considering the relatively thin myocardial thickness (Kanai, 2005; Nenadic et al., 2011; Pislaru et al., 2009; Chen et al., 2009). The Lamb wave model includes dispersive effects from the boundary conditions and separates the elastic and viscous components of μ, but the purpose of this paper is to demonstrate the feasibility of using ICE to generate and track transverse waves, and will compare its results to those previously reported using a shear wave model with similar bandwidth (50-350 Hz).

University's Institutional Animal Care and Use Committee (IACUC). The AcuNav was inserted through the jugular vein, and fed through the right atrium into the right ventricle (Fig. 1). Imaging planes were selected for minimal elevational motion and to keep the target tissue as much as possible within a single axial region of excitation (ROE) throughout the cardiac cycle. Motion confounds low-displacement velocity estimates, so with the current setup, targets beyond 20 mm were not considered. The data presented here are taken from long-axis views of the apical interventricular septum (IVS).

3.3.2 Interleaved Tracking

Due to system limitations, the entire lateral field of view can not be imaged simultaneously. Parallel beamforming and dynamic receive focusing only allow up to four A-lines to be recorded from a single transmit event. The parallel receive beams are centered around the focused transmit to maximize SNR while obtaining four separate A-lines in this experiment. 35 groups of four evenly spaced beams span the full 90° field of view, with 2.5° spacing between transmit locations. To image the full propagation of the wave, the superposition of repeated shear wave responses measured at different azimuthal beam groups is used.

Superimposing the responses over the entire 90° field of view would reduce uncertainty in the estimate of shear wave velocity, but it would take an impractically long time to record, as superimposing 35 consecutive responses would undoubtedly span multiple cardiac phases. Because of cardiac motion, minimizing the number of repeated interrogations used to generate a shear wave velocity estimate is essential to achieving quality, high-frame rate data. Fortunately, not all azimuthal angles contribute equally-useful information to the velocity estimate. Geometric spreading causes shear wave amplitudes to fall quickly as they propagate away from the excitation, so wide angles are unlikely so see ARF-induced waves above the physiological

motion noise floor. Additionally, within the lateral excitation beamwidth, the observed dynamics are more in response to direct excitation than to the characteristic propagation of the shear wave. The region of interest used in this work is covered by four transmit locations (16 receive locations). These locations are the four closest to the excitation (the center azimuthal line), not including the center transmit or the first transmit to its right. These lines span azimuthally 5° to 14°, which at 15 mm corresponds to a lateral span of 2 mm - 5 mm in the scan-converted data (Fig. 2). To reduce the number of necessary interrogations even further, we developed sequences that modulate the steering angle of the tracking beams between two azimuthal locations as the wave propagates in response to each excitation. The increased lateral field of view per excitation comes at the expense of the temporal sampling for each imaged line. Using the maximum frame rate achievable on our scanner with four parallel receive beams, we obtain for each excitation eight 4.56 kHz axial displacement estimates, recorded from 1 ms before excitation through 6 ms post-excitation to allow for interpolated motion estimation. Tracking lines 1-4 and 9-12 are recorded with the first excitation, and lines 5-8 and 13-16 are recorded with the second excitation. This 2-excitation imaging sequence is repeated 160 times at 40 Hz to capture four seconds of shear velocity data throughout multiple cardiac cycles.

3.3.3 Pulse Parameters

For both ARF excitations and tracking beams, 6.15 MHz pulses were used, with available foci between 10 and 20 mm, typically 15 mm. The impulsive excitation was generated with a 400-cycle (65 μs) pulse on the center line of the field of view to maximize acoustic output. The frequency was selected to fall within the bandwidth to the transducer, but below the center frequency to reduce attenuation effects. The shear waves generated by this excitation have frequency content between 50 and

300 Hz. Previous measurements and FEM modeling indicate that for simlilar pulse sequences (15 mm focus and 6 MHz center frequency), Mechanical Index (MI) is under 1.63 and tissue heating is low, 1.01°C over four seconds with 40 2-excitation acquisitions per second.

3.3.4 Shear Wave Speed Estimation

Figure 3 shows a flowchart of the signal processing chain used to obtain shear wave velocity estimates from the recorded IQ echo data. As described in detail by Hsu et al. (2007b), a phase-shift based displacement estimator (Kasai et al., 1985) is used to calculate the ARF induced displacements, using a 1.5- λ kernel. Once the displacements have been calculated, a quadratic motion filter is used to remove the bulk axial motion of the tissue from the ARF-induced displacements (Giannantonio et al., 2011). At each pixel, the displacement estimates from before the excitation and those greater than 3 ms after the excitation are fit to a quadratic function as an estimate of physiological motion. The motion is interpolated over the 3 ms after the excitation and subtracted from the data. The displacement estimates are then interpolated temporally to fill in the missing time steps due to the steering angle modulation and scan-converted into Cartesian coordinates with 0.1 mm x 0.1 mm pixel spacing.

Each of the 401 axial slices of the scan-converted image is considered independently for velocity estimation. Each axial slice is filtered with a second order temporal Butterworth bandpass filter with cutoff frequencies of 50 and 350 Hz to reduce noise outside of the expected bandwidth of the propagating wave. To compensate for reactive transducer kick-back, spatio-temporal locations in each slice that would correspond to shear wave speeds below 0.5 m/s (late times and near the excitation) or above 8 m/s (early times and far from the excitation) are assumed to be due to kick-back. A single kick-back profile is estimated from the average displacements

and subtracted from the slice, leaving only the propagating shear wave. To estimate the wave velocity, a version of the algorithm described by Palmeri et al. (2008) is used. The time-to-peak-displacement is then calculated for each lateral pixel. The time-to-peak data are then fit by linear regression, automatically removing outliers from motion artifact that cause the residual of the linear fit to fall below 0.5. The velocity is calculated at each depth, forming an A-line of velocity estimates, which, when repeated over the 160 acquisitions, forms a shear velocity M-mode image.

3.3.5 Region of Interest Tracking

Because the myocardium is moving relative to the transducer, anatomical locations will appear at different locations within the imaging plane at each shear wave acquisition. Within the M-mode of velocity estimates, the depths that are tissue and those that are blood will vary from frame to frame. Tracking the tissue borders improves visualization of the time-varying characteristics of the target tissue, and permits observation of axial stiffness variation.

To alleviate the need to manually segment every frame, nonrigid elastic registration, as detailed by Kybic and Unser (2003) was utilized to compute the motion between frames. Nonrigid elastic registration has been previously applied to ultrasound images to assess motion and strain (Ledesma-Carbayo et al., 2005; Elen et al., 2008; Myronenko et al., 2007). A multidimensional B-spline deformation model is used to estimate the warping function that describes the motion between each frame. This algorithm finds the deformation function $g(\mathbf{x})$ that optimally relates the test image f_t to the reference image f_r. To constrain the amount of warping of the image, the cost function used has terms for the sum-of-squared-difference (SSD) between the unwarped image and the target, as well as adjustable weighting functions for the gradient and curl of the computed displacement field:

$$E = w_{im}E_{im} + w_{div}E_{div} + w_{rot}E_{rot} \tag{3.2}$$

For these experiments, a knot spacing of 7 mm laterally and 5 mm axially was used. The weightings for w_{im}, w_{div}, and w_{rot} were 1, 2, and 1, respectively. For each sequence of data, a matched B-mode image was acquired immediately prior to each shear wave acquisition. These B-mode images were unwarped using the freely-available ImageJ (Abramoff et al., 2004) plugin UnwarpJ(Sorzano et al., 2005), and the transformation parameters describing each $g_j(\mathbf{x})$ saved. The proximal and distal tissue borders for the IVS ($\mathbf{x}_{p1}$, $\mathbf{x}_{d1}$) were manually marked in the first frame of each dataset. The computed transformations $g_j(\mathbf{x})$ were applied to the marked points in the reference image to compute their warped locations in the subsequent frames ($\mathbf{x}_{pj}$ and $\mathbf{x}_{dj}$). This automatically outlined the borders of the myocardium for most frames, with manual segmentation being used for those frames with obvious registration errors. While this allows the IVS's axial-lateral location to be tracked in each frame and accounted for, the lateral ROI is necessarily limited by the region of excitation and the location of the tracking beams in this implementation. Additionally, although the septum is tracked through each frame, the axial region of excitation limits the depths over which transverse waves can expect to be generated. Thus the final ROI to be considered is the intersection of the axial tissue region (typically 1-2 cm thick) as determined by the unwarping, and the region of excitation. The dynamic ROI calculated by unwarping is then used to window the shear wave velocity data, which have been independently calculated at every axial location.

3.3.6 Multi-beat Synthesis

To compare data acquired across multiple heartbeats, a technique called multi-beat synthesis (Hsu et al., 2007a) was used to register estimates from many frames onto a single heartbeat. The time of each ARF excitation is acquired with the ECG data. Each shear wave velocity estimate is thus assigned a fractional delay from the QRS complex in terms of the R-R interval. All of the shear wave velocity estimates can

then considered relative to a single, normalized heartbeat, grouped by their cardiac phase. 64 evenly spaced delays were used to group the velocity estimates over the cardiac cycle.

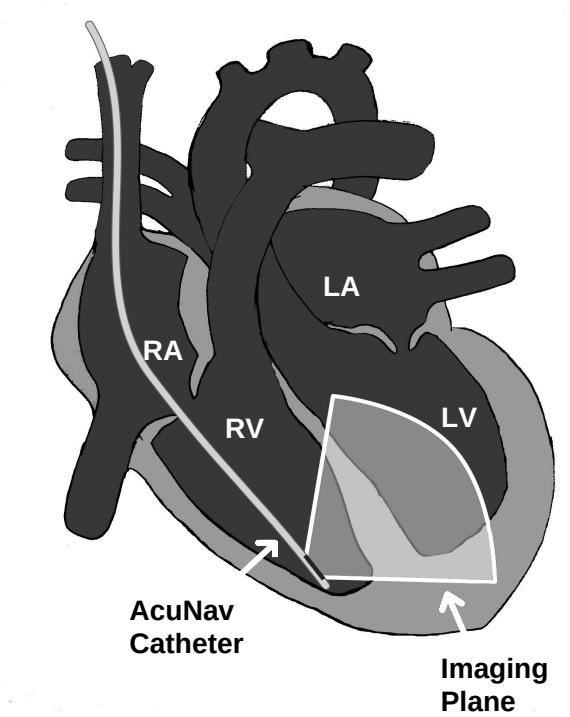

FIGURE 3.1: Ultrasound catheter tip placement. The imaging plane transects the interventricular septum.

3.4 Results

Figures 4-9 follow a single set of 160 acquisitions over four seconds from motion tracking through multibeat synthesis to demonstrate the post processing and generation of quantitative results. Figure 4 shows the center line of the B-mode image acquired with each acquisition as an M-mode for a single imaging sequence viewing the IVS. Highlighted on the image is the proximal septal boundary, as calculated in each frame by automatic registration. The motion of the septum is at times large, but very repeatable, and parts of the tissue remain in the expected region of excitation

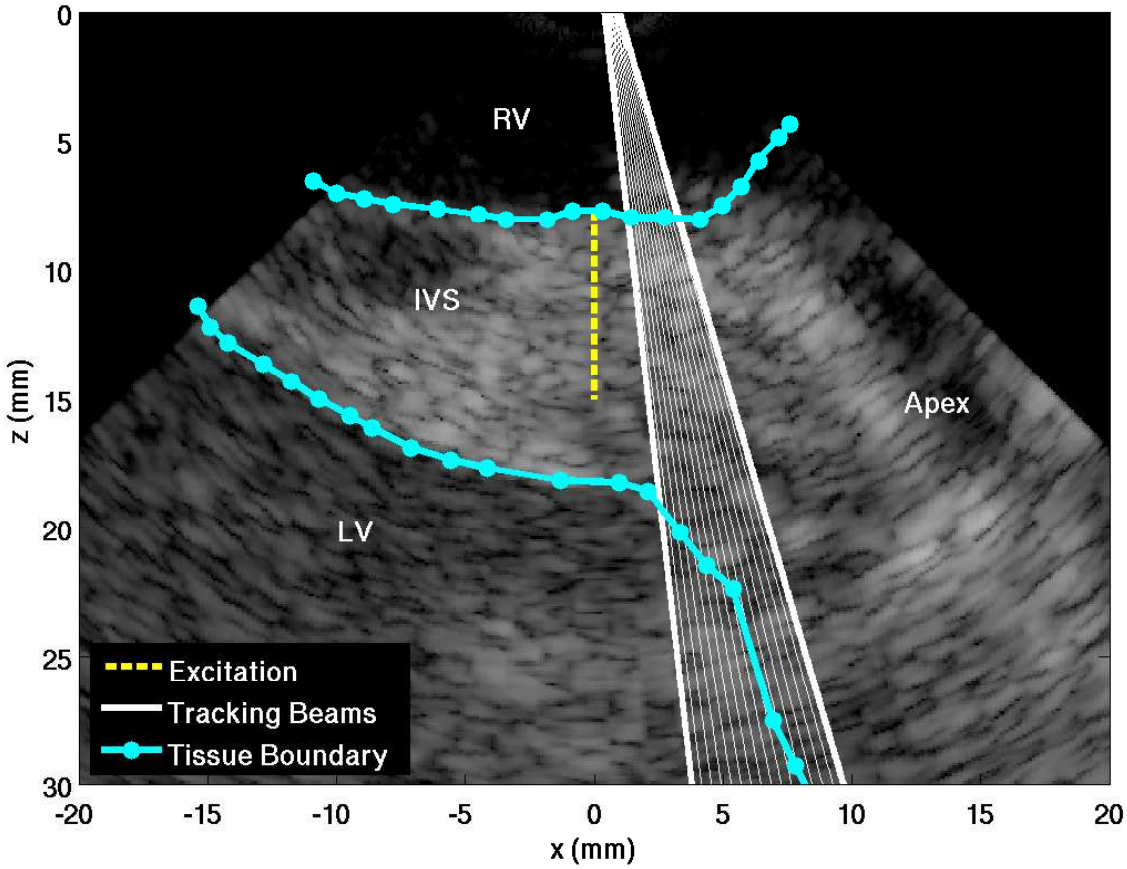

FIGURE 3.2: Shear Wave Imaging field of view. The ARF excitation is along the center of the image, generating displacements about the 15 mm focus, which are tracked propagating towards the apex.

(5-10 mm) throughout the cardiac cycle. Figure 5 shows the relative amplitude of scan-converted ARF displacements (averaged over the first 3 mm and 1 ms because the on-axis data are not recorded) through depth and across the 160 acquisitions for the same sequence shown in figure 4. Qualitatively, there is clear variation in the displacement magnitude, as seen previously in M-Mode ARFI experiments (Hsu et al., 2007b), but the axial motion obfuscates a quantitative assessment.

Figure 6 shows axial slices of the spatio-temporal volumes across the cardiac cycle, taken at the middle of the septum from the same pig, and post kick-back filter. The slices are consecutive, left-to-right, top to bottom, with each row covering a seperate

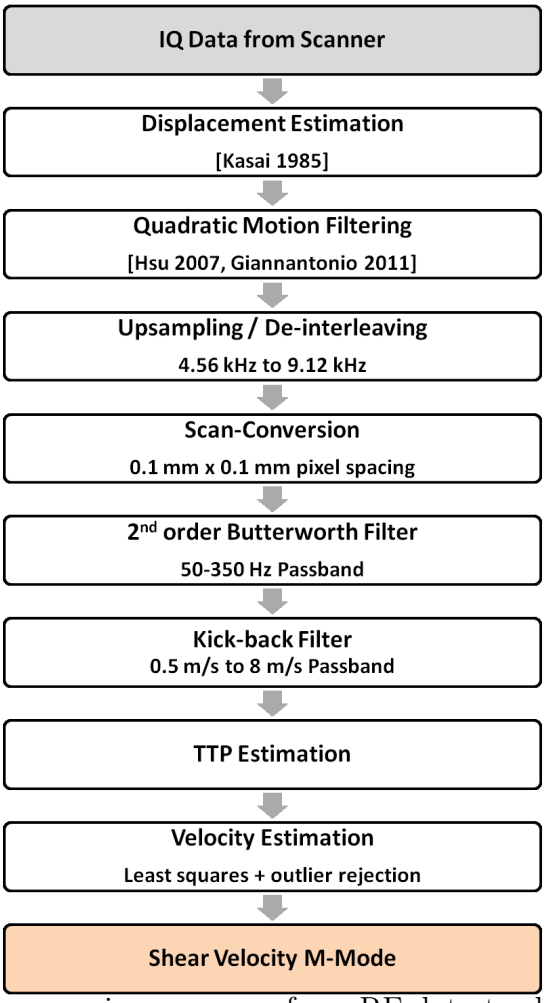

FIGURE 3.3: Data processing sequence from RF data to shear wave velocities

heart beat. Systole and diastole are marked on the ECG below. Though noisy, the amplitude of the transverse wave varies as indicated in figure 5, and the angle of the propagating wave (which corresponds to the velocity) varies with the cardiac cycle. The response across multiple beats is very repeatable. Systolic shear wave amplitudes tend to start around 5 μm near the excitation, and fall to 2 μm over 3 mm of propagation. Diastolic estimates, on the other hand, initially have 10-12 μm of amplitude, falling to 4-6 μm as they propagate. Figure 7 shows the M-Mode of shear wave velocity estimates through depth and across the 160 acquisitions, along

with the axial median shear wave velocity. The highlighted region of interest is the intersection of the axial ROE and the tracked tissue boundaries. Despite the low quality of many of the slices in figure 6, clear, repeatable variation is seen through the cardiac cycle. The individual estimates show variability, but the overall trend of stiffening and relaxation between 0.9-1.1 m/s and 3.5-5 m/s is clear. Diastolic estimates are especially smooth. Some axial variation is also seen, with the deeper systolic estimates appearing slightly elevated, but the temporal trends of stiffening and relaxation with the cardiac cycle dominate.

Figure 8 shows the distribution of individual velocity estimates from figure 7 in systole and diastole, as indicated by the cyan- and yellow-shaded regions on the ECG in figure 7. The mean values indicate a lower velocity ratio than the median values. Figure 9 shows the multibeat-synthesized data from figure 7. The variation through the cardiac cycle is clear and smoothly varying. A small amount of axial variation is present, but the predominant trend is temporal, with relatively stable velocities during diastole and systole, and a sharp rise in velocity at the onset of systole and a slightly more gradual relaxation at the beginning of diastole. The standard deviations are higher in systole than in diastole, and approximately proportional to the shear wave velocity. Figure 10 shows the shear velocity M-Modes and median velocities for the six animals. Heart rates and motion vary among the animals greatly. The quality of the images from the animals with elevated heart rates (3, 5) appears much worse than those with lower heart rates (1, 2, 4, 6). Table 1 shows the compiled systolic and diastolic shear wave statistics like those shown in figure 8 for each of the six pigs. The means, medians, and standard deviations of all of the velocity estimates are reported from the 160-acquisition sequences like those shown in figure 10. The ratios of means and medians are also shown. The mean diastolic velocities range from 1.42 ± 0.95 m/s to 2.68 ± 1.76 m/s, and the mean systolic velocites range between 3.06 ± 1.78 m/s and 5.12 ± 1.6 m/s. The median velocities, on the other hand,

range between 0.89 and 2.2 m/s in diastole and 2.60 and 5.14 m/s in systole. The systolic-diastolic ratio of means range between 1.77 and 3.02 and the ratio of the medians range between 2.1 and 3.66.

3.4.1 Comparison to Previous Studies

Our results are compared to those previously reported using open chest ARF-driven velocimetry technique, as well as to Kolipaka *et al*'s human MRE experiment(Kolipaka et al., 2010) and Kanai's Aortic Valve Closure (AVC) data(Kanai, 2005) in closed-chest human septum in Table 2 . Tabulated are the different experimental set-ups used to measure myocardial elasticity, as well as the estimated shear modulus in systole and diastole, and the ratios of systolic to diastolic shear modulus. The measured elasticities of this experiment mostly fall within the range of values reported in open-chest studies, although the diastolic estimates from pigs 2, 3, and 6, and the systolic estimate from pig 3 appear higher than previously seen. Compared to the MRE experiment, our diastolic velocities are lower and the systolic velocities distributed around the MRE result. Kanai's AVC data indicate systolic stiffness as high or higher than we measured. Overall, none of the data reported here for diastole or systole fall outside of the range of previously reported myocardial stiffnesses or ratios. Figure 11 shows the results of this experiment and the results of the other myocardial elasticity experiments from Table 2 as shear wave velocities rather than shear moduli for visual comparison. The results from this experiment are listed as "1" through "6" and are shown to be similar to those previously demonstrated.

3.5 Discussion

These results clearly indicate the feasibility of using shear wave velocimetry to image myocardial stiffness and contractility throughout the cardiac cycle with an ICE catheter probe. Despite the hardware limitations of the current platform, we were

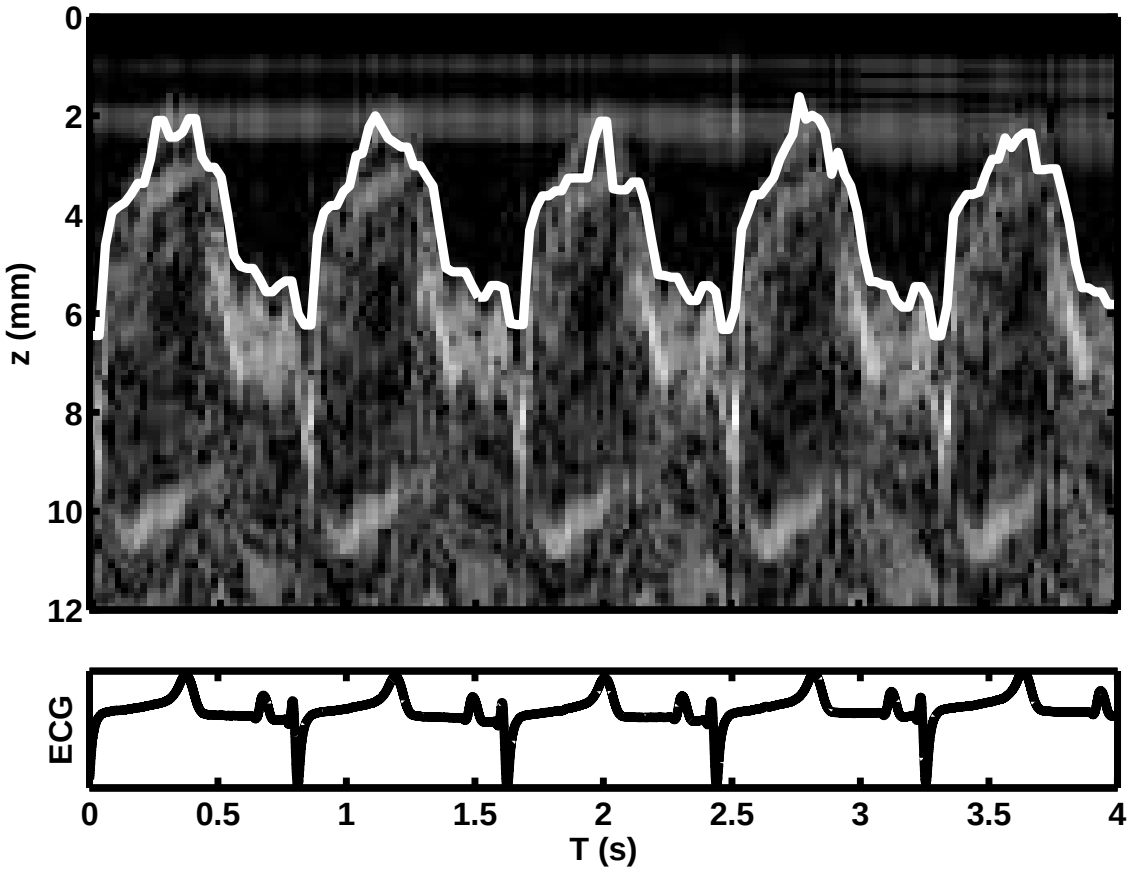

FIGURE 3.4: Axially tracked M-Mode of the IVS. The proximal border of the septum is drawn in white. The motion of the tissue varies repeatably with the cardiac cycle.

able to use creative beam sequencing to image both diastolic and systolic shear waves with the superposition of only two responses, providing rapid temporal sampling that captures the dynamic stiffening and relaxation of the septum. With the catheter placed near the apex of the RV, long axis views of the IVS were readily attained with sufficient thickness, repeatable motion, and high contractility. Views of the RVFW and of the free wall and septum in the RA were also available, but are not presented here because the RVFW in our young pigs was rather thin (less than 2 mm) and the RA has much lower contractile properties. These regions are likely candidates for further study and the regionally-varying dynamic elastic properties of the heart may provide additional information, but for the purposes of demonstrating

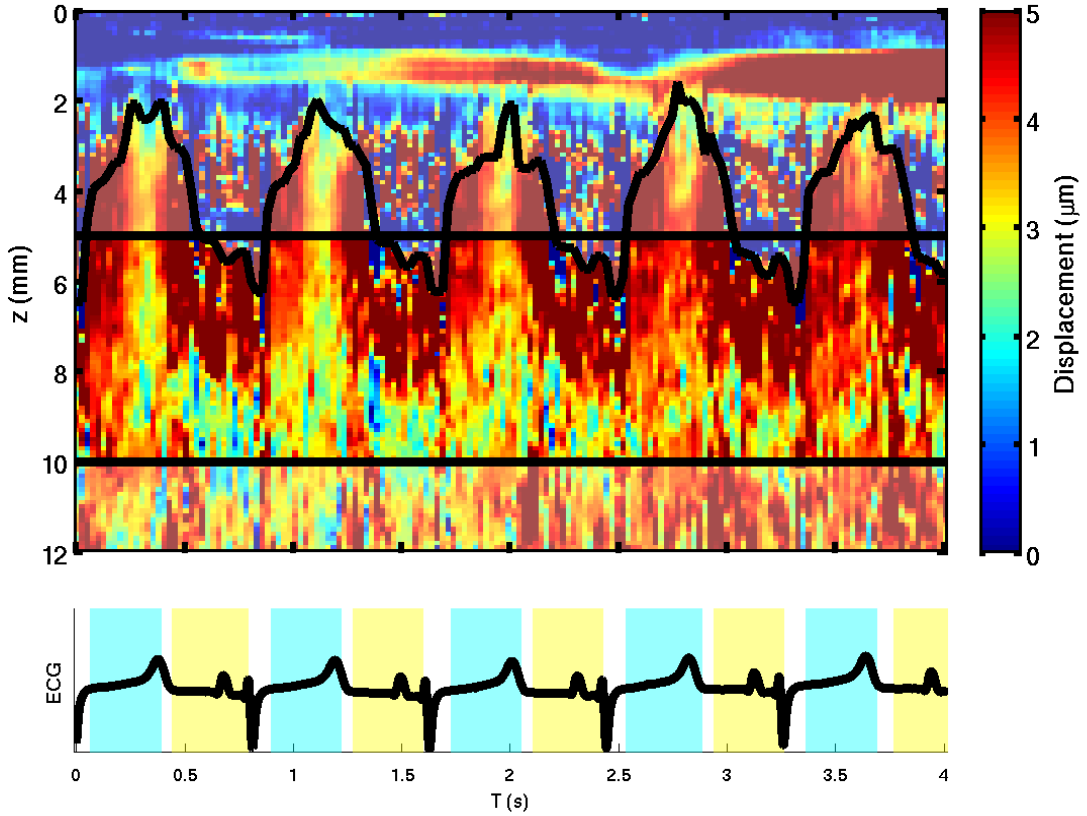

FIGURE 3.5: Transverse wave magnitude in IVS. Black lines indicate the expected region of shear wave generation, between 5 mm 10 mm. The displacement magnitude varies with depth and with the cardiac cycle. Cyclic variation of the displacements is seen with the cardiac cycle, but the axial motion obfuscates estimation of elastic properties.

the feasibility of using ICE to measure cardiac shear wave velocities *in vivo*, the IVS yields compelling data.

With motion filtering, the ARF-induced displacements were mostly separated from the bulk tissue motion and imaged, although in many cases the tissue motion and displacement estimation jitter were too great, resulting in motion artifact as seen in some of the frames of figure 6. Because of this variability in individual wave propagation estimates, putting the data synthesis at the end of our signal processing chain provides a larger number of observations to use, which in turn gives more confidence

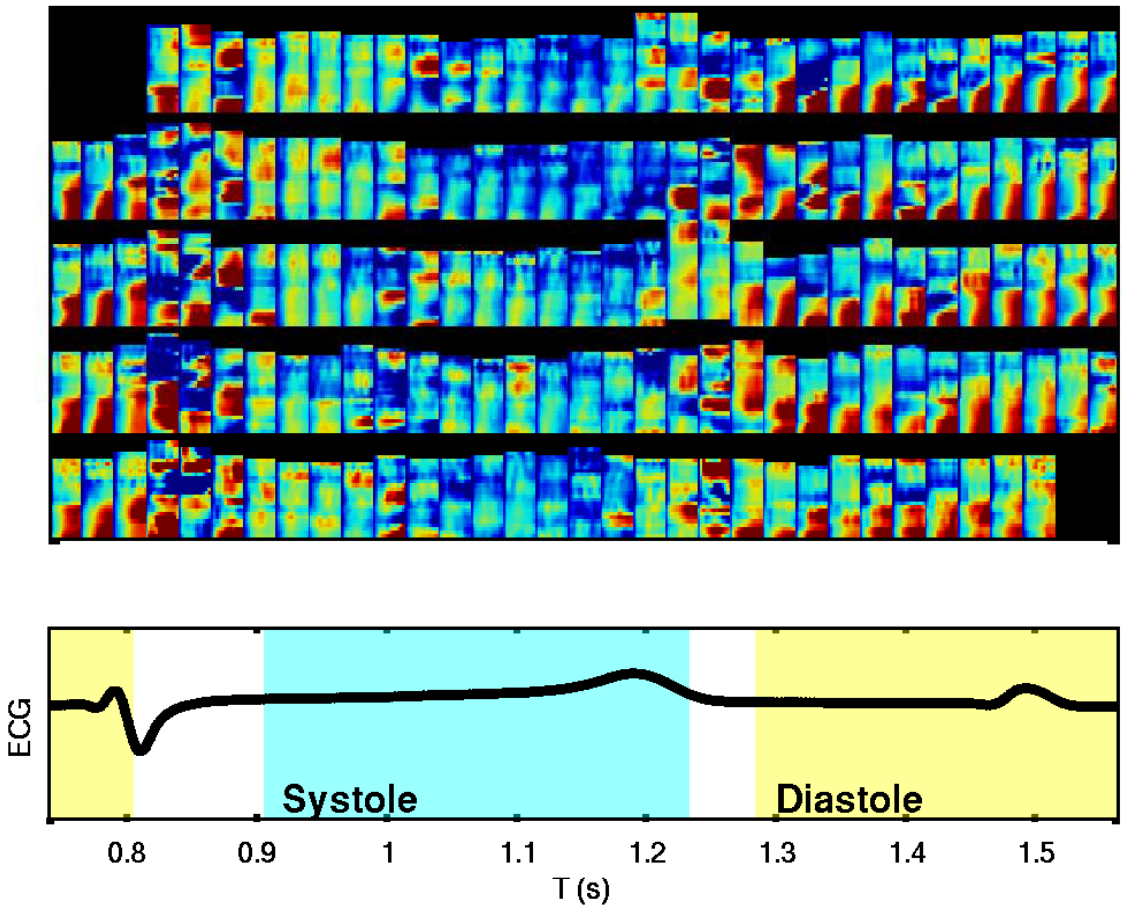

FIGURE 3.6: A selected axial slice of displacement data from each of 160 acquisitions through five heart beats, left to right, top to bottom, selected from the center of the septum. The time-to-peak-displacement fit is superimposed. Blue is no displacement, and red is 8 μm displacement. Systolic slices have steeper slopes (indicating faster propagation) and typically lower amplitudes than diastolic slices. Many of the slices are corrupted by motion. Each image spans 3 ms after the excitation and 2-5 mm laterally.

in our quantitative results. Using separate axial estimates and multi-beat synthesis, we are able to use over 1000 individual estimates for each phase as reported in table 2. Using median values reduces the effect of outliers, which would otherwise affect mean values especially if bad time-to-peak displacement estimates are close together, causing the estimated velocity to trend towards infinity. Obtaining many noisy velocity estimates and then combining them together appears to work better

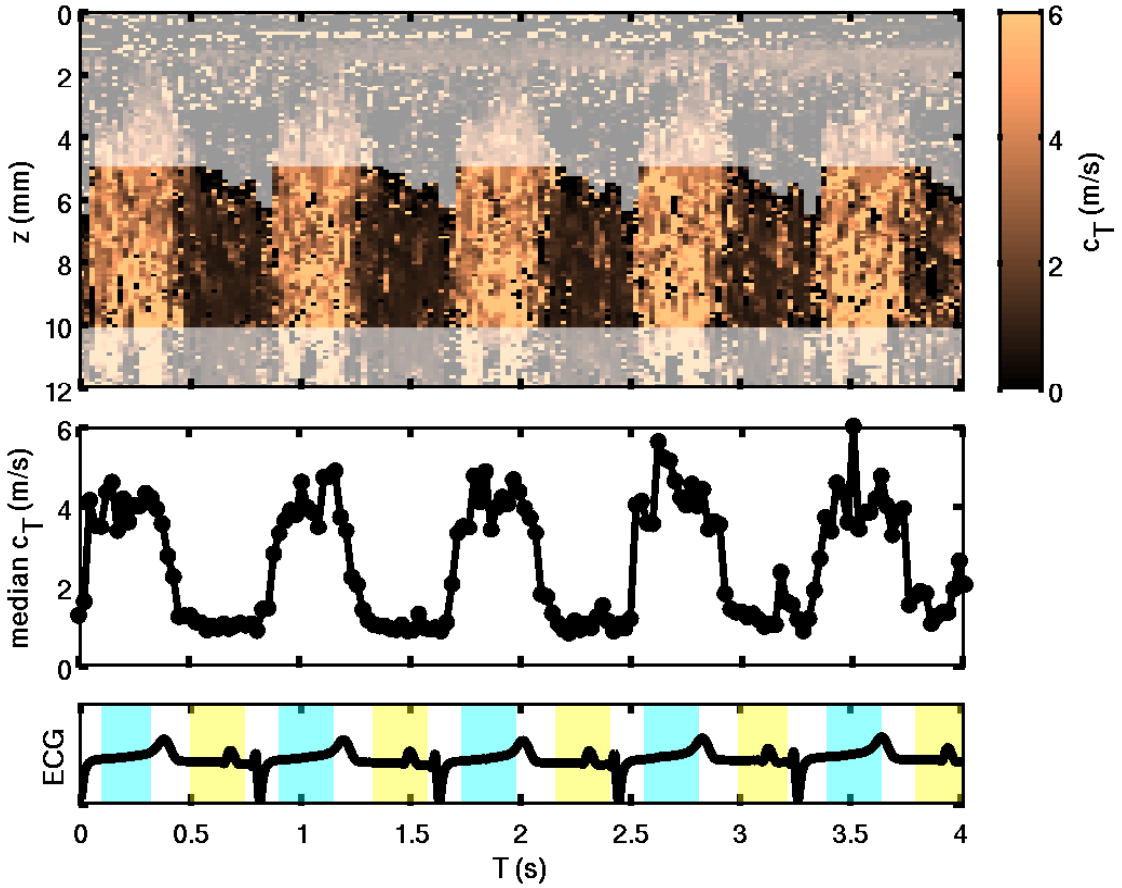

FIGURE 3.7: Shear wave velocities through depth (M-Mode) and axial median shear wave velocities across IVS, through five heartbeats. The highlighted region from 5-10 mm represents the intersection of the axial region of excitation (ROE) and the septal tissue location. The beat-to-beat repeatability of the stiffening and relaxation is very high, with systolic velocities between 3.5 and 5 m/s and diastolic velocities between 0.9 and 1.1 m/s.

than averaging the displacements axially and finding a single estimate as is normally done, at least in the case of small displacements and high motion. A single depth's displacement profile corrupted by motion could throw off the entire estimate of time-to-peak displacement and thus shear wave velocity for the kernel, but processing each depth independently avoids this because individually bad estimates can be filtered amidst otherwise good estimates.

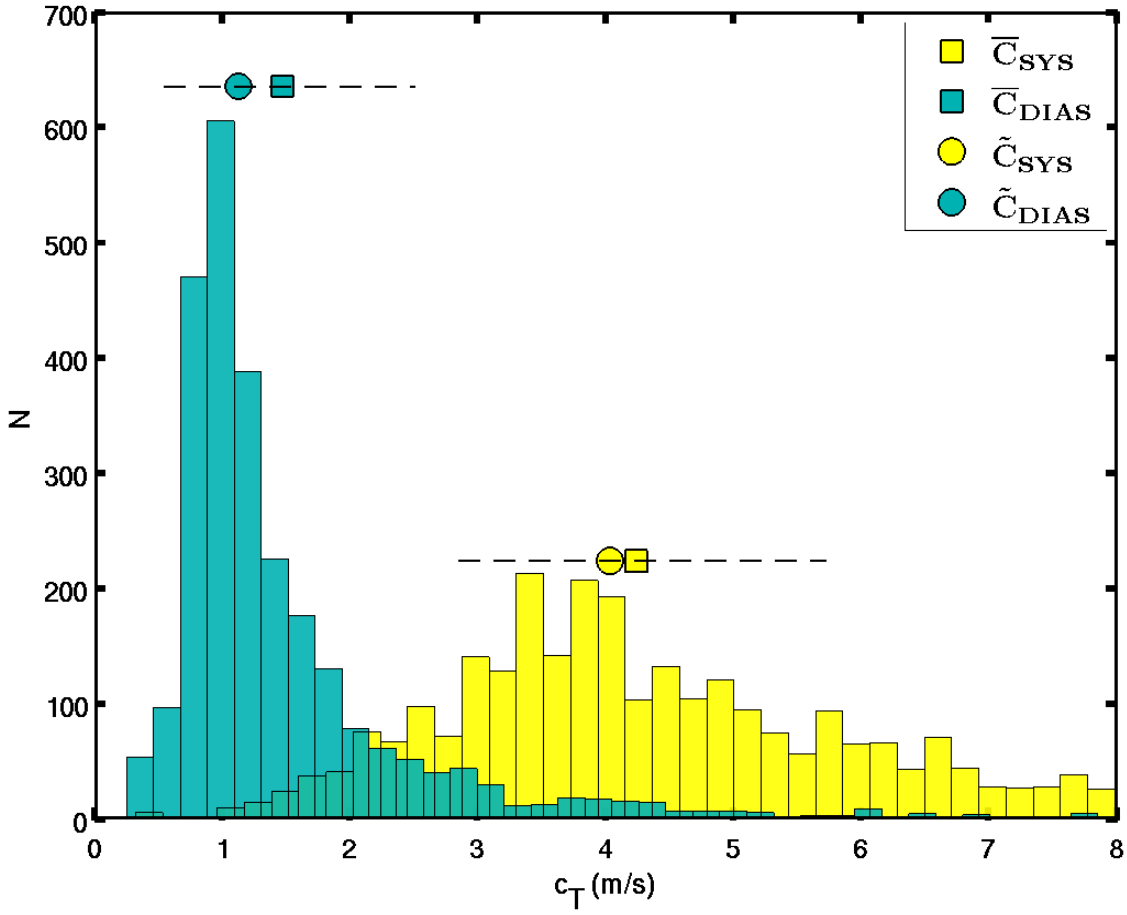

FIGURE 3.8: Distribution of all diastolic and systolic shear wave speed estimates over 160 acquisitions, extracted from Figure 3.7 according to the cyan and yellow shaded regions of the ECG. The medians and means are marked as squares and circles, respectively. The systolic-diastolic ratio of medians is 3.66 and the ratio of means is 3.02.

3.5.1 In Vivo Results

The diastolic and systolic velocities across all animals varied among animals, but the ratios were more consistent. The first pig had the highest ratio, but was also the oldest, with the thickest septum, which could be the reason for the increased contractility. The second and third pigs in figure 10 had elevated median diastolic velocities, although the minimum velocities appear visually similar to the first pig

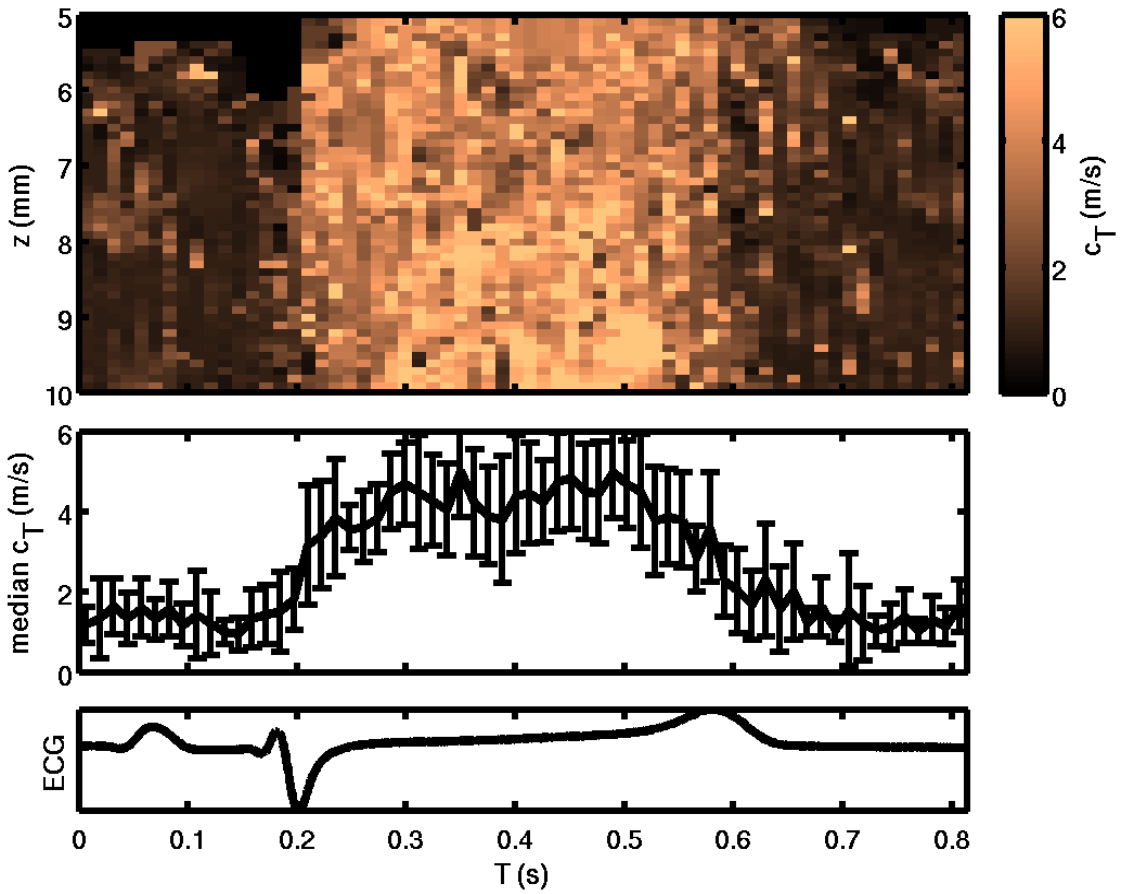

FIGURE 3.9: Multibeat synthesis of the M-Mode SWEI from figure 3.7 using 5 heartbeats of data. The trends visible in figure 3.7 remain, with reduced noise. The rise in stiffness immediately following the QRS complex is particularly sharp.

in figure 10. The shortened length of diastole due to the elevated heart rates of these animals could be contributing to this, although in the second pig, the 4th and 5th beats have very clean and consistent data in diastole with visually elevated velocities. The third pig has a higher heart rate than the second, and the distal part of its septum appears to behave similarly to the first pig, although the proximal tissue appears very noisy. The source of spatial variation could be due to the field of view. The third pig was imaged with a focal depth of 10 mm, and the proximal side of the ROE is at 5 mm, so the lateral extent of the field of view at the shallow depths is only 1-2.5 mm. For shallow imaging, a different set of steering angles for

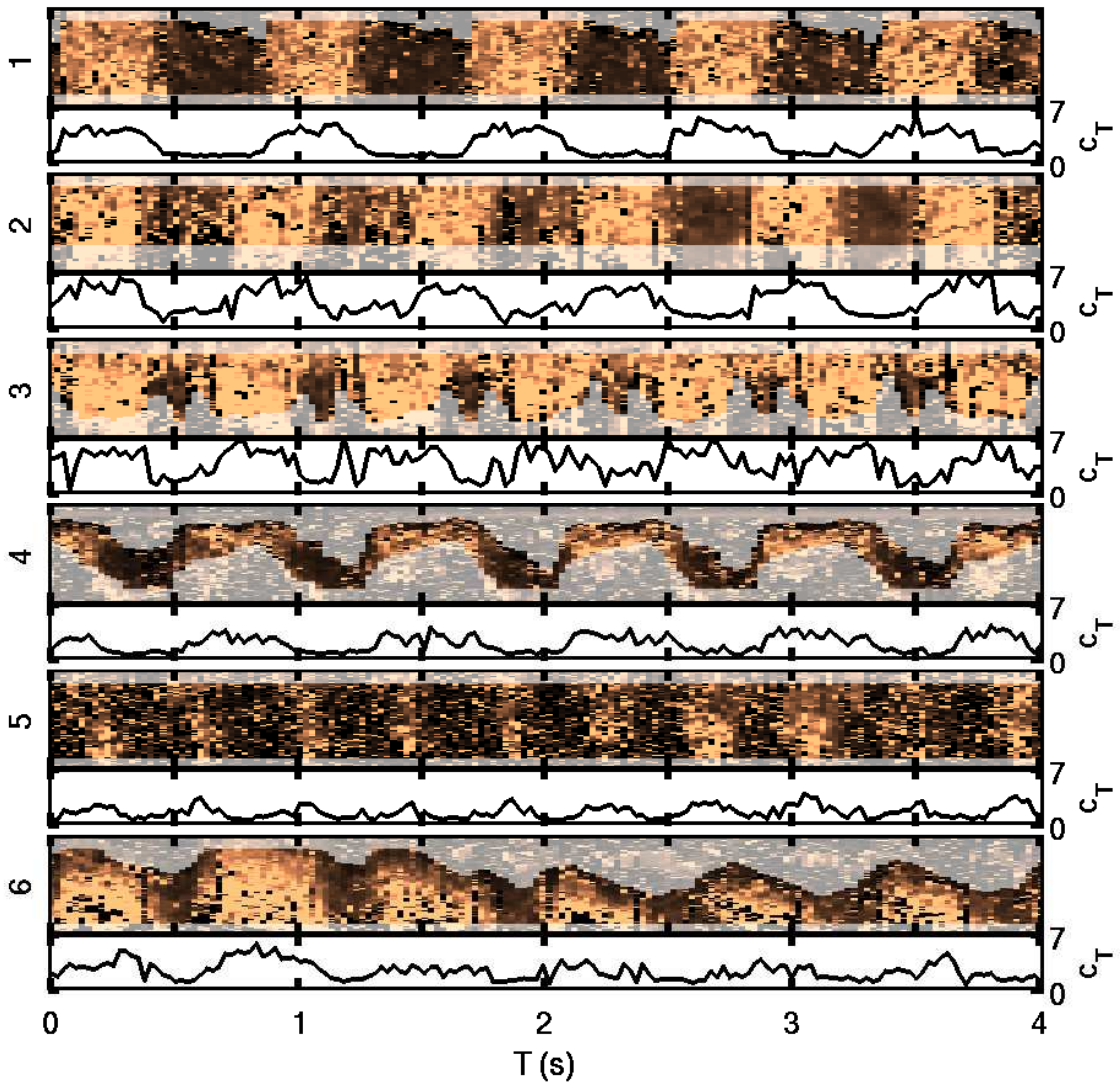

FIGURE 3.10: Shear wave velocity M-Modes and axial median profiles for each of the six pigs. Regions that fall either outside the tissue or outside of the region of excitation (ROE) are grayed out in the M-Mode and not included in the median estimate. Rejected estimates appear as black pixels. The color ranges from 0 m/s (dark brown) to 6 m/s (tan) The quality of the images declines with higher heart rates (pigs 3 and 5). All pigs exhibit cyclic variation of velocities.

wave tracking may yield superior results. The fourth pig had a very thin septum (2.5 mm in systole and 5 mm in diastole) with high motion, which may indicate that a different model (i.e. Lamb wave) would be more appropriate, but the velocity trends are consistent with the others. Following the tissue as it moves axially, the velocities

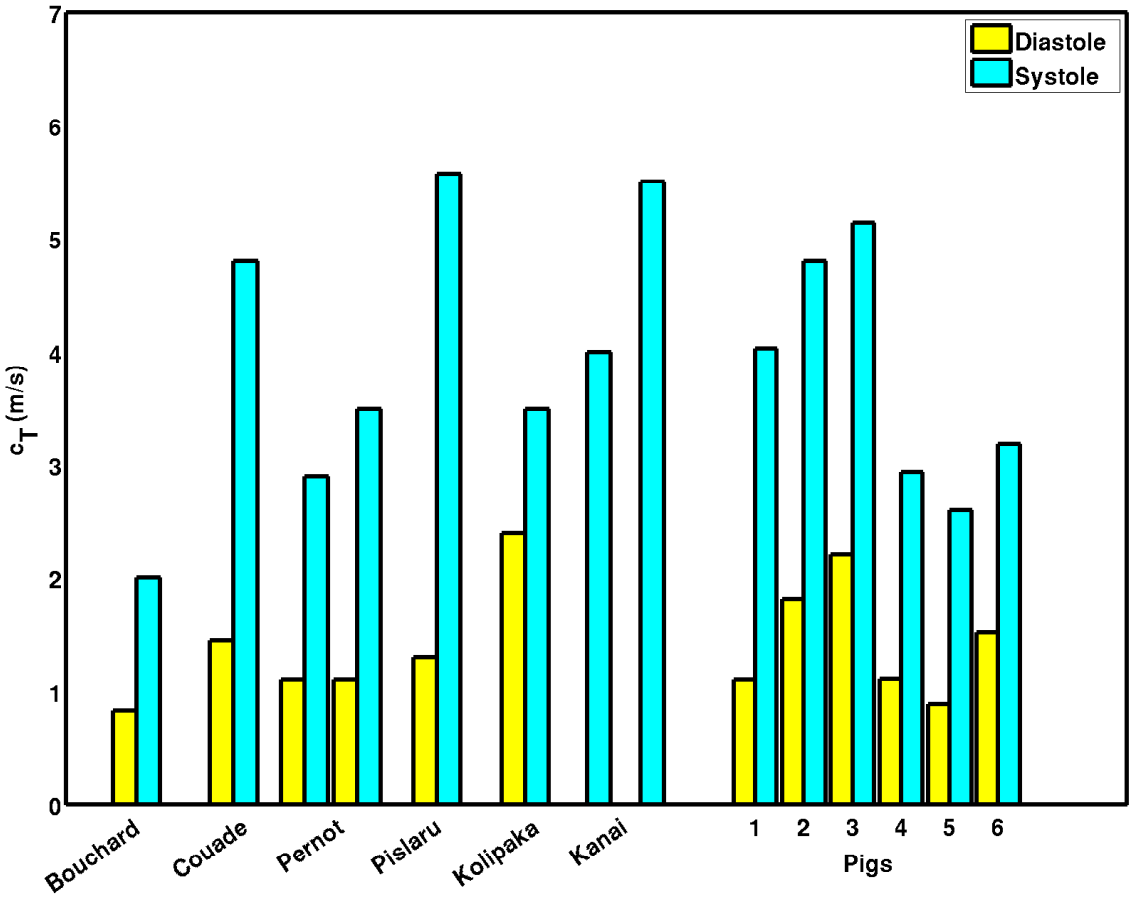

FIGURE 3.11: Comparison of shear wave velocities from this experiment with those previously reported in the literature. The methodology, animal model, and tissue targets vary between experiments, and all data reported as shear moduli have been converted to shear wave velocities.

consistently rise in systole and fall in diastole. This animal would be difficult to analyze with M-Mode ARFI due to the motion, but appears usable with SWV. The fifth pig initially looks especially bad, but its heart rate was above 150 BPM, and repeatable velocity peaks are in fact seen which correspond to systole. When calculating the ratios, however, the values for diastole and systole appear normal, altough systole is the low end, likely due to the very short systolic duration. The sixth pig has respiration motion, as well as axial variation in shear wave speeds, but otherwise exhibits the same characteristic stiffening and relaxation. Only in pigs 4

Table 3.1: Ages, Weights, Heart Rates (HR), Non-invasive Blood Pressure (NBP), and Systolic and diastolic septal shear wave velocity estimates for six healthy pigs

Pig	#	1	2	3	4	5	6
Age	days	123	72	74	76	81	74
Weight	kg	42.9	32.7	28.1	29.9	23.0	33.3
HR	BPM	73.7	87.7	102.3	77.1	148.0	91.8
NBP	mmHg	89/47	69/28	88/30	89/40	92/32	85/41
$\bar{c}_{Tsys}$	m/s	4.28	4.87	5.12	3.07	3.06	3.47
$\tilde{c}_{Tsys}$	m/s	**4.03**	**4.80**	**5.14**	**2.94**	**2.60**	**3.18**
σ_{sys}	m/s	1.49	1.61	1.60	1.71	1.78	1.92
$\bar{c}_{Tdias}$	m/s	1.42	2.15	2.68	1.50	1.49	1.97
$\tilde{c}_{Tdias}$	m/s	**1.10**	**1.81**	**2.20**	**1.11**	**0.89**	**1.52**
σ_{dias}	m/s	0.95	1.27	1.76	1.09	1.45	1.29
$\bar{c}_{Tsys}/\bar{c}_{Tdias}$		3.02	2.26	1.91	2.05	2.05	1.77
$\tilde{c}_{Tsys}/\tilde{c}_{Tdias}$		**3.66**	**2.66**	**2.34**	**2.64**	**2.91**	**2.10**

Table 3.2: Comparison of results to other selected papers. The median values were used from this work.

Source	Animal	Target	G_{Dias} (kPa)	G_{Sys} (kPa)	Ratio
Bouchard *et al.*	Canine	LVFW	0.69	4.00	5.81
Couade *et al.*	Sheep	LVFW	2.10	23.04	10.96
Pernot *et al.*	Rat	LVFW	1.21	8.41-12.25	6.95-10.12
Pislaru *et al.*	Pig	RVFW	1.7	31.0	18.23
Kolipaka *et al.*	Pig	LV	5.76	12.25	2.13
Kanai	Human	IVS		16.00-30.25	
Pig 1	Pig	IVS	1.21	16.24	13.42
Pig 2	Pig	IVS	3.28	23.04	7.03
Pig 3	Pig	IVS	4.84	26.42	5.46
Pig 4	Pig	IVS	1.23	8.64	7.02
Pig 5	Pig	IVS	0.79	6.76	8.53
Pig 6	Pig	IVS	2.31	10.11	4.38

and 6 is the proximal edge of the septum within the ROI, so similar spatial trends may be present in the other animals. This could be due to the intrinsic anisotropy of the septum due to fiber orientation, or to differences in RV and LV contractility. The distal portion of pig 6's septum look more like pigs 1-3, but the spatial variation

causes the median systolic value to be lower. Accounting for the variability among animals, and exploring the regional variations in contractility will be the topic of future work. Nonetheless, in all of the animals, we can see clear temporally-varying shear wave speeds with each heartbeat.

3.5.2 Comparison to Previous Studies

All of measured velocities in this experiment are within the ranges reported in the literature for myocardium in systole and diastole. There are, however, substantial differences within the values reported in the literature. A more elaborate experiment may need to be devised to compare the ultrasonically measured results to a gold standard like mechanical testing, although excised tissue degrades quickly and obtaining the exact interrogated piece of tissue in the same condition with the same fiber orientation would be difficult, as would applying the same pressures experienced *in vivo*. What would possibly be the closed-chest gold standard for comparison, MRE, is limited by being a global metric. Kolipaka *et al.* modeled the LV as a homogeneous shell; contractility variation, whether spatially or in timing, could be the source of the much lower reported ratio. Using the previously reported ultrasound data as a reference, the ranges of values measured here using ICE appear at least comparable. The differences between our results and those previously reported, and within those previously reported, could come from a number of sources. Different animal models and tissue targets were used which would certainly introduce variation, but even our data, which are all from pigs, show substantial animal-to-animal variability in the long-axis IVS. Anisotropy affected the shear speeds but not the ratios in Couade *et al.*'s work, and the fibrous nature of myocardium warrants further exploration of this where possible. Pernot *et al.* show a linear dependence on pre-load for systolic moduli between 80 and 160 mmHg, which could explain some of the systolic variability that we have seen. Dispersive methods like that shown by Pislaru *et al.*

use the phase velocities to find frequency dependent velocities, and the characteristic excitation varies between the experiments, so the spectral content of the propagating wave is yet another source of variation. Within the same experimental set-up, however, the excitation is constant, and the variation is likely due to actual variations in pressure or regional tissue properties.

3.5.3 Limitations and Future Work

The biggest limitations of this experiment were system capabilities. The scanners that currently support running customized ARF sequences on the AcuNav are capable of beamforming only four azimuthal lines per transmit. Newer systems can beamform more simultaneous lines, or even store individual channel data. Adapting these systems to work with the AcuNav would permit use of a defocused transmit for the tracking pulse and imaging the entire field of view simultaneously. Wide field-of-view tracking would improve velocity estimates by reducing the number of excitations needed from two to one, allowing simultaneous tracking of waves to the left and right of the excitation, and providing additional azimuthal locations for motion and kick-back filtering. With finer temporal sampling, we would be able to capture the dynamics of contraction and relaxation better, especially for cases of elevated heart rates. Future work will also include pressure measurements to normalize the effect of pre-load on systolic measurements (Pernot et al., 2011).

The spatially-varying properties may be the most interesting subject to explore, and a longer axial ROE, obtained with multiple excitations, would improve our ability to image these variations. Because the AcuNav is an FDA approved device, and the MI and thermal measurements and simulations indicate safety, clinical translation should be possible. Clinical work will also need to be done to determine the quantitative relationship between tissue health and observed transverse wave propagation, with respect to both the tissue model and the nature of the excitation. This study

was performed on the IVS, but LV contractility has typically been the parameter of interest. Further work needs to be done to relate properties measured in the IVS to those measured in the LVFW for indicating LV function. Extending this work to image the LVFW directly is also an area of future study, and we have identified two potential solutions. The first would be to insert the ICE transducer into the LV, either retrograde across the aortic valve or across the atrial septum and through the LA, although both of these entry paths carry additional risks. The second would be to use a larger or lower frequency ICE transducer to generate focused radiation force in the LVFW from the catheter in the RV. The second solution is likely more favorable from a safety standpoint, but may require a specialized transducer to generate sufficient radiation force at depth.

3.6 Conclusions

We have demonstrated the viability of using intracardiac echocardiography linear phased arrays to perform ARF-based velocimetry in myocardium though the cardiac cycle. We have shown cyclically varying shear wave speeds in the interventricular septum across six healthy animals, with systolic to diastolic shear modulus stiffness ratios between 4.4 and 13.4. Customized beam sequences make this measurement in sets of acquisitions at up to 40 frames per second. Operating within FDA limits, the AcuNav is well suited for clinical studies to explore the relationship between ARF-induced shear wave speeds and cardiac function. With appropriate considerations of the dynamic intracardiac environment, ARF shear wave velocimetry from an ICE catheter provides a minimally invasive way to quantify myocardial elasticity and contractility in the beating heart.

4

Intracardiac Acoustic Radiation Force Impulse (ARFI) and Shear Wave Imaging in Pigs with Focal Infarctions

This chapter was published in 2013 and is presented in its entirety (Hollender et al., 2013). This work represents the results of a long and challenging animal study. The imaging methods from chapter 3, along with new ones, representing the peak sequence complexity achieved with the S2000 scanner, are applied to an infarct model with the goals of imaging contractility changes in and around infarcted areas, and to look for remodeling in spared areas. To our surprise, the pigs developed "spotty" infarctions extending away from apex. This threw a cog in our wheels, because we had intended to use anatomical markers to define our infarcted, border, and spared regions. The data showed early on that there was involvement of non-apical regions and regions of spared myocardium near the apex, which would later be confirmed by the ex vivo MRI. This work would motivate the involvement of the EAM system to track specific catheter position, since there was no good way to register the ultrasound images to the gold standard MRI. With the EAM system located in our lab, however, we could not do longitudinal animal studies, and the experiment is yet to be attempted again.

4.1 Abstract

Four pigs, three with focal infarctions in the apical intraventricular septum (IVS) and/or left ventricular free wall (LVFW), were imaged with an intracardiac echocardiography (ICE) transducer. Custom beam sequences were used to excite the myocardium with focused acoustic radiation force (ARF) impulses and image the subsequent tissue response. Tissue displacement in response to the ARF excitation was calculated with a phase-based estimator, and transverse wave magnitude and velocity were each estimated at every depth. The excitation sequence was repeated rapidly, either in the same location to generate 40 Hz M-Modes at a single steering angle, or with a modulated steering angle to synthesize 2-D displacement magnitude and shear wave velocity images at 17 points in the cardiac cycle. Both types of images were acquired from various views in the right and left ventricles, in and out of infarcted regions. In all animals, ARFI and SWEI estimates indicated diastolic relaxation and systolic contraction in non-infarcted tissues. The M-Mode sequences showed high beat-to-beat spatio-temporal repeatability of the measurements for each imaging plane. In views of noninfarcted tissue in the diseased animals, no significant elastic remodeling was indicated when compared to the control. Where available, views of infarcted tissue were compared to similar views from the control animal. In views of the LVFW, the infarcted tissue presented as stiff and non-contractile compared to the control. In a view of the IVS, no significant difference was seen between infarcted and healthy tissue, while in another view, a heterogeneous infarction was seen presenting itself as non-contractile in systole.

4.2 Introduction

4.2.1 Myocardial Infarction

Bogen *et al.*Bogen et al. (1980) notes that myocardial infarction is characterized by a localized increase in myocardial stiffness and decreased contractility that evolves over weeks after the infarction event. Increased wall stresses in the rest of the ventricle cause it to grow and thin, increasing dysfunction and the subsequent risk of heart failure. The infarcted tissue is replaced by collagen, forming a stiff, fibrous scar (McKay et al., 1986; Uusimaa et al., 1997). Concurrent with scar formation, the ventricles may remodel to compensate for the thinned, scarred segments being unable to support wall stresses. Remodeling is a change in the size, shape, and function of the ventricle, and often a precursor to eventual heart failure.

Infarctions can be imaged with a number of modalities, including contrast-enhanced MRI (Lima et al., 1995; Kim et al., 1999, 2000; PG and J, 2012), PET (Matsunari et al., 2003), computed tomography (CT) (Mahnken et al., 2005), and most commonly, echocardiography (Heger et al., 1979; Hauser et al., 1985; Gruseels et al., 1995). Echocardiography is used to diagnose wall motion abnormalities as an indicator for infarction, but does not distinguish dead myocardium from "stunned" (Braunwald and Kloner, 1982; Bolli, 1990; Hare, 2007) or otherwise dysfunctional myocardium. A means to distinguish necrotic, stunned, hibernating, edemic, and healthy regions of tissue in the emergency room could greatly improve diagnoses and management (Pagley et al., 1997; Haas et al., 1997).

4.2.2 Acoustic Radiation Force Impulse and Shear Wave Elasticity Imaging

The motional response of tissue to external forces can be used to infer information about the tissue's mechanical or elastic properties. Acoustic Radiation Force Impulse (ARFI) imaging uses focused, 10-100 μs ultrasonic pulses to locally transfer

momentum into the tissue via absorption. The tissue transiently displaces away from the transducer around the focus, and the relative magnitude of this induced displacement between different excitations can be imaged with high-framerate ultrasound and used to make images of relative elasticity. Another way to characterize elasticity is to image at the propagation velocity of transverse (shear) waves through a medium. Under a linear, semi-infinite, purely-elastic assumption, the shear wave velocity is related to the shear modulus by $c_T = \sqrt{G/\rho}$, where c_T is the velocity in m/s, G is the shear modulus in kPa, and ρ is the density, in g/cm^2. This is known as Shear Wave Elasticity Imaging (SWEI), and acoustic radiation force (ARF) is a convenient way to generate shear waves within the ultrasonic field of view (FOV).

Cardiac elasticity imaging with these ultrasonic techniques and others has been an area of increasing interest for its potential in directly imaging the mechanical compliance of dysfunctional, infarcted or fibrotic regions of myocardial tissue Kanai (2005); Hsu et al. (2007b); Bouchard et al. (2009b); Pislaru et al. (2009); Couade et al. (2011); Pernot et al. (2011); Bouchard et al. (2011). These studies have all imaged a transient mechanical response with ultrasound to characterize myocardial stiffness. Kanai imaged the transient Lamb wave generated in the IVS in response to aortic valve closure, but the other work has required external excitation of the myocardium, either mechanically or with Acoustic Radiation Force (ARF). In order to generate a highly localized excitation, the animals' chests were opened and the excitation transducer was coupled directly to the myocardium.

Intracardiac Echocardiography (ICE) holds promise for obtaining the proximity to the tissue needed to generate and track tissue response to ARF excitations. ICE is commonly used for function assessment and therapy guidance Mullen et al. (2003); Chu et al. (1994); Daoud et al. (1999); Marrouche et al. (2003); Vaina et al. (2006), and has already been shown to be feasible for cardiac ARFI imaging Hsu et al. (2005); Hollender et al. (2011). Because the imaging transducer is located so

close to the myocardium, less ultrasonic energy is needed to excite the tissue, and the response can be imaged without the clutter associated with imaging across the chest wall. This work uses an intracardiac implementation to explore the possibility of using Shear Wave Elasticity Imaging (SWEI) and Acoustic Radiation Force Impulse (ARFI) imaging to distinguish healthy myocardium from infarcted myocardium. While a transthoracic means to image cardiac elasticity with ultrasound would have the greatest clinical potential for diagnosing AMI, this implementation may benefit patients in procedures where ICE is already called for and the location of infarcted myocardium is of interest (transcatheter ablation or pacemaker lead placement, for example). Moreover, this work aims to explore the elastic appearance and behavior of infarctions in a closed-chest animal model.

4.3 Methods

4.3.1 Experimental Setup

All data presented were acquired with 10-French ICE catheters, either the Siemens Acuson AcuNav (Siemens Medical Systems, Mountain View, CA, USA) or on a Biosense Webster SoundStar (Biosense Webster Inc, Diamond Bar, CA, USA), running on a Siemens S2000 scanner. Both transducers use the same 64-element, 7.25 MHz linear phased array, with a 7 mm aperture in azimuth, but the SoundStar has an additional magnetic positioning sensor in its tip.

Demodulated in-phase and quadrature (IQ) ultrasound data from custom pulse sequences were recorded with matched ECG data from eight porcine subjects in compliance with protocols from Duke University's Institutional Animal Care and Use Committee (IACUC). One of the pigs was used as a control, and the other seven were subjected to ischemia through a series of foam embolizations to the left anterior descending (LAD) coronary artery, designed to mimic chronic ischemia in the apical IVS and lead to heart failure, but which ultimately created a pathology

more like acute myocardial infarction (AMI). Additionally, in all but one of the initial injections, foam was unexpectedly also delivered to the left circumflex (LCX) coronary, resulting in infarction of the LVFW as well. Unfortunately, four of the animals did not survive to the first follow-up study. The four remaining animals (three embolized and one control) comprise the cohort for the data presented here.

The ICE catheter was either fed through the right atrium into the right ventricle (RV), or inserted retrograde across the aortic valve into the left ventricle (LV). The animals were each imaged four times: once prior to the embolization, and three times following, over a time period of approximately 150 days. The first follow-up imaging session was at 40 ± 12 days after embolization, the second at 53 ± 11 days, and the final study at 130 ± 24 days. The catheter was placed in the LV only during the final imaging study for safety purposes, after which the animals were sacrificed and their hearts sent for contrast-enhanced MRI imaging and subsequent histology. Imaging planes were selected to view the ventricular free wall, either from the RV outflow tract or near the apex, as well as the IVS, under the condition that the tissue was at most 20 mm from the transducer face. In each view, up to three M-Mode and one 2-D datasets were collected. In each imaging session, at least one view of the IVS and one view of the RVFW were obtained. Where independent views of the IVS or RVFW could be obtained, additional views of the same wall were imaged, especially when the presence of infarction was suspected. A total of 196 datasets were collected across the 16 imaging sessions.

4.3.2 Custom Beam Sequences

The impulsive excitation was generated with a 6.15 MHz 400-cycle (65 μs) pulse, using a single focus selected to maximally intersect the myocardium throughout the cardiac cycle. Available foci were every 2.5 mm betwen 7.5 mm and 20 mm. Previous intensity measurements and thermal FEM modeling(Palmeri and Nightingale, 2004)

(data not shown) indicated that for similar pulse sequences (15 mm focus and 6 MHz center frequency), the Mechanical Index (MI) is under 1.63, the I_{SPPA} was under 2000 W/cm^2 (derated at α=0.3), and tissue heating at the focus is low, 1.01°C over four seconds with 80 excitations per second. The I_{SPTA} will thus be as high as 10 W/cm^2 during transmission of ARF pulses at 80 times per second. The beams were repeated and steered in two different tracking schema, to make the two types of images. A summary of the parameters are found in Table 4.1.

Table 4.1: Parameters for Imaging Sequences

Common Parameters	
Center Frequency	6.15 MHz
PRF	9.12 kHz
Excitation Pulse Duration	64 μs
Excitation Focus Range	7.15 mm - 20 mm
Tracking Pulse Bandwidth	50 %
Tracking Transmit Focus	400 mm
Imaging Depth	40 mm
B-Mode Parameters	
Field of View	90°
Beam Spacing	0.65°
M-Mode ARFI-SWEI Parameters	
Excitation Steering Angle	0°
Tracking ROI	15° right of center
Tracking Lines	16
Tracking Duration	5 ms
Excitations per Ensemble	2
Ensemble PRF	40 Hz
Number of Ensembles	160
Synthesized 2D ARFI-SWEI Parameters	
Excitation Steering Angles	-22.5° - +22.5°
Excitation Angular Spacing	2.7°
Tracking Duration 3 ms	
Tracking ROI	16° right of each excitation
Tracking Lines per Excitation (ARFI)	1
Tracking Lines per Excitation (SWEI)	3
Number of Synthesized Images	17

M-Mode ARFI-SWEI Sequences

To generate high temporal sampling of the cardiac dynamics, the excitation beam was held in the same location and rapidly repeated to generate M-Modes of shear wave velocity and displacement magnitude. The tissue response was measured between 0° and 15° to the right of the center of the B-Mode field of view as the superposition of two identically-generated responses, each imaged at different lateral locations. A diagram of the tracking configuration is shown in figure 4.1(a). Four parallel tracking beams were simultaneously recorded at a maximum depth of 40 mm, repeated at 9.12 kHz for 5 ms following each excitation. The receive beams directions were rapidly modulated during tracking, such that each receive beam alternately sampled two locations at 4.56 kHz each, for a total of 8 tracked angles per excitation. The tracking locations were changed on the second excitation for a total of 16 tracking lines across the two excitations. The tracking transmit beams had a 6.15 MHz center frequency, and were focused at 400 mm to distribute transmit energy across the dynamic-receive-focused receive beam locations. The entire excitation-tracking ensemble was repeated 40 times per second for four seconds, with a 90° field-of-view B-Mode image acquired between each ensemble.

Synthesized 2D ARFI-SWEI Sequences

An ECG-gated multi-beat synthesis method was used to generate sequences of 2D ARFI and SWEI images that image multiple locations throughout the cardiac cycle. Because the excitation-response ensemble takes at least 5 ms per line, each ARFI or SWEI image takes much longer to acquire than a B-Mode image; in moving or changing imaging targets, this introduces artifacts associated with the time delays between imaging each angle. To address this, custom sequences were written that change the order in which the angles are imaged on each successive beat. A diagram is shown in figure 4.2. Over a number of beats, each angle in the field of view gets

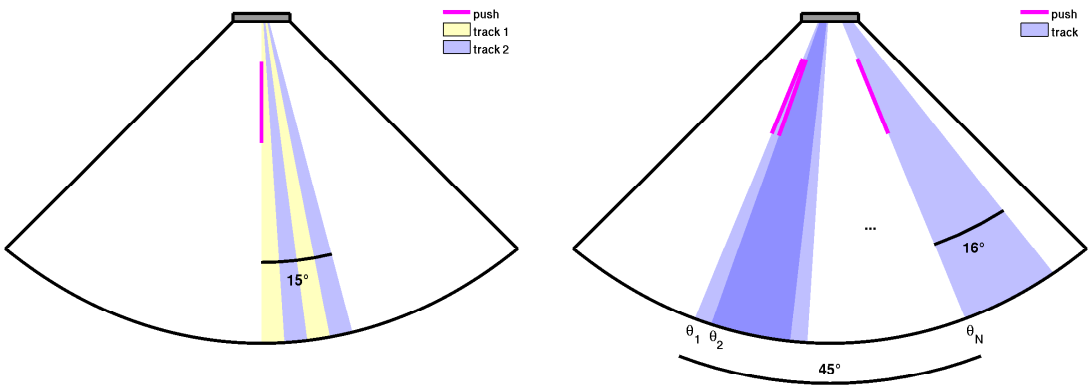

(a) (b)

FIGURE 4.1: (a) Locations of the M-Mode ARFI-SWEI excitation and tracking regions. Four closely-spaced parallel tracking lines are rapidly steered between the two yellow tracking regions following the first excitation, and between the two blue tracking regions after the second excitation, for a total of 16 tracking lines. (b) Locations of the synthesized 2D ARFI-SWEI image sequence acquisition ROIs. Four parallel tracking lines cover 16 degrees to the right of each of the N excitation locations. In this work, N=17 and the excitations are spaced 2.66° apart.

imaged at each delay in the cardiac cycle. There are a number of ways to configure the modulation of angles and delays with ECG triggering, but we selected a method that uses 17 excitations per image, and synthesizes 17 images over a configurable time selected to cover approximately one beat to stay within the memory restrictions of our system. On the first beat, the excitation steering angle progressed from left to right in 2.66° increments at intervals of 1/17th of the R-R interval, starting on the first QRS complex at the leftmost beam (beam 1) and ending approximately on the following QRS complex with the rightmost beam (beam 17). B-Modes were acquired between each ensemble, and the delay between ensembles was set so that the last beam was acquired approximately a full beat after the first. On the second beat, the ensembles progressed from left to right again, but started at beam 2 on the QRS complex, and then acquire beams 3 through 17, followed finally by beam 1. The pattern continued as the third beat started with beam 3, the fourth with beam 4, and so on and so forth to the final acquisition, which excited first beam

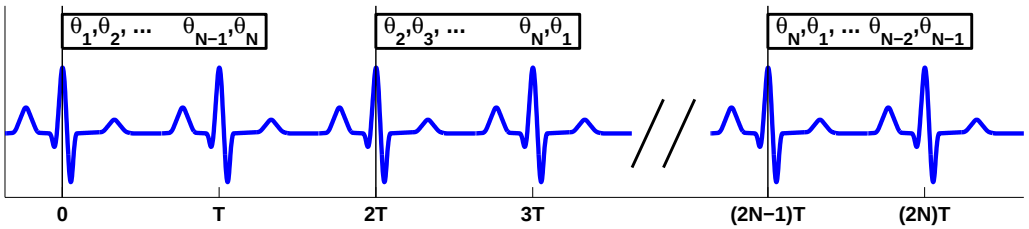

FIGURE 4.2: The ECG-triggered acquisition scheme used to synthesize 2D ARFI and SWEI image sequences. Each box represents an acquisition, indicating the order in which the scan lines are excited and tracked. The width of each box is the total time to acquire all N scan lines in each acquisition. T is the RR-Interval, and the vertical black lines represent ECG trigger signals. The work in this paper uses N=17.

17 on the QRS, followed by beams 1 through 16 over the final beat. The entire sequence actually took 34 heartbeats to acquire (rather than the minimum of 17), since the ECG trigger could not be configured to fire immediately following each set of 17 ensembles, requiring an extra beat between each acquisition set to reset. To track the on-axis (ARFI) and off-axis propagation (SWEI) from each excitation, four receive beams were used, one aligned with the excitation, and the other three spanning 16 degrees to the right of the acquisition, as shown in figure 4.1(b). To reduce respiration motion artifact in the synthesized image sequences, respiration was temporarily held during acquisition. More lateral locations or time steps could not be synthesized with this setup, since our 17-time, 17-push-location image sequences generated the largest files that could be saved by our scanner (200 MB).

4.3.3 Shear Wave Speed Estimation

A phase-shift based displacement estimator (Kasai et al., 1985) was used to calculate the ARF-induced axial displacements, using a 1.5-λ kernel, progressively calculating the displacements between each successive pair of frames in the ensemble. To calculate the total displacement from the pairwise estimates, the stepwise displacement estimates were integrated. Once the displacements had been calculated, a third-order

polynomial motion filter was used to remove the bulk axial motion of the tissue from the ARF-induced displacements (Giannantonio et al., 2011). For each ensemble in the M-Mode data, the temporal displacement estimate profiles were linearly interpolated up to 9.12 kHz to fill in the missing time steps due to the steering angle modulation. These displacement data, when tracked at the same steering angle as the excitation, are referred to as Acoustic Radiation Force Impulse (ARFI) displacements, while the rest of the data are used for velocity estimation.

At each depth and steering angle, the time to peak slope, or arrival time, was estimated using a sub-sample peak estimator that fit a quadratic polynomial to the peak rise in displacement and its temporally-adjacent estimates. Spatio-temporal samples corresponding to shear wave speeds less than 0.5 m/s or greater than 8 m/s were not considered when selecting the peak value. Simple linear regression was performed on all of the arrival times at each depth to obtain an estimate of the transverse wave velocity Palmeri et al. (2008). These velocity estimates are also referred to as Shear Wave Elasticity Imaging (SWEI) (Sarvazyan et al., 1998) and shear wave speed estimates. The estimation process was repeated independently for each repeated excitation ensemble. The M-Mode sequences formed 470 x 160 pixel M-Mode images through depth and across multiple heartbeats, to which a 5 x 3 pixel median filter was applied to remove outliers. For the synthesized 2-D images, the ARFI and SWEI estimates from each response were sorted to form sets of data, where each set contained all of the responses for a given ECG trigger delay, one at each lateral steering angle. For all of the ensembles acquired with the same delay, each shear wave speed estimate was assigned to the 15° ROI from which it was calculated and overlapping estimates for each lateral line were averaged together, weighted by the magnitude of their complex cross-correlation coefficients. The ARFI data did not overlap, so were assigned directly to their lateral location.

4.3.4 Multi-beat Synthesis

To compile the data acquired across multiple heartbeats, a technique called multi-beat synthesis (Hsu et al., 2007a) was used to register estimates from many frames onto a single heartbeat. Using matched ECG data, each displacement and velocity estimate was registered to the preceding QRS complex, placing all estimates on a single beat. For the 2-D image sequences, this resulted in a single estimate at each combination of steering angle and cardiac phase, making a series of seventeen, 470 x 17 pixel (pre-scan-conversion) ARFI images. SWEI images were similarly formed, but had an additional 16° in their field of view due to the extent of the rightmost tracking kernel (figure 4.1(b)), which resulted in 470x23 pixel images. For the M-Mode sequences, the 160 temporal samples cover the all phases of the cardiac cycle for the center steering angle. Forty evenly spaced time bins were used to subdivide one heart cycle, with each of the 160 estimates placed into the nearest bin. The estimates within each bin were then averaged together, weighted by their correlation coefficients, to form two 470 x 40 pixel M-Modes, one for ARFI displacement and one for shear wave speed.

4.3.5 Model Fitting

To form a more quantitative comparison among M-Mode images, 10 averaged profiles of displacement and velocity were computed from each synthesized M-Mode. The borders of the tissue were drawn by hand using the center line of the B-Modes for guidance, and the profiles averaged between deciles spaced between the axial boundaries so that each profile followed the same piece of axially-moving myocardium. Each of the 10 ARFI or SWEI profiles was then fit to a simple, six-parameter piecewise-linear model. The parameters were diastolic value, systolic value, end-diastole time, diastolic-systolic transition time, systolic duration, and systolic-diastolic transition time. A shear wave speed temporal profile for a single location and its corresponding

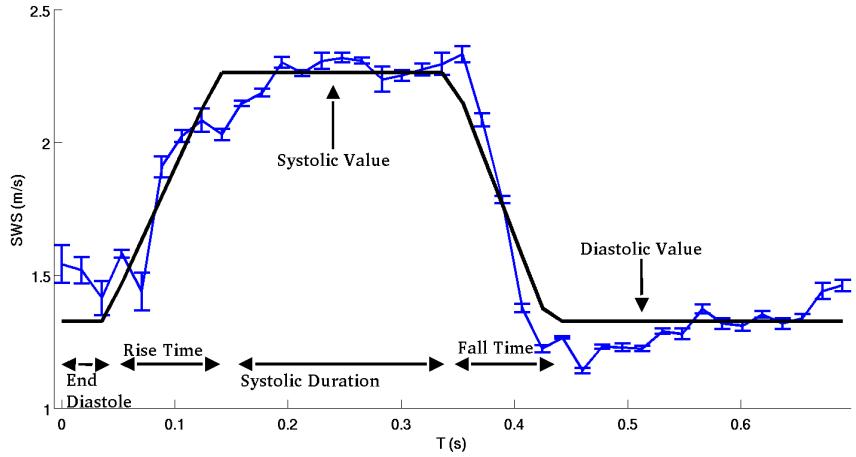

FIGURE 4.3: Single-depth shear wave speed temporal profile with the simple model overlaid. The model parameters are fit to the means at each time step.

model are shown in Figure 4.3. During diastole and systole, the model is constant, and during the transition times, the model is linear. MATLAB's *fit* function was used, implementing a constrained, robust, nonlinear least squares Levenberg-Marquardt algorithm to do the fitting. The model is simple, but allows a numeric comparison between large amounts of data contained in each M-Mode. The parameters of interest reported in this work are the diastolic and systolic values.

4.4 Results

Over all animals and all imaging sessions, 154 M-Mode images and 42 2-D image sequences were acquired in various views of the left and right ventricle. The results presented here are a subset of the views for which lateral tissue motion and the imaging angle were comparable.

4.4.1 Left Ventricular Free Wall Infarction

Figure 4.4 shows a single frame of the B-Mode clips acquired in the LVFW of one of the infarcted pigs on the left and the control pig on the right. The left image shows a large focal infarct in the LVFW, while the right image is nearly the same view, but

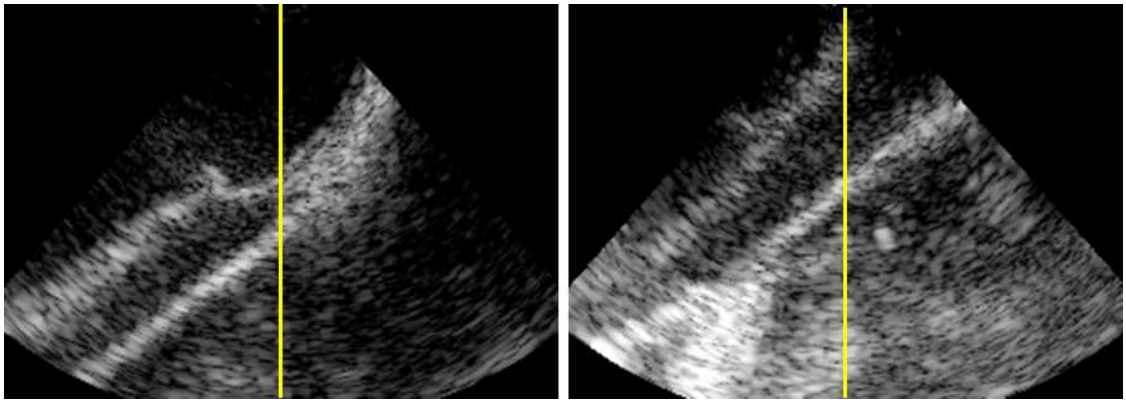

FIGURE 4.4: B-Mode frames of the LVFW. The left image is taken from one of the infarcted pigs 126 days after infarction, and shows a large focal infarct in the frame. The right image, from the control (146 days after its sham procedure), shows the same view, but without any infarction. The yellow line indicates the steering angle of the ARF excitation for the M-Mode sequences.

shows no signs of damage. ARFI and SWEI estimates will be compared in the data acquired from these views.

Figure 4.5 shows the M-Modes of displacement magnitude and shear wave speed for the control pig's LVFW over six beats. The axial and temporal trends in shear wave speed and velocity are highly repeatable from beat to beat and correspond with the associated ECG. It is also of note that depth variation is seen in the SWEI image but not in the ARFI image.

Figure 4.6 shows six frames from the multi-beat synthesis 2-D SWEI and ARFI image sequence for the same view shown in Figure 4.5. A similar trend of elevated shear velocities and suppressed displacements are seen during systole, compared to diastole. Dimmed pixels, which show the underlying B-mode, correspond to low cross correlation coefficients or regions outside of the myocardium.

Figure 4.7 shows the SWEI and ARFI M-Modes for the two views in Figure 4.4 after multibeat synthesis, along with the associated ECG and (uncalibrated) LV pressure curve. The diastolic speeds appear elevated in the infarction compared to the control, and the displacements are correspondingly lower in the infarction. A

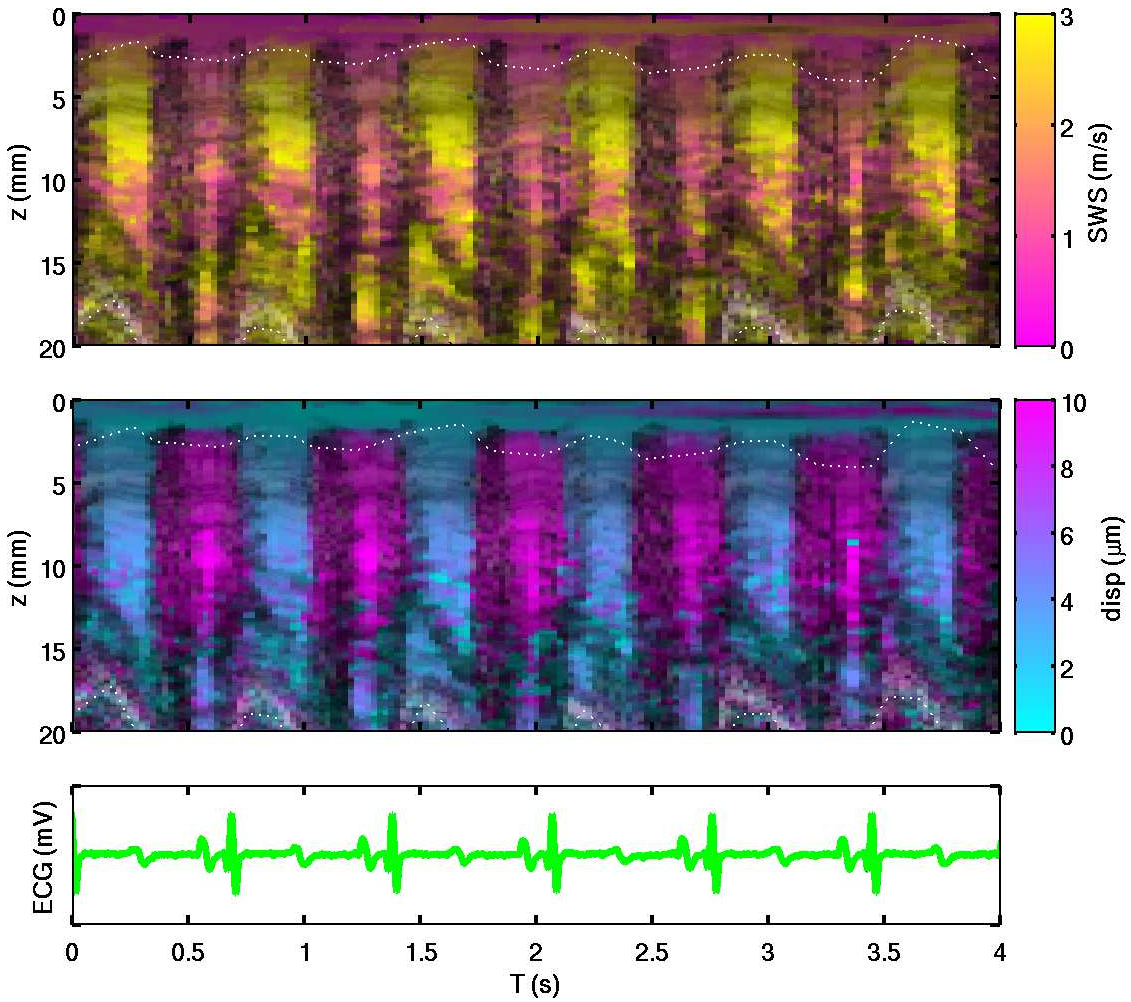

FIGURE 4.5: SWEI (top row) and ARFI (middle row) M-Modes of the LVFW from the control animal, with the corresponding ECG (bottom row). Data were taken 146 days after the first imaging date. High shear wave speeds and low displacements (yellow and cyan, respectively) correspond to stiff myocardium in systole, and slow speeds and high displacements (magenta) correspond to compliant myocardium. Desaturated pixels correspond to points outside of the depth of field and those with low complex cross correlation coefficients. In each of the six beats, the axial and temporal trends in both ARFI and SWEI measurements are highly repeatable.

small amount of relaxation is seen in the infarction from 350-500 ms.

Box plots are shown in Figure 4.8 for the model parameters fit to the data in figures 4.7 and the rest of the datasets from those views. Statistically significant difference in the means at the 5% level is indicated by the shear wave speeds for all

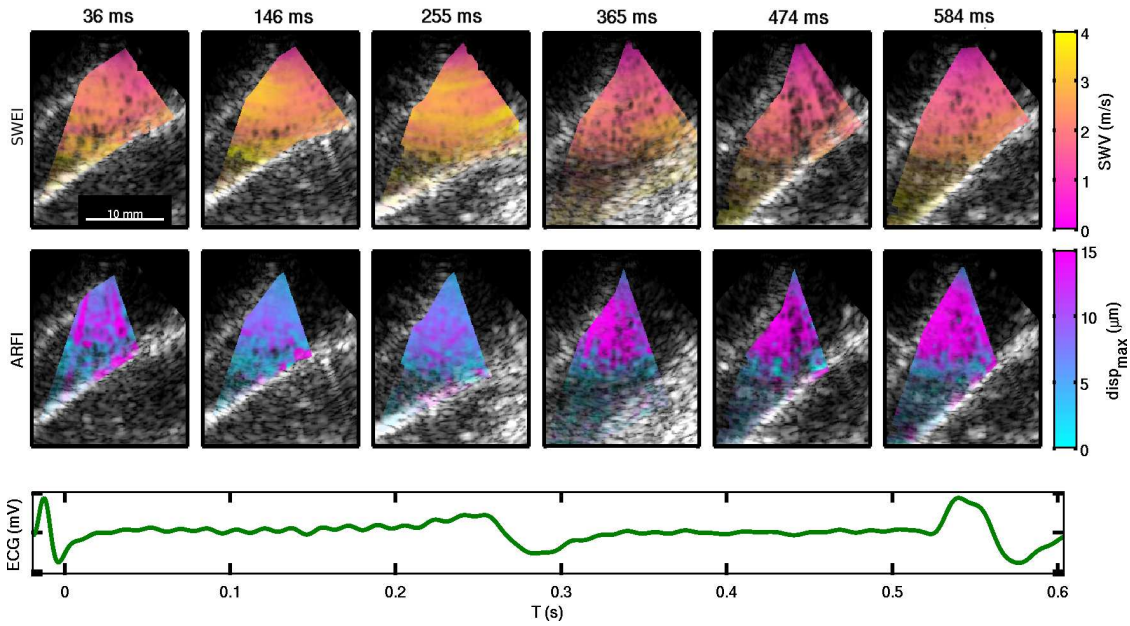

FIGURE 4.6: SWEI (top row) and ARFI (middle row) images of the LVFW from the control animal at various points in the cardiac cycle, displayed over the corresponding B-mode images, with the associated ECG trace (bottom row). Similar speeds and displacement trends are seen as in Figure 4.5, with general spatial uniformity and temporal contraction. Transparent colored pixels correspond to low cross correlation coefficients.

Infarct-Healthy pairs except "Infarct 2" and "Healthy 3". In the ARFI displacement data, statistical significance is only indicated between "Infarct 2" and "Healthy 1" and "Infarct 2" and "Healthy 2".

Figure 4.9 shows the same frames from the 2D sequence as Figure 4.6, but for Pig #2 with the infarcted portion of the free wall shown in Figure 4.7. Images were taken 126 days after infarction. The displacements and velocities remain low and high, respectively, throughout the cardiac cycle. During mid diastole, a small region of elevated displacements is seen in the infarct, shown by the magenta region in the upper right portion of the images at 412 ms.

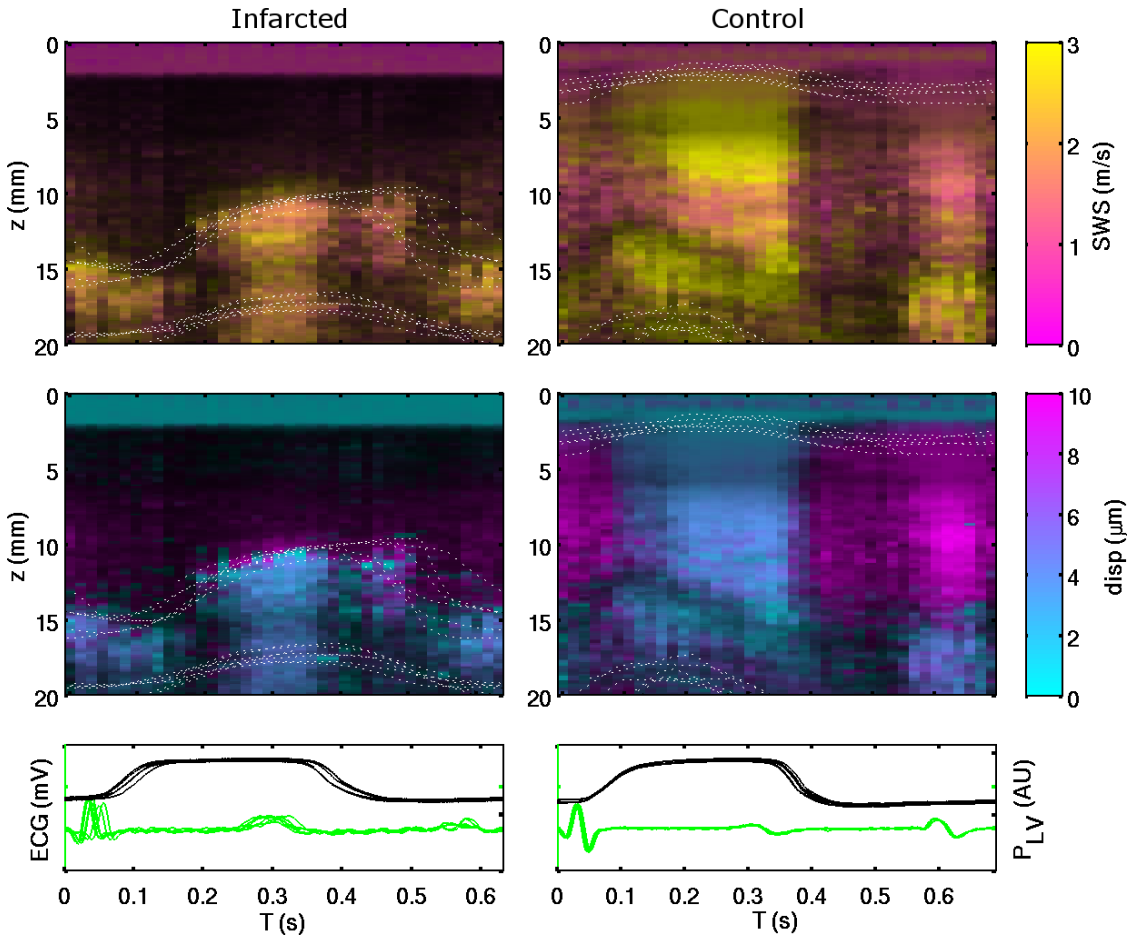

FIGURE 4.7: Multibeat-synthesized SWEI (top row) and ARFI (middle row) M-Modes of the LVFW. The left images are taken from an infarcted region of Pig #2 126 days after infarction, and the right are taken from the control animal at 146 days after a sham procedure. The bottom row shows the associated ECG and pressure traces. Elevated diastolic shear wave speeds and corresponding lower ARFI displacements are seen in the infarction. Thin, dotted white lines delineate the axial tissue boundaries from all contributing beats, such that overlapping lines indicate repeatability of the axial tissue motion between beats.

4.4.2 Intraventricular Septum Infarction

A comparison of ARFI and SWEI data imaging healthy and infarcted myocardium within the same animal is shown in Figure 4.10. The tissue in the infarcted region was thinned, and presented a conduction delay in the B-Mode. The ARFI and SWEI M-Modes, however, show no apparent change along the lines measured. The healthy

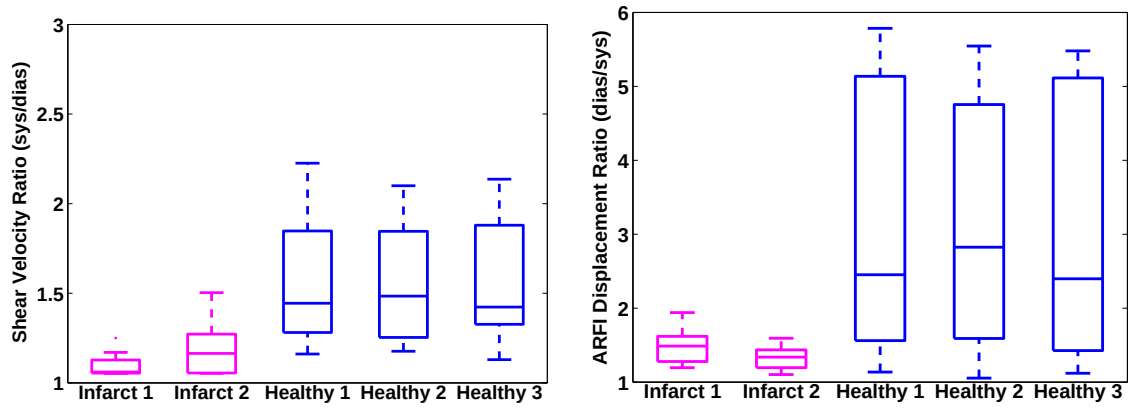

(a) (b)

FIGURE 4.8: Model parameters fit to each of the datasets acquired of the LVFW view during the final imaging study. Error bars indicate the standard deviation across the LVFW for 10 independent model fits. Data from the control pig, labeled "Healthy", show higher contractility than those from the infarcted pig in both ARFI and SWEI.

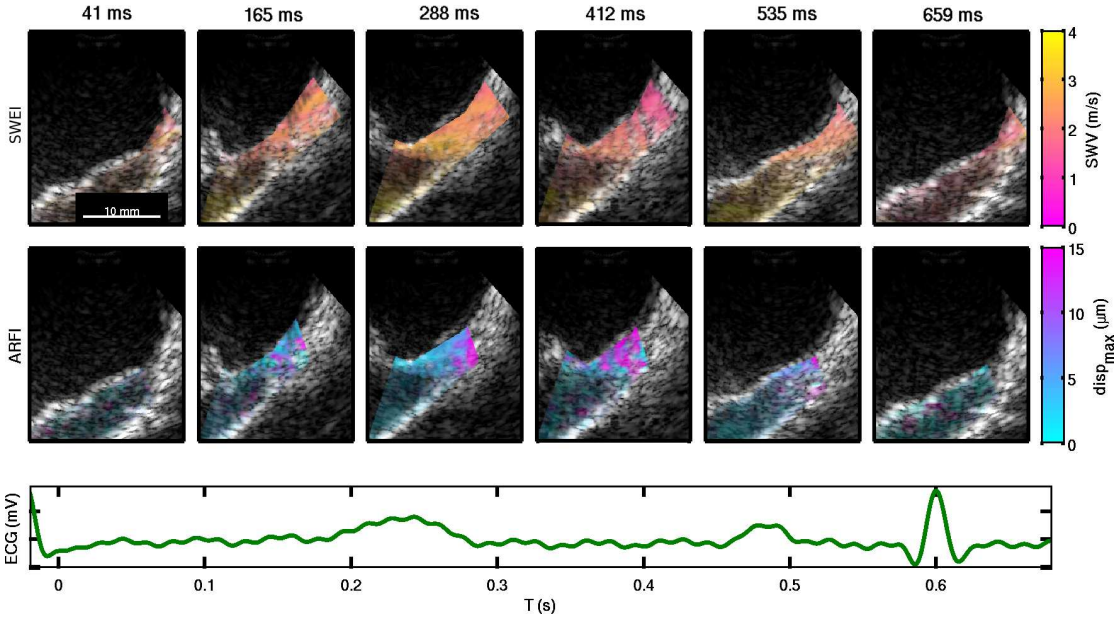

FIGURE 4.9: SWEI (top row) and ARFI (middle row) frames from the synthesized 2-D image sequence of a region of infarcted LVFW, and the corresponding ECG (bottom row). The infarcted tissue maintains low displacements and high velocities throughout the cardiac cycle, indicating that it is stiff and non-contractile. During mid-diastole (412 ms), a small region of higher displacements and lower velocities seen in the upper right part of the image

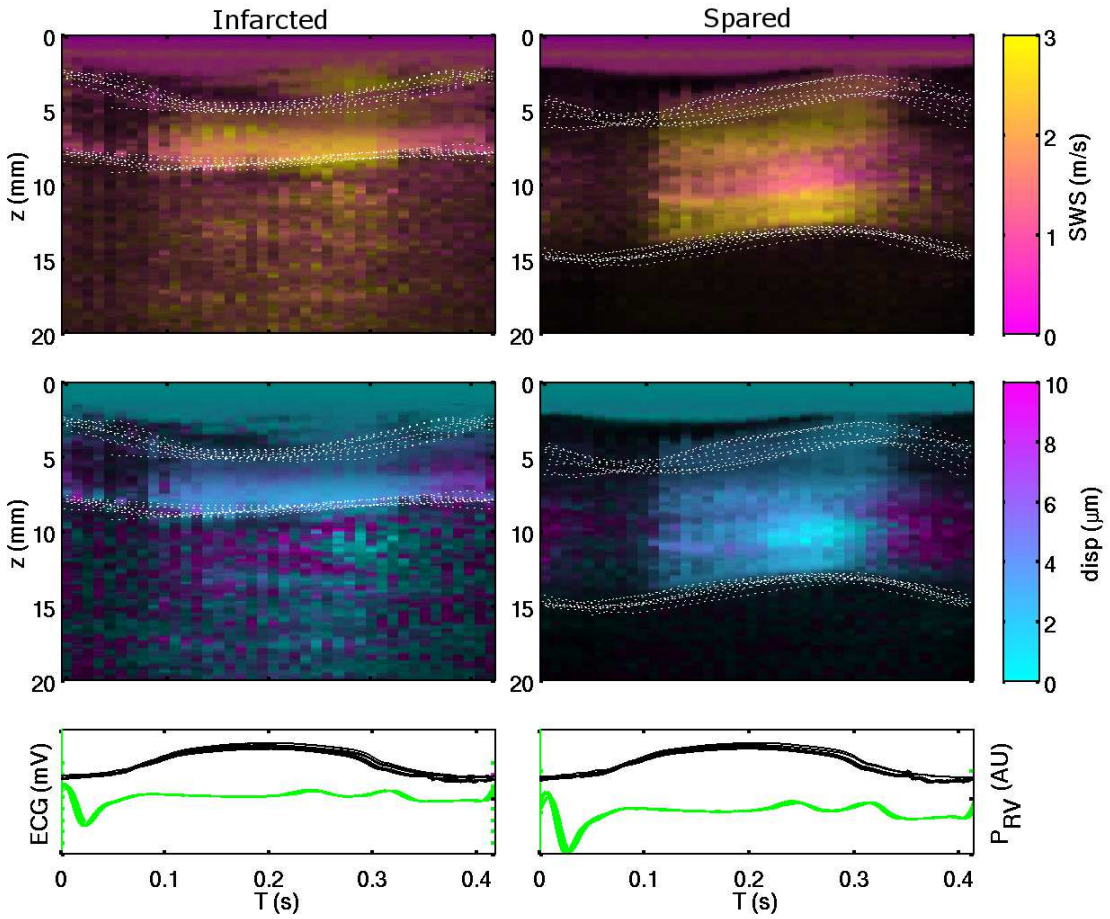

FIGURE 4.10: Multibeat-synthesized M-Mode SWEI (top row) and ARFI (middle row) of the IVS for an infarcted region (left) and spared region (right) of the same animal 140 days after infarction, with traces of ECG and relative pressure (bottom row). The spared region indicates potential transmural anisotropy, while the infarcted region does not. Though thinned in the infarct, peak contractility appears similar in both tissue samples, and both regions show diastolic compliance.

tissue shows strong shear wave speed variation transmurally through the septum.

Figure 4.11 shows the box plots for the views of the IVS shown in Figure 4.10, along with the other two repeated acquisitions at each view. No statistically significant differences are seen, although the shear wave speed ratios seem to have lower bounds in the spared tissue, and the ARFI ratios seems to be somewhat higher in the spared tissue.

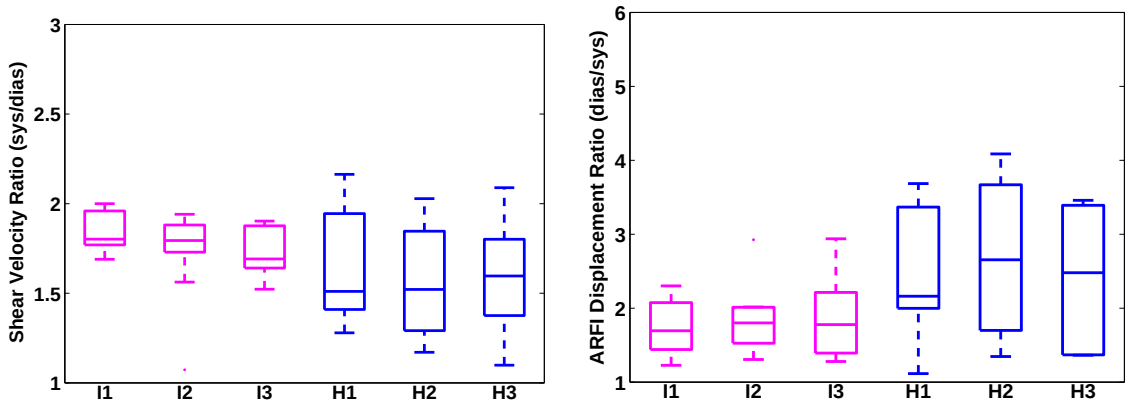

(a) (b)

FIGURE 4.11: Model parameters fit to each of the datasets acquired for the IVS views shown in Figure 4.10. Error bars indicate the standard deviation spatially across the septum for 10 independent model fits. SWEI data indicate higher variation in the larger, spared region, but higher ratios in the thinned region, while ARFI data indicate higher, though not significantly so, ratios in the spared region.

4.4.3 Remodeling

The ejection fractions for the pigs, from three views, are presented in table 4.2. All of the animals, including the control, had a moderately decreased ejection fraction 9-10 days after the embolization. Data from the later studies are not available.

Table 4.2: Ejection Fraction Measurements

Ejection Fraction (%)	Pre-embolization	9-10 Days Post-embolization	p
Pig 1	58.3 ± 8.1	54.7 ± 5.9	NS
Pig 2	52.5 ± 7.6	51.0 ± 2.6	NS
Pig 3	51.0 ± 8.5	40.7 ± 6.7	0.089
Pig 4 (Control)	54.3 ± 3.2	46.0 ± 3.0	0.015

NS = Not Significant. p-values represent a two-tailed Welch's t-test at the $\alpha = 5\%$ significance level.

The diastolic shear wave speeds, taken from the model fits to all datasets in both the RVFW and the IVS, are shown in figure 4.13. In all but Pig #1, the diastolic shear wave speed increased with significance $p<0.05$ by the final imaging study, including the control animal. In the RVFW, none of the diastolic shear wave

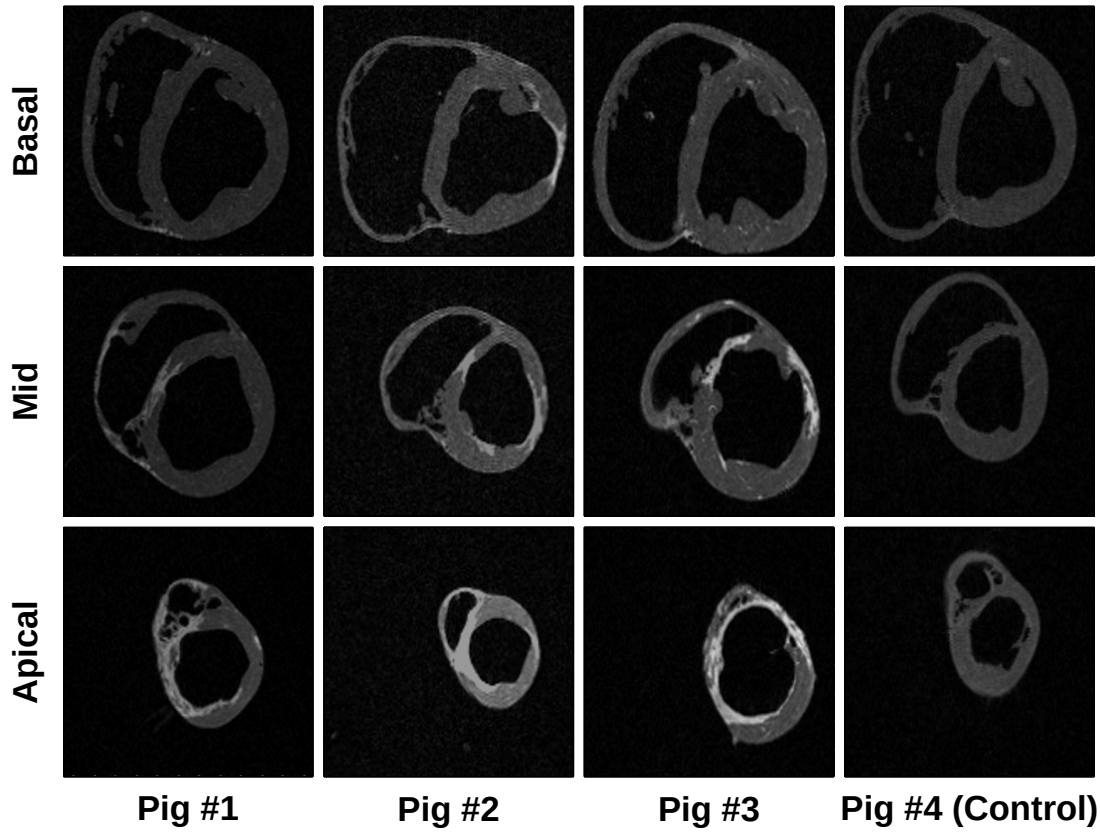

FIGURE 4.12: Slices of the *ex vivo* contrast-enhanced MRI volumes. The right ventricles were distended in the fixation process, but infarcts are clearly visible in the IVS of Pigs 1-3, as well as the LVFW of pigs 2 and 3.

velocities were increased at the final imaging study.

Cross-sectionally, comparing all of the views of the IVS from the final imaging study between all of the animals, no difference were seen in diastolic shear wave speeds between pigs. The animals with infarcts had diastolic speeds of 1.289 ± 0.033, 1.354 ± 0.029, and 1.366 ± 0.059 m/s, respectively, while the control animal had diastolic speeds of 1.420 ± 0.042 m/s. If anything, the average diastolic velocities for the control are a bit *higher* that the infarcted estimates, but grouping the infarcted animal estimates together, and performing a one-way ANOVA against the control, the means are not significantly different ($p = 0.058$).

Individual views of non-infarcted septum were also compared across the four

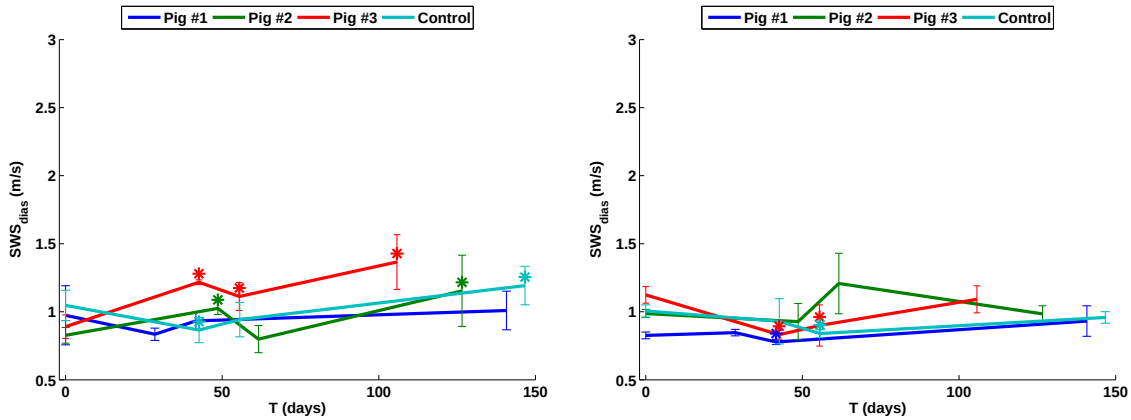

FIGURE 4.13: Diastolic shear wave speeds in the IVS (a) and RVFW (b) for the four animals over 150 days. Stastical significance in a Student's two-tailed T-Test is shown relative to the first imaging session for each animal, and demarcated with an asterix.

pigs. The most common view was of the IVS, and multibeat-synthesized M-Modes of the IVS are shown for the four pigs in Figure 4.14. Substantial remodeling is not apparent in the ARFI or SWEI data, as clean contractility with similar shear wave speeds is observed. A statistical analysis by one-way ANOVA indicates no difference in the diastolic means between the infarcted animals and the healthy (all infarcted $\mathrm{SWS}_{dias} = 1.444 \pm 0.059$ m/s, control $\mathrm{SWS}_{dias} = 1.414 \pm 0.102$, $p = 0.801$).

Figure 4.15 shows the box plots for the model parameters fit to the data in Figure 4.14. Pig "infarct 3" has higher contractility than the control in the ARFI ratio, but not the SWEI ratio, and none of the other diseased pigs showed significant differences in either measurement.

4.4.4 Heterogeneous Infarction

In one of the animals, views were obtained of a thinned region of apical septum from the LV. The catheter was able to be drawn back, moving the field of view to more basal, spared septum. At approximately 5 mm intervals, images were taken. A diagram of the approximate imaging locations is shown in Figure 4.16. The B-Mode

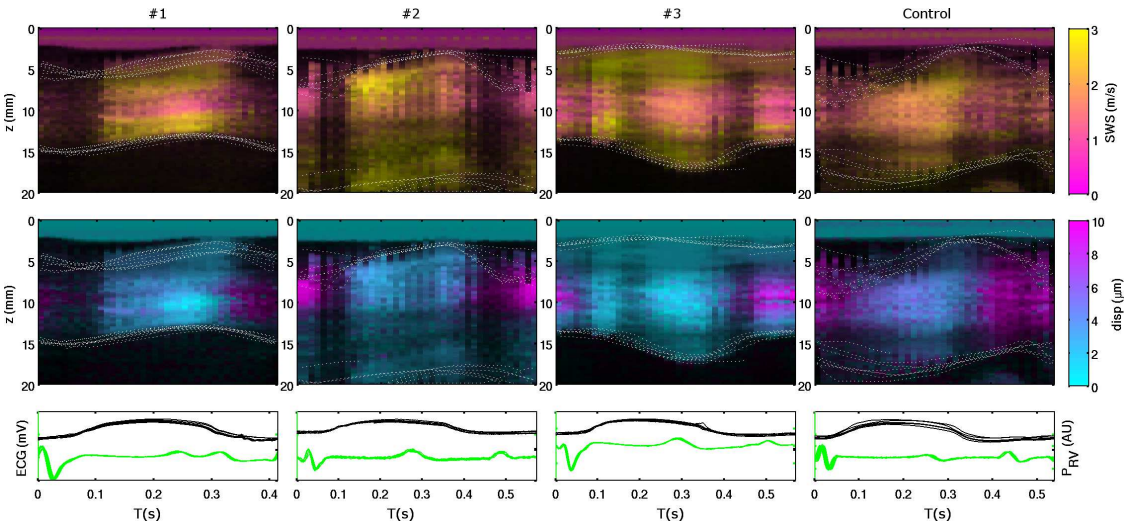

FIGURE 4.14: Multibeat-synthesized M-Mode SWEI (top row) and ARFI (middle row) of the IVS for the four pigs, with associated ECG and pressure traces (bottom row). Images were acquired at the final imaging session for each animal (140, 126, and 105 days after infarction, respectively, for Pigs #1-3, and 146 days after the sham procedure for the control). No global remodeling is indicated between the spared regions of the IVS in the infarct animals (left three columns) and the healthy tissue of the control (rightmost column).

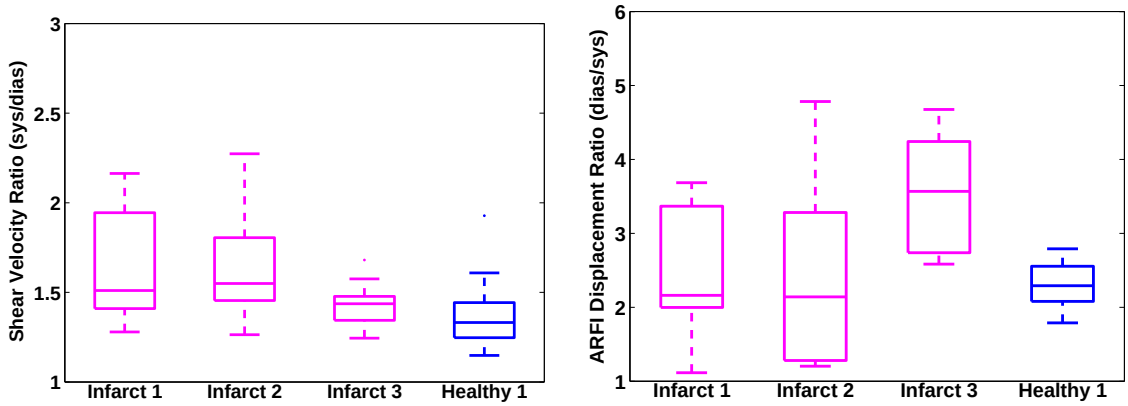

(a) (b)

FIGURE 4.15: Model parameters fit to the datasets acquired from spared septum in the four animals during the final imaging studies. Data from the diseased pigs, labeled "Infarct", show no significant signs of remodeling, compared to the control. The ARFI data show Pig #3 to have significantly *higher* ARFI ratios than the control. Error bars indicate standard deviation across the septum among 10 independent model fits.

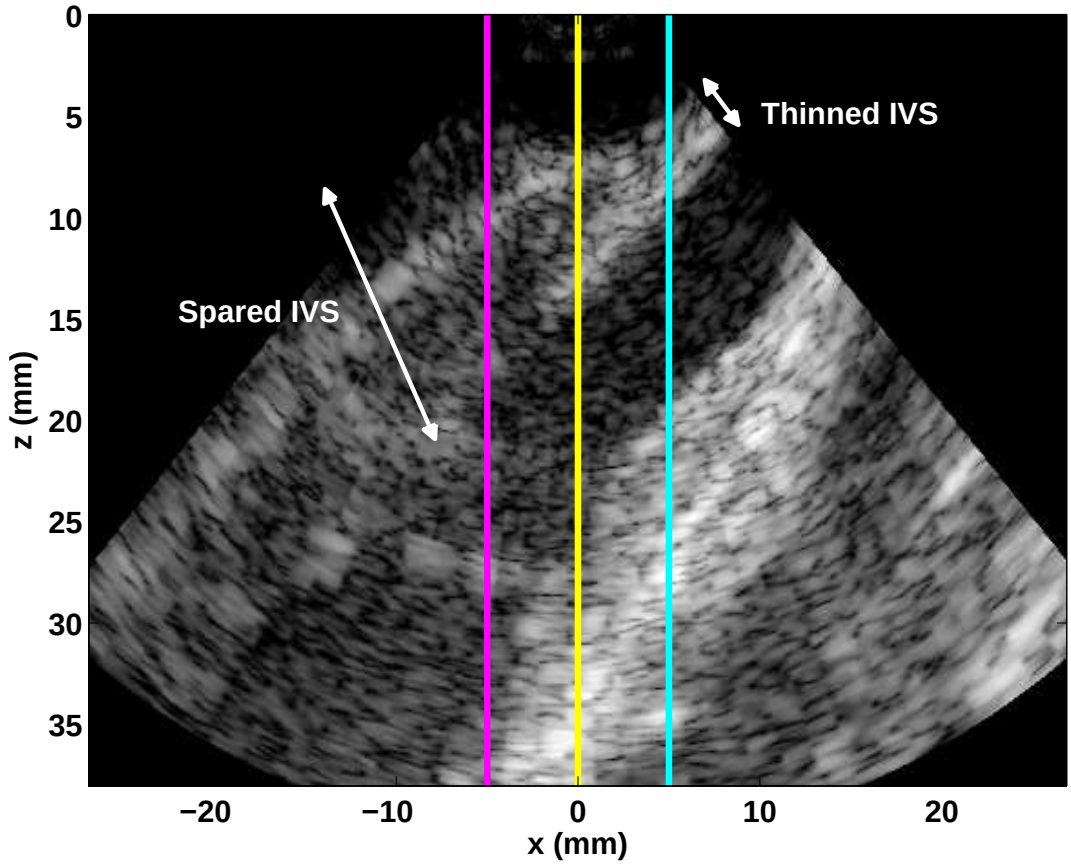

FIGURE 4.16: B-Mode image of the IVS, with spared septum on the left (basal), and infarcted septum on the right (apical), taken 126 days after infarction in Pig #2. The three lines indicate the imaging locations for the M-Modes.

shown is from the center of the three locations.

Figure 4.17 shows the SWEI and ARFI M-Modes recorded for the rightmost line in Figure 4.16. Transmural variation of ARFI and SWEI is seen during systole in each beat, with more spatially-uniform values in diastole. These features are present in each beat of the M-Mode. Figure 4.18 shows the multibeat-synthesized SWEI and ARFI M-Modes for the three locations indicated in Figure 4.16. The most basal (spared) image is on the left, and the most apical (infarcted) is on the right (the synthesis of Figure 4.17. The spared septum shows uniform contraction transmurally, while the infarcted septum is thinned and shows transmural variation

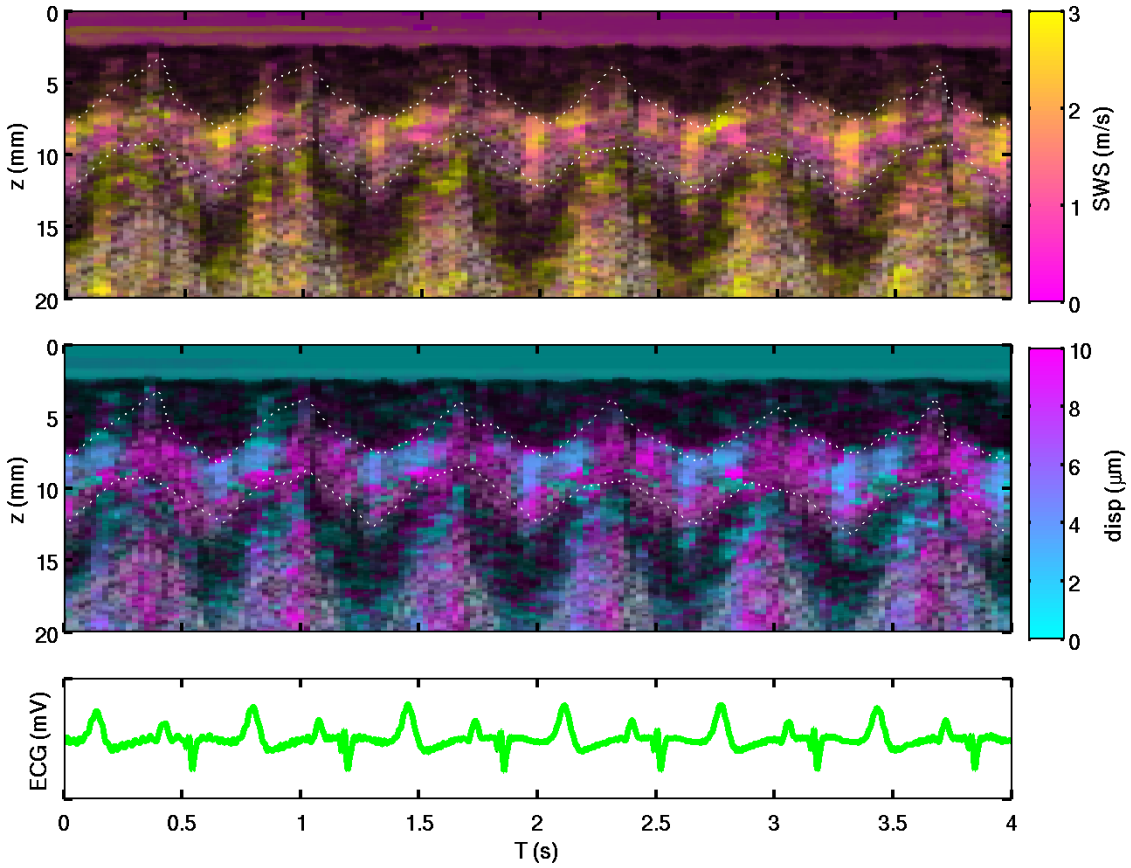

FIGURE 4.17: SWEI (top row) and ARFI (middle row) M-Modes of the septum and the corresponding ECG trace (bottom row), recorded at the rightmost (cyan) line indicated in Figure 4.16. Both ARFI and SWEI measurements indicate transmural heterogeneity during systole and axially uniform estimates in diastole, 126 days after infarction. These spatio-temporal trends are visible in each beat.

in the stiffness and contractility properties. The RV side of the IVS in the right image maintains high displacements and low shear velocities throughout the cardiac cycle.

Figure 4.19 shows images from the 2D synthesized sequence for the view from Figure 4.16. The spatio-temporal nonuniformity is highlighted in this view, as the LV and basal regions of the image contract in systole, while the apical RV side remains compliant. Visual registration of laterally moving tissue is readily possible with the 2D field of view.

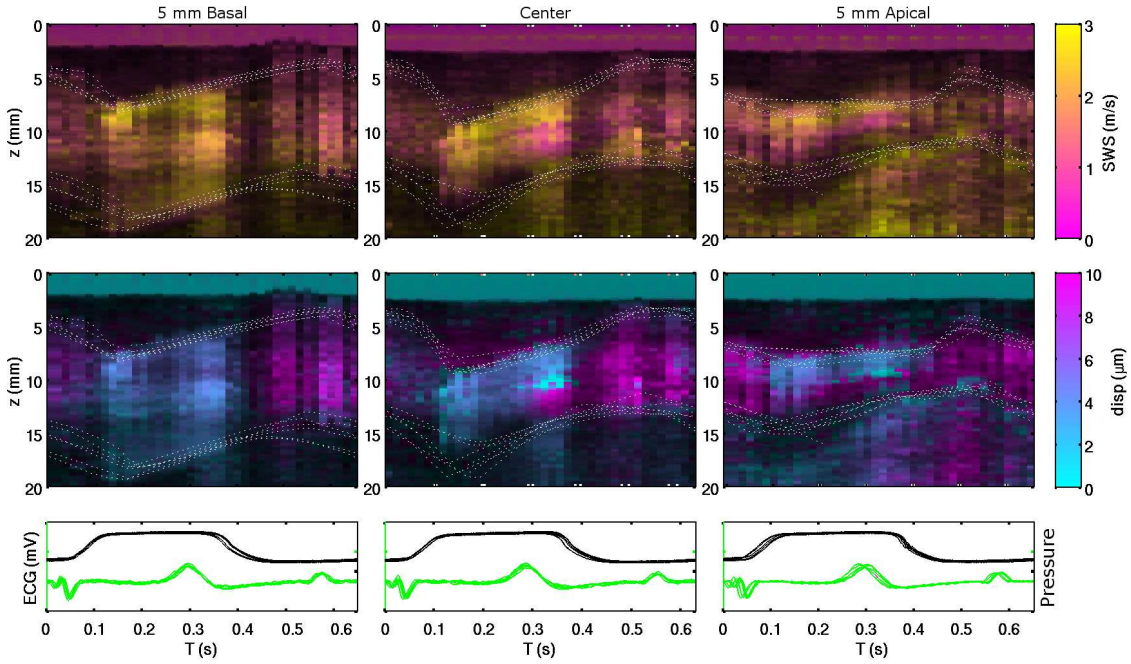

FIGURE 4.18: Multibeat-synthesized SWEI (top row) and ARFI (middle row) M-Modes of the septum, at the locations indicated in Figure 4.16, with corresponding ECG and pressure traces (bottom row). The apical septum is thinned and shows transmural variation in systolic stiffness in both ARFI and SWEI measurements for the center and apical views (middle and right columns) 126 days after infarction.

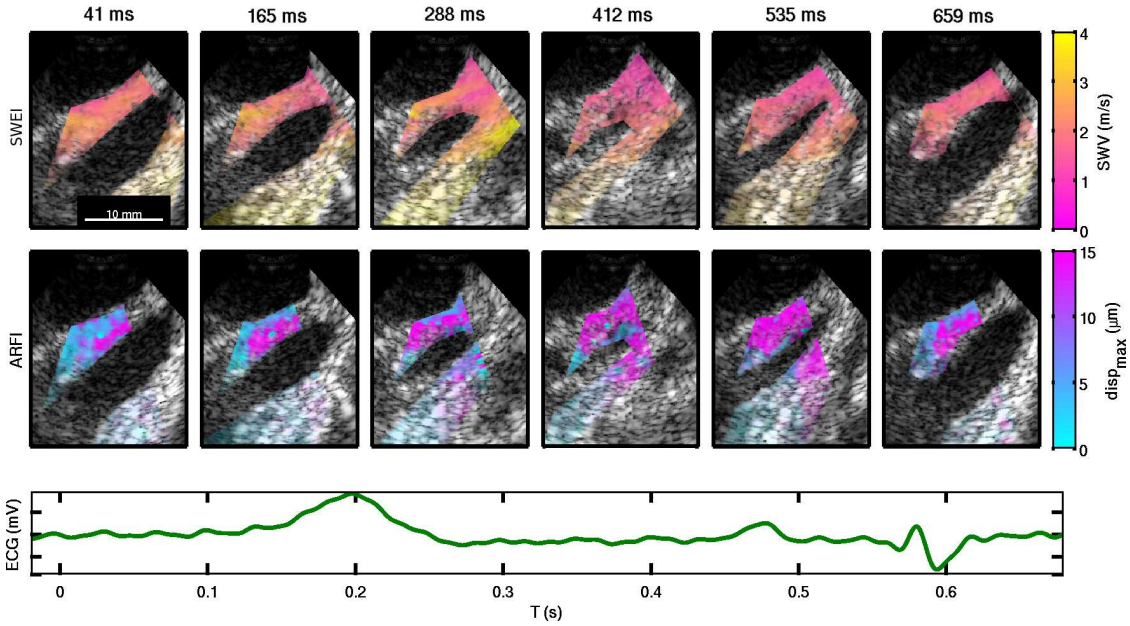

FIGURE 4.19: SWEI (top row) and ARFI (middle row) frames from the 2-D image sequence of a heterogeneously-infarcted region (Figure 4.16), and the corresponding ECG trace (bottom row). In the ARFI images, the RV side of the IVS near the apex does not contract during systole, showing elevated displacements, while the LV side of the IVS contracts and relaxes normally

4.5 Discussion

We were able to use ARF delivered by an ICE transducer to generate and track transient displacements and resultant shear waves through systole and diastole in an animal model. In 122 of the 154 M-Mode images, clear trends of higher displacements (increased compliance) during diastole and lower displacements (increased stiffness) during systole were observed. In the remaining 32 images, no cyclic variation was seen- the images had either low displacements within the myocardium through the entire cardiac cycle, or low cross-correlation coefficients indicating motion. In 104 of the 122 M-Modes with cyclic ARFI displacements, the matching SWEI images showed clear trends of increased shear wave speeds in systole and decreased speeds in diastole. The high beat-to-beat repeatability facilitated multi-beat synthesis, and the results allowed us to observe interesting spatio-temporal abnormalities in the infarcted myocardium. The ARFI data showed a clean signal indicating at least some systolic contraction in a higher number of M-Mode images than the matched SWEI images (79% vs 68%), due to the additional step of estimating the transverse wave velocity. ARFI images showed less sensitivity to myocardial fiber orientation than SWEI images, since we were only able to measure the shear wave propagation in a single direction. The combination of both ARFI and SWEI allowed us to separate changes in substrate stiffness from variations in relative fiber orientation, which, without three dimensional tracking of wave propagation, is not possible with shear wave imaging alone.

4.5.1 Left Ventricular Free Wall Infarction

In the two views of the LVFW, high shear wave speeds and little contraction were seen in the infarcted region compared to the healthy tissue. The relatively higher variance of the ARFI estimates for the healthy tissue (Figure 4.8) is due to depth

of field and attenuation effects over the much larger axial thickness of the free wall, which extends beyond 20 mm. Figure 4.5 shows that the axial and temporal trends through the LVFW and across the heart cycle are shown with high beat-to-beat repeatability. Looking at the upper end of each box for ARFI or SWEI in Figure 4.8 indicates large differences between the infarcted and control tissues in terms of the spatial *peak* contractility. The 2-D image sequences (Figures 4.6 and 4.9) show the relative spatial homogeneity of each of the tissue regions. The 2-D SWEI images have low resolution due to the averaging of overlapping 16° ROIs, but with the higher-resolution ARFI images do provide insight into the azimuthal distribution of stiffness. Interestingly, in the healthy tissue, a gradient is visible with depth during diastole, potentially indicating somewhat increased stiffness towards the epicardium. These low displacements and elevated velocities at depth during diastole are seen in the deep parts of Figure 4.7 as well. This may indicate that the epicardial part of the myocardium is more rigid than the endocardium, but effects of boundary conditions and ARF penetration depth obfuscate a stronger conclusion

4.5.2 Intraventricular Septum Infarction

The views of the IVS (Figure 4.10) show a primarily negative result for distinguishing what appeared to be infarcted tissue from normal tissue within the same heart by ARFI and SWEI. The shear wave speeds and ARFI displacements in the thinned myocardium seem to follow the same contraction and relaxation of the spared region. A number of factors complicate this conclusion, however. First, the IVS displays transmural anisotropy in the shear wave speed images of the spared region, but not in the infarcted region. The band in the middle of the spared septum shows low shear wave speeds and low displacements during systole, while no such region exists in the presumed infarct. This causes the average systolic shear wave speed to be lower, and the standard deviation to be higher, in the spared region, which are

both seen in figure 4.11(a). The ARFI ratios, on the other hand, appear somewhat higher in the spared septum, though statistical significance is not acheived. Neither of these change the fact, however, that the thinned region region of myocardium is compliant during diastole with shear wave speed near 1 m/s. We hypothesized that this could be stunned or hibernating myocardium, which would be dysfunctional without being fibrotic. Although the tissue may not actively contract itself, the contraction of adjacent, healthy tissue may stretch this tissue, creating the systolic stiffness. However, neither the *ex vivo* MRI (figure 4.12), nor the histological staining (not shown) indicated that Pig #1 had a thinned region of its septum that was not infarcted. The existence of this apparent "soft infarction" warrants further study to determine whether it is the result of an imaging artifact or a real pathology.

4.5.3 Remodeling

Over the course of the study, we observed a small stiffening of the IVS during diastole in two of the three infarcted pigs as well as the control, and no significant change in RVFW diastolic stiffness, leading us to believe that we either did not acheive, or were not able to detect diastolic heart failure in these animals. The ejection fractions (Table 4.2) did not differentiate the infarcted animals from the control at 9-10 days post-embolization, although in the later studies regional akinesis of the infarct areas was observed, and expected to have decreased the EFs below normal, though those data are unavailable. Additionally, cross-sectionally comparing all of the diastolic shear wave speeds in regions of spared IVS during the final imaging session, no signs of elevated diastolic stiffness were present in the SWEI data for the infarcted animals. Comparing similar views of the septum (Figure 4.14), we see variation, but no significant differences between the spared regions of the infarcted pigs and those of the control. The average diastolic velocities were nearly identical (1.414 m/s in the control, 1.444 m/s in the infarcted animals, $p = 0.801$). Figure

4.14 shows the M-Modes taken of the IVS, and we can see that the exact imaging plane varies between the views. The variation introduced by different imaging angles and targets indicates the importance of obtaining measurements of the same part of the tissue, at the same angle, for performing matched comparisons. Perhaps the strongest conclusion to be made from these data is that the heart is not mechanically homogeneous and that substantial regional variation exists even in healthy hearts. To make the truest comparison between diseased tissue and healthy, either the imaging planes need to be closely matched, or a map of regional properties needs to be created that can be aligned and registered between subjects.

4.5.4 Heterogeneous Infarction

In Figures 4.18 and 4.19, ARFI and SWEI agree on the decreased systolic stiffness of the RV side of the IVS near the apex, so the variation cannot be attributed simply to anisotropy. This result, like the other IVS result, was surprising, as it was expected that the thinned myocardium would be stiff and non-compliant throughout the cardiac cycle. *Ex vivo* contrast-enhanced MRI indicated the apical septum to be infarcted, but aligning the specific ultrasound viewing angles to the MRI data was not possible due to deformations introduced in fixing the heart for scanning. It is possible that the ultrasound imaging plane intersected infarcted, viable, or a mix of both types of tissue at different stages of the cardiac cycle. This infarcted region of the IVS may have been subjected to passive tension as the surrounding tissue contracted, such that the increase in stiffness on the LV side during systole was due to stretching rather than muscular contraction. Another confounding factor was substantial lateral motion of the septum in these images. The tissue moved back and forth underneath the ROI, and in the apical image, the ROI approached the apex itself at the peak lateral motion. Looking at the 2-D images, however (Figure 4.19), clear elastic distinction between the RV and LV sides of the septum

was observed during systole in the ARFI images, and the moving septum is readily followed through the frames.

4.5.5 Limitations

To limit the anesthesia time of the animals, the data acquired were processed offline after each experiment. Single 2-D diastolic ARFI-only images were typically acquired before each set of M-Mode and 2-D ARFI and SWEI images to determine the appropriate focal configuration to use, but feedback on the quality of the acquired data was limited during the experiments. Images were typically acquired in whatever views situated the tissue within 2 cm of the transducer face with limited perceived motion, but the porcine cardiac anatomy created challenges in catheter positioning, and in some cases, the only available views of the septum or free wall had a large amount of motion.

Lateral and elevational wall motion, particularly during contraction and active relaxation, created decorrelation in the tracking data, which reduced the confidence of the displacement estimates and subsequently-calculated velocities. In the images shown, the saturation of each pixel is tied to the cross correlation coefficients of the contributing excitation-tracking ensemble, and low cross correlation coefficients exponentially de-weight the saturation, showing more of the underlying B-Mode, such as in Figure 4.17. This occurs in blood and in regions of high motion. The tissue is outlined with small dotted white lines in the M-Modes to show the tissue boundaries, but in the 2-D images, the blood signal was manually masked out, rather than just using the correlation coefficients. When making multi-beat synthesized M-Modes, the multi-beat averaging was weighted by the correlation coefficients to reduce the effect of outliers, but the motion from beat to beat is so repeatable that decorrelated pixels were often averaged with the also-decorrelated pixels from the following beats, as in Figure 4.18. Real-time guidance of ARFI and SWEI will aid future studies in

imaging plane alignment, particularly with respect to fiber orientation. Additionally, as the heart beats, the angle between the ARF excitation and the tissue may change with cardiac motion. In the M-Mode images, this may mean that a different part of the tissue is imaged in systole than in diastole. While the multibeat-synthesis 2D image sequences address this, some M-Mode results could be subject to potential artifacts caused by the lateral and elevational heterogeneity of the tissue around the focus.

The effect of fiber orientation, was more of a confounding factor on the shear wave speed data than was initially expected. While ARF excitations occur mostly perpendicular to fibers, shear wave propagation is tracked by a linear phased array in a specific dimension, which can be parallel or perpendicular to the fiber orientation. ARFI was therefore less affected than SWEI, and in cases where the shear wave speeds varied *without* a corresponding change in the ARFI, we expect to be imaging fiber orientation variation rather than substrate stiffness changes. Future studies of shear wave speeds and myocardium will have to control for relative fiber angle closely, or else move towards tracking the wave propagation in 3-D, which would allow the anisotropic shear wave propagation to be imaged in all directions.

Beyond anisotropy, frequency dispersion affects the generalization of the shear wave speed estimates. In some views, the myocardium is less than 5 mm thick, whereby a shear wave model may not be appropriate, as the tissue may be excited in an antisymmetric Lamb wave mode. Nenadic *et al* (Nenadic et al., 2011) describe an approach for modeling such dispersion. In addition to boundary condition-induced dispersion, myocardium is expected to exhibit a degree of dispersion associated with its viscoelastic properties as well. How these properties provide different information than the basic group velocity approach used here will also need to be explored in future work.

Perhaps the greatest limiting factor, however, is the limited range of imaging.

Because the AcuNav is such a small probe, it was difficult to generate and track shear waves at depth. Whereas images were acquired with up to a 45° field of view down to 4 cm, images with excitation foci beyond 15 mm were less successful at generated distinct shear waves than those which used transmit F-numbers less than 2. This limited the usable field of view to a small region, which in turn limited the amount of the heart that could be characterized in any single image. Some views did show spatial variation within the small window (Figure 4.19, for example), but we predict that the capabilities of the system would greatly benefit from an increase in the usable field of view provided by stronger, more focused excitations. A larger transducer, an elevational focus, or longer excitation pulses may provide options in the future for accomplishing this. A wider viewing angle for tracking the wave may also provide better separation of the tissue motion from the ARF-induced motion and eliminate the need for multiple excitations per SWEI estimate altogether. This may be achieved through the higher receive bandwidth of newer hardware, either with parallel beamforming of many beams or through coherent plane wave compounding (Montaldo et al., 2009).

This work explored the possibility of using SWEI and ARFI M-Mode and synthesized 2-D measurements to characterize infarcted myocardium. Spatio-temporal abnormalities were observed in the SWEI and ARFI data that corresponded to regions of myocardial infarct, and these abnormalities were repeatedly imaged across several beats. Variability between imaging planes due to anisotropy, viewing angle, and tissue motion confounds generalization of these results, and highlights the need for tightly controlling for catheter position. Some abnormal regions showed increased systolic compliance while others showed decreased diastolic compliance. These results indicate the potential for ICE ARFI and SWEI techniques to be used to characterize diseased myocardial stiffness directly, but also highlights the complexity of performing elasticity imaging in beating myocardium.

5

Matched Single- and Multiple- Track Location Shear Wave and Acoustic Radiation Force Impulse Imaging: Comparison of Suitability for Micro-Elasticity (μ-E) Imaging

This chapter was submitted for review in 2014. This work represents a detailed study of a number of phenomena that our lab has observed, as well as presents the details of STL-SWEI.

5.1 Abstract

Acoustic radiation force impulse (ARFI) imaging and shear wave elasticity imaging (SWEI) use the dynamic response of tissue to impulsive mechanical stimulus to characterize local elasticity. A variant of conventional, multiple track location SWEI (MTL-SWEI), denoted single track location SWEI (STL-SWEI) offers the promise of creating speckle-free shear wave images. This work compares the three imaging modalities using a high push and track beam density combined acquisition sequence to

image inclusions of different sizes and contrasts. STL-SWEI is shown to have significantly higher CNR than MTL-SWEI, allowing for operation at higher resolution. ARFI and STL-SWEI perform similarly in the larger inclusions, with STL-SWEI providing better visualization of small targets ≤2.5 mm in diameter. The processing of each modality introduces different trade-offs between smoothness and resolution of edges and structures; these are discussed in detail.

5.2 Background

5.2.1 Acoustic Radiation Force Impulse Imaging

Acoustic Radiation Force Impulse (ARFI) Imaging has been under investigation since the early 2000's (Nightingale et al., 2002), with early work proposing its use for identifying breast tumors (Sharma et al., 2004). ARFI images provide information about relative differences in tissue stiffness, similar to those generated with compressive strain imaging methods. However, ARFI offers advantages resulting from the generation of the mechanical excitation within the structure of interest and its limited susceptibility to out of plane motion artifacts. To generate a two-dimensional image, ARFI ensembles are translated across the imaging field of view (FOV), in the same way that a Color Doppler image is created. Images are typically generated of the tissue displacement response, located within the excitation region and measured for 1-2 ms after excitation. For a given force, displacement is inversely proportional to tissue stiffness, and ARFI images portray relative differences in the displacement response within each excited region, either as the displacement at a fixed time step, or the maximum displacement. The 3D distribution of radiation force, variations in acoustic attenuation, and the transient nature of ARFI excitations complicate the specific relationship between absolute displacement and material stiffness such that quantitative elasticity estimates are only possible with careful calibration; in most

in vivo imaging scenarios, ARFI images provide qualitative maps of relative elasticity. Structural edges can be seen within a push beam (Dahl et al., 2007), so the resolution in ARFI images may be limited by the resolution of the tracking beams (Palmeri et al., 2006a), and as such be comparable to that of B-mode. For imaging small structures, however, contrast-to-noise ratio (CNR) is often considered to be the limiting factor, and the contrast in ARFI images has been shown to be reduced when the size of the push beam exceeds the size of the structure being imaged (Nightingale et al., 2006),(Palmeri et al., 2006a). This work will explore these effects in further detail and examine their impact on imaging small targets.

5.2.2 Shear Wave Elasticity Imaging

Shear Wave Elasticity Imaging (SWEI), originally described by Sarvazyan et. al. (Sarvazyan et al., 1998), and first demonstrated *in vivo* by our group (Nightingale et al., 2003), quantifies tissue stiffness by exciting the tissue with an ARFI push beam and monitoring the associated shear wave propagation through the region of interest. Time-of-flight (TOF) based reconstruction algorithms are then used to estimate the shear wave speed (SWS) (Palmeri et al., 2008; Wang et al., 2010; Rouze et al., 2010; Muller et al., 2009; Tanter et al., 2008; McAleavey et al., 2009a; McLaughlin and Renzi, 2006b; Chen et al., 2004), which in linear elastic materials is proportional to the square root of the shear modulus G divided by the density ρ:

$$\text{SWS} = \sqrt{\frac{G}{\rho}} \tag{5.1}$$

SWS typically has units of m/s, G has units of kPa, and ρ has units of g/cm^3 and is generally assumed to be close of 1 g/cm^3 in tissue. We define a 2D spatial coordinate system with z being the axial direction in line with the ultrasound beam, and x being the lateral direction, transverse to the beam, in which shear wave will

propagate. x_p and x_t will represent the push and track beam locations in the lateral dimension, respectively. We define the arrival time $T(z, x_t, x_p)$ as a characteristic of the shear wave generated at location (z, x_p) and tracked at location (z, x_t). T is typically chosen to be the time of peak axial velocity, displacement, or match-filtered velocity or displacement (i.e. the peak of the cross-correlation between a signal and a reference). When the track beam is aligned with the push beam, the initial arrival time is $T(z, x_p, x_p)$. Figure 5.1[A] shows a diagram of the most basic single push beam, two track beam configuration, and figure 5.2 shows the most complete configuration for a single depth, with the displacement shown at different times after excitation for all combinations of x_t and x_p. T increases as x_t moves away from x_p, at a rate determined by the local shear wave speed $\mathrm{SWS}(z, x)$. For a push location x_p, we expect the arrival time T measured at location x_t to be

$$T(z, x_t, x_p) = T(z, x_p, x_p) + \mathrm{sgn}(x_t - x_p) \int_{x_p}^{x_t} \frac{1}{\mathrm{SWS}(z, x)} dx. \tag{5.2}$$

To distinguish the conventional type of SWEI from the variation discussed in the next section, it will be denoted from here on as multiple track location SWEI (MTL-SWEI). To make an estimate of shear wave speed in MTL-SWEI, we hold x_p constant, and take the partial derivative of equation 5.2 with respect to the tracking positions x_t, and invert $\partial T / \partial x_t$ to get the shear wave speed at each tracking location x_t:

$$\mathrm{SWS}_{\mathrm{MTL}}(z, x_t, x_p) = \mathrm{sgn}(x_t - x_p) \left(\frac{\partial T(z, x_t, x_p)}{\partial x_t} \right)^{-1} \tag{5.3}$$

In practicality, a finite set of track locations $\mathbf{x_t} = \langle x_{t1}, x_{t2}, ..., x_{tN} \rangle$ are used. This is visualized in figure 5.2 as tracking the wave as it propagates vertically along a column. In the example of figure 5.1[A], $\partial T / \partial x_t$ is estimated from two track beams, x_{t1} and x_{t2}, as the ratio of the beam separation $x_{t2} - x_{t1}$ to the finite difference

between the estimated arrival times $\hat{T}$:

$$\hat{\mathrm{SWS}}_{\mathrm{MTL}}(z, x_t, x_{p1}) = \frac{x_{t2} - x_{t1}}{\hat{T}(z, x_{t2}, x_{p1}) - \hat{T}(z, x_{t1}, x_{p1})}, \quad \text{for } x_{t1} < x_t < x_{t2}. \tag{5.4}$$

With more than two track beams, linear regression or another estimator may be used to find the slope of the arrival times (Palmeri et al., 2008; Wang et al., 2010; Rouze et al., 2010). The resulting estimate $\mathrm{SWS}_{\mathrm{MTL}}$ will then reflect the shear elasticity of the tissue region between the widest-spaced tracking beams used in the estimation. The selection of push location x_p theoretically does not affect the derivative estimate, provided that the separation between the push and track beams $|x_t - x_p|$ is neither too small (the tissue motion does not represent a propagating shear wave) nor too large (the shear wave amplitude is too small to detect). In MTL-SWEI, multiple push locations x_p can be used to extend the field of view and/or provide overlapping estimates of the same region (Tanter et al., 2008).

5.2.3 Single Track Location SWEI

Single Track Location Shear Wave Elasticity Imaging (STL-SWEI) is a novel variant of SWEI derived from the work of McAleavey et al. (2009a). Mathematically, it can be considered as finding the partial derivative of the arrival times T with respect to x_p instead of x_t:

$$\mathrm{SWS}_{\mathrm{STL}}(z, x_t, x_p) = \mathrm{sgn}(x_p - x_t) \left(\frac{\partial T(z, x_t, x_p)}{\partial x_p} \right)^{-1} \tag{5.5}$$

Rather than tracking the speed of a single propagating shear wave going through multiple tracking locations, this approach employs multiple, laterally-offset push beams and a single tracking location. This is shown in figure 5.2 as tracking the propagation across a row. The simplest two push beam configuration is shown in figure 5.1[B]. The difference in arrival time T of the propagating shear waves is

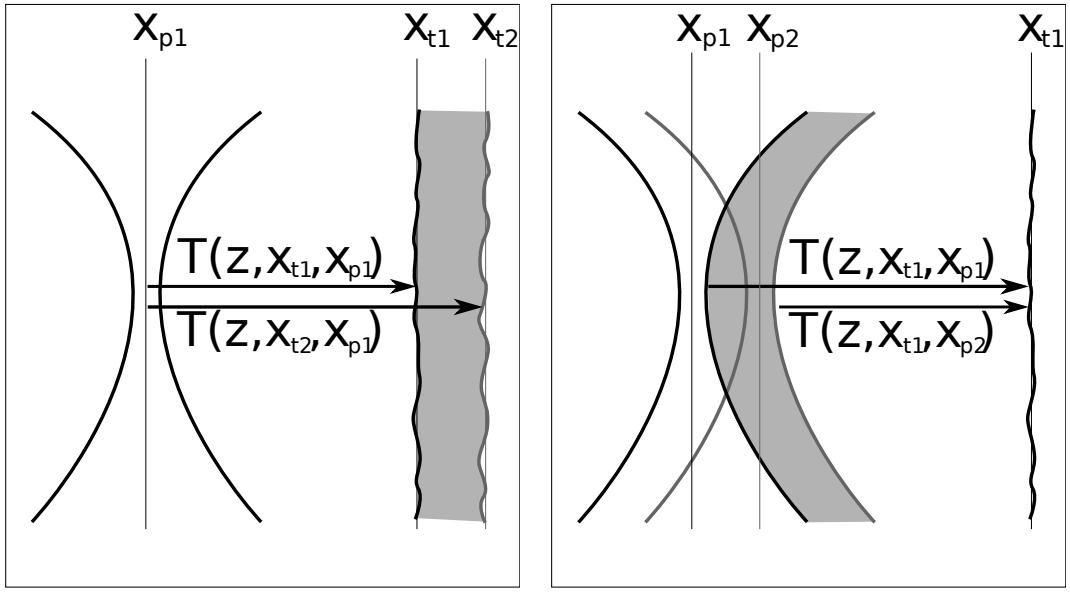

MTL-SWEI (A) STL-SWEI (B)

FIGURE 5.1: In both MTL-SWEI and STL-SWEI, the wave speed at each depth is calculated by dividing the known distance Δx by the difference in shear wave arrival time. The tracking beams illustrated show random speckle bias through depth. The interrogated region is shaded. (A) MTL-SWEI configuration. A single shear wave generated at x_{p_1} is tracked at multiple locations spaced laterally $\Delta x = x_{t_2} - x_{t_1}$ apart. (B) STL-SWEI configuration. Two push beams separated by $\Delta x = x_{p_2} - x_{p_1}$ produce shear waves recorded at a single tracking location x_{t_1}.

quantified at a single tracking location x_{t1}, and combined with the known distance between the pushing beam sources:

$$\hat{\text{SWS}}_{\text{STL}}(z, x_{t1}, x_p) = \frac{x_{p2} - x_{p1}}{\hat{T}(z, x_{t1}, x_{p2}) - \hat{T}(z, x_{t1}, x_{p1})}, \quad \text{for } x_{p1} < x_p < x_{p2}. \tag{5.6}$$

This has especially favorable behavior with respect to its interaction with speckle noise, as discussed in the next section. With more than two push beams, regression is possible over x_p in the same way as it is for MTL-SWEI over x_t. An important distinction is that the $\hat{\text{SWS}}_{\text{STL}}$ estimate reflects the stiffness in the region of tissue between the *pushes* (more specifically between the leading edges of the pushes, in the case of using time-to-peak-velocity), as outlined in figure 5.1[B]. The velocity

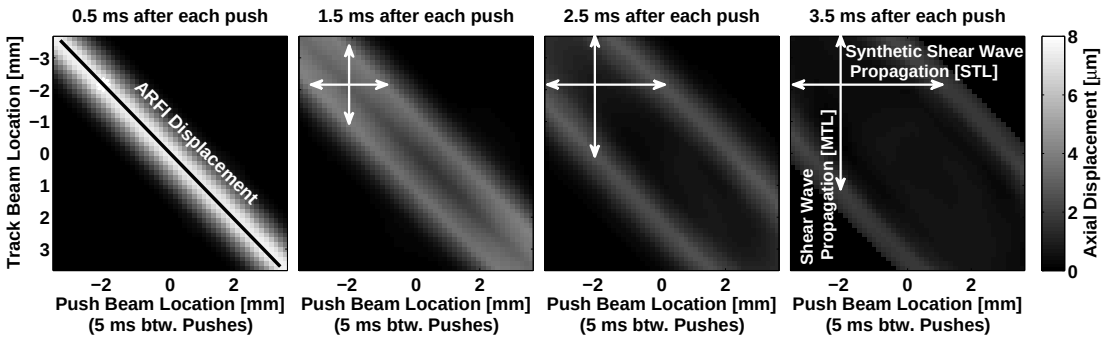

FIGURE 5.2: Images of propagating shear wave displacement from a simulated dataset. The y-axis portrays track beam locations, which are monitored at the same time using parallel beamforming methods. The x-axis represents push beam locations, which are interrogated sequentially. Displacement through time is monitored for each push at all track beam locations. MTL-SWEI employs linear regression along the vertical axis x_t (i.e., between the wave arrival times and the track beam locations, shown as the why vertical arrows), whereas STL-SWEI employs linear regression along the horizontal axis x_t (i.e., between the wave arrival times and the push beam locations, shown as the white horizontal arrows). ARFI images are created from the early time displacements tracked at the push locations.

estimate is not dependent upon the specific track beam location, only subject to the same constraints on $|x_p - x_t|$ as MTL-SWEI, which limit the usable lateral field of view for any single track beam to the regions around the track beam with sufficient displacement SNR. Following on this reciprocity, multiple track locations serve the same purpose at multiple push locations in MTL-SWEI to extend the usable lateral field of view (up to the widest spacing of push beams) and/or provide overlapping estimates. The trade-off for creating STL-SWEI images rather than MTL-SWEI images is that STL-SWEI sequences *require* exciting the tissue at every location to be measured. STL-SWEI systems will therefore have lower maximum framerates and higher acoustic exposures than MTL-SWEI systems, with values almost identical to ARFI imaging.

5.2.4 Sources of Noise in Elasticity Imaging

There are two main types of noise associated with ARFI and SWEI estimates: jitter and bias. Jitter is uncorrelated random noise that degrades displacement estimation, and is affected by the electronic signal to noise ratio (SNR), decorrelation of the RF signals due to motion, as well as the frequency design of the track beams (Walker and Trahey, 1995; Pinton et al., 2006). Jitter directly adds noise to ARFI images, and adds uncertainty to the estimation of $\hat{T}$, which affects arrival time estimates for both types of SWEI. The other type of error is bias, which is correlated noise that is not averaged out over multiple acquisitions. In ultrasonically-tracked displacements, speckle noise can be thought of as a bias, since the speckle pattern is stationary in the absence of motion. Speckle has well-defined statistics (Wagner et al., 1983, 1988; Walker and Trahey, 1998), but the specific pattern for any imaged structure cannot be predicted. Similar behavior is seen in both ARFI and MTL-SWEI images. Some of the noise in ARFI images is spatially correlated and is remains stationary across multiple acquisitions (McAleavey et al., 2003). The key assumption that motivates STL-SWEI imaging is that at each tracking location (depth and steering), the displacement value returned by the estimator is representative not of the motion at the center of the tracking beam, but of the motion at an unknown, but biased position offset in 3D from the beam. This is discussed in Elegbe *et al's* work, where arrival time of the shear wave is shown to be biased with some degree of spatial correlation (Elegbe and McAleavey, 2013). Denoting the jitter as η and the bias as a vector $\vec{\varepsilon}(z, x_t)$, we can add these terms to our definition of $\hat{T}$, using only the lateral component of the bias $\varepsilon_x(z, x_t) = \vec{i} \cdot \vec{\varepsilon}(z, x_t)$:

$$\hat{T}(z, x_t, x_p) = T\left(z, x_t + \varepsilon_x(z, x_t), x_p\right) + \eta \tag{5.7}$$

For the MTL-SWEI finite difference case, as $x_{t2} - x_{t1}$ approaches 0, the effect of ε_x starts to dominate the estimate of $\hat{T}(z, x_{t2}, x_{p1}) - \hat{T}(z, x_{t1}, x_{p1})$, and, since the arrival

time derivative is the denominator of the shear wave speed estimate, the errors become very large. Overlapping estimates will suppress the random jitter error η, but will not remove the speckle bias ε. Regression over more than two track locations will also suppress the noise, but the bias is spatially correlated, so the effectiveness of the regression is likely determined by how many independent speckles are included. On average, the derivative of the arrival times represents the shear wave speed, so using a linear regression or pairs of more widely-spaced track beams reduces the effect of the bias on each estimate at the expense of spatial resolution. The resolution of SWEI methods is thus limited by the regression kernel size, as well as the shear wave frequency and bandwidth (Deffieux et al., 2012; Rouze et al., 2012).

STL-SWEI, on the other hand, is not susceptible to speckle bias that affects MTL-SWEI estimates, since STL-SWEI uses the same bias realization on its tracking location to measure the passage of each shear wave. Since the bias is fixed with the scattering realization, this only adds a constant offset to all arrival times at each depth and tracking location, and does not affect estimation of the partial derivate with respect to x_p. The offset in local tracking location in STL-SWEI has the same effect as a small offset in the push location would in MTL-SWEI, which is to say, effectively none. In place of speckle bias, aberration or focal errors that create distortion in the push beam geometry introduce the equivalent errors to STL-SWEI estimates, but these are less egregious than the speckle bias, which is inherent to the process of B-mode ultrasound beamforming.

5.3 Methods

5.3.1 Experimental Setup

A custom zerdine phantom (CIRS) was imaged with a prototype Siemens 12L4 linear array transducer connected to a Siemens Acuson SC2000 ultrasound scanner (Siemens Healthcare, Mountain View, CA). The phantom contained four stepped

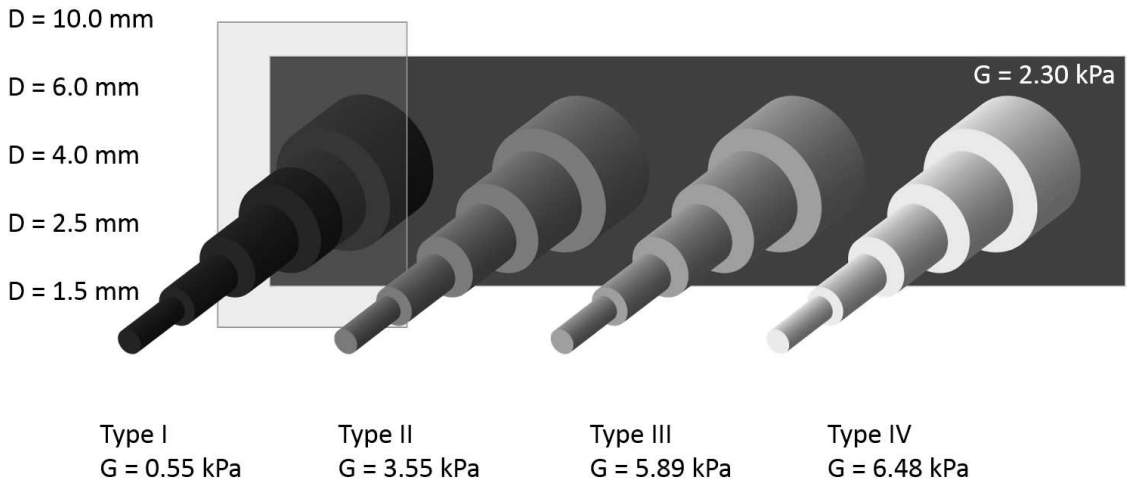

FIGURE 5.3: Stepped cylindrical inclusion phantom used for the experiment.

cylinder inclusions, with diameters of 1.5 mm, 2.5 mm 4 mm, 6 mm, and 10 mm. The cylindrical inclusions had nominal shear moduli G of 0.67 kPa, 5.33 kPa, 8.00 kPa, and 10.67 kPa, and a background with $G = 2.67$ kPa. Each combination of inclusion size and stiffness was imaged with six independent speckle realizations. A diagram of the phantom is shown in figure 5.3. The actual moduli of the inclusions are known to vary from the nominal values, so the phantom was calibrated using Siemens' quantitative elasticity measurement (qEI) software and a 9L4 linear array transducer on a Siemens Acuson S2000 scanner. Calibration measurements were taken in the largest inclusions to avoid boundary effects. Table 5.1 shows the calibration data, indicating lower estimated shear moduli than the nominal values. Values are reported as mean plus or minus one standard deviation over six acquisitions.

5.3.2 Pulse Sequences

In order to maintain registration and to provide a closely-matched comparison between the three types of images without biasing the results in favor of one type, a pulse sequence was designed to acquire all three images in a single acquisition. A series of 400 cycle, 4.6 MHz excitation pulses, focused at 25 mm with an F-number

Table 5.1: Phantom Elasticity Calibration

	G_{nom} (kPa)	SWS_{qEI} (m/s)	G_{qEI} (kPa)
Background	**2.7**	1.51 ± 0.03	$\mathbf{2.30} \pm 0.09$
Type I	**0.7**	0.74 ± 0.03	$\mathbf{0.55} \pm 0.05$
Type II	**5.3**	1.88 ± 0.04	$\mathbf{3.55} \pm 0.16$
Type III	**8.0**	2.43 ± 0.02	$\mathbf{5.89} \pm 0.12$
Type IV	**10.7**	2.54 ± 0.02	$\mathbf{6.48} \pm 0.08$

*Values are reported as mean ± one standard deviation over six measurements. SWS_{qEI} is reported by the software, and G_{qEI} is calculated as $\text{SWS}^2_{\text{qEI}}$ from equation 5.1, assuming $\rho = 1$ g/cm^3.

of 2, were sequentially delivered every 0.16 mm (1/4 of the lateral beamwidth) across a 20 mm lateral field of view. Two 5 MHz tracking frames were recorded before each excitation and 40 after, at a frame rate of 10,000 fps to image the induced shear waves. For each excitation location, the sample was excited three times with different tracking configurations. Tracking lines were recorded at the excitation, and with 0.16 mm spacing to either side of the excitation, offset between 1.3 mm and 6.5 mm from the excitation, for a total of 32 lines to the left, one in line with, and 32 lines to the right of each excitation. A diagram is shown in figure 5.4. To acquire this dataset with 126 excitation locations and 8190 total tracking locations, 7 separate sub-acquisitions were used to meet the parallel receive beamforming and bandwidth limits of the scanner. The first three sub-acquisitions excited 42 locations each, tracking the locations to the right of each excitation with plane wave transmits and parallel receive beamforming. The second three sub-acquisitions excited the same set of locations, but used tracking beams to the left of each excitation. The final sub-acquisition excited the same locations a third time, but used focused tracking transmits to track the tissue in line with the excitation. The entire acquisition took approximately 60 seconds per image with extended delays between pushes, but with more parallel beams and a single continuous acquisition sequence, each 126-push dataset could be acquired in approximately 500 ms. Such beam density may be

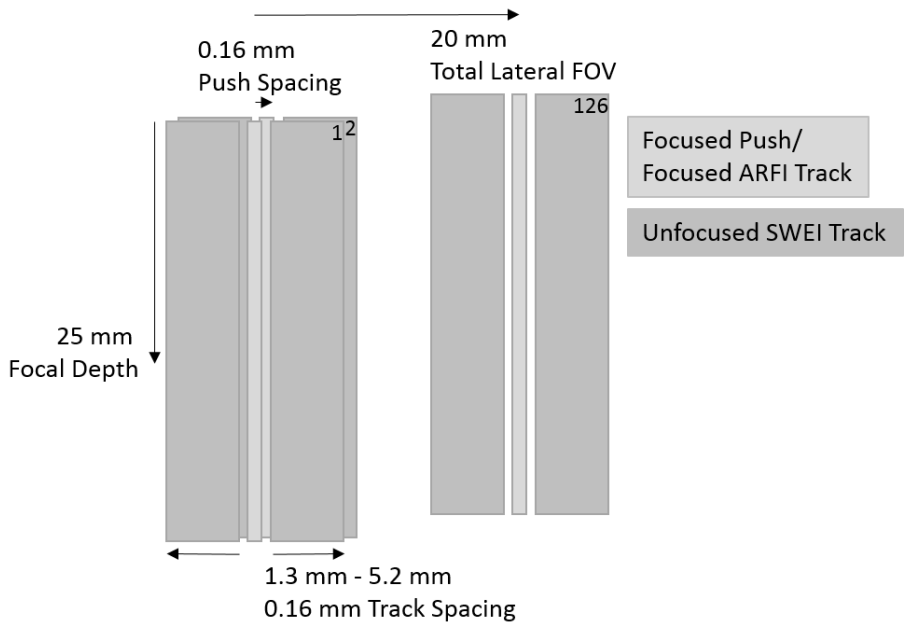

FIGURE 5.4: Acquisition sequence. 126 excitations are tracked to the left and right at 0.16 mm track beam spacing. Push beam location translates 0.16 mm laterally between each acquisition. Focused track beams are used for measuring on-axis (ARFI) displacements.

unnecessary for *in vivo* imaging, but the fine spacing of the push and track beams allows analysis of the resolution limits of each modality.

5.3.3 Image Formation and Post-Processing

For each type of elasticity image, Loupas's algorithm (Loupas et al., 1995) was used with a 1.2 mm (4λ) kernel to estimate axial displacement relative to an anchored reference frame prior to excitation. ARFI images were depth-normalized using an averaged reference axial displacement profile taken from the homogeneous background. Images are displayed as the ratio of the reference displacement profile to the measured profile for each lateral beam. Note that this is the normalized *inverse* of displacement. This gives the background signal a mean value of 1, and the signals from each inclusion indicate the ratio of shear modulus in the inclusion relative to the background (Palmeri et al., 2006a). For both STL-SWEI and MTL-SWEI, the

displacements were differentiated through tracking time ("slow time") at each pixel and band-pass filtered with a 3rd order Butterworth filter with cutoff frequencies of 50 and 1000 Hz. The filtered axial velocities were next fed through a directional filter (Deffieux et al., 2011) for each push location (MTL-SWEI) or track location (STL-SWEI) to remove reflection artifacts. The axial displacements (ARFI) and velocities (SWEI) were each median filtered axially with a 0.54 mm kernel. The arrival time of the shear wave at each location was found from the peak of the velocity signal at each pixel, using quadratic subsample estimation, and excluding candidate estimates representing velocities far outside the expected range (greater than 6 m/s or less than 0.5 m/s). A moving lateral linear regression was applied around each sample, with varying kernel sizes from 0.16 mm (2-sample difference) to 4 mm (26-sample regression). For MTL-SWEI, each of the 126 push locations formed a 10.4 mm wide sub-image from all of the track beams associated with it. The same is true of STL-SWEI, but each sub-image represents a single track location and the pushes within 5.2 mm to either side. For the STL-SWEI images, an additional depth-dependent lateral shift was applied to each sub-image to compensate for the shape of the push beam (appendix B). Each sub-image was then laterally cropped to the center 6 mm, since velocity estimates with greater than 3 mm separation between the push and track beams had low displacement SNR; this also served to avoid boundary effects when using large kernel sizes. Finally, the 126 cropped sub-images for each mode were aligned and combined by taking the median at each aligned pixel.

5.3.4 Image Statistics

Once the matched ARFI, MTL-SWEI, and STL-SWEI images were created, image statistics were computed for each combination of target size and stiffness. Statistics were computed separately for each combination of regression filter kernel (for SWEI images), and timestep (for ARFI images). The region of interest (ROI) inside of

the lesion was defined as the circle with 2/3 the radius of the expected inclusion, concentric with the inclusion. The background was defined as a ring concentric with the inclusion and cropped to the axial depth of field, with an inner radius of 120% of the expected inclusion size, and an outer radius of 10 mm. The same ROIs were used for all three imaging modalities.

Contrast

Contrast was computed from the differences in the median pixel values of the inside and outside ROIs:

$$\text{contrast} = \frac{|\mu_{in} - \mu_{out}|}{\mu_{out}} \tag{5.8}$$

Medians were selected over means to keep the measurements robust to outliers, since shear wave speed is calculated as the reciprocal of arrival time differences, and some estimates are large outliers associated with arrival time differences close to 0. This also has the added benefit of making contrast agnostic of the fact that we are using inverted displacement images for ARFI. To get traditional ARFI displacement image contrast, the values are exactly the reciprocal of the inverse displacement image contrast.

Contrast-to-Noise Ratio

The contrast-to-noise ratio (CNR) was computed as the difference in the median pixel values of the regions, divided by the image noise, taken as the standard deviation of the background.

$$\text{CNR} = \frac{|\mu_{in} - \mu_{out}|}{\sigma_{out}} \tag{5.9}$$

Resolution

The lateral resolution in each image was computed by fitting a trapezoidal function to the inclusion data. The image values were averaged through depth about the

center 0.5 mm of the target. A series of candidate trapezoids were tested by filtering an ideal square function, appropriately positioned and sized to match each target, and scaled based on qEI calibration measurements, with varying boxcar filters, using normalized cross correlation to compare the shapes. Subsample peak estimation was used to find the boxcar filter size that most closely reproduced the data, and the lateral resolution is reported as 60% of the boxcar width, to represent the 20-80% edge width of the trapezoid.

5.4 Results

5.4.1 ARFI Time Step Dependence

Figure 5.5 shows the ARFI displacements every 0.2 ms after excitation for the Type IV, 6 mm inclusion. The top row shows the raw displacements, and the bottom row shows the inverted displacements, normalized to the background displacement at each time step. The stiff inclusion appears to grow as the tissue motion evolves. The maximum displacement image keeps the lesion at its minimum size, but has inferior contrast to some frames. The higher-contrast region inside the inclusion appears to shrink with time step.

Figure 5.6 shows a single depth of each normalized inverted ARFI image, taken through the center of each 6 mm inclusion. The fourth image corresponds to the data shown in figure 5.5. The horizontal axis shows tracking time. Both contrast and the lesion boundary characteristics vary with tracking time step, as shear waves generated at each push location reflect off the boundary and come back to interfere with the displacement response at the push location. Superimposed on the image for reference are lines radiating from each boundary indicating one half of the shear wave speed (the round trip speed) in each medium. The distortion in each case appears to propagate away from the boundary at approximately one half the shear wave speed.

ARFI contrast, CNR, and resolution as a function of time step are shown in

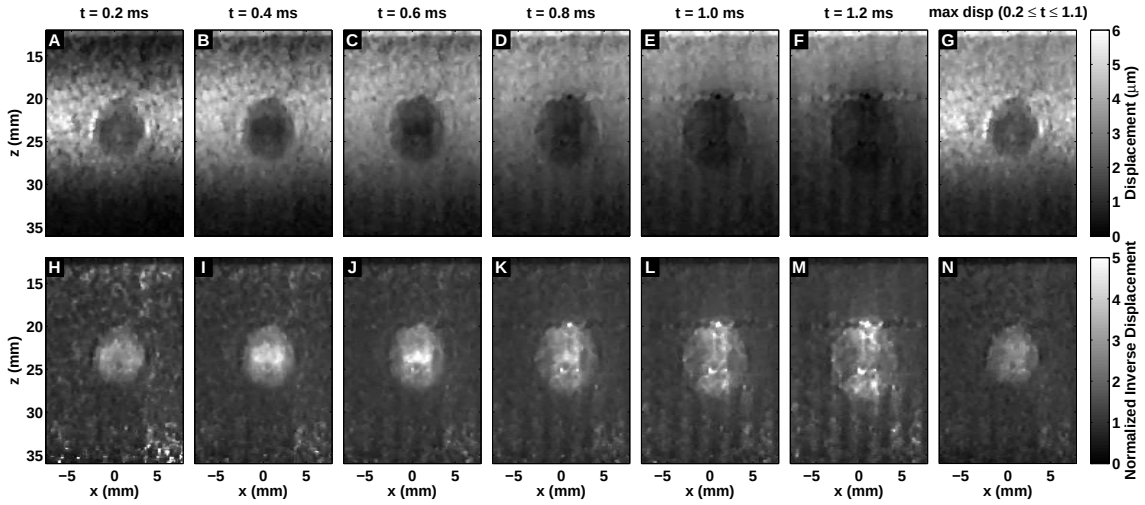

FIGURE 5.5: ARFI frames of the 6 mm, Type IV kPa inclusion at different times after excitation. The last column (G,N) shows the maximum displacement image. The first row (A-G) shows displacements, and the second row (H-N) shows inverse displacements normalized by the background profile. The lesion size appears to grow with time after excitation.

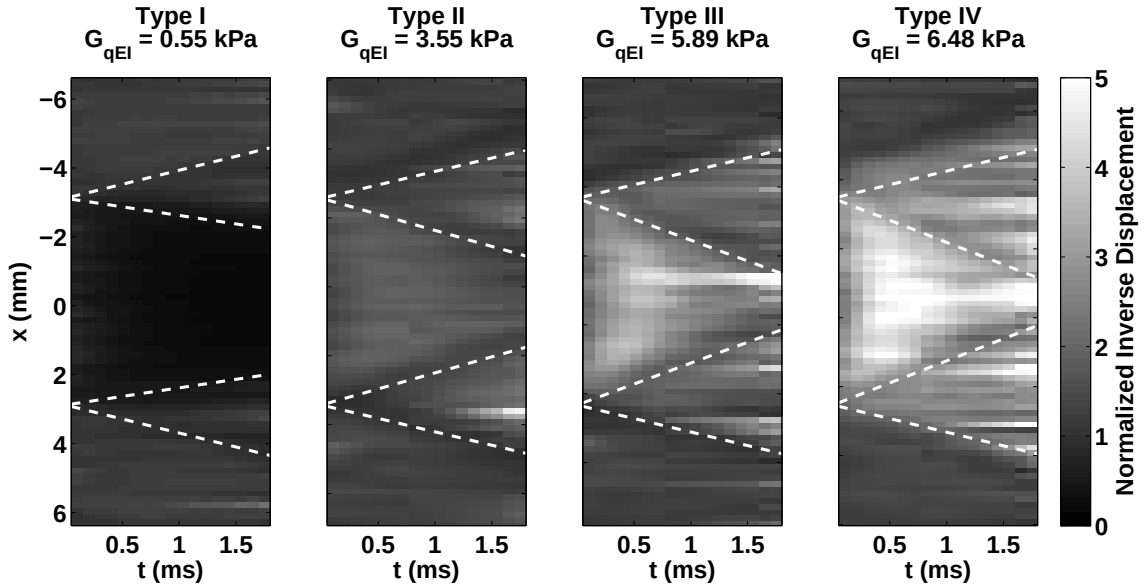

FIGURE 5.6: Evolution of inclusion boundaries through tracking time for each of the 6 mm targets in normalized inverse ARFI. Lines representing half of the expected shear wave speed in each medium are drawn propagating from each boundary. The Type IV inclusions corresponds to the data shown in figure 5.5.

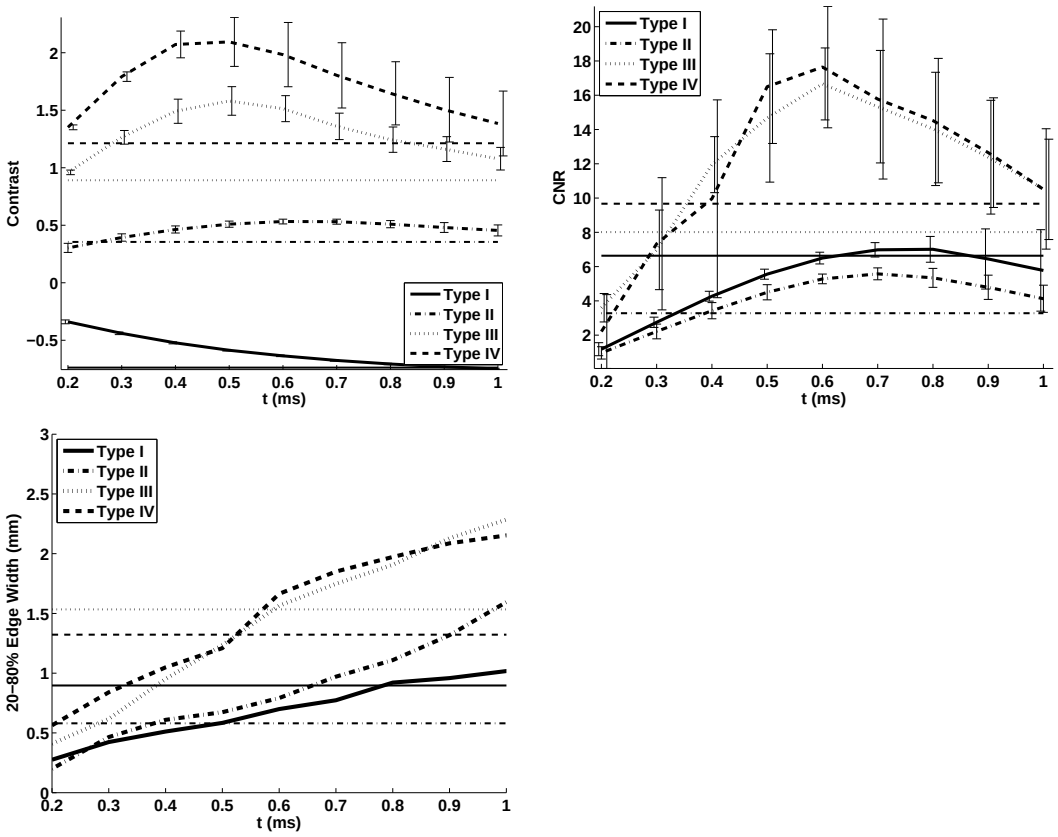

FIGURE 5.7: ARFI contrast, CNR, and resolution as a function of tracking time step for each fo the 6 mm inclusions. Line style indicates the type of target, and horizontal lines indicate the values associated with the corresponding maximum displacement images.

figure 5.7. The horizontal lines indicate the values associated with the corresponding maximum displacement image. Contrast is maximized between 0.5 ms and 1 ms after the push for the stiff inclusions, and has not peaked at 1 ms after the push for the soft inclusion (more negative contrast is better for the soft inclusion). The maximum displacement values show suboptimal contrast, especially for the stiffest inclusions. Corresponding CNR values show more clearly that for ARFI images, CNR is maximized within the first millisecond, and reaches values up to twice as high as the maximum displacement image values. Lateral resolution decreases (edge width increases) with time step, approximately following the trends predicted by half of the

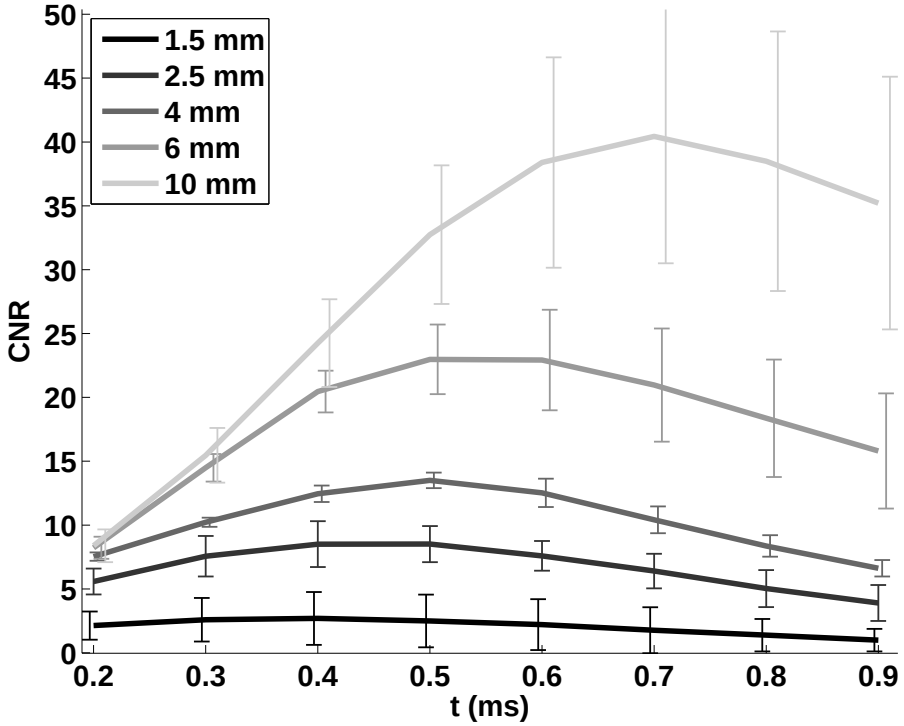

FIGURE 5.8: ARFI CNR as a function of time step for each of the Type IV inclusions. The size of the target determines the time step with the maximum CNR.

shear wave speed (figure 5.6). The maximum displacement images have resolution similar to the frames 0.5 ms after excitation, which experimentally confirms the findings in simulations by Palmeri *et al* (Palmeri et al., 2006a). Figure 5.8 shows the CNR for each size of the Type IV targets, indicating that the CNR peaks at different time step based on target size. Based on this result, to balance maximizing CNR with maintaining resolution, a time step of 0.3 ms was selected for the 1.5 and 2 mm inclusions, a time step of 0.4 ms was selected for the 4 and 6 mm inclusions, and a time step of 0.5 was selected for the 10 mm inclusions for display and comparison.

5.4.2 Image Comparison

Images showing each combination of size and stiffness lesion are shown in Figs. 5.9, 5.10, and 5.11. In all three figures, a 0.33 x 0.33 mm median filter has been applied to the final images. For the ARFI images, values are shown as the inverse

of displacement, relative to the background, and depth-normalized. For the SWEI images, values are shown as shear modulus G, with a dynamic range of 0 to 9.3 kPa. ARFI images have the equivalent dynamic range, at 0 to 4 times the normalized inverse background displacement value. For the MTL- and STL-SWEI images, the image shown is the median value of shear modulus G for all overlapping estimates within 3 mm of the excitation, which translates to 20 estimates for each pixel. In each set of images, lesion conspicuity increases with lesion size and contrast. The largest and stiffest inclusions show higher contrast in ARFI than in the corresponding SWEI images. The large, soft inclusions appear as ovals in all images.

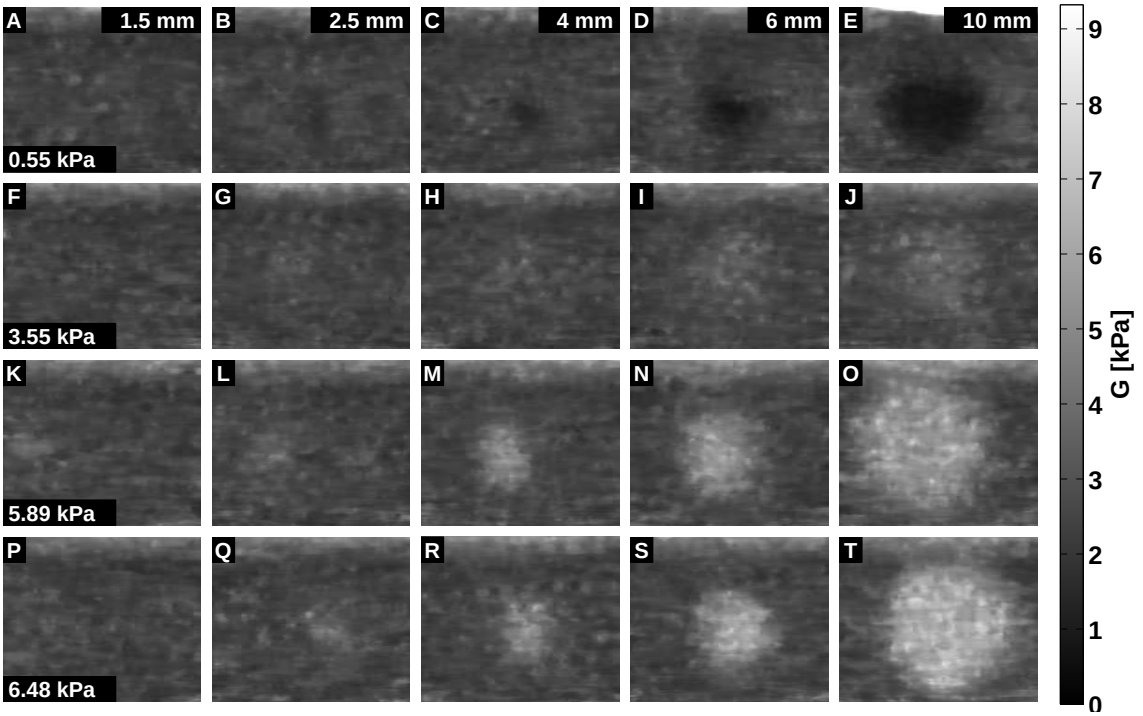

FIGURE 5.9: MTL-SWEI images images for each size and stiffness target. A 3.66 mm regression filter was used to calculate shear wave velocities from arrival times, and a 0.33 x 0.33 mm median filter has been applied to the images. Values are displayed as estimated shear modulus with a dynamic range of 1.75 to 7 kPa.

For a direct comparison, the images for the Type IV ($G_{\mathrm{qEI}} = 6.48$ kPa) inclusions are again shown in figure 5.13 for each of the three elasticity imaging modalities.

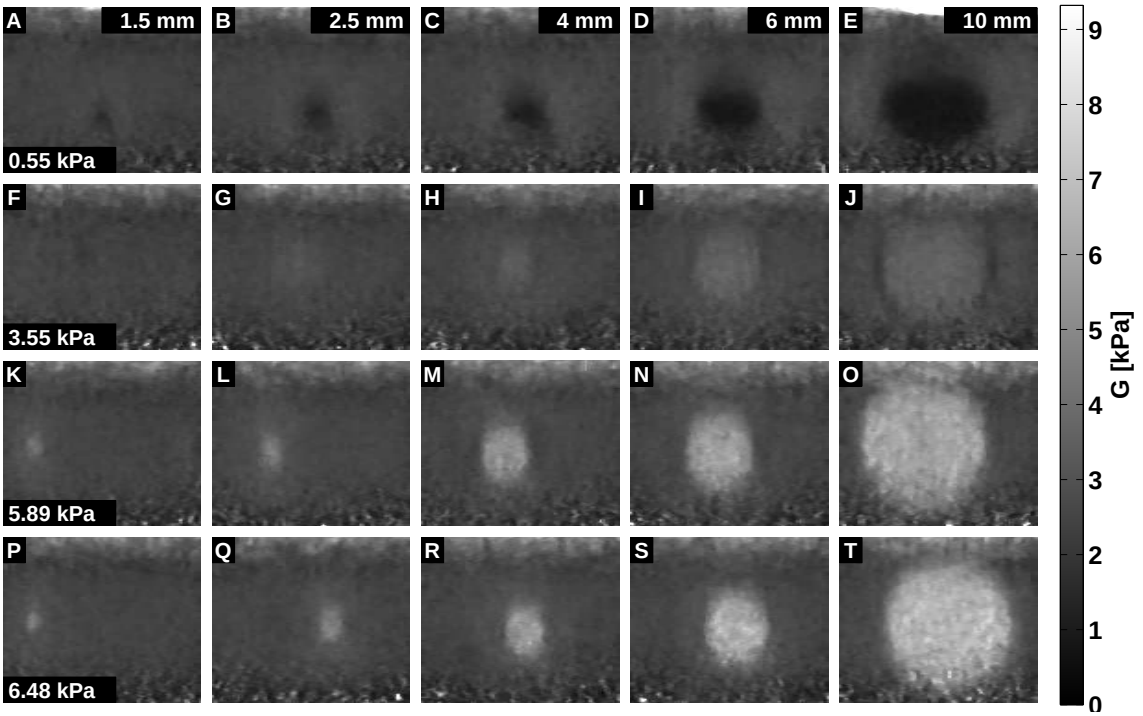

FIGURE 5.10: STL-SWEI images images for each size and stiffness target. A 0.67 mm regression filter was used to calculate shear wave velocities from arrival times, and a 0.33 x 0.33 mm median filter has been applied to the images. Values are displayed as estimated shear modulus with a dynamic range of 1.75 to 7 kPa.

In the MTL-SWEI images (figure 5.13[A-E]), the large inclusions are easily distinguished, while the smaller targets start to become lost in the background variation. The spatial variability in the estimates is correlated across different excitation location sources, so is not removed when overlapping estimates are combined. This can be seen in figure 5.12, which shows the arrival times for all of the sub-images that go into the full SWEI images.

The STL-SWEI images (figure 5.13[F-J]), on the other hand, show similar contrast to MTL-SWEI, but are both smoother and have sharper edges. The ARFI images (figure 5.13[K-O]) show higher contrast than the SWEI images for the 4 mm and larger targets, but have more background noise than STL-SWEI. In terms of texture, the ARFI images fall between the STL-SWEI and MTL-SWEI.

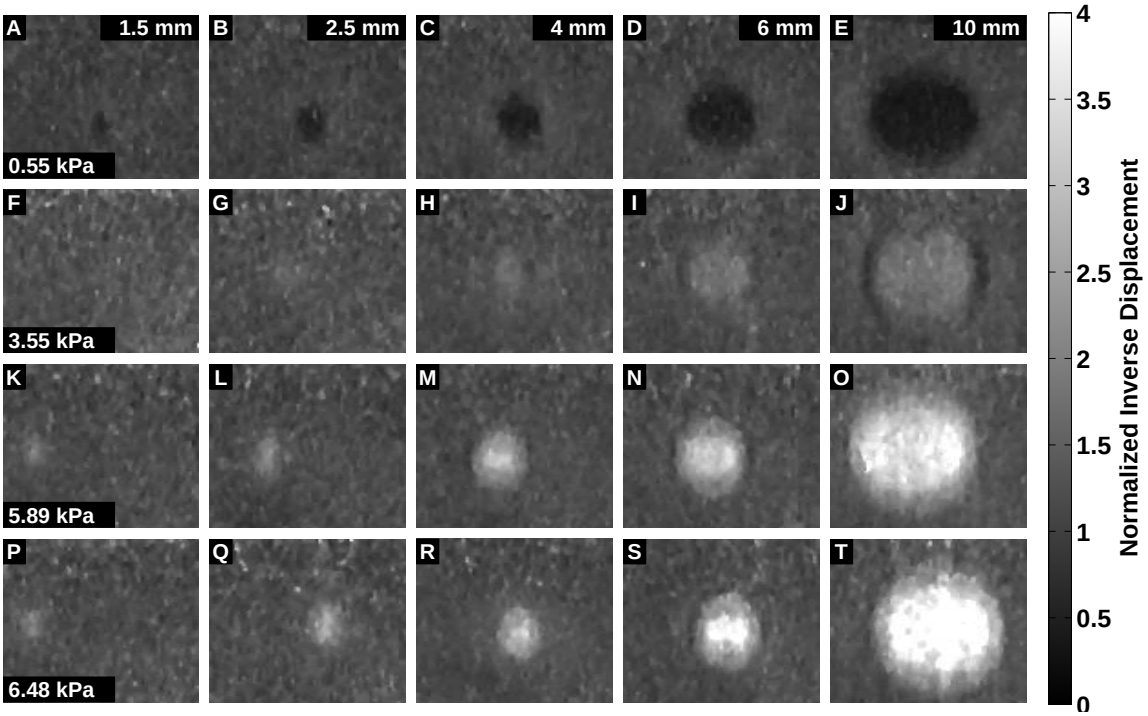

FIGURE 5.11: ARFI images for each size and stiffness target at 0.3 ms (1.5 and 2.5 mm), 0.4 ms (4 and 6 mm) or 0.5 ms (10 mm) after excitation. A depth-dependent normalization has been applied. Values are shown as inverse displacement relative to the background with a dynamic range of 0.75 to 3. A 0.33 x 0.33 mm median filter has been applied to the images.

5.4.3 Contrast

Figure 5.14 shows contrast as a function inclusion size for the Type IV inclusions and the different modalities. The nominal contrast should be 1.82 based on G_{qEI} measurements, shown as the gray horizontal line. ARFI has the highest contrast, followed by STL-SWEI and then MTL-SWEI. For all modalities, contrast is underestimated for the small targets.

Figure 5.15 compares the contrast of the 6 mm inclusions across stiffnesses and modalities, using the commercial qEI measurements from the largest inclusions (table 5.1) for the x-axis values. Contrast in all cases trends linearly with stiffness, although the contrast is slightly underestimated relative to the nominal contrast of

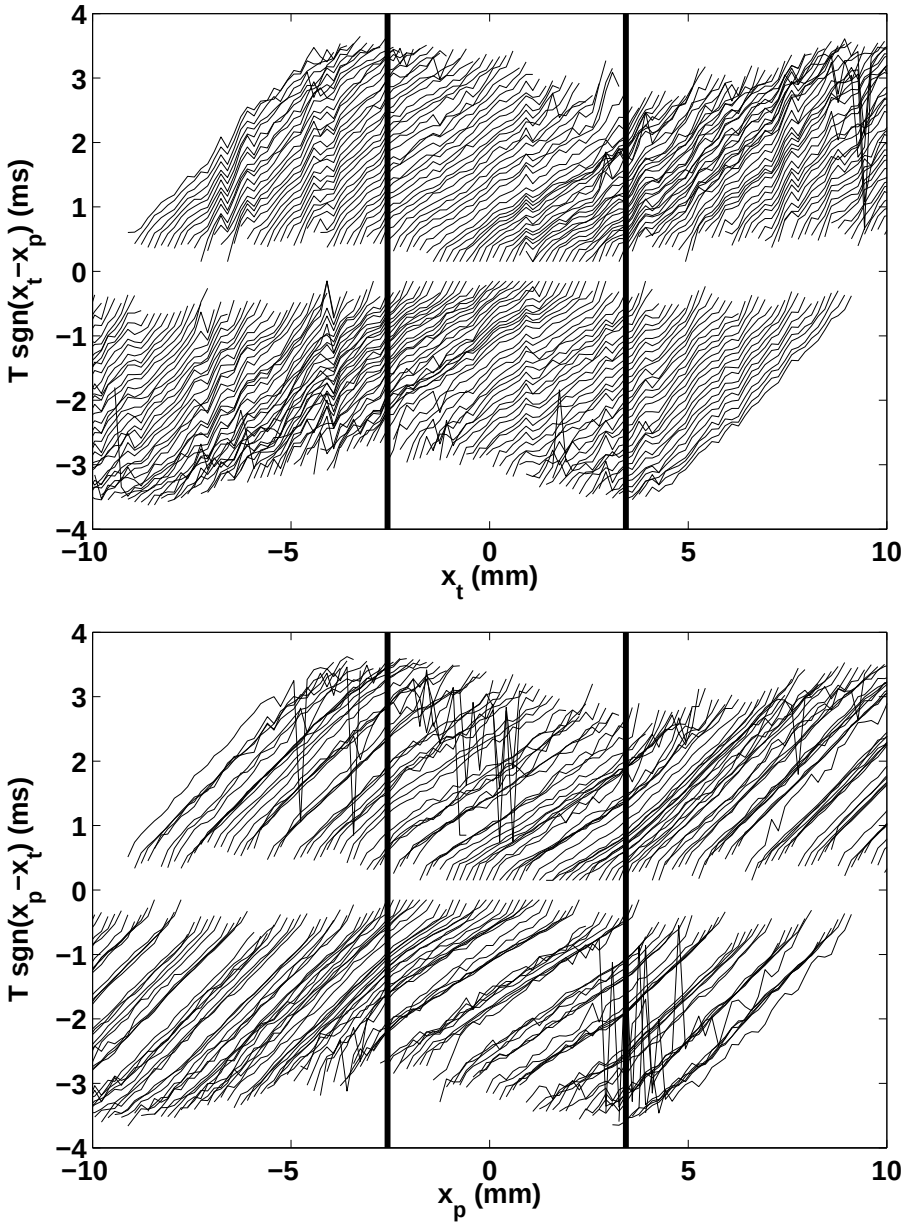

FIGURE 5.12: Arrival times for MTL-SWEI (top) and STL-SWEI (bottom) across the center of the Type IV ($G_{\mathrm{qEI}} = 6.48$ kPa), 6 mm inclusion. The vertical bars indicate the inclusion boundary. Arrival times measured to the left of the push have been negated to improve readability. The speckle bias is apparent in the MTL-SWEI processing as the waviness in the slope of each line in the top frame. The speckle bias appears in the STL-SWEI (bottom frame) as a constant offset to each line, which does not affect slope estimation.

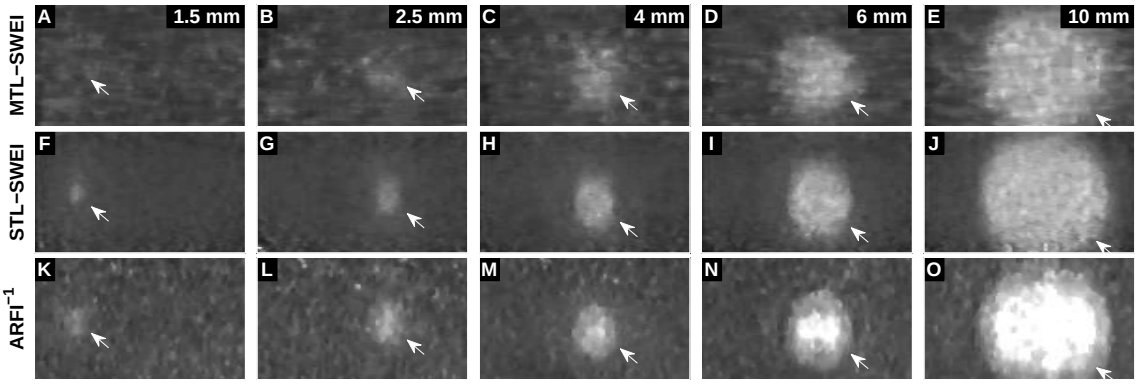

FIGURE 5.13: SWEI (MTL) [A-E], SWEI (STL) [F-J] and ARFI [K-O] images of Type IV ($G_{\text{qEI}} = 6.48$ kPa) cylindrical inclusions, excerpted from figures 5.9, 5.10, and 5.11.

Table 5.2: Contrast Measurements (6 mm Targets)

Type	qEI	MTL-SWEI	STL-SWEI	ARFI
I	$\mathbf{-0.76} \pm 0.04$	$\mathbf{-0.62} \pm 0.01$	$\mathbf{-0.67} \pm 0.01$	$\mathbf{-0.52} \pm 0.01$
II	$\mathbf{0.55} \pm 0.12$	$\mathbf{0.37} \pm 0.05$	$\mathbf{0.43} \pm 0.01$	$\mathbf{0.42} \pm 0.01$
III	$\mathbf{1.57} \pm 0.09$	$\mathbf{1.31} \pm 0.12$	$\mathbf{1.48} \pm 0.07$	$\mathbf{1.53} \pm 0.10$
IV	$\mathbf{1.82} \pm 0.06$	$\mathbf{1.52} \pm 0.12$	$\mathbf{1.74} \pm 0.07$	$\mathbf{2.14} \pm 0.10$

the phantom for the SWEI images.

Table 5.2 shows the contrast values calculated with each modality for the 10 mm targets. The values from the calibration (table 5.1) are shown for reference.

5.4.4 Contrast-to-Noise Ratio (CNR)

Figure 5.16 shows the the contrast-to-noise ratio (CNR) for each of the Type IV inclusions in each modality, as a function of inclusion size. ARFI has the highest CNR for the largest targets, while STL-SWEI has higher CNR for the smaller targets. MTL-SWEI has the lowest CNR for all sizes. In each case, the SWEI regression filter size or ARFI time step were picked to maximize CNR, so ARFI is shown at 0.6 ms after excitation, STL-SWEI uses a 1 mm kernel, and MTL-SWEI uses a 3 mm kernel.

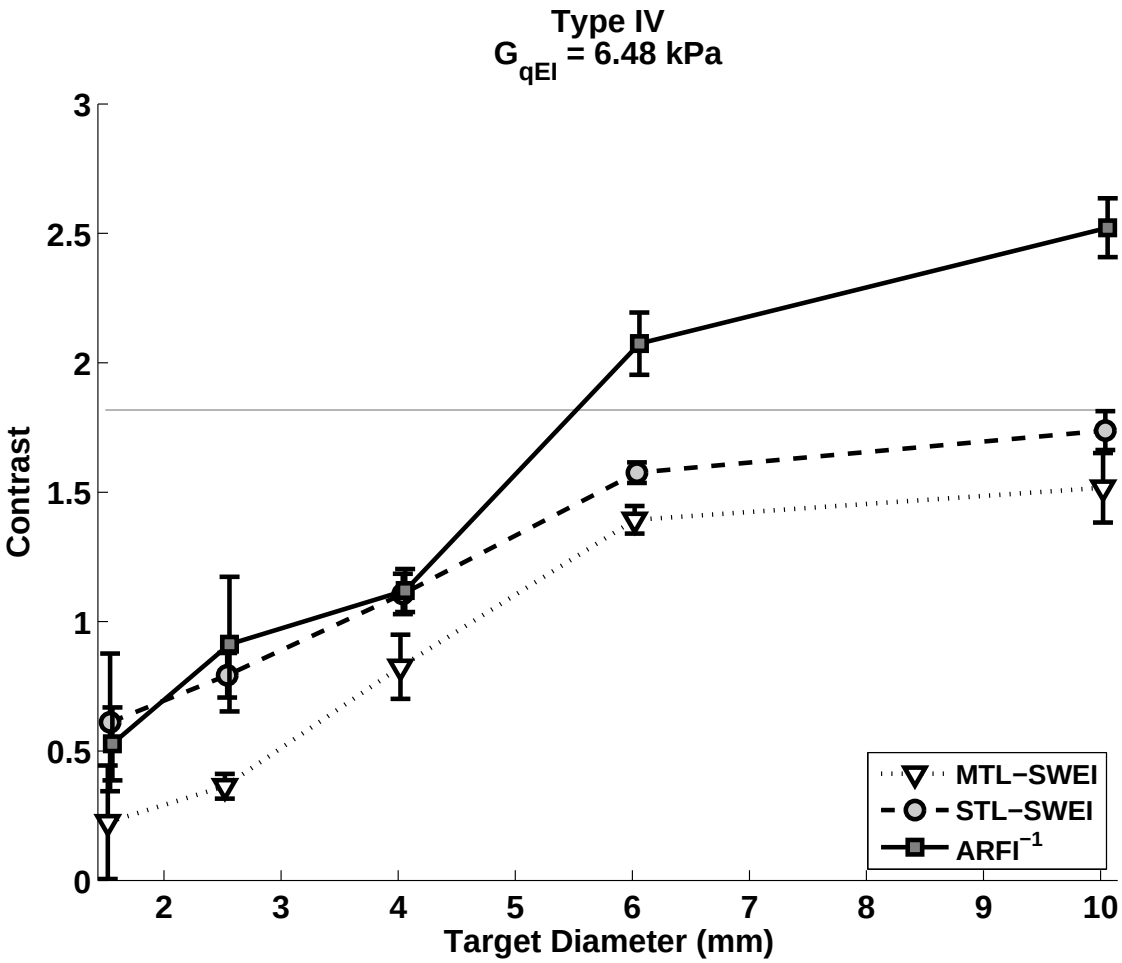

FIGURE 5.14: Contrast as a function of inclusion size for the Type IV ($G_{\mathrm{qEI}} = 6.48$ kPa) inclusions. MTL-SWEI shows lower contrast for all target sizes than ARFI and STL-SWEI. ARFI has the highest contrast, especially for the 6 mm inclusions. For the smallest inclusions, the difference between STL-SWEI and ARFI is small. The expected contrast from qEI measurements is shown as a horizontal gray line. For all modalities, contrast decreases for the smaller inclusions.

5.4.5 System Resolution Trade-offs

For the 6 mm diameter, Type IV inclusion, CNR is plotted against lateral resolution in figure 5.17. This figure portrays the "trade-off curves" between system resolution and CNR for each of the imaging modalities, based on post-processing variables. The points on the trade-off curve for ARFI shows different values of time step, starting at 0.2 ms after the excitation in the bottom left, and incrementing each 0.1 ms to the

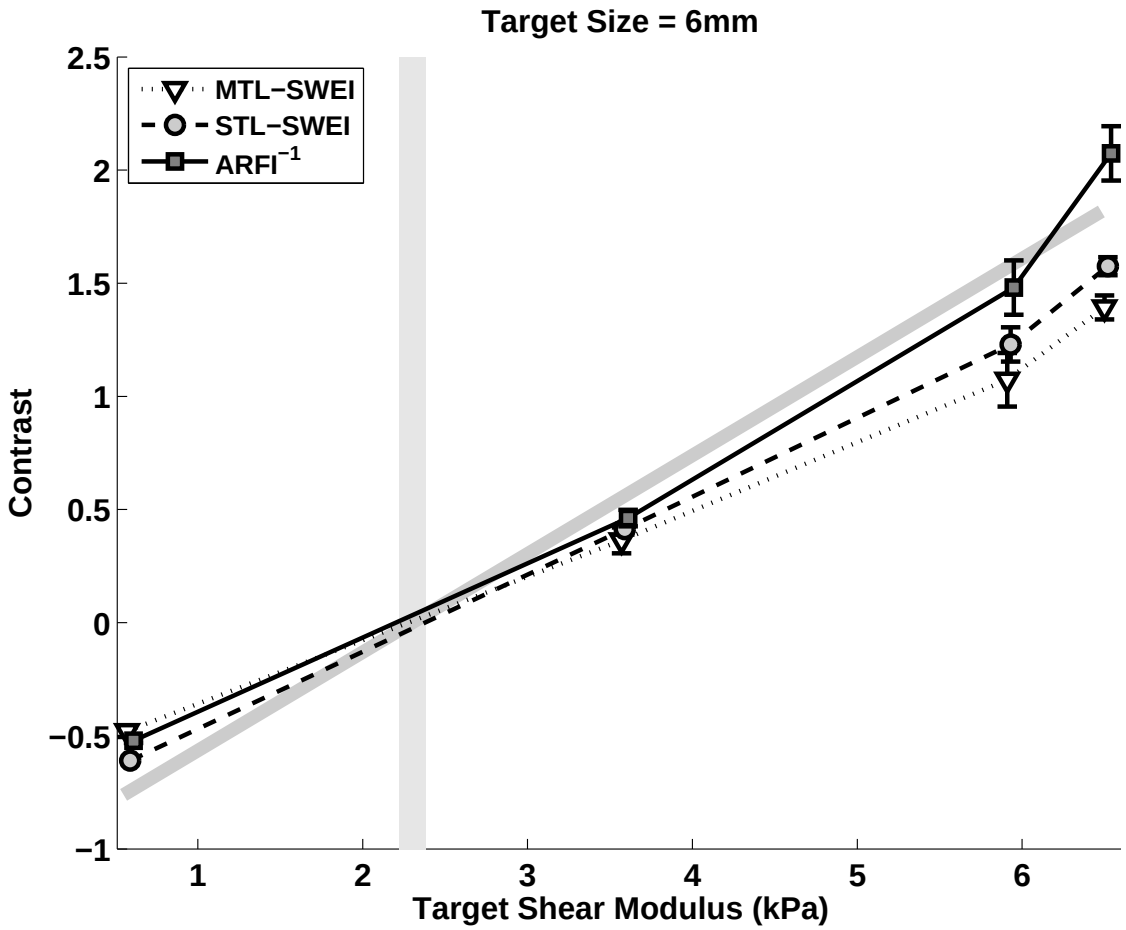

FIGURE 5.15: Contrast as a function of nominal shear modulus for the 6 mm inclusions. The background modulus is shown as a vertical gray bar at $G = 2.3$ kPa. Contrast trends linearly with nominal inclusion modulus for all elasticity imaging modes. The diagonal gray line represents agreement with commercial software-acquired shear wave speeds.

right, with the highest CNR achieved at 0.5 ms. The points on the STL-SWEI and MTL-SWEI curves indicate different regression filter kernel sizes, with better CNR and worse resolution associated with larger kernels. ARFI and STL-SWEI show the best combination of CNR and resolution, at 0.5 ms after excitation for ARFI and a 1 mm kernel for STL-SWEI. STL-SWEI obtains higher CNR than ARFI for kernels larger than 1 mm, and ARFI achieves finer resolution for time steps below 0.4 ms. The height and width of the semitransparent gray ovals show the standard deviation

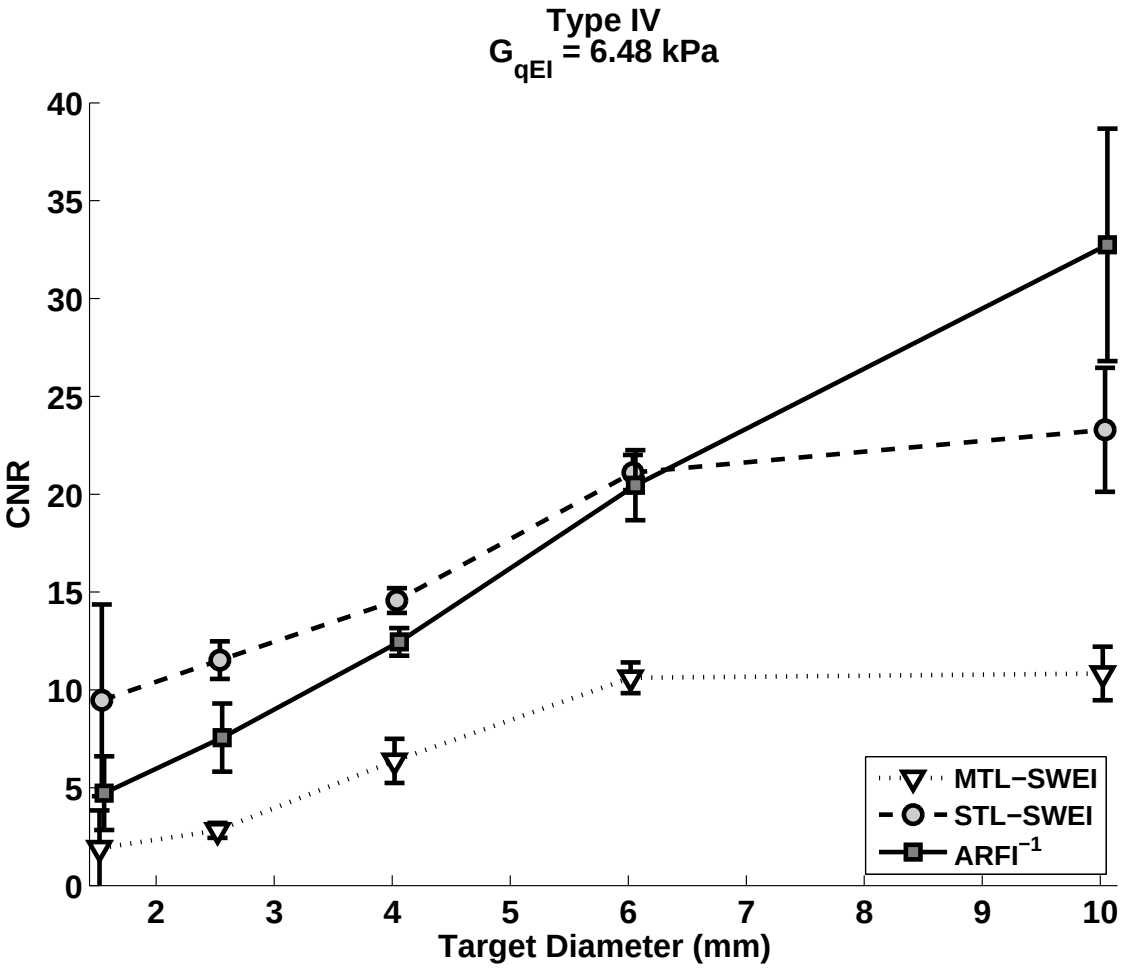

FIGURE 5.16: CNR as a function of inclusion size for the Type IV ($G_{\mathrm{qEI}} = 6.48$ kPa) inclusions. ARFI has the highest CNR for the 10 mm targets, but STL-SWEI has better CNR for the rest of the sizes. STL-SWEI and ARFI have uniformly higher CNR than MTL-SWEI.

of each measurement over the six acquisitions.

5.4.6 Towards Micro-Elasticity (μ-E): 1.5 mm Inclusions

The tradeoff of different regression kernels and ARFI time steps is visualized in figure 5.18 for the 1.5 mm, Type IV inclusion. In the top row, MTL-SWEI fails to visualize the lesion effectively, with high noise associated with small kernels and low contrast associated with large kernels. In the middle row, STL-SWEI clearly shows the lesion with the correct size, trading resolution for noise suppression from left to right and

eventually losing contrast as the kernel size exceeds the target size. In the bottom row, ARFI shows the inclusion, but overestimates the size and shows more noise in the background and inclusion than STL-SWEI. The CNR-resolution tradeoff curves are shown in figure 5.19. The CNR of this target is significantly lower than the CNR shown for the 6 mm, Type IV target from figure 5.17. While SWEI and ARFI both underestimate the stiffness of the inclusion (owing to resolution effects), STL-SWEI shows the lesion shape much more clearly than the other modalities, especially for the 0.67 mm kernel size.

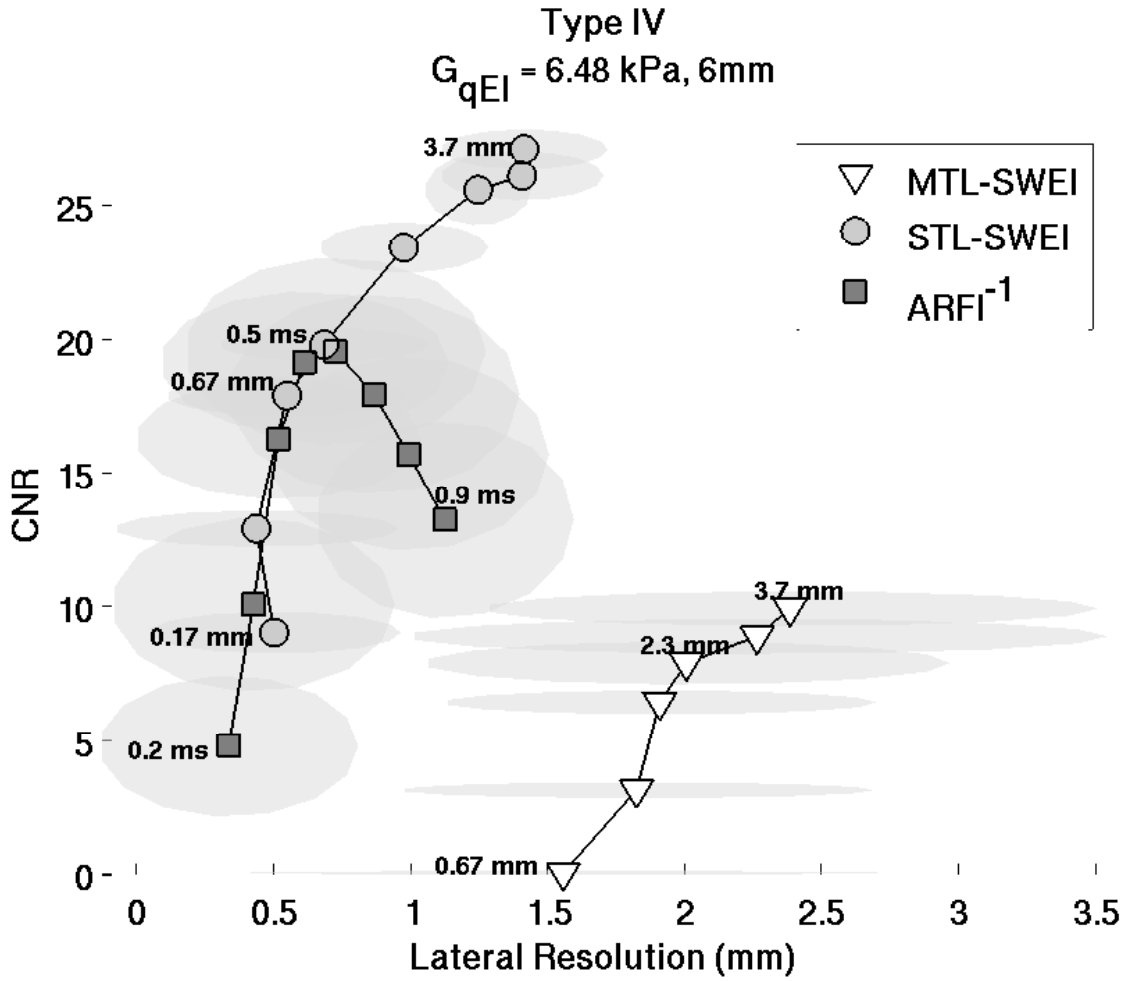

FIGURE 5.17: CNR and resolution tradeoff curves for ARFI, STL-SWEI and MTL-SWEI for the Type IV, 6 mm inclusions. The curve represents different time steps for ARFI (0.2 ms : 0.1 ms : 0.9 ms) and different regression filter sizes for STL-SWEI and MTL-SWEI. The regression filter kernel sizes are 0.16, 0.33, 0.66, 1.00, 1.66, 2.33, 3.00, and 3.66 mm, with smaller kernels having lower CNR and higher resolution than larger ones. ARFI and STL-SWEI achieve the highest combination of resolution and CNR, and show much higher resolution and CNR than MTL-SWEI.

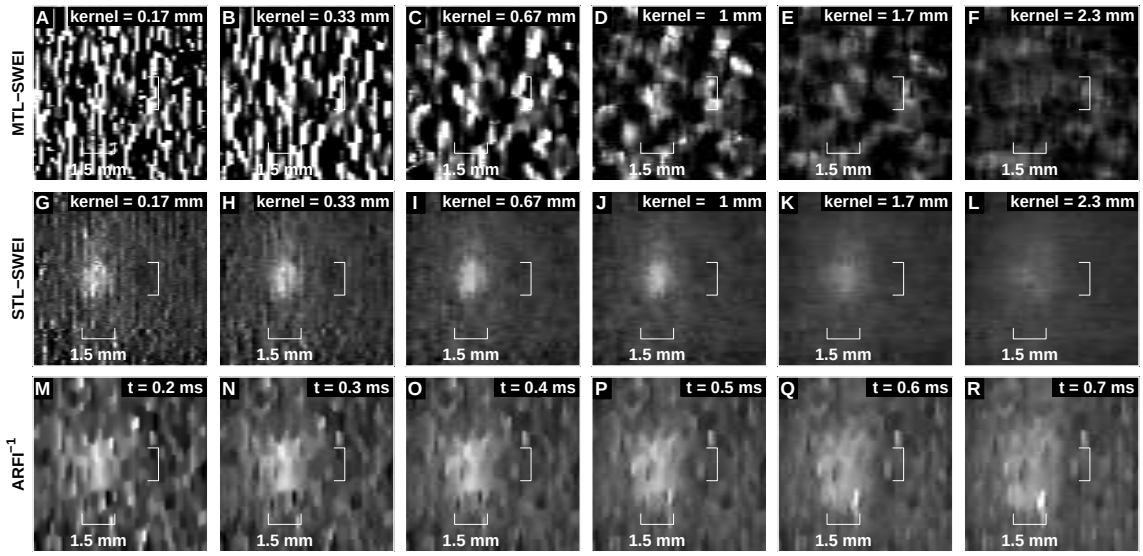

FIGURE 5.18: MTL-SWEI [A-F], STL-SWEI [G-L], and ARFI [M-R] images of the 1.5 mm, Type IV ($G_{\mathrm{qEI}} = 6.48$ kPa) inclusion at different regression filter values (for SWEI) and different time steps (for ARFI). The dynamic range and field of view have been reduced to improve inclusion visualization. Unlike the other figures, no median filter has been used in these images to highlight appreciation of the noise levels and edge resolution, though it is applied for the computation of the parameters in figure 5.19. The target is most clearly visualized and correctly sized in STL-SWEI.

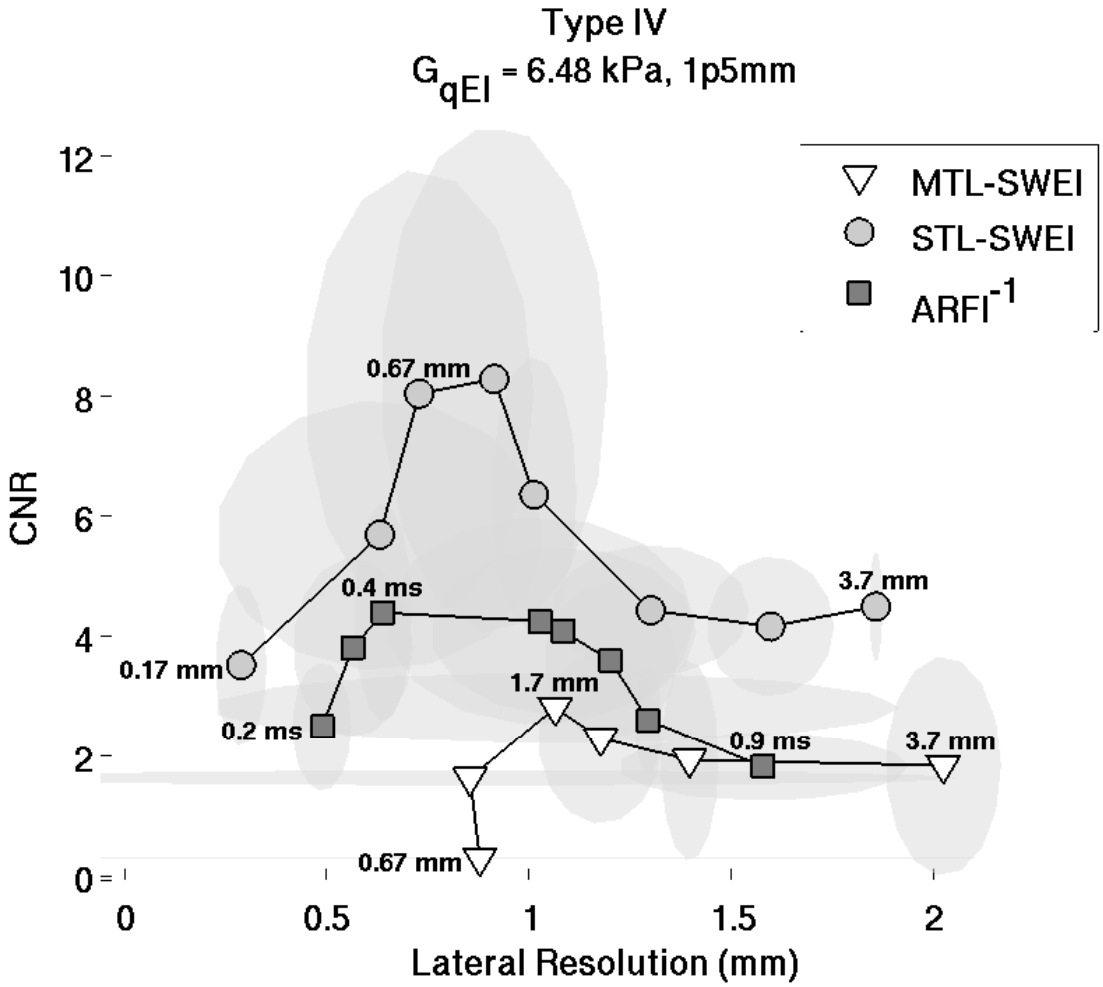

FIGURE 5.19: CNR and resolution tradeoff curves for ARFI, STL-SWEI and MTL-SWEI in the Type IV, 1.5 mm targets. The curve represents different time steps for ARFI (0.2 ms : 0.1 ms : 0.9 ms) and different regression filter sizes for STL-SWEI and MTL-SWEI. The regression filter kernel sizes are 0.16, 0.33, 0.66, 1, 1.66, 2.33, 3, and 3.66 mm, with smaller kernels having lower CNR and higher resolution than larger ones. STL-SWEI shows higher resolution and CNR than ARFI, and MTL-SWEI performs the poorest.

5.5 Discussion

5.5.1 ARFI Time Step Dependence

Early after excitation, the displacement magnitude is driven by the acoustic radiation force and the tissue's shear modulus at the point of excitation. The region under excitation shears against the surrounding tissue, which is initially stationary. As the motion evolves, the surrounding tissue moves axially as the shear waves begin to propagate. When the shear waves encounter a boundary, reflections are generated that propagate back towards the excitation. The time for the reflection to return to the excitation region is dictated by the shear wave speed, which results in the apparent "propagation" in figure 5.6. The distortion propagates out from the boundary at *half* the shear wave velocity to account for the round trip travel time. Once the wave has returned to the excitation, the observed displacements are a combination of the recovery and the reflected shear wave, which makes their magnitude become unreliable and results in the decreased resolution seen in figure 5.7. It is also important to note that the resolution of ARFI images is thus dependent on the target being imaged - an image of a very stiff inclusion will degrade quite quickly. Therefore, using the earliest possible time step will minimize the effect of shear waves and make the highest resolution images. However, looking at the CNR curves, it is apparent that there is a trade-off between resolution and CNR associated with the selection of a time step. This is in part due to decorrelation in the displacement estimates due to scatterer shearing under the point spread function for large focal displacements (McAleavey et al., 2003; Palmeri et al., 2006b). Once the shear wave propagation starts to spatially low-pass filter the scatterer motion, the jitter is reduced. Furthermore, the effects of CNR and resolution are not independent of one another. While this work used the center half of the target to calculate CNR and avoid boundary effects, in the smallest inclusions, shear waves are interfering across the entire inclu-

sion very quickly - for the 1.5 mm, Type IV inclusion, even an infinitesimally narrow push in the center of the inclusion would have reflections interfering within 0.5 ms. This reduces the contrast, and therefore CNR, for the small inclusions. Figure 5.8 illustrates this effect, showing that CNR is maximized at different time steps for each target size. This necessitated the use of a variable time step for each image in figure 5.11, and each point in figures 5.14, 5.15, and 5.16. We elected not to use the maximum ARFI displacement image, because while it showed clear definition of the stiff inclusions, it underestimated contrast, as can be seen comparing panels I and N in figure 5.5.

5.5.2 Modality Comparison

The larger and higher contrast lesions are visible in all the imaging modalities (figures 5.9, 5.10, and 5.11), while the smaller and lower contrast lesions are less clearly distinguished from the background in MTL-SWEI. ARFI shows the highest contrast for the largest inclusions, exceeding the expected contrast from qEI measurements in the largest inclusions (figure 5.14). STL-SWEI has the best visualization of the smallest targets, with reduced noise in the background. On direct comparison, the Type IV inclusions of all sizes are visible in each modality (figure 5.13), although the level of noise in the MTL-SWEI images is such that target boundaries are unclear and and smallest inclusions are hardly distinguishable from the background. The blurred edges in the MTL-SWEI images relative to the STL-SWEI images is at least in part due to the larger regression kernel size required for the MTL-SWEI images, since the CNR levels in the MTL-SWEI images would have completely obfuscated target visualization if the kernel size was set to 0.67 mm (the value used for STL-SWEI). The SWEI images both appear to show axial compression of the soft inclusions and extension of the stiff inclusions. ARFI images show this as well, though to a lesser extent. This is hypothesized to be due to preferential detection of the faster wave

around axial boundaries.

For all modalities, the highest contrast occurs in the largest lesions (figure 5.14). ARFI shows the closest contrast to the expected values based on the qEI measurements (figure 5.15), although it does *overestimate* contrast for the large stiff targets, possibly an artifact of differences in the tissue recovery dynamics between the target and background. Despite the increased noise in the MTL-SWEI images, both SWEI methods show similar contrast values for each size and type of inclusion (table 5.2), and only slightly underestimate contrast relative to the qEI measurements, possibly due to averaging in some degree of boundary blurring (this would be expected to be elevated for MTL-SWEI since it uses a larger kernel, which is indeed what we see). CNR also trends with inclusion size (figure 5.16), but shows interesting behavior for the smallest targets, as STL-SWEI CNR exceeds ARFI CNR for the 6 mm and smaller targets. For the large inclusions, the contrast in ARFI outweighs the increased background noise relative to SWEI, since contrast can be selected to exceed nominal values indicated by qEI with time step selection (compare the values in table 5.2 with the curves in top panel of figure 5.7). For the smaller inclusions, the resolution degrades so quickly that the time-step of peak contrast is not reached before edge degradation from shear waves reaches across the target. STL-SWEI, however, does not have this limitation, so contrast starts to converge for smaller inclusions, and the speckle-free background yields higher CNR. This is most clearly seen in figure 5.18, whose third column does not show the increase in ARFI contrast seen in figure 5.5. The blurring effect due to shear wave interference motivates the use of an early time step to resolve the target size correctly, but the background noise at the early time steps is CNR-limiting.

Based on CNR and resolution, ARFI and STL-SWEI show the highest combination in the 6 mm inclusion, at 0.4 ms for ARFI and a 0.67 mm kernel for STL-SWEI (figure 5.17). Using later time steps in ARFI only increases CNR to a point, after

which the absolute displacement magnitudes diminish and jitter noise dominates the estimate. This is why the trade-off curve curls back down and to the right with increasing time steps, and is consistent with the results of figure 5.7. As the kernel size is increased for STL-SWEI and MTL-SWEI, CNR improves at the expense of resolution, and is expected to continue trending up and to the right until the kernel size exceeds the target size. This effect is seen in the 1.5 mm, Type IV target, as for kernels larger than 1 mm, the CNR starts coming back down due to contrast suppression (figure 5.19). Also, in the 1.5 mm inclusions, ARFI uniformly underperforms STL-SWEI due to the edge degradation curbing ARFI's otherwise good contrast characteristics. The target is clearly detected in ARFI, but visualization is limited either by jitter in the early time steps or blurring in later time steps (figure 5.18 [M-R]).

It is important to note that the lateral resolution described here is the *system* resolution, and that the *fundamental* resolutions of STL-SWEI and MTL-SWEI are determined by the frequency and focus design of the push and track beams respectively. Over many speckle realizations, MTL-SWEI may hypothetically average out to the same edge resolution as STL-SWEI, but in the context of a practical imaging system, only a single speckle realization is available without using incoherent spatial or frequency compounding. Because the distortions introduced in MTL-SWEI arrival times by speckle are consistent across multiple pushes (figure 5.12), they cannot be averaged out without some form of resolution-degrading spatial regularization like a large linear regression. Thus, although the chief benefit of STL-SWEI over MTL-SWEI may be in the suppression of noise through the cancellation of the speckle bias, for a given level of CNR necessary for target visualization, an STL-SWEI system can be operated with less spatial regularization and thus higher effective resolution than MTL-SWEI.

5.5.3 Study Limitations and Practical System Design Notes

Although the study was designed to compare ARFI, MTL-SWEI and STL-SWEI in a closely-matched imaging case, it is limited in a few ways:

Frequency Design

On our current scanner hardware, we could have created the ARFI images at a higher tracking frequency than SWEI images, thanks to the lack of parallel receive needed to track ARFI displacements. When tracking so many parallel lines, we reach the maximum receive bandwidth of the scanner, and cannot track parallel beams with higher frequency with preserved bandwidth. To match the sequences, we limited the tracking frequency for ARFI to match the SWEI tracking, at 5 MHz. While this means that, on our current hardware, the ARFI images shown here are in a way sub-optimal, it allowed for a comparison of the modalities without frequency design differences.

Transmit Focusing

We used diverging wave transmits and parallel receive beamforming for SWEI tracking. While the beamforming doesn't really affect STL-SWEI since the bias cancels itself out, the MTL-SWEI data may be adversely affected by the lack of transmit focusing. Recently developed advanced beamforming techniques, such as approximations of synthetic aperture imaging like coherent compounding (Montaldo et al., 2009) would reduce the speckle size, but are not currently implemented on our equipment. With synthetic transmit focusing, the spatial regression kernel required to smooth out the speckle bias in MTL-SWEI could be reduced, as the point spread function would be narrowed by approximately 25% (the relative PSF width for two-way as opposed to one-way focusing). However, even with these techniques, the results here indicate that a 25% reduction in speckle size is unlikely to bring

MTL-SWEI into contention with the speckle-free STL-SWEI, though it would be an improvement nonetheless.

Depth of Field

Another effect present in these images is a limited depth of field. Although the focal depth was chosen to center the targets within the depth of field, the large inclusions reach the edges. SWEI images degrade outside of the depth of field as the beam shape changes and the direction of propagation assumptions fall apart. ARFI images, on the other hand, are depth-normalized to provide a homogeneous background level appearance. This study was not designed to look at the CNR and resolution characteristics away from the focus, so all results represent the behavior within the depth of field. Further comparison and analysis will be necessary to evaluate performance shallow or deep to the focus. Figure 5.11 does show that at the edges of the depth of field in the 10 mm inclusions [E,J,O,T], the top and bottom of the lesion have lower contrast than in the center. This may indicate that although depth-dependent gain creates an axially-flattened background signal, it does not provide the same imaging quality away from the focus. For practical ARFI and SWEI imaging with a large depth of field, multiple focal zones could be used, either in the style of supersonic shear waves (Bercoff et al., 2004), or acquired sequentially (Rosenzweig et al., 2014).

Motion

This study did not evaluate the effects of motion. Axial tissue or transducer motion creates challenges for ARFI imaging, since the displacement signal is often being estimated on top of background motion, and incomplete filtering of the motion creates errors in the ARFI displacement magnitude that do not necessarily affect the estimates of arrival time, which are generally amplitude-independent for SWEI. How-

ever, axial motion filters have been studied extensively (Giannantonio et al., 2011), and if we assume effective axial motion filtering, ARFI images may be *more* resistant to inter-push motion than STL-SWEI images, since each measurement of ARFI displacement is only dependent on a single push and STL-SWEI measurements assume that the tissue remains relatively stationary over at least two pushes - more if one wants to perform a linear regression. Furthermore, any decorrelation in the tracking beams between excitations will cause partial introduction of speckle bias in STL-SWEI due to incomplete cancellation of the bias, whereas it will create partial suppression of speckle bias in MTL-SWEI through averaging. However, if the motion over the duration of the acquisition is large enough relative to the speckle size to see independent speckle realizations between MTL-SWEI pushes, the images are likely to be blurred and distorted to the extent that the presence of speckle noise suppression through averaging is a moot point. These effects will need to be explored in future work.

Attenuation, Dispersion, and Tissue Geometry

Although the ARFI images shown here were calibrated by the background response to show values proportional to shear modulus, this calibration is not always possible *in vivo*, since the absorption properties of tissue often vary from those of the phantom, and can be heterogeneous. Without calibration, ARFI imaging still provides a signal that may be useful for lesion identification, but does not provide absolute quantification. Whether or not this would reduce clinical efficacy is unclear, and dependent on the task. However, it should also be noted that shear wave speed measurements, while an absolute measurement themselves, do not completely represent tissue elasticity in the presence of dispersion effects due to viscoelasticity or geometry (Chen et al., 2004; Nenadic et al., 2011). Our phantom was linear, elastic, and, on the scale of our measurements, semi-infinite, so the assumptions are likely good

here, but depending on the specific μ-E imaging task, additional work would need to be done to prove that absolute tissue quantification is possible from the shear wave speed.

Minimum System Requirements

A system with the ability to rapidly record individual channel data at high bandwidth would allow for optimal acquisition of ARFI, MTL-SWEI and STL-SWEI simultaneously, with the tracking for each push in the sequence beamformed everywhere in the field of view at arbitrarily high pixel density. However, a very simple system could theoretically also build the combined dataset from the superposition of a series of individual single-push-beam, single-track-beam responses, collectively covering all combinations of push and track beam positions. Such a system would take a relatively long time to acquire the image, but would not require state-of-the art hardware. Practically, ARFI and SWEI imaging systems will need to balance and optimize spatial sampling and framerate for the particular application, given the constraints of the hardware and software. An ARFI imaging system only needs a single track beam per excitation, and must sequentially steer the excitations across the field of view. STL-SWEI can also be implemented with a single track beam and sequentially-steered push beams, although such a system would have the field of view limitations of a single-push beam MTL-SWEI image. A small number of fixed-position parallel-receive track beams allows for superposition for averaging and/or extending the lateral field of view in the same way that MTL-SWEI uses multiple offset pushes. A small number of parallel-receive beams could also provide overlapping estimates if the beams are placed at fixed offsets relative to each push. An MTL-SWEI system only realizes the frame rate improvements over STL-SWEI through parallel receive beamforming, which require significantly higher bandwidth. Superposition of the responses from a small number of pushes reduces the burden

on parallel receive, but at the expense of the high frame rate and low acoustic exposure.

5.6 Conclusion

This experiment investigated the performance of ARFI and SWEI for visualizing small structures. STL-SWEI processing allowed SWEI images to be generated with CNR and resolution similar to ARFI for large inclusions, and with better CNR and resolution for smaller targets. STL-SWEI significantly outperformed MTL-SWEI in terms of image quality, creating less noisy and higher resolution images, although MTL-SWEI may remain the only viable option for tasks where framerate, motion, or acoustic exposure are limiting factors. Since the time required to acquire an STL-SWEI image is no more than that for ARFI imaging, in situations were an ARFI image could be acquired, STL-SWEI can provide imaging of small structures at higher CNR and resolution than ARFI, with the absolute quantification of SWEI.

6

Imaging Radiofrequency Ablation Lesions in Three Dimensions with Acoustic Radiation Force Impulse Methods using an Intracardiac Echocardiography Transducer

This chapter is heavily adapted from a proceedings paper presented at the 2013 IEEE International Ultrasonics Symposium. Much of statistical analysis of the ablation pairs was done as part of Lily Kuo's M.S. thesis, and as such, is not included here. Instead, the paper is greatly expanded to include more experimental results, which are largely dealt with quantitatively. For a quantitative comparison of the imaging modalities, chapter 5 already provides a more tightly controlled examination without the uncertainties of the ablations themselves. This chapter tests ARFI, MTL-SWEI and STL-SWEI in four different ex vivo tests that seek to bridge the gap from most controlled, least similar to in vivo imaging, to the least controlled, most similar to in vivo imaging. These images help to differentiate between the challenges intrinsic to imaging ablations with the tiny ICE array from those associated with cardiac motion.

6.1 Abstract

Radiofrequency ablation (RFA) is used to locally disrupt electrical propagation in myocardium and treat arrhythmias, and direct visualization of ablation lesion by acoustic radiation force methods may benefit RFA procedures. This work compares four imaging modalities, B-Mode, ARFI, STL-SWEI and MTL-SWEI, in their ability to resolve RFA lesions in four *ex vivo* experiments. Ablation lesions are shown to be marked by at least a local halving of ARFI displacements and doubling of shear wave speeds. In a controlled ablation, STL-SWEI and ARFI are shown to have similar CNR, better than MTL-SWEI and B-Mode. The SWEI modalities are demonstrated to have improved imaging of distal lesion boundaries. Gaps smaller than 5 mm are visualized in ablation lines made of discretely-spaced ablations, and complex structures are reconstructed through depth in an "x" ablation experiment. Scans of suspended atria show increased noise, but successfully visualize ablations in ARFI, MTL-SWEI and STL-SWEI.

6.2 Introduction

Atrial Fibrillation and other cardiac arrhythmias are often treated with Radiofrequency Ablation (RFA) (Calkins et al., 2012). RFA uses high-frequency electrical current generated from the tip of a catheter to locally heat the myocardium to the point where proteins denature and electrical conductivity is cut off. The treatment can cure the patient of the disease, unlike cardioversion or drug therapy, but 20% of patients will need the procedure repeated within the first year, and 30% by the end of the second (Shah et al., 2012). The placement of lesions is often guided by Intracardiac Echocardiography (ICE), fluoroscopy, and/or electroanatomical map-

ping (EAM). ICE is commonly used to confirm contact of the ablation catheter tip with the myocardium, but cannot reliably distinguish healthy tissue from ablated (Fisher et al., 1997). Instead, the duration, power, and temperature of the ablation are used to predict lesion size, and the electrical activity on the endocardium is used as confirmation of ablation. Because partially-treated tissue may become transiently electrically inactive, the ability to image the size, shape, and transmurality of the generated lesions, which has been previously unavailable, could improve the efficacy of the procedure (Melby et al., 2008; Kowalski et al., 2012).

Intracardiac Acoustic Radiation Force Impulse (ARFI) and Shear Wave Elasticity Imaging (SWEI) are two novel ultrasound-based imaging methods that show promise for assessing RFA lesions by estimating the local mechanical compliance of the myocardium (Pernot et al., 2009; Eyerly et al., 2012). ARFI images show the amplitude of induced displacement in response to excitation by acoustic radiation force. To excite the tissue, a 10-100 μs ultrasonic pulse is focused at the target region, transferring momentum to the tissue through absorption. This type of pulse is much longer than an imaging pulse, resulting in enough energy deposition to generate a 1-20 μm shear displacement, but short relative than the dynamics of the mechanical response, such that it is still considered impulsive. In response, tissue displaces briefly away from the transducer, and elastically recovers within a few milliseconds, propagating shear waves orthogonal to the excitation axis. During this motion, the target region is imaged with high speed ultrasound (>1000 fps) so that the subsample axial tissue motion can be estimated at each depth. The process is repeated many times, steering the excitation beam to each location of interests to construct an image of local displacement magnitude. Stiff tissue displaces less than soft tissue, so the ARFI signal is an image of tissue compliance. SWEI (Sarvazyan et al., 1998) uses the same acoustic radiation force excitation, but uses the motion offset from the excitation to track the propagation of the transverse waves generated

by the excitation. The local group velocity of the induced wave is proportional to tissue stiffness, such that in a semi-infinite, incompressible, linear elastic medium, $c_T = \sqrt{G/\rho}$, where c_T is the wave velocity in m/s, G is shear modulus in kPa, and ρ is the density in g/cm^2. While these assumptions don't typically hold for myocardium, the wave velocity is itself an indicator of local myocardial stiffness. ARFI has traditionally been thought to be higher resolution than SWEI, but recent work has shown that Single Track Location SWEI (STL-SWEI) may enable higher resolution systems than traditional SWEI (Elegbe and McAleavey, 2013). This work compares B-Mode, ARFI, MTL-SWEI and STL-SWEI's abilities to resolve lesion geometry in controlled ablations of *ex vivo* porcine and canine myocardium.

6.2.1 Methods

6.2.2 Experimental Setup

Ex Vivo samples of healthy porcine and canine myocardium were used with different ablation geometries and imaging sequences to obtain calibrated images of tissue elasticity before and after ablation. Tissue samples were degassed prior to imaging. Siemens Acuson AcuNav 10 French ICE catheters (Siemens Medical Systems, Mountain View, CA), connected to a Siemens Acuson SC2000 ultrasound scanner running custom software, were used to perform all imaging.

6.2.3 Beam Sequences

Three types of beam sequences were used to acquire B-Mode, ARFI, MTL-SWEI and STL-SWEI images:

Linear-Translated Scan Sequences

In the first set of sequences, the AcuNav was operated in linear mode to minimize the effect of steering angle. 90 Vpp, 300-cycle, 6 MHz push pulses were used to generate ARFI displacements and shear waves in the tissue. Each excitation was

generated with a 32 element sub-aperture (3.54 mm), focused at 15 mm. To track displacements, 32 parallel lines were beamformed around the excitation, extending 2.25 mm to either side of the excitation. The tissue was imaged at 10,000 frames per second for 5 ms following each excitation. The ensemble was electronically stepped across the aperture in 16 steps, with a push beam spacing of 0.15 mm, which matched the track beam spacing. The entire aperture was used in receive. To synthesize 3-D volumes, the tissue was translated with a translation stage in the lateral and elevational planes, such that the groups of 16 ensembles could be stitched together into total imaging grid measuring 28.8 mm laterally and 14.4 mm in elevation (with 0.3 mm increments in elevation). A diagram appears in figure 6.1(A).

Phased-Translated Scan Sequences

To test the performance of sequences that could be operated in an *in vivo* setting, a second set of sequences was constructed. These imaging sequences were designed to acquire ARFI, STL-SWEI and MTL-SWEI simultaneously. A 45° azimuthal viewing angle was interrogated with 32 90 V_{pp}, 300 cycle, 6 MHz excitations. The sequences used diverging wave transmits and 32 parallel receive focused beams to track displacements, placed in line with the 32 push locations, and fixed regardless of which line was being pushed. To synthesize 3-D volumes, the issue was translated in the elevation dimension with a translation stage. (figure 6.1(B)).

6.2.4 Phased-Rotation Scan Sequences

Using the insights from chapter 5, the phased sequences were later redesigned to increase the push density and only use receive beams that would provide useful data. The number of pushes was increased from 32 to 50, maintaining a 45° field of view. The new sequences also used diverging wave transmits, but tracked 21 parallel-receive focused beams surrounding each push, with a 0.9° spacing between both push and

track beams. The response was tracked for 0.5 ms prior to the excitation and 2.5 ms after the excitation, at a frame rate of 16,000 fps. For these scans, to synthesize 3-D volumes, the catheter was rotated by hand, using an optical encoder to measure angle. The diagram appears in figure 6.1(C-D).

6.2.5 Ablation

Four different controlled *ex vivo* ablation procedures were performed to provide targets for 3-D reconstruction. Diagrams of the imaging setups appears each appear in figure 6.1

Ablation Pairs

These scans were performed with the translated sequences. After the initial scan of ARFI and SWEI, a pair radiofrequency (RF) ablations were performed along the center lateral line using a BioSense Webster ThermoCool irrigated tip ablation catheter (Biosense Webster, Diamond Bar, CA). 22 W of power was applied for 60 seconds with 30 mL/min saline flow to create each ablation lesion. The distance between the centers of the lesions ranged from 10 to 12 mm, so that the gap between lesions was between 2 and 5 mm. After ablation, the tissue was scanned again with ARFI/SWEI. Following imaging, the tissue was frozen and stained with a triphenyltetrazolium chloride (TTC) protocol. After staining, the tissue slices were frozen in O.C.T Compound at -20C, and sliced using a Microm HM 505 E cryotome (Thermo Fisher Scientific, Waltham, MA) in 150 μm increments in the elevational direction to make images aligned with the axial-lateral planes of the ultrasound images. Photographs were taken of each slice from a mounted camera, and the green channel of the RGB color images was extracted to provide contrast between the stained (red) and unstained (white) regions of myocardium. The experiment was repeated for three lesion pairs, each in a separate *ex vivo* sample.

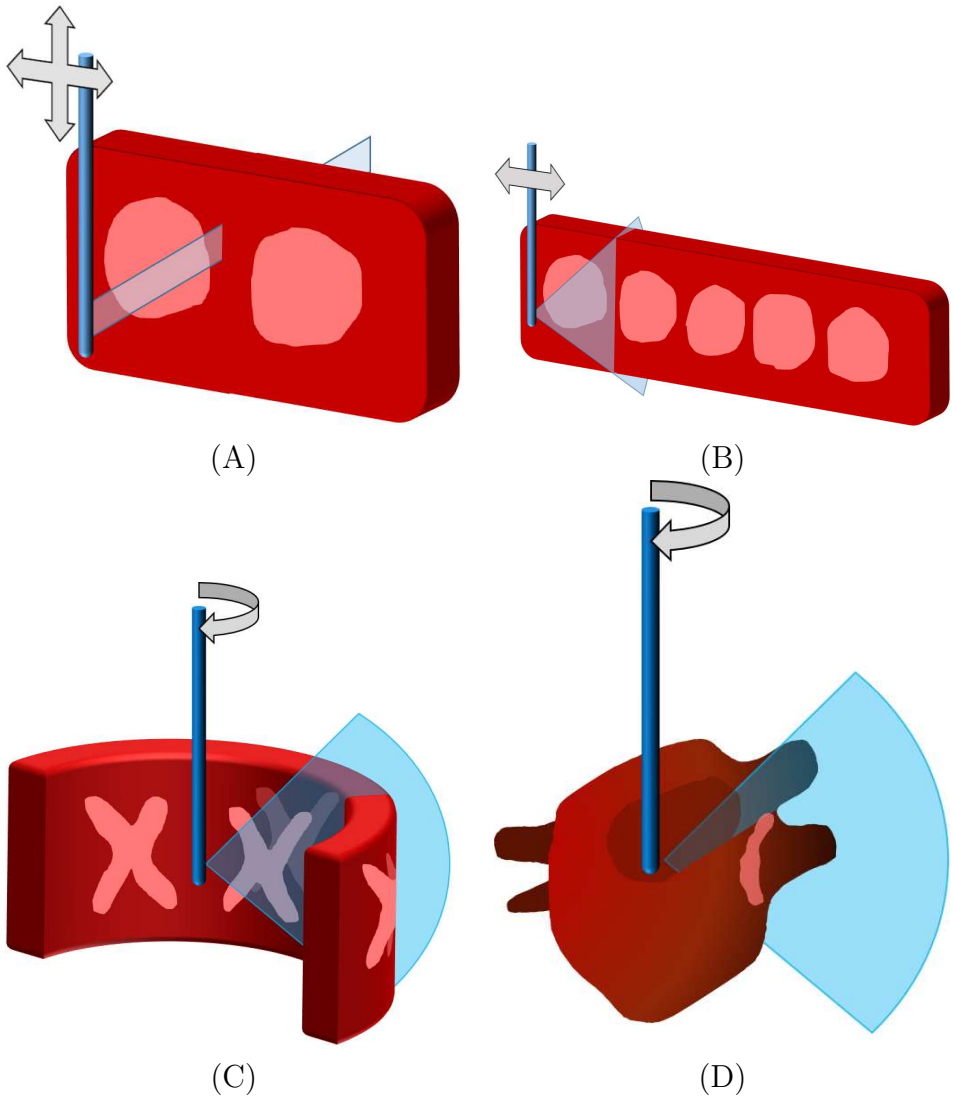

FIGURE 6.1: Four ablation and imaging scenarios used to test 3-D imaging of ablation lesions. (A) Lesion pairs. The spacing between the ablation sites was controlled. The AcuNav imaged directly forward, and was translated laterally and in elevation to scan the volume (the "linear-translated" scan). (B) Lesion line. The spacing between lesions was controlled. The AcuNav had a 45° lateral field of view, and was translated in the elevation plane (the "phased-translated" scan). (C) "X" ablation. One ablation was ablated from the endocardium, one from the epicardium, and one from both. The AcuNav had a 45° lateral field of view, and was rotated to cover a 180° elevational field of view (the "phased-rotated" scan). (D) Pulmonary vein isolation. Lines of ablation were created around the suspended pulmonary veins. The AcuNav had a 45° lateral field of view and was rotated to cover a 90° elevational field of view (the "phased-rotated" scan).

Ablation Lines

A second set of scans was completed with the first phased imaging sequences, translated in elevation every 0.3 mm. In each scan, a series of ablations were performed in a line along the elevational field of view, centered within the lateral field of view. The same ablation protocol as for the pairs was used. This experiment was repeated three times at three different spacings between ablation sites: 6,7, or 8 ablations were performed with 12, 10 or 8 mm between sites, respectively.

"X" Ablation

A third type of scan used the second type of phased sequences, but used a piece of RVFW mounted on an arc in a water tank. The AcuNav was suspended in the tank through a US Digital HB6M optical encoder, so that an 3-D volume could be swept out only by rotating the transducer. This was designed to more closely simulate the type of imaging that would occur *in vivo*. The ablation, in this case, was designed to have a more characteristic three-dimensional shape than a single lesion. Three "x" shapes were ablated onto the tissue in a series of four ablations. The first "x" was ablated from the endocardial surface, using continuous motion of the ablation catheter over the course of the ablation rather than individual points. A second ablation was placed to the right of the first, also ablated on the endodardium. However, after the second lesion was created, the same locations were ablated from the epicardial surface, using pins through the tissue at the tips of the "x" to align the two shapes. A third ablation was placed to the right of the second, and ablated only from the epicardium. 240 images were collected along a 180° sweep before and after ablation.

Pulmonary Vein Isolation

The final type of scan used an excised canine heart and lungs, suspended upside down in a water tank. The LV was split down the apex so that the AcuNav could be inserted down through the LV, across the mitral valve, and into the LA, with views of the LA wall and pulmonary veins. A line of ablation lesions was generated around the pulmonary veins to be imaged with the same phased-rotational imaging setup as the "x" ablation.

6.2.6 Displacement and Shear Wave Speed Estimation

The axial tissue displacements between successive frames were estimated with a phase-root seeking algorithm (Pesavento et al., 1999) with a 5-λ kernel. For the linear scans, ARFI images were formed by averaging the integrated displacements at the center 4 imaging lines 0.2 ms after the excitation. For the phased scans, ARFI images were made 0.5 ms after excitation. For both scans, the displacement estimates away from the center were used to generate shear wave estimates. For each excitation, the progressive displacement curves were filtered with a 50 Hz - 1 kHz bandpass filter, and a directional filter (Deffieux et al., 2011). The arrival time was estimated at each pixel as the time to peak velocity, using quadratic subsample peak estimation. To estimate MTL-SWEI shear wave speeds, the reciprocal of the time difference between adjacent receive locations was found for each push and filtered with a 1 mm x 1 mm median filter to provide spatial smoothing. The same process was used for STL-SWEI, but the difference was found between adjacent push locations for each track line. For MTL-SWEI, the overlapping estimates at each depth and tracking location were combined by taking the median across pushes, and for STL-SWEI, the estimates at each depth and push location were combined by taking the median across the tracks.

6.3 Results

6.3.1 Ablation Pairs

Figure 6.2 shows an example of the conventional lateral-depth (XZ) planes of one of the ablation lesions pairs before and after ablation. Each row shows a different imaging modality from the same dataset, along with the green channel values from the photograph of the stained tissue sliced approximately along the same axis as the ablations. Warping during the freezing and slicing process created misalignment and distortion between the stained photographs and the ultrasound volumes. ARFI images are shown as inverse displacement, and SWEI images are shown as the shear modulus G, found as the square of shear wave speed, in kPa. The images show low displacements and elevated shear velocities inside of the ablated regions, as well as increased echogenicity in the B-Modes.

Figure 6.3 shows the same dataset as figure 6.2, but sliced at a single depth and displayed in the lateral-elevational (XY) plane. The depth of field effects are absent and the images appear more uniform.

Figure 6.4 shows all seven ablation lesion pairs in each modality, along with the histology slices in the first column. The lesions are comparable in size to those indicated by the histology, with varying contrasts. The gap between the pairs of ablations is visible in each ARFI and SWEI image. Contrast varies between rows, with some rows (like the fourth) showing significantly lower contrast than others (like the third), but agree between ARFI, STL-SWEI and MTL-SWEI. The SWEI images appear to have higher contrast, but also more noise, compared to the ARFI images. Some of the B-Mode images show contrast corresponding to the ablated areas, but others do not.

Figure 6.5 shows the median and standard deviation values inside and outside of each pair of ablation lesions before and after ablation from each of the XY scans

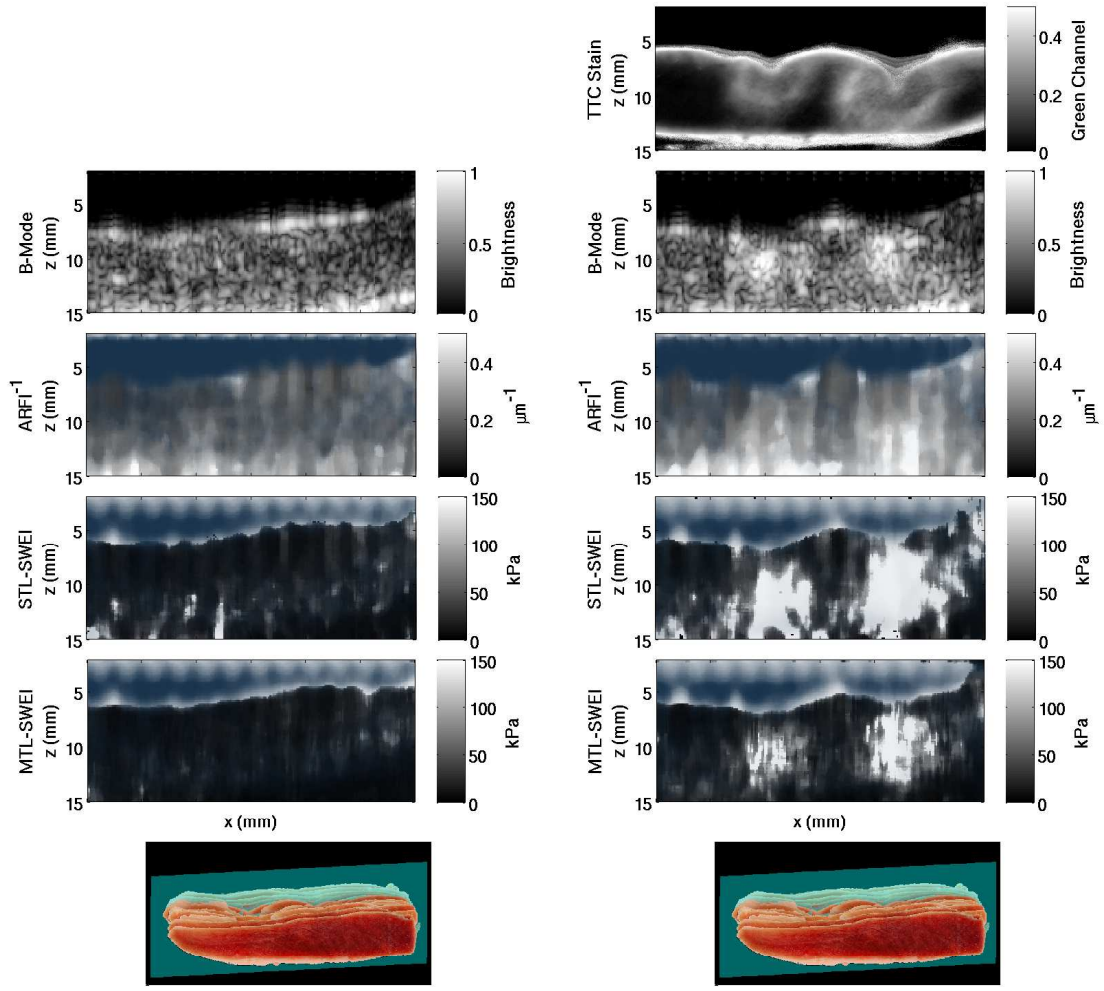

FIGURE 6.2: Histology, B-Mode, ARFI, STL-SWEI and MTL-SWEI slices of an ablation pair 3-D dataset, sliced in the elevation dimension and displayed in the lateral-axial plane. The left column shows the baseline images, and the right column shows the images after ablation.

in figure 6.4. The background values are unaffected by ablation, while the ablated regions increase in value for all modes. STL-SWEI and MTL-SWEI show the greatest relative increase with ablation, but are associated with larger error bars as well. Table 6.1 shows the mean and standard deviation of the median values measured inside and outside of the lesion pairs. These are reported in their conventional forms, as μm and m/s for ARFI and SWEI, respectively. A small increase in stiffness was observed in the background following ablation, but a larger, significant change was seen at the

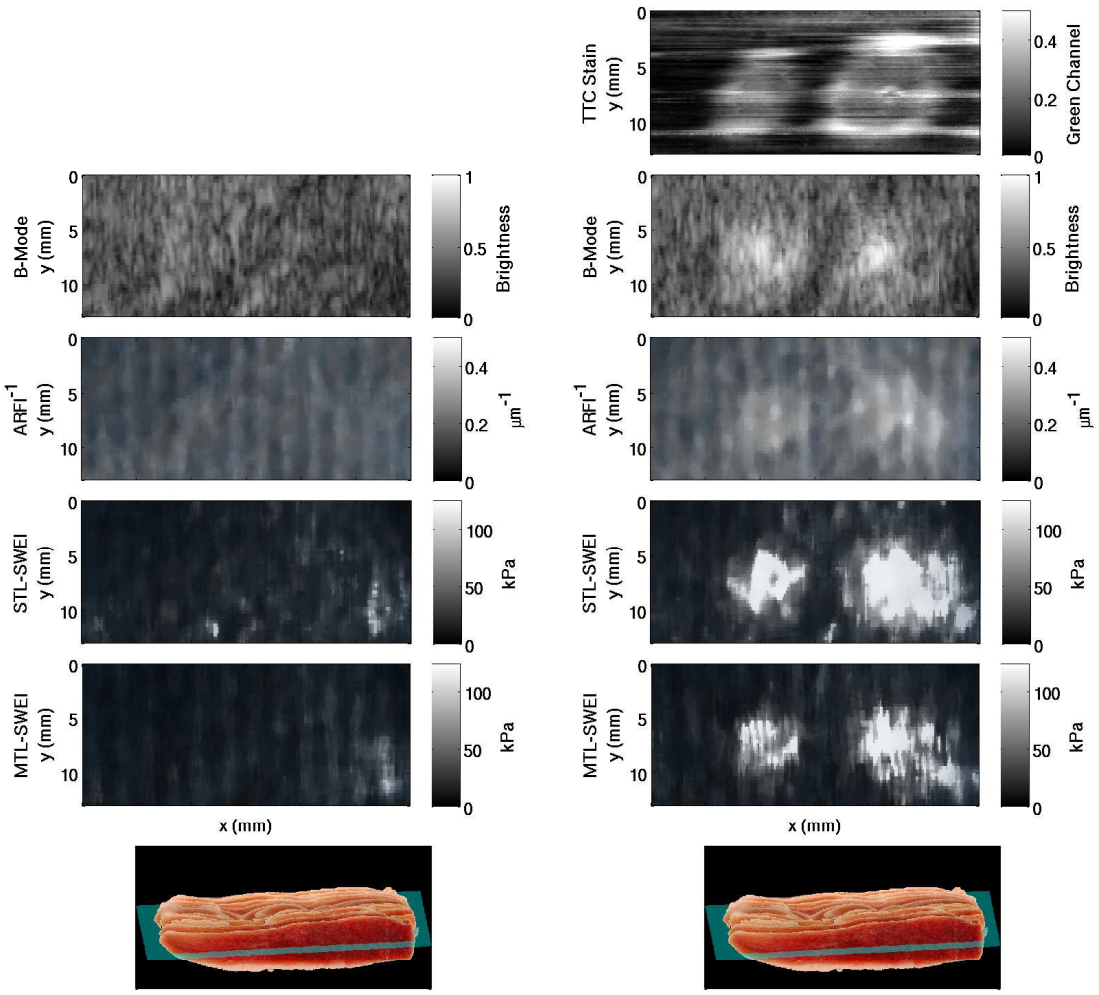

FIGURE 6.3: Histology, B-Mode, ARFI, STL-SWEI and MTL-SWEI slices of an ablation pair 3-D dataset, sliced in the axial dimension and displayed in the lateral-elevational plane. The left column shows the baseline images, and the right column shows the images after ablation.

lesion sites following ablation, as speeds more than doubled, displacements fell by more than half, and B-Mode brightness increased by 40%.

Figure 6.6 shows the Contrast-to-Noise-Ratios (CNR) for the lesion pairs for each modality, using the standard deviation of the background as the estimate of image noise ($\sigma = \sigma_{out}$). STL-SWEI has the highest CNR, followed by MTL-SWEI, ARFI, and then B-Mode.

Figure 6.7 shows the CNR values, recomputed using a weighted sum of the stan-

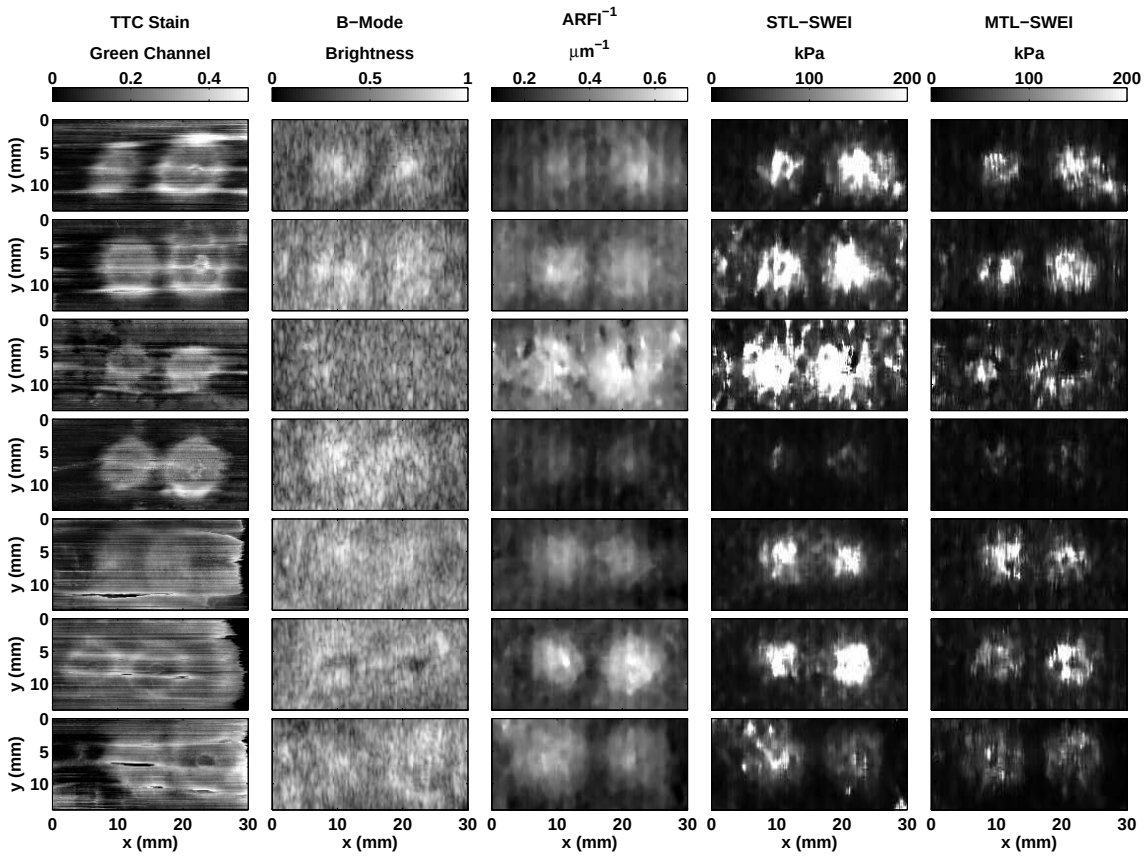

FIGURE 6.4: C-Scans of the seven ablation lesion pairs. Some misregistration is visible between the histological data (column 1) and the ultrasound data. The lesions appear hyperechogenic in B-mode

dard deviations inside and outside of the lesions as the image noise:

$$\sigma = \sqrt{(1/N_{in} + N_{out})(N_{in}\sigma_{in}^2 + N_{out}\sigma_{out}^2)} \tag{6.1}$$

ARFI and STL-SWEI now show nearly identical CNR values, while MTL-SWEI is lower and B-Mode is the lowest.

Table 6.1: Average Lesion Values

	Background			Lesion Site			
	Baseline	Post-RFA	p	Baseline	Post-RFA	p	units
BMODE	0.5 ± 0.1	0.5 ± 0.1	NS	0.5 ± 0.1	0.7 ± 0.1	<0.001	AU
ARFI	4.9 ± 1.3	4.2 ± 1.0	NS	5.0 ± 1.4	2.2 ± 0.6	0.0012	μm
STL-SWEI	4.3 ± 1.8	4.6 ± 1.1	NS	4.1 ± 1.5	13.0 ± 4.0	<0.001	m/s
MTL-SWEI	3.4 ± 0.9	3.8 ± 0.7	NS	3.4 ± 1.0	8.7 ± 2.3	<0.001	m/s

NS = Not Significant. p-values represent a two-tailed, unpaired Welch's t-test over the mean values from the seven pairs of lesions at the $\alpha = 5\%$ significance level.

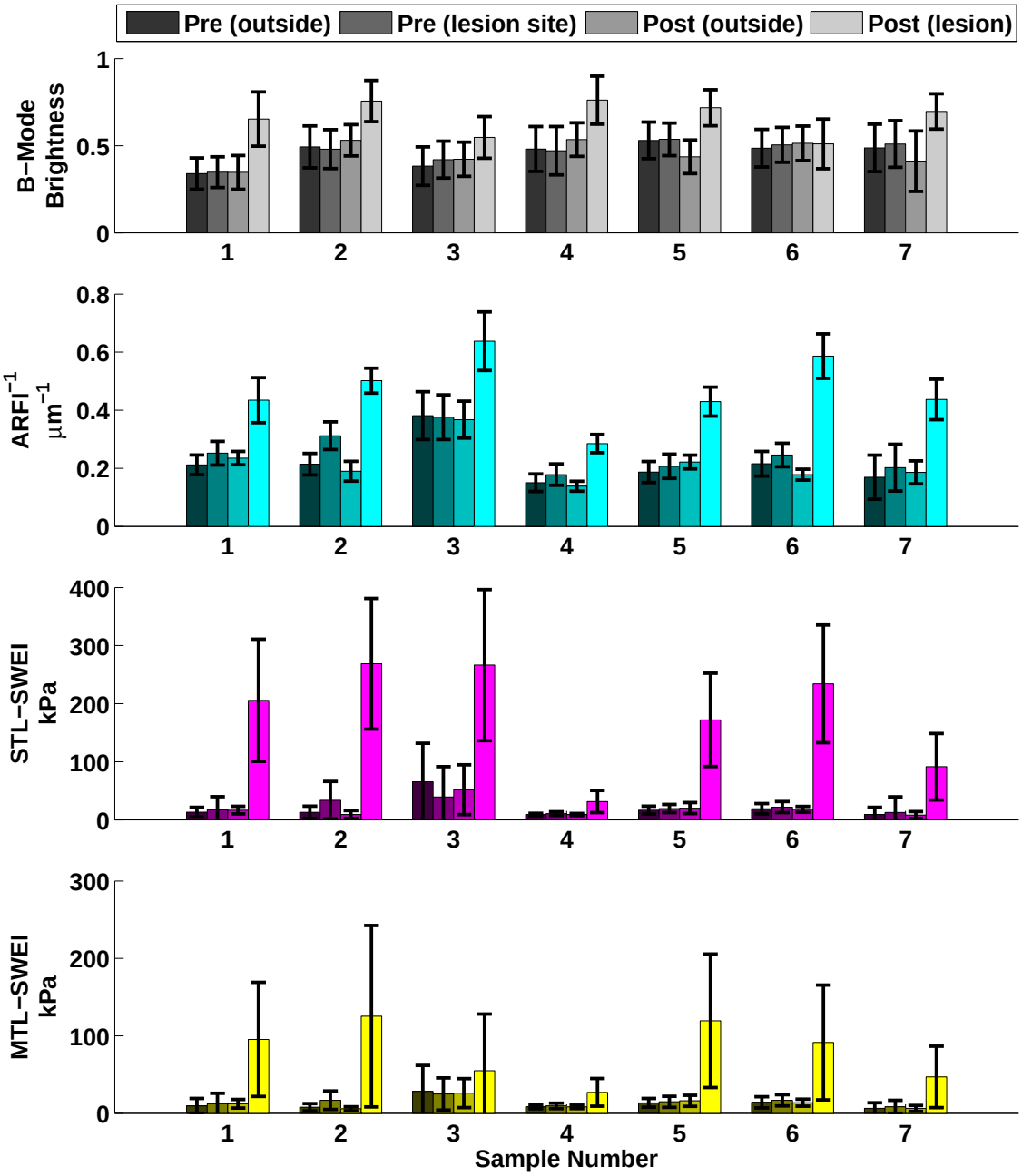

FIGURE 6.5: Medians and standard deviations of the values inside and outside of the ablations before and after ablation for each mode.

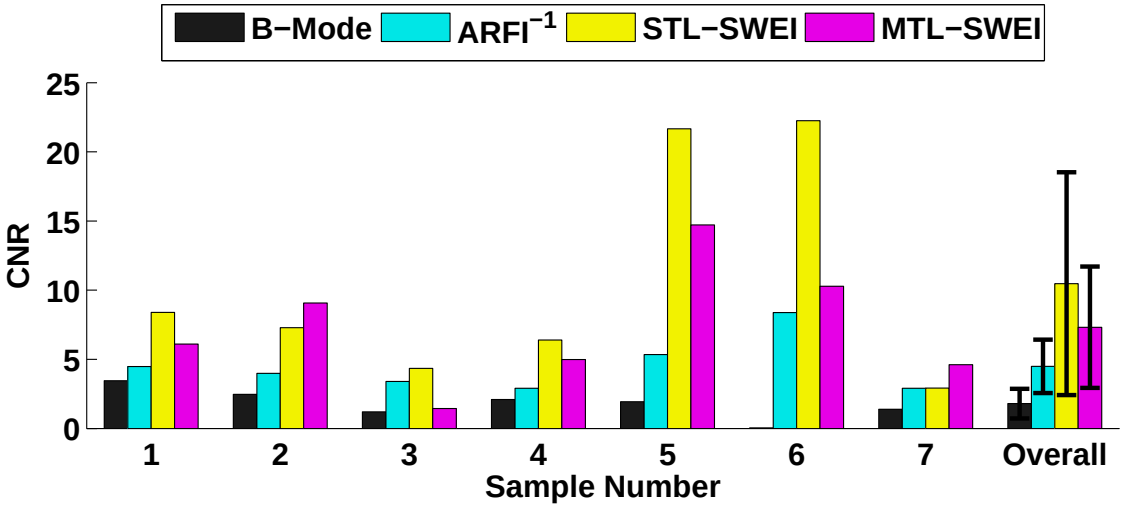

FIGURE 6.6: Contrast-to-Noise ratios for each sample and modality, using only the background deviation $\sigma = \sigma_{out}$. The last set of bars shows the means and standard deviations of the CNR values across the 7 samples.

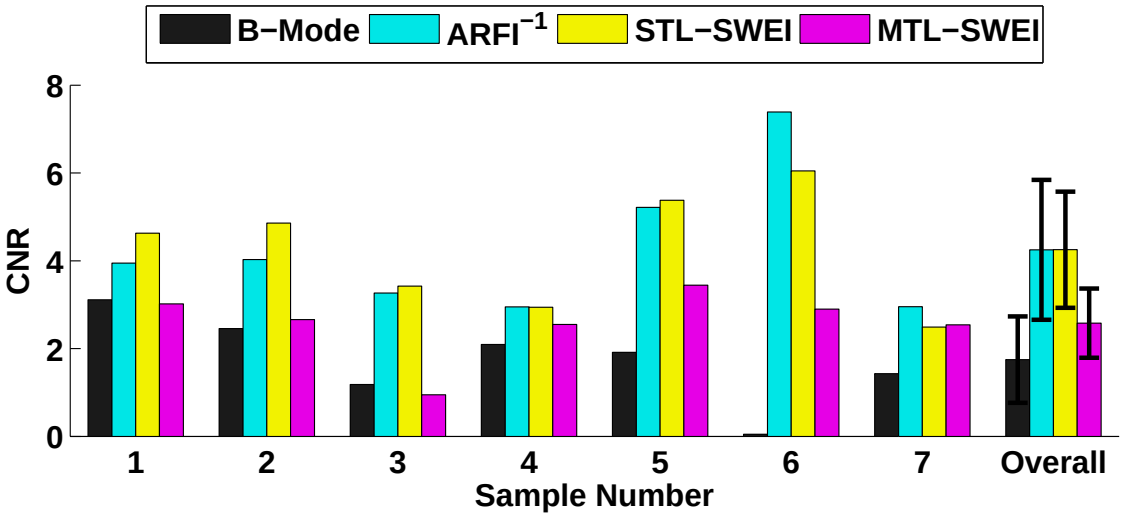

FIGURE 6.7: Contrast-to-Noise ratios for each sample and modality, using total standard deviation $\sigma = \sqrt{(1/N_{in} + N_{out})(N_{in}\sigma_{in}^2 + N_{out}\sigma_{out}^2)}$. The last set of bars shows the means and standard deviations of the CNR values across the 7 samples.

6.3.2 Line Ablations

Figure 6.8 shows the phased-linear scans of the ablation line with 8 mm spacing before and after ablation. The red lines dots indicate the location and spacing of the ablations. The volume is sliced in the lateral dimension (shown in axial-elevation plane) in frames (A) and (B), and in the axial dimension (shown in the lateral-elevation plane) in frames (C) and (D). The gaps in the lesion line are visible in the XY scans, with higher contrast in the SWEI images than in the ARFI. The lateral edges of the ARFI image appear bright in the pre-abaltion scan, corresponding to low displacements at the highest steering angles. The STL-SWEI images appear smoother in the lateral dimension than the MTL-SWEI images. The streaking artifact at the right side of the images is due to the translation stage reaching its maximum elevational extent.

Figures 6.9 and 6.10 shows the phased-linear scans of ablation lines with 10 and 12 mm spacing, respectively. As the spacing between lesions increases, the gaps become more apparent in the ARFI and SWEI images. The attenuation of ARFI displacements with depth makes the bottom of those images bright, and obfuscates distinction of the bottom of the lesions from the bottom of the tissue, as both are marked by low displacements.

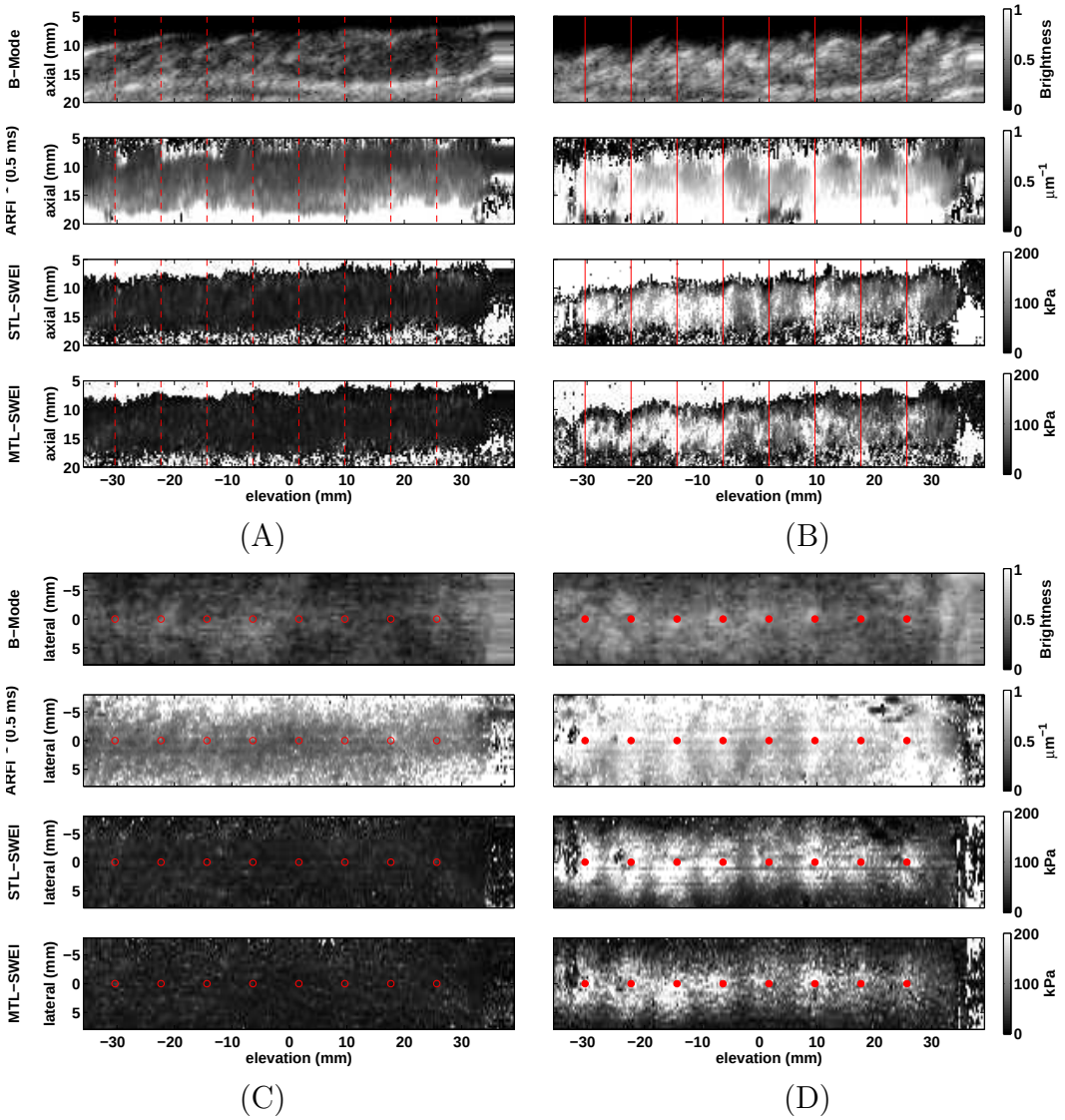

FIGURE 6.8: Phased-linear scan of the 8 mm lesion line. (A) Axial-Elevational slice, pre-ablation. (B) Axial-Elevational slice, post-ablation. (C) Lateral-Elevational slice, pre-ablation. (D) Lateral-Elevational slice, post-ablation. The red dots mark the ablation sites.

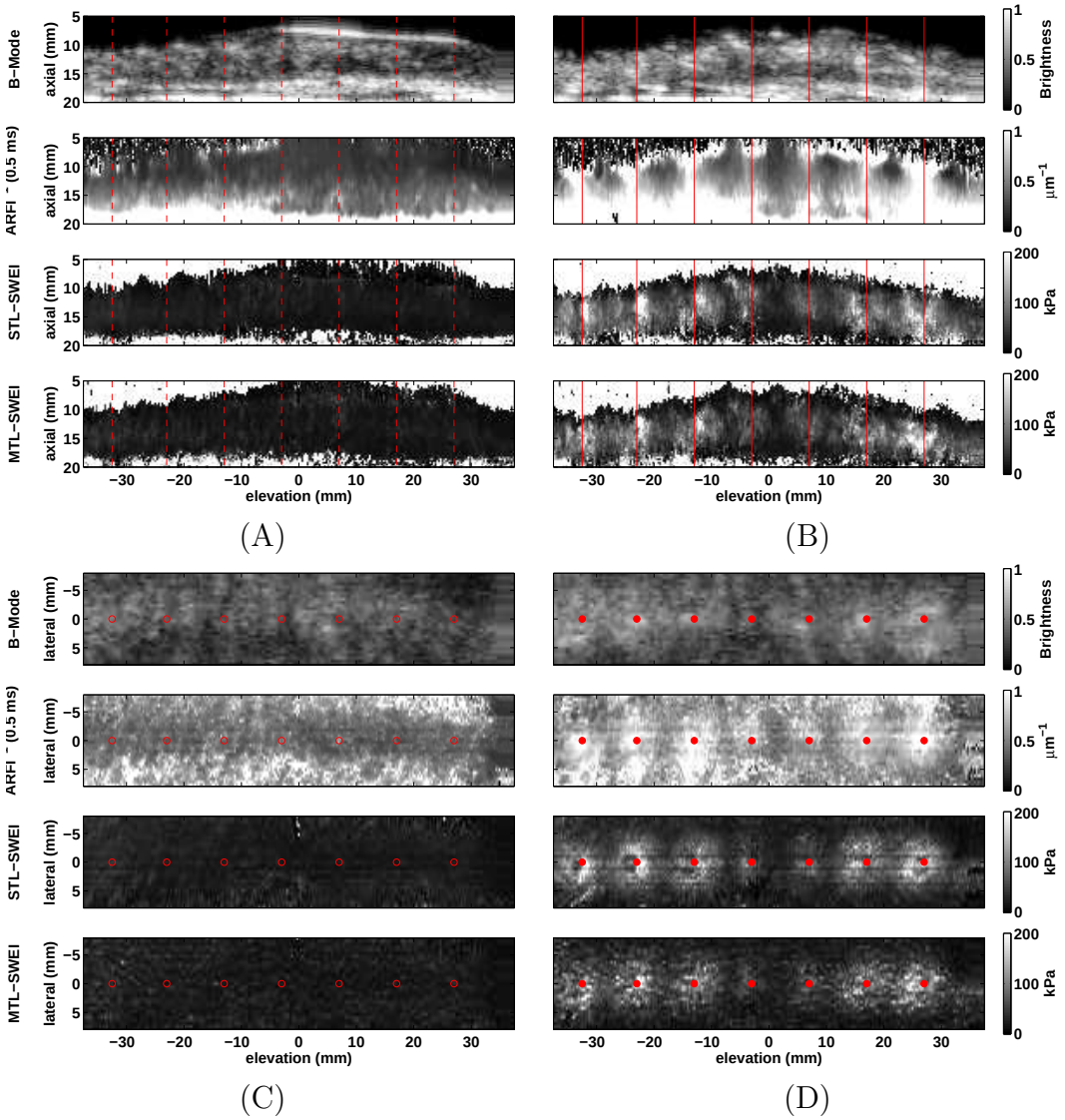

FIGURE 6.9: Phased-linear scan of the 10 mm lesion line. (A) Axial-Elevational slice, pre-ablation. (B) Axial-Elevational slice, post-ablation. (C) Lateral-Elevational slice, pre-ablation. (D) Lateral-Elevational slice, post-ablation. The red dots mark the ablation sites.

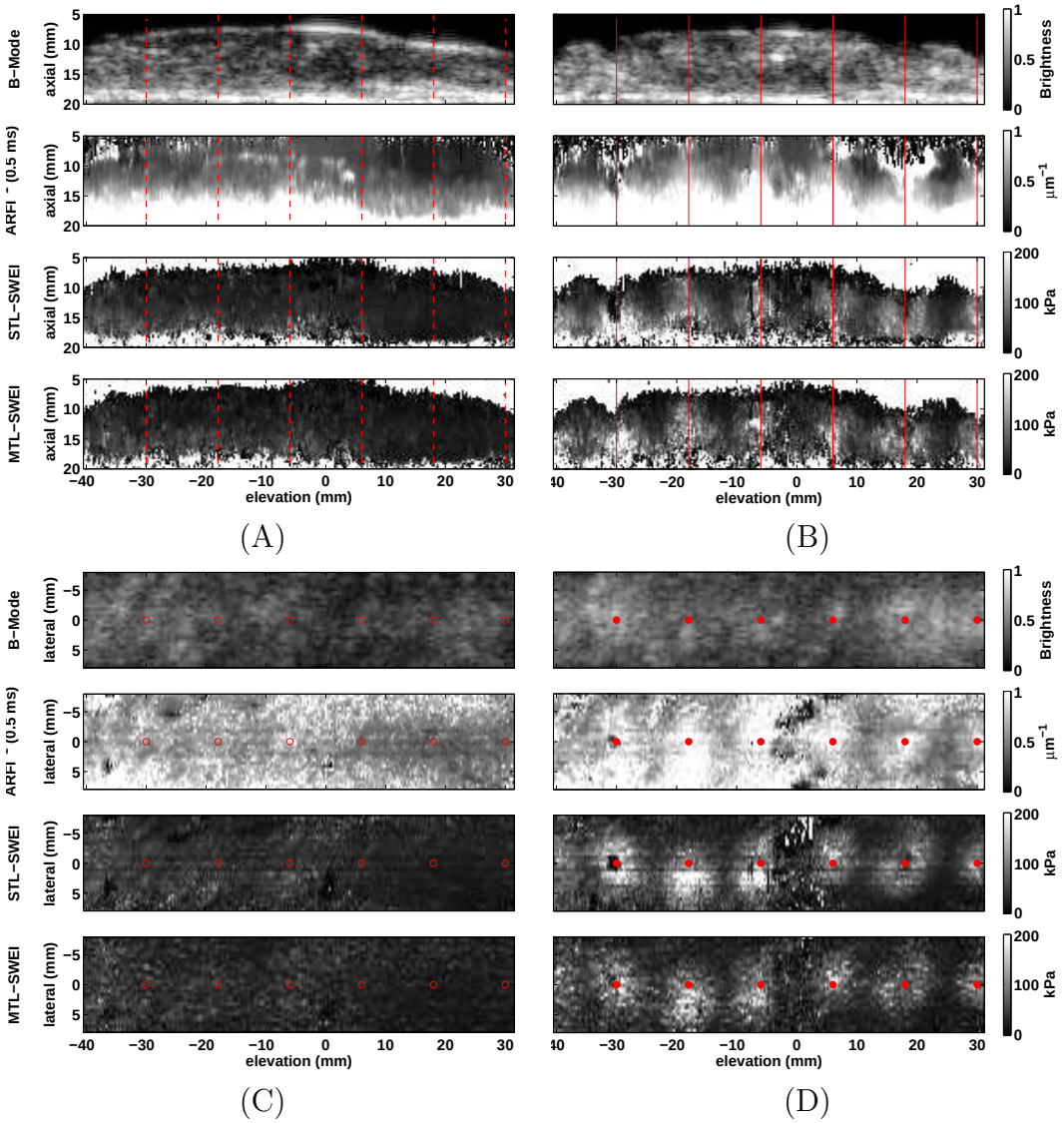

FIGURE 6.10: Phased-linear scan of the 12 mm lesion line. (A) Axial-Elevational slice, pre-ablation. (B) Axial-Elevational slice, post-ablation. (C) Lateral-Elevational slice, pre-ablation. (D) Lateral-Elevational slice, post-ablation. The red dots mark the ablation sites.

6.3.3 "X" Ablation

Figure 6.11 shows renders at two different angles of the section of RVFW prior to ablation. The tissue appears uniform in B-Mode. Unlike the previous two subsections, the values are reported in their conventional, directly estimated forms (μm for ARFI and m/s for SWEI). The ARFI images show depth-dependent displacement magnitude and lower displacements with steering, but no clear trends in the elevation steering direction. MTL-SWEI and STL-SWEI both show regions of elevated stiffness on either end of the sample.

Figures 6.13-6.15 slices the volumes from figure 6.12 at equal depths from the transducer face, moving deeper in to the tissue from top to bottom. The ARFI images have had the dynamic range shown at each depth scaled by the median displacement at that depth from the pre-ablation scans. In all three modalities, the center "x" is visible at depths up to 22 mm, after which its shape becomes obfuscated. The left "x" is preferentially visible shallow and the right "x" is more visible in the deeper slices. The epicardially-ablated "x" also appears slanted out-on plane, as the tissue does not form a perfect cylinder around the AcuNav.

Figure 6.16 shows post-study photographs of the "X" ablations from both the endocardial and epicardial side. The ablation lines appear thinner and more well defined on the epicardial side.

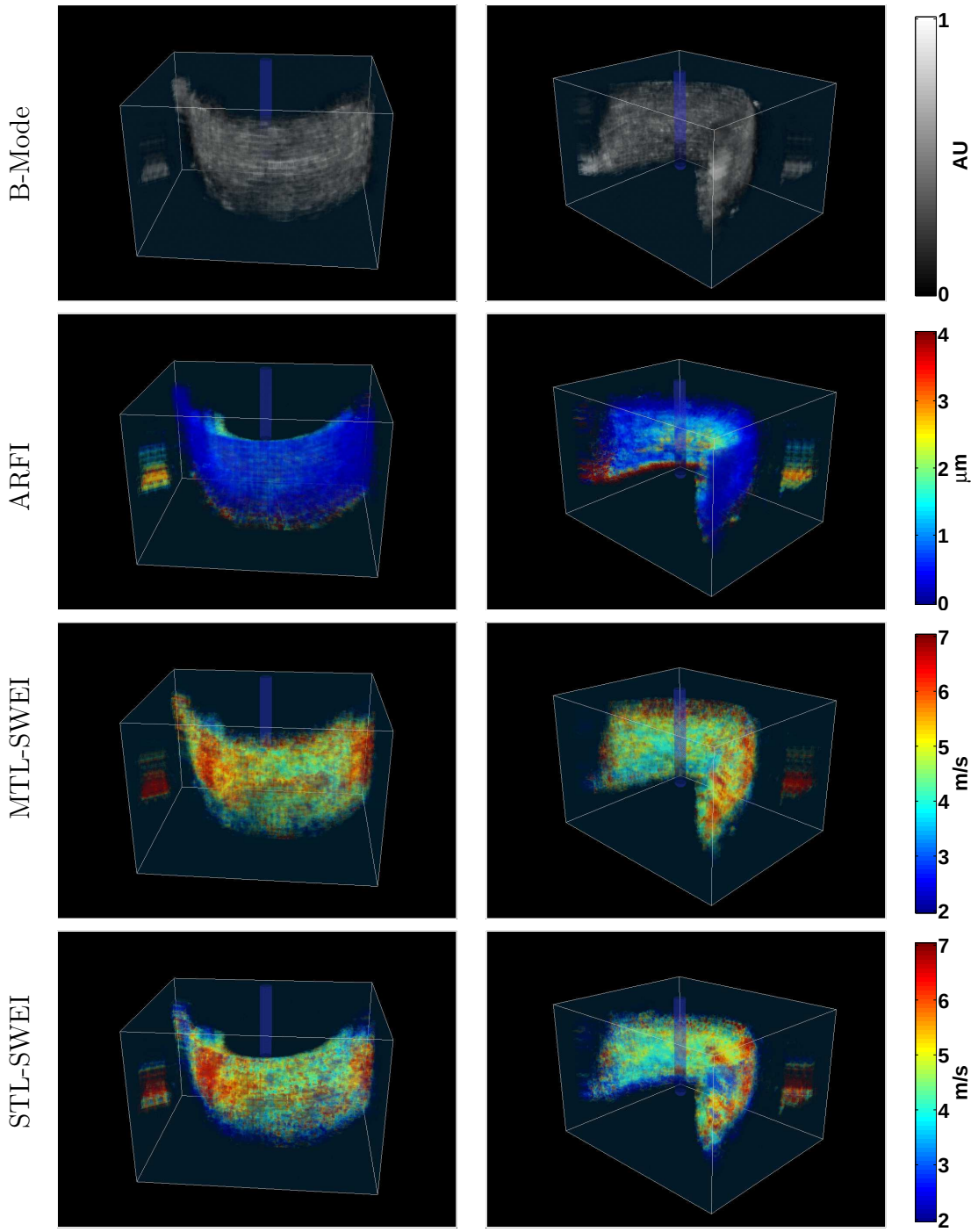

FIGURE 6.11: Renders of the 3-D reconstructed volume of canine RVFW prior to the "x" ablation. A stiff region is seen on the edges of the sample.

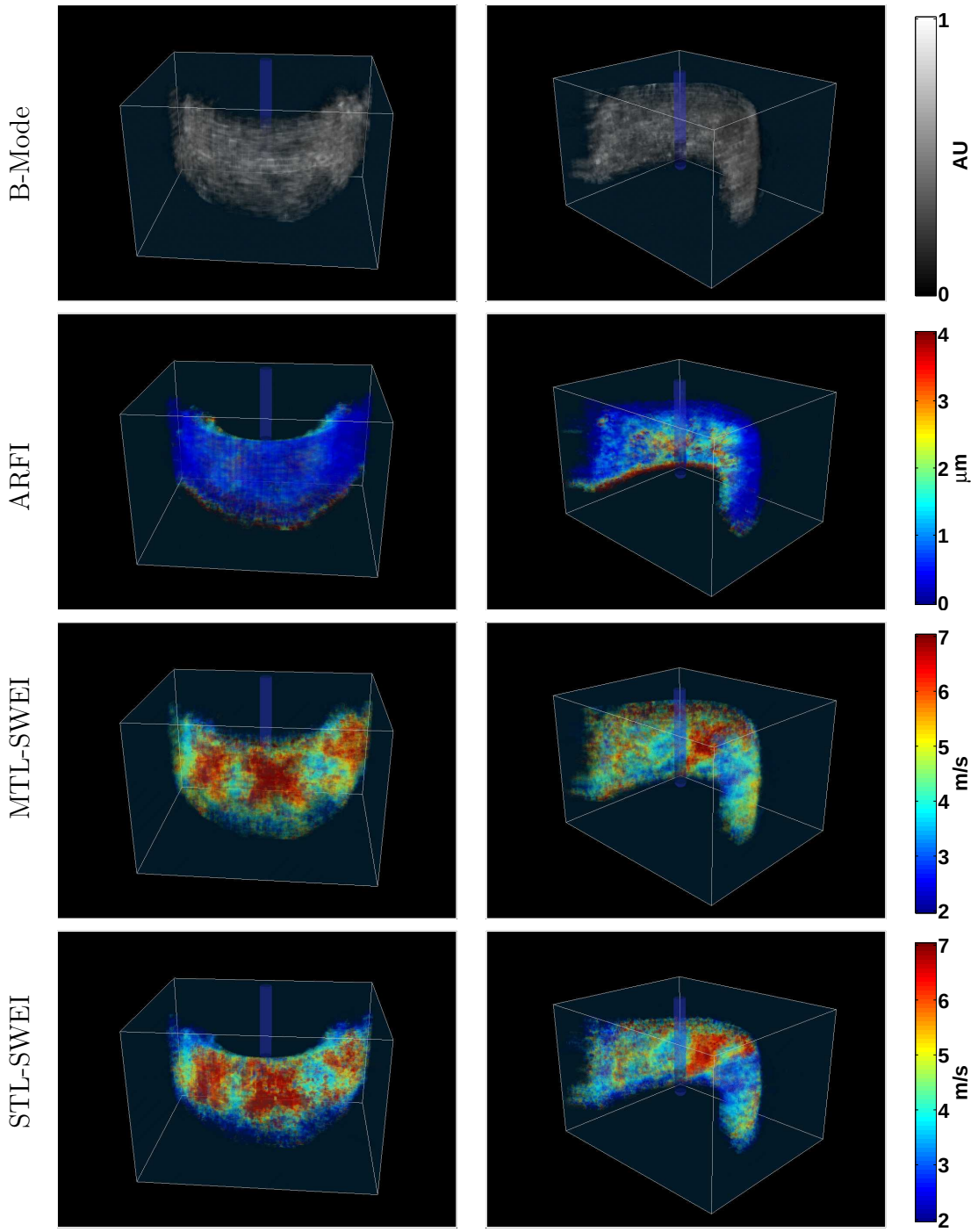

FIGURE 6.12: Renders of the 3-D reconstructed volume of canine RVFW following the "x" ablation. The "x" structures are clearly visible in the SWEI images, but harder to resolve in the ARFI images due to the steering and depth dependence of the signal.

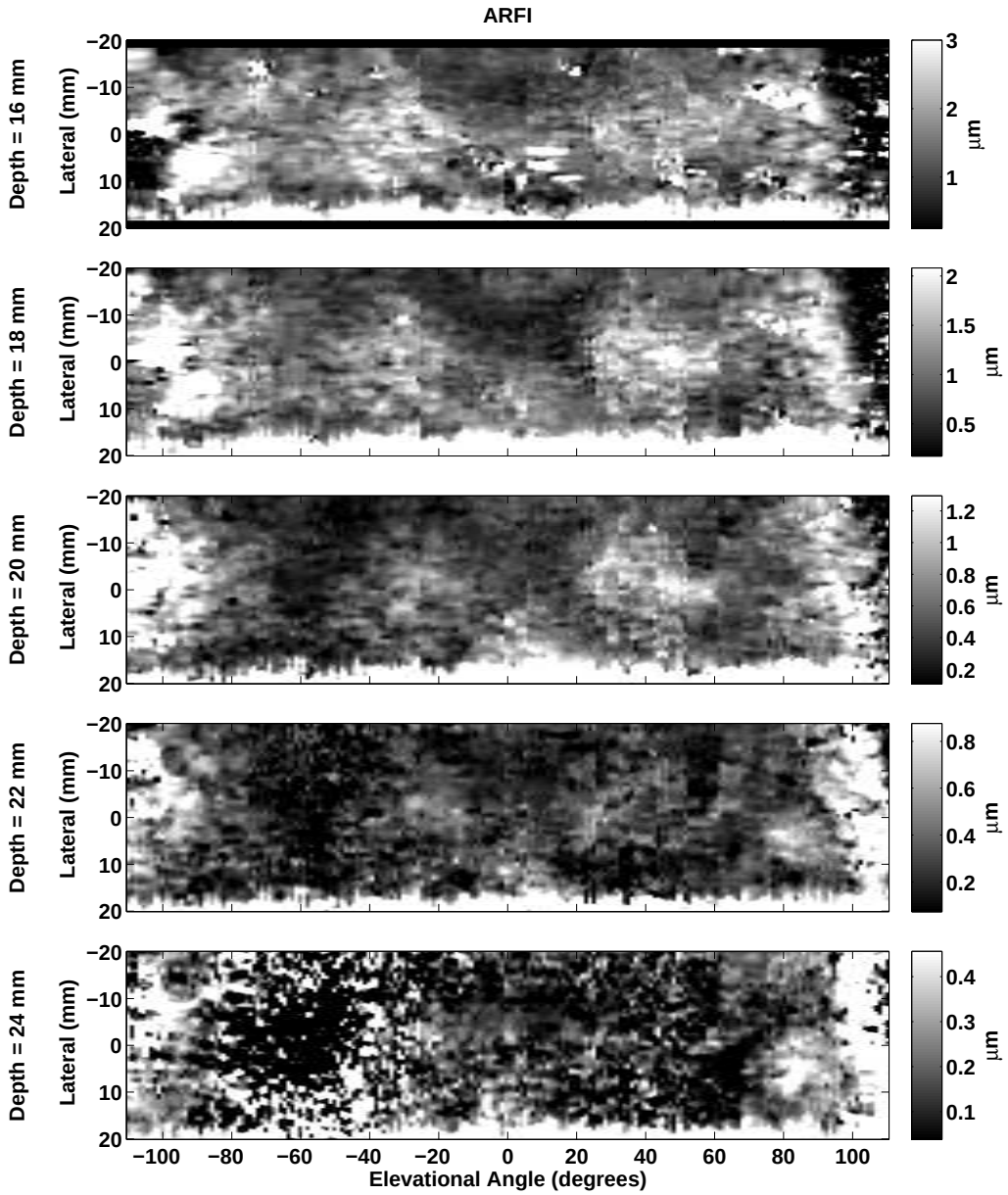

FIGURE 6.13: ARFI images of the "x" ablation volume sliced at different axial depths. Note that the dynamic range of the colorbar decreases with depth. The "x" on the left was ablated from the endocardium, the "x" in the middle from the enocardium and epicardium, and the "x" on the right from the epicardium only.

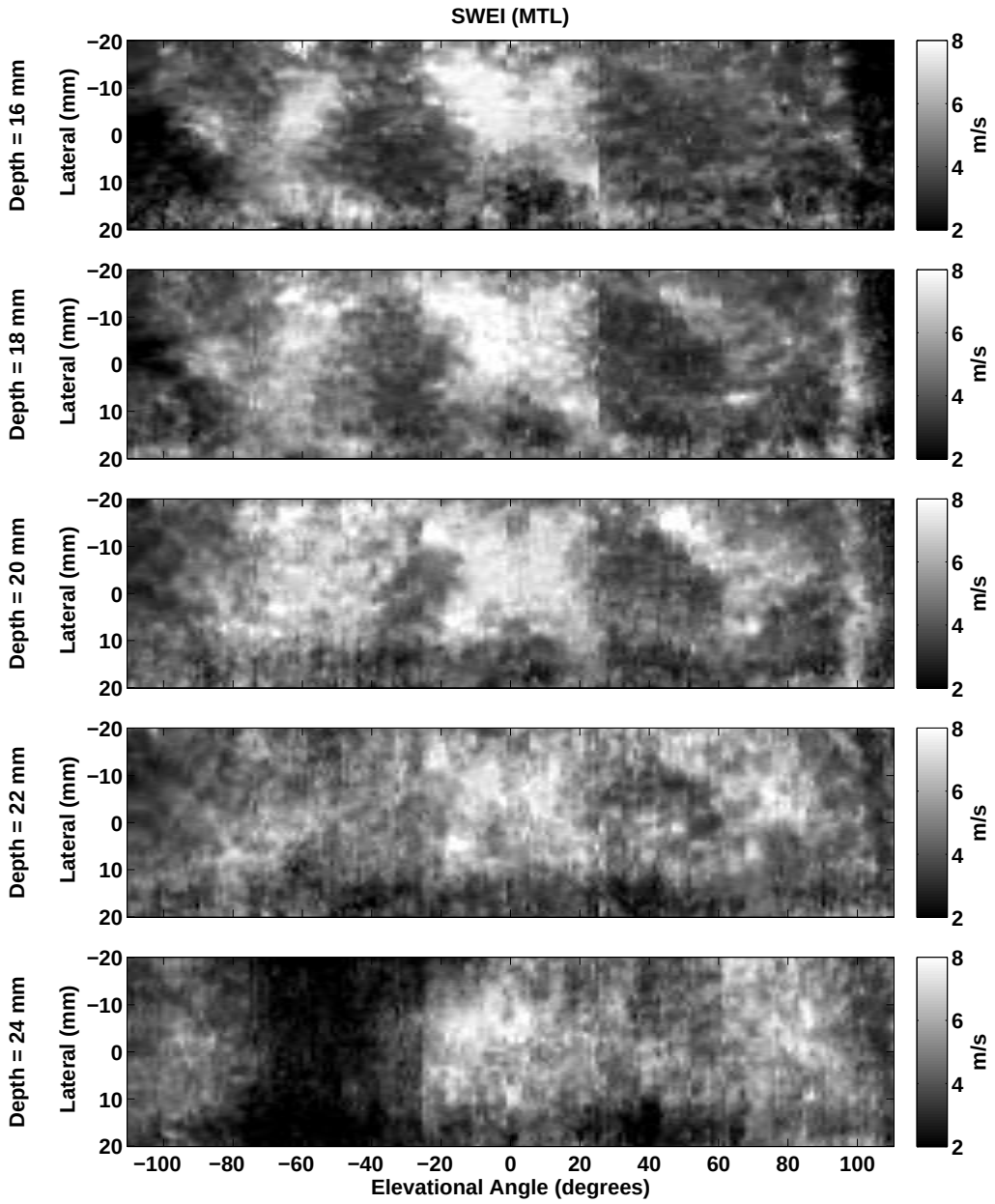

FIGURE 6.14: MTL-SWEI images of the "x" ablation volume sliced at different axial depths. The "x" on the left was ablated from the endocardium, the "x" in the middle from the enocardium and epicardium, and the "x" on the right from the epicardium only.

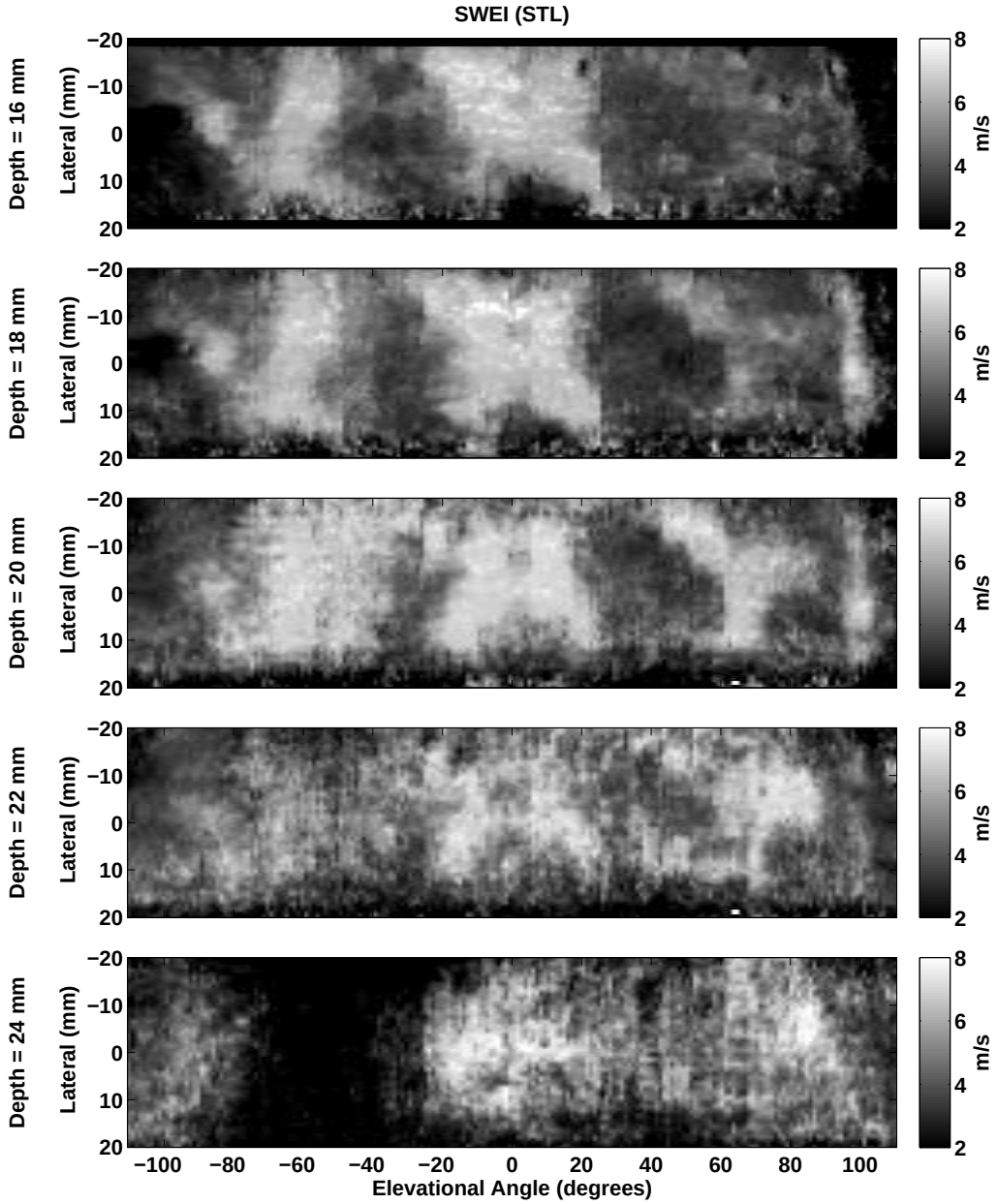

FIGURE 6.15: STL-SWEI images of the "x" ablation volume sliced at different axial depths. The "x" on the left was ablated from the endocardium, the "x" in the middle from the enocardium and epicardium, and the "x" on the right from the epicardium only.

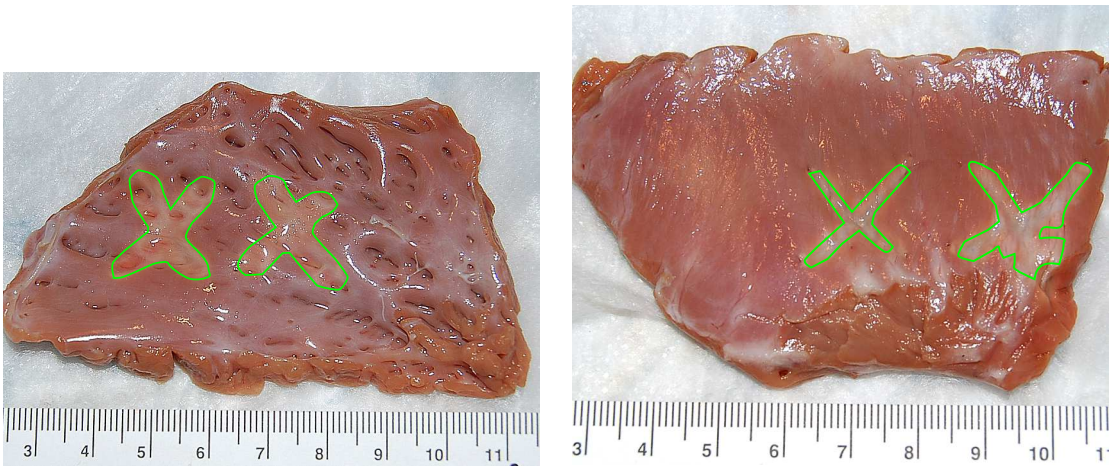

(A) Endocardial View (B) Epicardial View

FIGURE 6.16: Post-scan photographs of the "X" Ablations. The boundaries of the surface discoloration have been outlined in green.

6.3.4 Pulmonary Vein Ablation

Figure 6.17 shows renders of a phased-rotation scan of an *ex vivo* pulmonary vein ablation. On the left side of the render, the opening of one of the veins is visible in all modes. The tissue appears heterogeneous in ARFI, STL-SWEI and MTL-SWEI prior to ablation, and the ARFI images show decreased displacements with steering. After the ablation from the epicardium, a lesion becomes visible, in the ARFI image as ablations below 2 μm on to the right of the catheter near the center, and on the STL-SWEI and MTL-SWEI images as a region of elevated speeds greater than 5 m/s in the same area. The MTL-SWEI image shows a larger region of elevated velocities than the STL-SWEI image. Figure 6.18 shows the same volume, cut in the lateral dimension and displayed in the axial-elevational plane. The ablation lesion is more clearly visualized as a spot of lower displacements and elevated stiffness. The region of disagreement between MTL-SWEI and STL-SWEI corresponds to depths shallow to the focus ($<$ 12.5 mm).

Figure 6.19 shows a zoomed-in render of another pulmonary vein ablation. A section of myocardium appears ablated in ARFI and MTL-SWEI and to a lesser extent in STL-SWEI. Cutting along the center azimuth line again, figure 6.20 shows the ablated region clearly in all three images. The B-Modes in the top row also indicate some elevational artifacts. The IQ brightness is normalized by the maximum value in each image, so certain elevational planes appear brighter or darker, though structures can be followed through the slices. Also, on the right hand upper corner, a few elevational planes seem out of order.

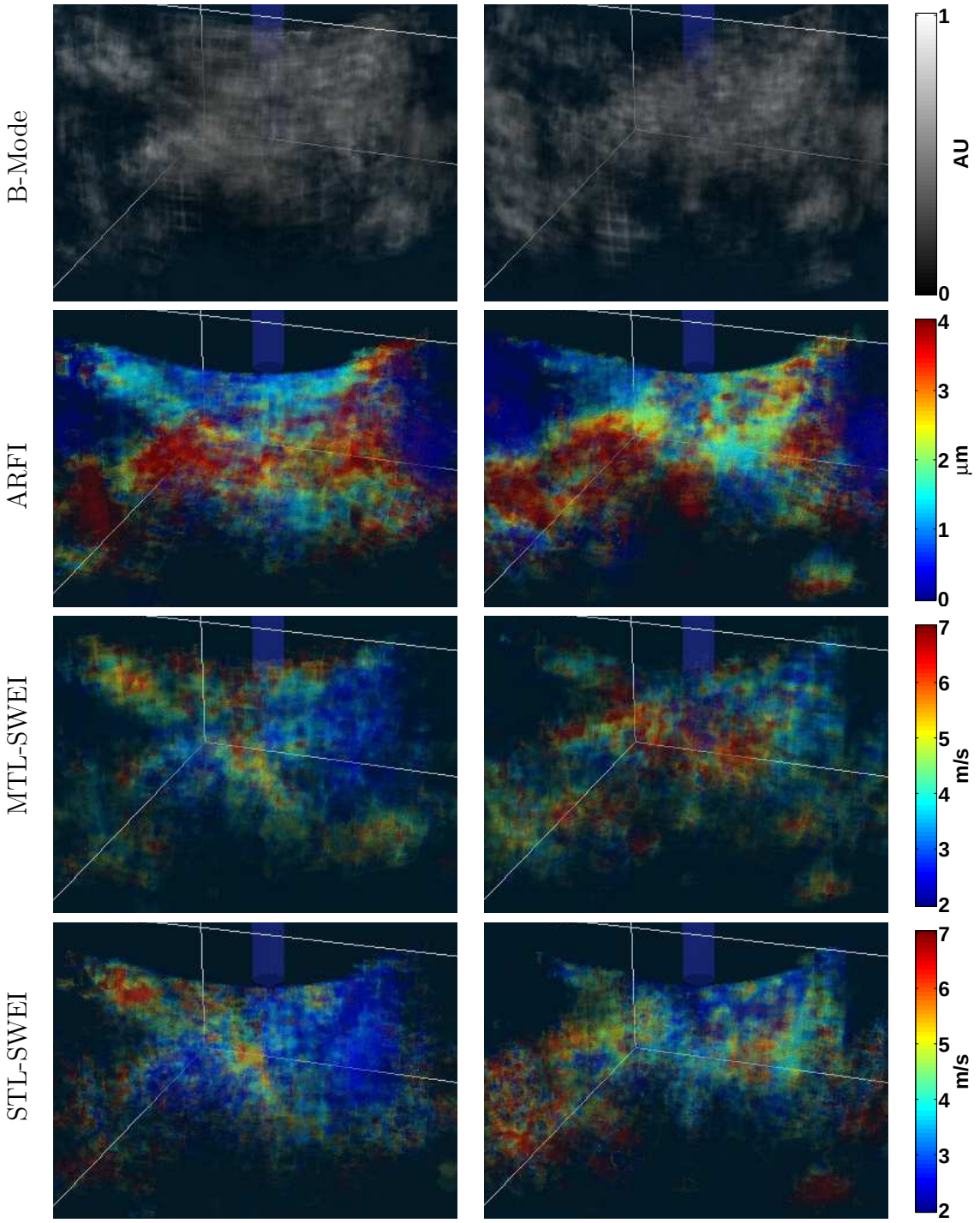

FIGURE 6.17: Renders of a 3-D reconstructed volume of the LA before (left column) and after (right column) ablation in an *ex vivo* sample. The opening of one of the pulmonary veins is visible on the left side. An ablation is visible directly in front of (towards the camera) and to the right of the catheter.

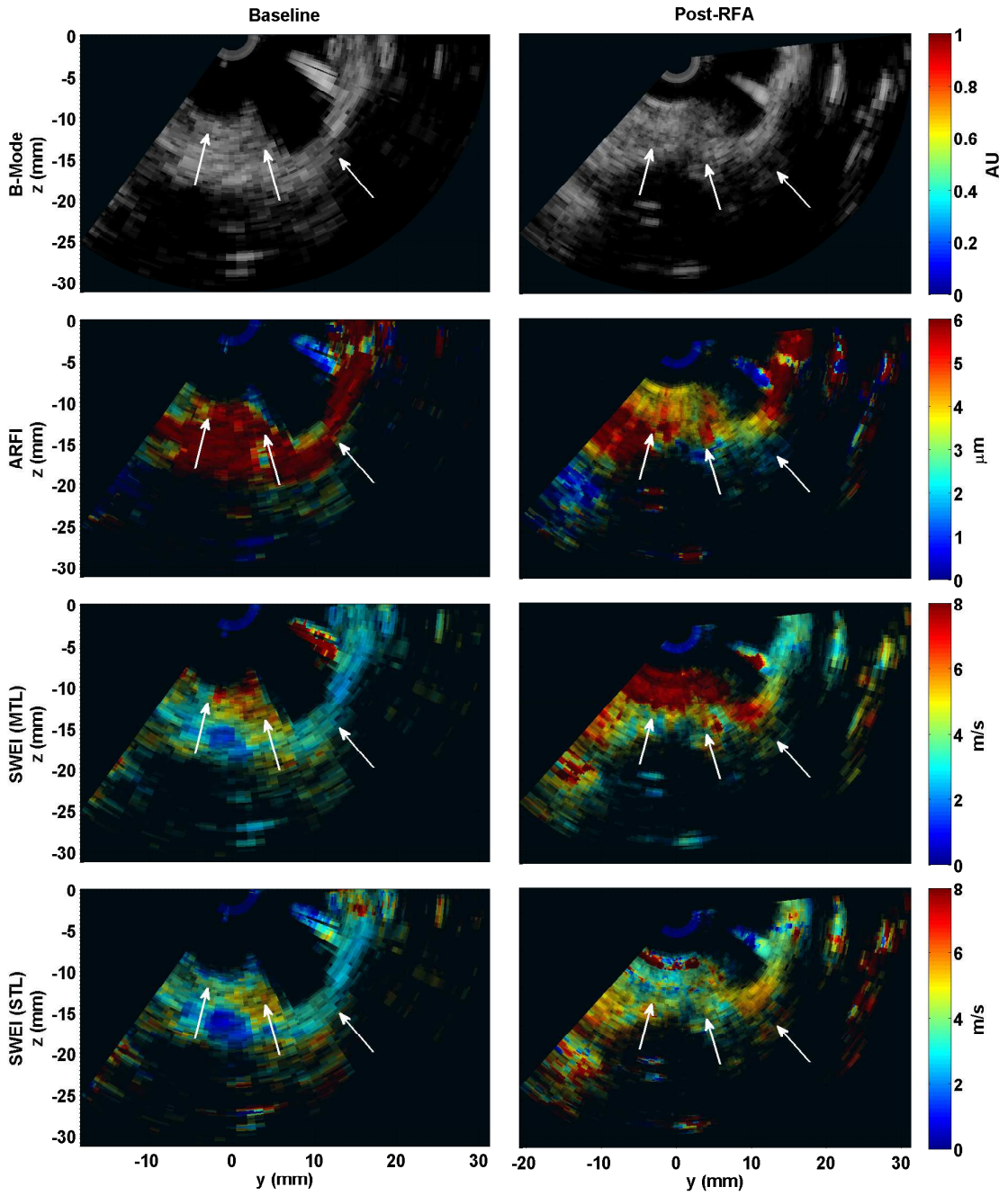

FIGURE 6.18: *Ex Vivo* pulmonary vein ablation volume from figure 6.17, sliced down the center azimuthal line. The ablation side is indicated by the white arrow, and marked with lower displacements and elevated velocities in the ARFI and SWEI images, respectively.

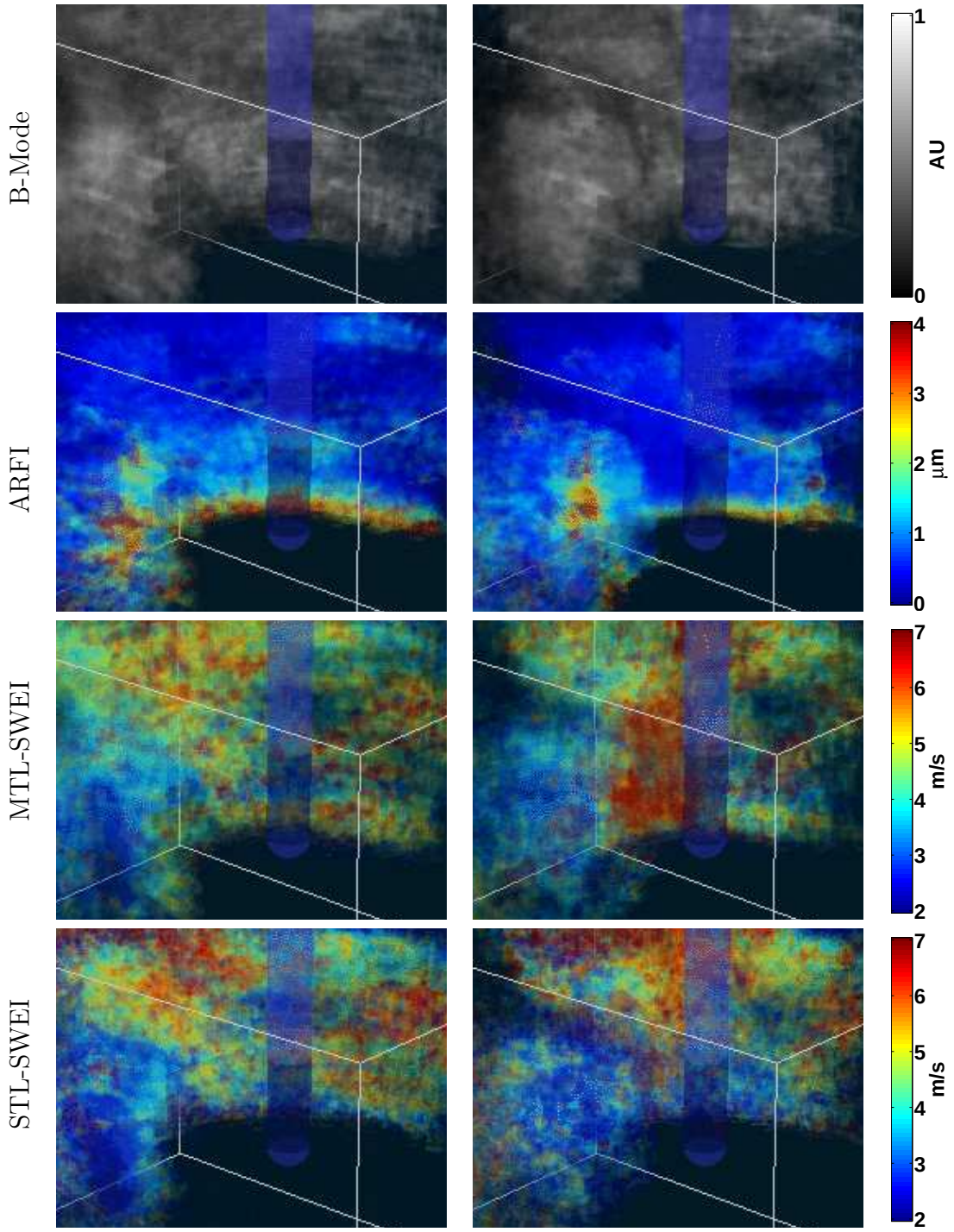

FIGURE 6.19: Renders of a 3-D reconstructed volume of an ablation in *ex vivo* canine LA. The ablation is visible to the left of the catheter tip, especially in STL-SWEI.

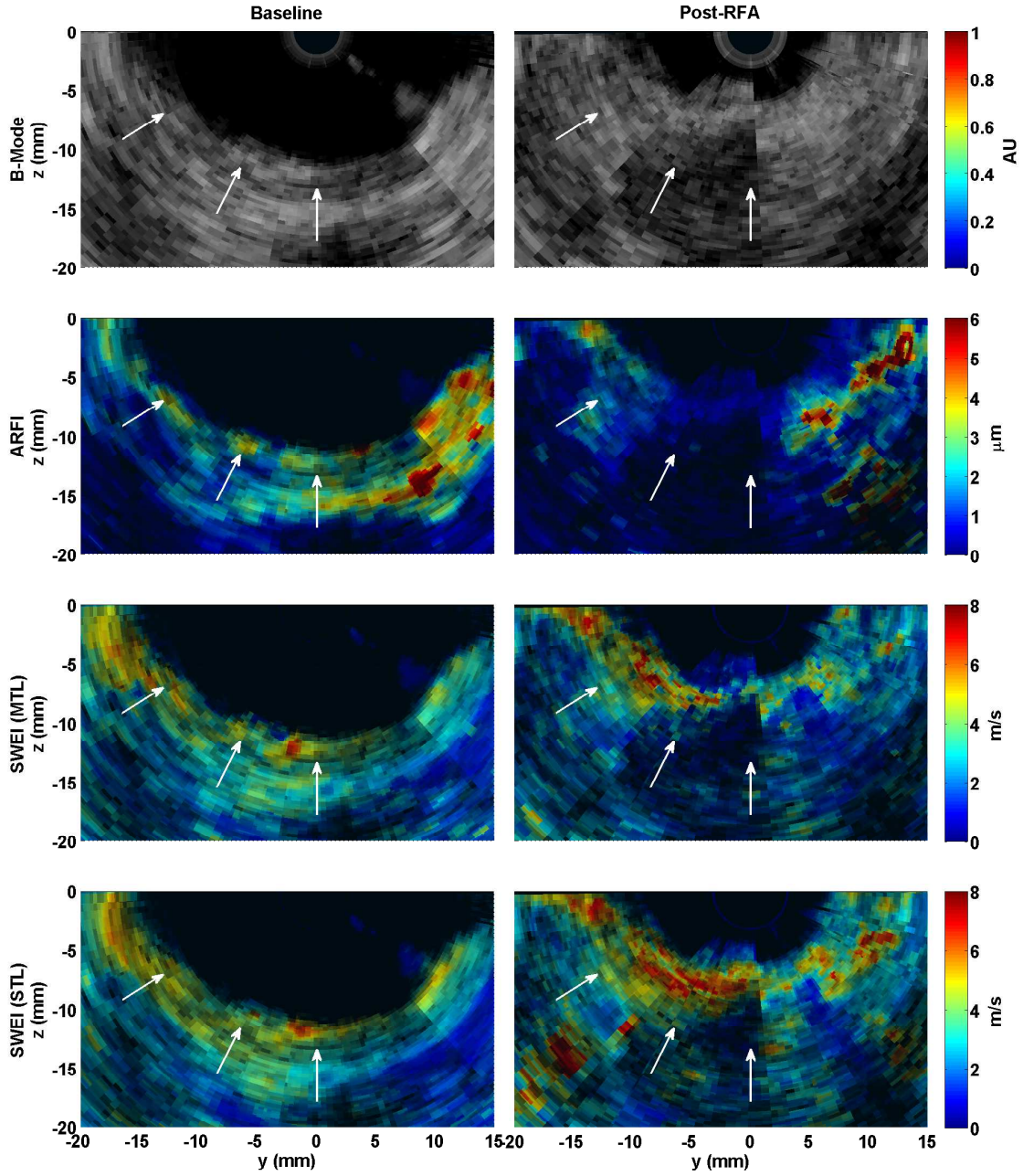

FIGURE 6.20: *Ex Vivo* pulmonary vein ablation volume from figure 6.19, sliced down the center azimuthal line. The ablation side is indicated by the white arrow, and marked with lower displacements and elevated velocities in the ARFI and SWEI images, respectively.

6.4 Discussion

6.4.1 Ablation Pairs

In all cases, the ablation lesions were visible in each of the elasticity imaging modalities, with a clear gap visible between the lesions. Somewhat surprising was the heightened echogenicity of the B-Mode at the center of the ablation lesions, as we expected the lesions to be invisible in B-Mode (column 2 of figure 6.4). It has been reported that lesion boundaries are in some patients hyperechoic (Fisher et al., 1997), so in this experimental setup, we suspect that this is the case.

Shear wave estimation was challenging within the lesions, both due to reflection artifacts and a low displacement signal. Even with many overlapping estimates, spatial smoothing needed to be applied with the 1 mm kernels, so μ-E imaging was not achieved with this setup. Inside the lesions, the finite differences in arrival times approached 0, even when imaged at 10,000 fps, which made the shear wave speed estimates noisy.

Another confounding factor was the parallel receive beamforming; to beamform 32 simultaneous lines, the transmit must be unfocused to deliver acoustic energy to all lines, and the demodulated IQ data for each line is sampled only just above the Nyquist limit. This is expected to broaden the speckle pattern, and the low sampling rate may provide worse displacement estimates than oversampled cases. The effect of broad speckle is expected to reduce MTL-SWEI estimates but not STL-SWEI(Elegbe and McAleavey, 2013), which may account for the increased noise in MTL-SWEI, which are otherwise formed from the same arrival time data as STL-SWEI. Furthermore, STL-SWEI reported velocities between 20 and 50% higher than MTL-SWEI, which is unexpected, and may the be result of a sequencing error.

ARFI, by contrast, can be performed with tightly focused tracking beams, and the low displacement signal in lesions does not confound additional processing steps.

The error bars on the ARFI data (figure 6.5) are much smaller than those on the SWEI estimates, although the contrasts are also lower. The CNR estimates (figure 6.6) initially indicated that STL-SWEI performed the best, followed by MTL-SWEI, ARFI, and then B-Mode. ARFI's underperformance relative to what would be predicted by chapter 5 is, in this case, partially explained because the arrival time differences were so small for SWEI that the values inside the lesion became very large, and their high variation which was not being accounted for in the CNR measurement. Using a weighted sum of the standard deviations based on the number of pixels in the lesion and backfground ROIs (figure 6.7), the high variance in the SWEI ablation estimates could be penalized, and the results brought into agreement with the predicted performance, with STL-SWEI and ARFI performing nearly identical, followed by MTL-SWEI and then B-Mode.

6.4.2 Ablation Lines

The phased-linear scans of ablation lines were able to resolve the individual ablations that made up each of the ablation lines in both the axial-elevational (ZY) and lateral-elevational (XY) planes. The ablations appear to have sizes between 5 mm and 1 cm in diameter, but the edges of the ablations appear as gradients in all three elasticity modes. Even so, gaps <5 mm wide whose appearance in the ARFI and SWEI images showed values similar to the pre-ablation images were visible between the individual ablations. Only the 8 mm - spaced ablation line showed a contiguous section of lesion on the left side, but in the XY plane, it appears that the ablation line becomes quite thin (<5 mm) in the lateral dimension between the ablation centers. There are regions of less-elevated stiffness above and below the connected centers in the ZY plane, but without knowing what shear modulus corresponds to electrical ablation, it is impossible to determine the hypothetical functional integrity of this line. A determination of the threshold mechanical properties as they pertain to transient

and permanent disruption of electrical activity is one of the critical pieces of work that remains to be done.

In the ZY planes (panels A and B of figures 6.8-6.10), the depth dependence of ARFI displacements limits its ability to resolve the deep edge of the ablations, and angular sensitivity of the elements decreases displacements at the lateral edges of the field of view. Because the images are displayed as inverse displacement, the deep parts of the tissue sample where the radiation force does not penetrate become white pixels, indicating displacements <0.8 μm; They would show an equivalent loss of contrast in their conventional, displacement magnitude form. These effects could be corrected with calibration by the pre-ablation image, or by using a model of expected transmit pressures and attenuation, using the B-Mode data to separate blood from myocardium. Both of these topics will need to be explored in future work. STL-SWEI and MTL-SWEI show a more clear delineation of the distal edges of the lesions but the B-Mode is the most useful means of assessing which parts of the image correspond to which anatomy.

While STL-SWEI is expected to suppress speckle noise to the point where it can operate at substantially higher resolution than MTL-SWEI, the benefits of STL-SWEI over MTL-SWEI are not seen in the elevation dimension, in which we have the gaps. The lateral speckle texture is visibly suppressed in the STL-SWEI images, although it is replaced with three horizontal striations in the XY plane, visible in panels C and D of all of the images. These may have been due to rounding errors during sequencing creating offsets placement of the push beams. Later-developed sequences eliminated this artifact, which was no longer present in the phased-rotational scans.

6.4.3 "X" Ablation

The "x" ablation was the most successful 3-D reconstruction to date (figures 6.11 and 6.11), particularly with STL-SWEI, highlighted by figure 6.12. The center "x", ablated from both the inside and outside is very visible on the SWEI renders. The endocaridal and epicardial "x"s are visible in the volume, although harder to appreciate in still 3-D renders. ARFI is significantly less effective at visualizing the structure because of the depth-dependence displacement. While the ARFI images have reasonable image quality, the size of the "x" is too large relative to the ARFI depth to be imaged with any uniformity. The slices through the STL-SWEI volume (figure 6.15), however, show excellent resolution of the "x" shapes. The line of ablations wound up being positioned as an angle relative to the scan, which is why the left, endocardial "x" appears centered near the bottom of the images and the right, epicardial "x" near the top. Additionally, the tissue didn't wrap to form a perfect cylinder, so the epicardial "x" appears at an angle through depth, with the left side appearing at more shallow depths than the right side. The endocardial ablation appears to have line widths on the order of 0.5 cm to 1.0 cm, similar to what we saw in the previous section with the line ablations, but now with clear contiguity. Comparison to the photographs (figure 6.16) shows similar dimensions for the left ablation. The ambiguity of the top junction of the center "x" also corresponds to the photograph. The epicardial ablations appeared significantly thinner in the photographs, possibly due to absence of endocardial structure, which may have conducted heat away from the tip for those ablations. The left side of the epicardial "x" is very clearly visible at 18 and 20 mm in the STL-SWEI images, and does show thinner dimensions than the epicardial ablations. At 22 mm and beyond, however, the penetration of the radiation force has diminished, and noise starts to take over, preventing clear resolution of the fine "x"'s placed on the epicardium. A second scan

from the epicardial side may have elucidated this point further, and more generally, imaging targets in multiple orthogonal directions is likely to be further elucidate the differences in axial, lateral and elevational resolution.

6.4.4 Pulmonary Vein Ablation

The pulmonary vein ablation scans sought to translate the success of the "x" ablation one step closer to *in vivo* relevance. The intent was to obtain a view of the pulmonary vein ostia, and pan the AcuNav's field of view across the ostium. With maximum diameters reported up to 18.8 mm ((Wittkampf et al., 2003)), it was hoped that the 20 mm lateral field of view at a 20 mm focal depth would be sufficient for creating the images. However, even coming up through the mitral valve, obtaining views that fixed the ostium at that depth and positioning proved challenging due to the variable shape of canine atria and limited space in which to maneuver the catheter. Furthermore, because of the AcuNav's small array size, images made with focal depths <15 mm had better SNR than those with deeper foci. The scan geometries that we settled for had the AcuNav partially in the ostium, with a view of the opposite wall, such that between a 90° and 180° scan could be made of a side of the ostium. These views also allowed for epicardial ablation around the pulmonary vein within the field of view.

As can be seen in the rendered volumes (figures 6.17 and 6.19), the overall atrial geometry of the atrium is difficult or impossible to make out from this limited field of view. The opening to one of the pulmonary veins is visible in figure 6.17, but separating the 3-D geometry within the volume from the volume's donut-shaped field of view is difficult.

However, the results do demonstrate that ICE ARFI and SWEI can visualize ablated areas of atrial wall, as the geometry remains mostly consistent before and after ablation, and the ablated regions show lower displacements and higher velocities

in ARFI and SWEI images, respectively. The ARFI images are again limited by the depth of penetration and steering angle effects, providing large lateral gradients within the field of view and through depth. The images sliced through the center of the lateral field of view (figures 6.18 and 6.20) show a more clear view of the ablations, which were placed to coincide with the center of the lateral field of view when possible.

In the first ablation (figure 6.18), STL-SWEI and MTL-SWEI disagree about the shear wave speed in the upper left side following ablation. This is likely due to the proximity of the tissue to the transducer, and the use of a focal depth of 15 mm for the entire scan. ARFI does indicate that the tissue is ablated, so MTL-SWEI might seem to be better in this case, but it is likely that shear wave propagation in that region is hard to characterize, and that MTL-SWEI and STL-SWEI simply fail in different ways. The ablation is visible in STL-SWEI, albeit with decreased contrast, such that the ablation only looks as stiff as the structure to it's left in the pre-ablation scan.

In the second ablation (figure 6.20), MTL-SWEI again reports higher contrast than STL-SWEI, although all three modalities show the ablated region. In the slices, we see that the tissue has been moved closer to the transducer. Because the heart is suspended in the tank and ablated from the outside, the ablation catheter pushes the atrial wall inward during ablation. In this case, the tissue did not completely move back to its original position. However, the ablated region is quite visible in all three modalities, with velocities above 6 m/s and displacements below 1 μm, compared to pre-ablation values of 4.5 m/s and 3.5 μm, respectively. The stitching artifacts in the upper right corner of the Post-RFA B-Mode indicate that the small time delay between the acquisition of the ARFI and SWEI images and the recording of the position (the amount of time for LabView to detect that a new file had been written), was enough that the catheter may have continued to be rotated forward

or backward. Effort was made to minimize this, by holding the catheter steady during acquisitions until the point was collected, but in this instance, some mis-registration occurred. In a clinical implementation of this system, acquisition of position should be triggered automatically by the ultrasound scanner to maintain the tightest possible registration between the images and their positions.

Another limiting factor to note is that of transducer "kickback". Because the AcuNav is so small and light, the vibrations of the transducer face that create the focused push also cause the transducer to recoil, which appears in the images as a uniform displacement through all depths. This can be filtered out by subtracting the displacements that appear everywhere within the field of view from each time step, but since the apparent displacements can be on the same order of magnitude as the ARFI displacements (ones of microns), any error in the subtraction filter results in apparent variation in the ARFI image along that line. Kickback could be suppressed by feeding the catheter through a sheath such that it had mechanical support, as was the case for these scans, but in cases where the catheter was free to move, entire 3-D scans were corrupted by this motion. Those scans were acquired before access to near-real-time processing was available, though, so with rapid feedback, adjustments can be made when kickback is apparent. For future developments, a longer array, possibly with more mass at the tip, may be necessary to expand the lateral field of view, extend the usable focal depths, and both generate larger displacements and resist kickback.

6.5 Conclusion

ARFI, STL-SWEI, and MTL-SWEI were used to image ablations in *ex vivo* porcine and canine myocardium. Three different imaging scans (linear-translation, phased-translation, phased-rotation) were used to image four increasingly complicated ablation scenarios. The pairs of ablation lesions indicated performance in line with

the predicted performance, with STL-SWEI and ARFI having similarly high CNR, followed by MTL-SWEI. Ablations were shown to be marked by at least a halving of displacements and a doubling of shear wave speeds. The lines of ablations were individually visualized by ARFI, STL-SWEI and MTL-SWEI. All three modes could resolve <5 mm gaps in lines 0.5 - 1 cm ablations at spacings between 8 and 12 mm, although the SWEI methods could better visualize the lesions through depth. The "x" ablation showed that with rotation of the catheter, as would be done in an *in vivo* setting, and with sequences that are fast enough to be run during atrial diastole, high quality volumes can be stitched together from a series of images that show not just regions of ablation, but actual three dimensional structure and geometry. The final scans, of the pulmonary veins of suspended atria, were able to demonstrate successful imaging of ablations on the pulmonary vein ostia, but also highlighted tissue heterogeneity, scan geometry, and noise considerations that motivate the further engineering that will be necessary to make a reliable tool for clinical use.

7

Three-Dimensional Fusion of Shear Wave Imaging and Electro-Anatomical Mapping for Intracardiac Radiofrequency Ablation Monitoring: Initial *in vivo* results

This chapter is adapted from a proceeding paper presented at the IEEE Ultrasonics Symposium in 2013, but expanded to include more data beyond the initial study. These results are the penultimate combination of the tools described in this thesis, tested in an in vivo imaging scenario.

7.1 Abstract

Acoustic radiation force impulse (ARFI) and shear wave elasticity imaging (SWEI) are ultrasonic methods of imaging the mechanical properties of the myocardium that may provide direct visualization of ablation lesion formation through their implementation on intracardiac echocardiography (ICE) imaging catheters, which are commonly used to guide RFA. This work demonstrates that the 3-D tracking from an electroanatomical mapping system can be used to perform offline reconstruction of myocar-

dial ARFI and SWEI volumes from series of ARFI and SWEI images, and explores the spatial integrity of these 3-D datasets with regard to the task of imaging RFA lesions. Case studies are shown where the ablations do not form a contiguous line, where mis-registration of the 3-D positioning and ARFI/SWEI images ruins reconstruction, and where large gaps in the sampled volume left by frames dropped for transducer kickback create smeared, low resolution volumes. When focal lesion groups are created by RFA and the series of ARFI and SWEI images are acquired with sufficient spatial sampling, reconstructed volumes show clear delineation fo the ablation sites in both ARFI and SWEI images and volumes, with good correspondence between ablated sites and image features.

7.2 Introduction

Radiofrequency Ablation (RFA) is a common treatment for atrial fibrillation (AF) and other cardiac arrhythmias (Calkins et al., 2012). Electroanatomical mapping (EAM) gives electrophysiologists the ability to construct a 3-D shell of anatomy and local activation time to guide ablation lesion placement. Intracardiac echo (ICE) is commonly used during RFA to visualize the myocardium-catheter contact in real-time(Khaykin et al., 2008). Acoustic radiation force impulse (ARFI) imaging and shear wave elasticity imaging (SWEI) have shown promise for assessing ablation lesion dimensions by imaging the local mechanical properties of tissue, with ablated tissue presenting as a region of low compliance(Pernot et al., 2009; Eyerly et al., 2010; Arnal et al., 2011; Eyerly et al., 2012). The spatial extent of the formed lesions is critical to their efficacy (Melby et al., 2008; Kowalski et al., 2012), but while planar substrate images can identify the transmurality of lesions and their extent in the lateral imaging plane, they cannot individually determine the out-of-plane extent of the lesions. This work uses the 3-D spatial tracking of the EAM system to register

series of ARFI-SWEI images in 3-D space, and combines the data into a volumetric maps of myocardial stiffness.

7.3 Methods

7.3.1 Experimental Setup

Ultrasound data were acquired with 10-French Biosense Webster SoundStar (Biosense Webster Inc, Diamond Bar, CA, USA) ICE catheters, running on a Siemens SC2000 ultrasound scanner (Siemens Medical Systems, Mountain View, CA, US). 3-D positioning data were acquired using a Biosense Webster CARTO3 EAM system, running the CartoSound module to interface with the SC2000 and display the live B-Mode fan from the ICE catheter positioned in 3-D on the EAM cartoon shell. A series of healthy canine subjects were used in compliance with the protocols from Duke University's Institutional Animal Care and Use Committee (IACUC). Each animal was anesthetized, and both the SoundStar imaging catheter, and a Biosense Webster NaviStar radiofrequency ablation/mapping catheter were introduced into the heart either via the jugular or femoral veins and steered to the chamber of interest. Prior to imaging, a 3-D electroanatomical map of the chamber of interest was recorded using the CARTO3's built-in mapping tools to guide lesion placement and imaging catheter positioning. Fast anatomical mapping and/or point-by-point electrical mapping were used to build the 3-D shell. Once the shell of the endocardial geometry was complete, imaging targets were selected to keep the tissue within 2 cm of the catheter face over an elevation-rotation scan of at least 45°, and ideally keep the tissue perpendicular to the imaging beams. In later studies, the ablation catheter would be steered into the field of view to confirm that sufficient contact with the walls could be maintained in the target ablation area. The catheter was steered in elevation by rotating the handle of the catheter, which added a further preference for views that did not require substantial use of the steering mechanisms on the SoundStar. The

lateral wall of the right atrium, from a jugular insertion point, provided one of the most reliable targets. In other cases, a 14 Fr steerable sheath (Medtronic Cryocath, Kirkland, Quebec) was used to steer the SoundStar within the heart without using the SoundStar's built-in steering. This allowed the SoundStar to be rotated within the sheath so that the imaging transducer's tip would rotate on-axis. To accomplish this, the ICE catheter had to be inserted such that only 1 cm or so of the catheter extended beyond the sheath, only enough to expose the imaging array.

Prior to ablation, the target myocardium was imaged with a series of ECG-gated ARFI and SWEI images, steered by the operator in the elevation plane to sample the tissue approximately with between 25 and 50 images over the elevational field of view. The total number of images for the study was limited to 100, which was the maximum number of ICE positions that the CARTO3 could digitize. The ECG delay was selected to time data acquisition during the diastole of whichever chamber was being imaged. Before acquisition of each image, respiration was held at full expiration (when everything ran smoothly, two images were sometimes acquired in a single breath hold). Each position in the CARTO3 was recorded on command with three seconds of retrospective video frames from the SC2000 and the corresponding position and ECG data. After each image acquisition, the CARTO3 was dialed to the correct frame in the three-second clip corresponding to image acquisition by the SC2000, as indicated on a command prompt visible on the SC2000 monitor's frame data. A frame was then saved to the software, which would store the catheter position for offline processing. The IQ ultrasound data for each of the images were stored for offline processing, and therefore the ARFI and SWEI images are not displayed by the CartoSound module. To operate this multi-device system, four people were needed with careful communication, one each at the ventilator, operating table, SC2000, and CARTO3. A diagram of the system is found in figure 7.1. The sequence of acquisition was as follows:

1. Person A steers the ICE catheter to the approximate desired positions and request a breath hold.

2. Person B pauses the ventilator at full expiration.

3. Person A tunes the ICE Catheter position to the precise position and signals for an acquisition.

4. Person C acquires an image with the SC2000.

5. Person D watches the CARTO3 screen for the visual cue that acquisition is complete and saves the three second clip.

6. Person C confirms completion of the acquisition.

7. Person B resumes ventilation.

8. Person D reviews the last three seconds on the CARTO, dials to the appropriate frame, and saves the position.

9. Person A steers the ICE catheter to the next imaging position

In some experiments, step 7 would be initially skipped, and the team would go back to step 3 after step 8 to acquire a second image on a single breath hold.

7.3.2 Ablation

Under ICE imaging guidance, the catheter operator attempted to create a short line of contiguous lesions through the region of interest, each typically ablated 60 seconds at 65°C, although final selection of ablation protocol was left to the ablator's discretion. Over the course of the ablation, a series of points were recorded in the CARTO system on demand as requested by the operator of the ablation device. These points represent the position of the ablation catheter tip at those times, and

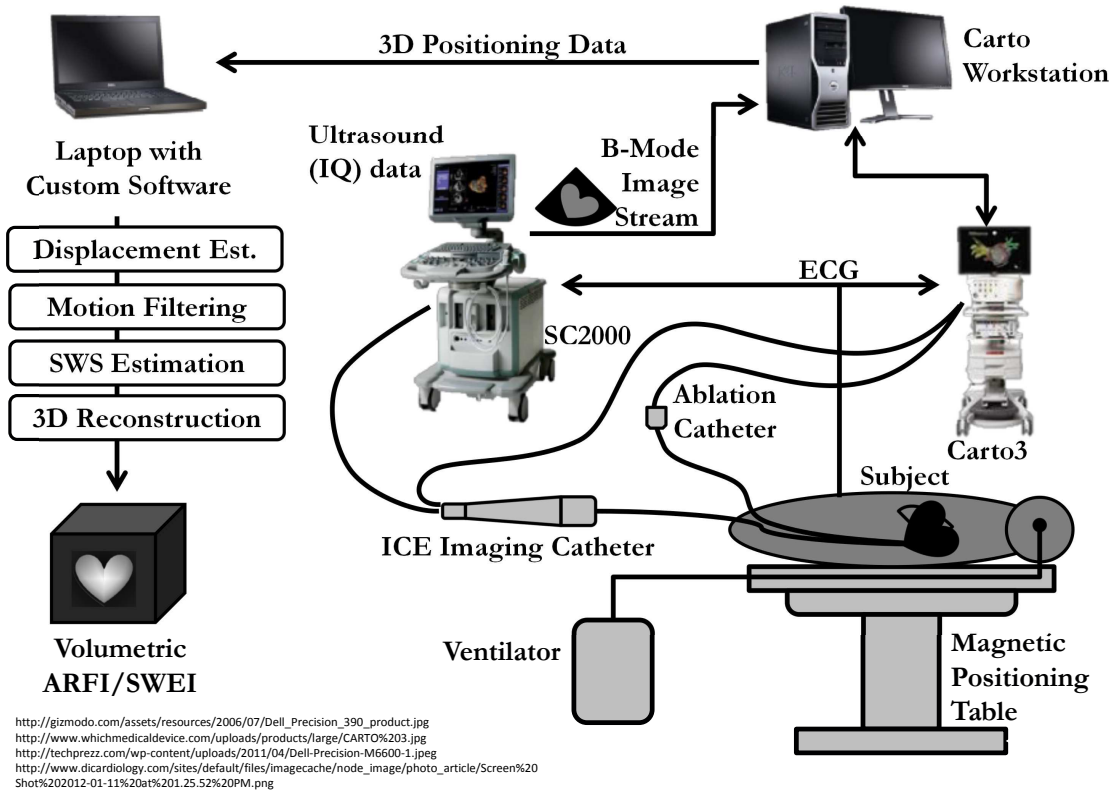

FIGURE 7.1: Image fusion data acquisition system diagram. The SC2000 records the ultrasound data, while the CARTO3 records 3D positioning data. The subject for this experiment was the canine subject.

are represented in the CARTO system as colored spheres whose size was arbitrarily configurable within the system, but whose value was left at the default of 2 mm. Points were acquired to build a representative set of the ablated region, although in some cases, the motion of the ablation catheter during the ablation made creation of a contiguous lesion impossible. Additionally, in one animal, although the CARTO points indicated a tightly spaced line of ablation, an equipment malfunction with the ablation device caused no lesions to be formed.

7.3.3 Processing

Post-procedure, the catheter position data, electroanatomical data, and ablation location markers, were exported from the CARTO3 for offline processing. Each ultrasound dataset from the scanner was formed into a set of matched B-Mode, ARFI, STL-SWEI and MTL-SWEI images. Each image set was registered in 3-D by using the rotation-translation matrix stored for its matching high-resolution B-Mode frame from the CARTO3 data. The transformation was performed by multiplying the coordinates of each pixel in the imaging plane $\vec{x}$ by the transformation matrix $\mathbf{T}(\alpha, \beta, \gamma, x_0, y_0, z_0)$, to get the transformed coordinates $\vec{x_T}$:

$$\begin{bmatrix} x_T \\ y_T \\ z_T \\ 1 \end{bmatrix} = \begin{bmatrix} & & & x_{T0} \\ \mathbf{R}(\alpha,\beta,\gamma) & & & y_{T0} \\ & & & z_{T0} \\ 0 & 0 & 0 & 1 \end{bmatrix} \begin{bmatrix} x \\ y \\ z \\ 1 \end{bmatrix}, \tag{7.1}$$

where $\mathbf{R}(\alpha, \beta, \gamma)$ is the 3×3 rotation matrix as a function roll, pitch, and yaw, respectively, and $\langle x_{T0}, y_{T0}, z_{T0} \rangle$ is the transformed origin location. The rotation matrix is given by:

$$\mathbf{R} = R_z(\alpha)\, R_y(\beta)\, R_x(\gamma) \tag{7.2}$$

for which

$$R_z(\alpha) = \begin{bmatrix} \cos\alpha & -\sin\alpha & 0 \\ \sin\alpha & \cos\alpha & 0 \\ 0 & 0 & 1 \end{bmatrix}$$

$$R_y(\beta) = \begin{bmatrix} \cos\beta & 0 & \sin\beta \\ 0 & 1 & 0 \\ -\sin\beta & 0 & \cos\beta \end{bmatrix} \tag{7.3}$$

$$R_x(\gamma) = \begin{bmatrix} 1 & 0 & 0 \\ 0 & \cos\gamma & -\sin\gamma \\ 0 & \sin\gamma & \cos\gamma \end{bmatrix}$$

The myocardium was segmented in each image by using the matched, low-resolution B-Mode data to exclude ARFI or SWEI estimates from the blood or from beyond the pericardium. Due to transducer kickback, incorrect ECG triggering, or excessive cardiac motion, some datasets had background motion that could not be separated from the induced displacement signal, and were excluded entirely. To interpolate the planar data onto a volume, the endocardial surface from the EAM was used as a reference. The extent of the endocardial surface to use was found by converting the Cartesian coordinates of the ARFI and SWEI data into spherical coordinates. Each transformation matrix $\mathbf{T}$ represents a new coordinate system, so a set of orthonormal bases was found for each image. The "apex" of each planar sector scan (the geometric point where all of the scan lines intersect, located for this experiment 8.54 mm behind the transducer face) was also found as the origin of each transformed system. The apexes were averaged across frames, as were the base vectors representing the orientation of each image. This gave an estimate of the position and orientation of the overall scan geometry, even though the individual frames are only roughly aligned. The pixels in each image that represented myocardium were individually transformed on this new spherical coordinate system. The endocardial

surface, stored as a series of 3-D points defining the vertices of the cartoon mesh, was transformed into spherical coordinated relative to the overall scan geometry. Points on the mesh that fell outside the total azimuthal and elevational field of view of the images were excluded. A new surface with 1° spacing in the azimuthal and elevational directions was created to cover the field of view of the images. The new mesh's radial coordinates were calculated with the "TriScatteredInterp" function in matlab using the transformed mesh coordinates. To create a volume extending through the endocardium and out to the epicardium, radial offsets were added to the interpolated surface. The point cloud of all the ARFI or SWEI data from the planar images in the original 3-D Cartesian coordinate system was fit to a volumetric interpolation function by linear interpolation using TriScatteredInterp. The coordinates of each candidate surface were transformed back into the original Cartesian 3-D system, and the interpolation was finally applied to find the value at each point on the surface.

While the the transformation matrix $\mathbf{T}$ allows the 2-D B-Mode, ARFI, and SWEI images to be projected into the 3-D heart, its inverse, $\mathbf{T}^{-1}$, can also be used to transform from the 3-D coordinate system onto the local coordinate system for each image. This was used to project the ablation lesion markers back onto the individual B-Modes for comparison with the ARFI and SWEI data on an image-by-image basis. The transformed sphere coordinates were used to find the pixels where each sphere intersected the imaging plane. Because the ablation markers are arbitrarily scaled, there was the possibility that images would intersect ablation without intersecting the actual sphere. To manage this, the sphere was not given a hard cutoff. Within 2 mm of the center of the sphere, B-mode pixels would be tinted red, but at ranges up to 6 mm from the sphere, a diminishing intensity of color was used to tint the B-mode, along with a shade representing distance Blue, and fully desaturated, is 6 mm from the center, while red and full saturation represents less than 2 mm. Intermediate colors are determined by the "jet" color map and a linear increase in

saturation.

7.3.4 Custom Beam Sequences

For the first animal, imaged for the original publication of this work, the following sequences were used: For both ARF excitations, 90 V_{pp}, 300-cycle, 6 MHz pulses were used, with foci selected between 10 and 20 mm, selected on an acquisition basis to intersect the myocardium. The 42° field of view was covered by 32 excitations for both ARFI and SWEI sequences. Both sequences imaged the tissue at each location at framerate of 16,000 fps for 3.0 ms, with the excitation at 0.5 ms. The difference between the ARFI and SWEI sequences is in the high-speed imaging of the tissue following excitation. For the ARFI sequences, a focused transmit beam was used, aligned with each excitation beam, and 8 parallel receive lines were beamformed within the lateral beamwidth of each excitation. This created a sector scan with 256 lateral lines. For the SWEI images, a spherical wave was transmitted, focused at the apex of the imaging plane. 32 parallel receive lines were beamformed, steered to each of the 32 excitation locations. The same receive lines were used for all excitations. This allowed the shear wave speed to be measured redundantly at each location and averaged. After the completion of the work in chapter 5, the sequences were redesigned to include more, tighter spaced, excitations, and to put the track beams only as far away from any push as the shear wave was expected to travel. These imaging sequences acquired ARFI, STL-SWEI and MTL-SWEI simultaneously. 50 pushes covered a 45° viewing angle, also using 90 V_{pp}, 300 cycles, and 6 MHz excitations. 21 beams were spaced around each push, at 0.9° spacing to match the push spacing. 3 ms were again used for the tracking duration at 16,000 fps and the push at 0.5 ms.

7.3.5 Shear Wave Speed Estimation

A phase-root seeking algorithm (Pesavento et al., 1999) was used to estimate axial tissue displacement, using a 5-λ kernel to calculate the motion between successive frames of the high frame-rate tracking. To create ARFI images, the progressive displacements were integrated after the excitation, and the maximum displacement in the first 10 samples (0.7 ms) was used as the ARFI displacement value. For the SWEI images, a third order Butterworth bandpass filter was applied to each 16 kHz velocity profile, with cutoffs at 50 Hz and 1 kHz. A directional filter (Deffieux et al., 2011) was then applied to each ensemble to remove reflections. The directional filter was applied in the lateral track location before computation of MTL-SWEI, and in the push dimension before computation of STL-SWEI. The time-to-peak velocity at each pixel for each excitation was then computed from the filtered data using quadratic subsample estimation. At each axial depth, arrival times were computed for each combination of excitation and track location. To estimate MTL-SWEI shear velocity, the slope of the arrival times was found by linear regression over 5 adjacent locations. For STL-SWEI, it was found by linear regression for each track line across the arrival time at 5 adjacent push locations. The slopes were inverted, and velocities averaged across the excitations (MTL-SWEI) or track beams (STL-SWEI) to obtain the final images.

7.4 Results

7.4.1 Initial In Vivo Scan

A render of the right atrial electroanatomical map from the first animal is shown in figure 7.2. Activation time is mapped to color, and shows a gradient, progressing from the SA node to the AV node. The black outlines of fan beams indicate the locations of the ARFI images for the pre-ablation scan. The SWI images, and the

corresponding post-ablation images, were taken from approximately the same positions and orientations. The red dots mark the locations of RF energy delivery, and the presumed sites of lesion formation.

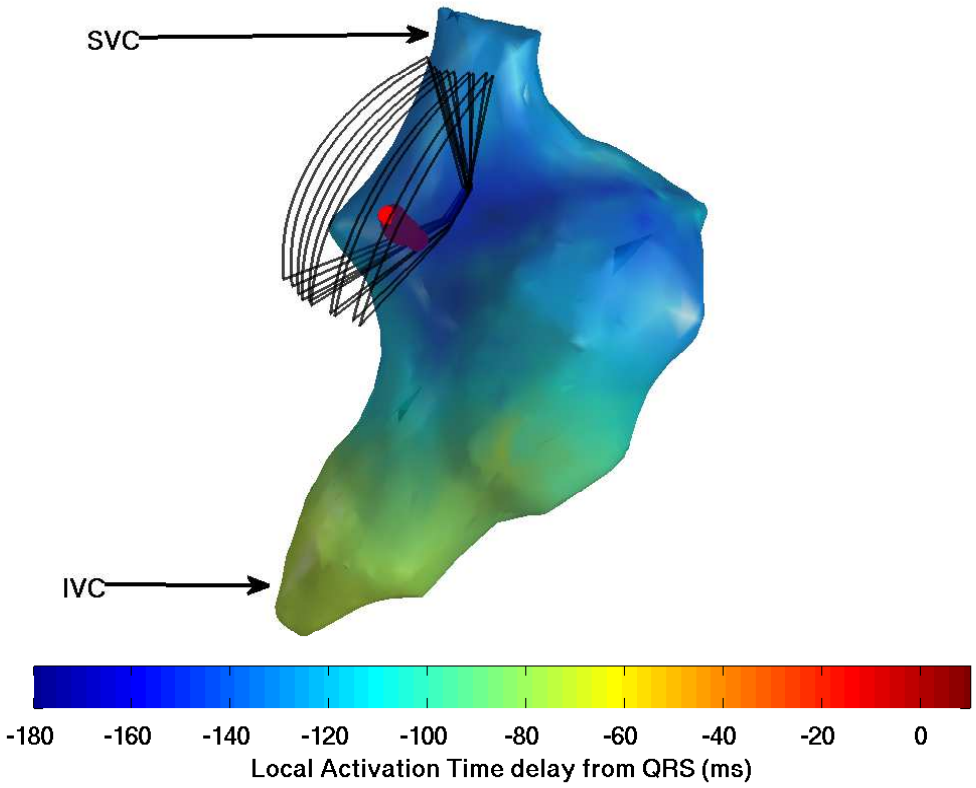

FIGURE 7.2: Render of local activation time (LAT) delay for the Right Atrium. The fan beams indicate the direction and orientation of the ARFI images, pre-ablation, and the red dots indicate the ablation sites.

Figure 7.3 shows the pre- and post-ablation ARFI images of the region surrounding the lesions. The left column (7.3(a,c,e)), show the pre-ablation scans, while the right column is the post-ablation scans. In 7.3(a), the individual ARFI images are shown registered in 3-D, segmented to remove signals from outside the myocardium, as well as regions of off-axis clutter from an adjacent pectinate muscle. In Figure 7.3(c), the images from (a) have been interpolated onto the endocardial

surface. In figure 7.3(e), many surfaces parallel to the endocardium have been generated. Masked by the extend of the myocardium, they cover the entire section of myocardium within the FOV. They are displayed as a stack of semitransparent slices. A region of low displacement is coincident with the ablation site markers, approximately 5-7 mm wide (compare to the 4 mm diameter spheres).

Figure 7.4 shows the before- and after-ablation SWEI images of that same region in figure 7.3. Regions of elevated velocity are present post-ablation in the areas of ablation, but the images are noisy, and of generally low quality.

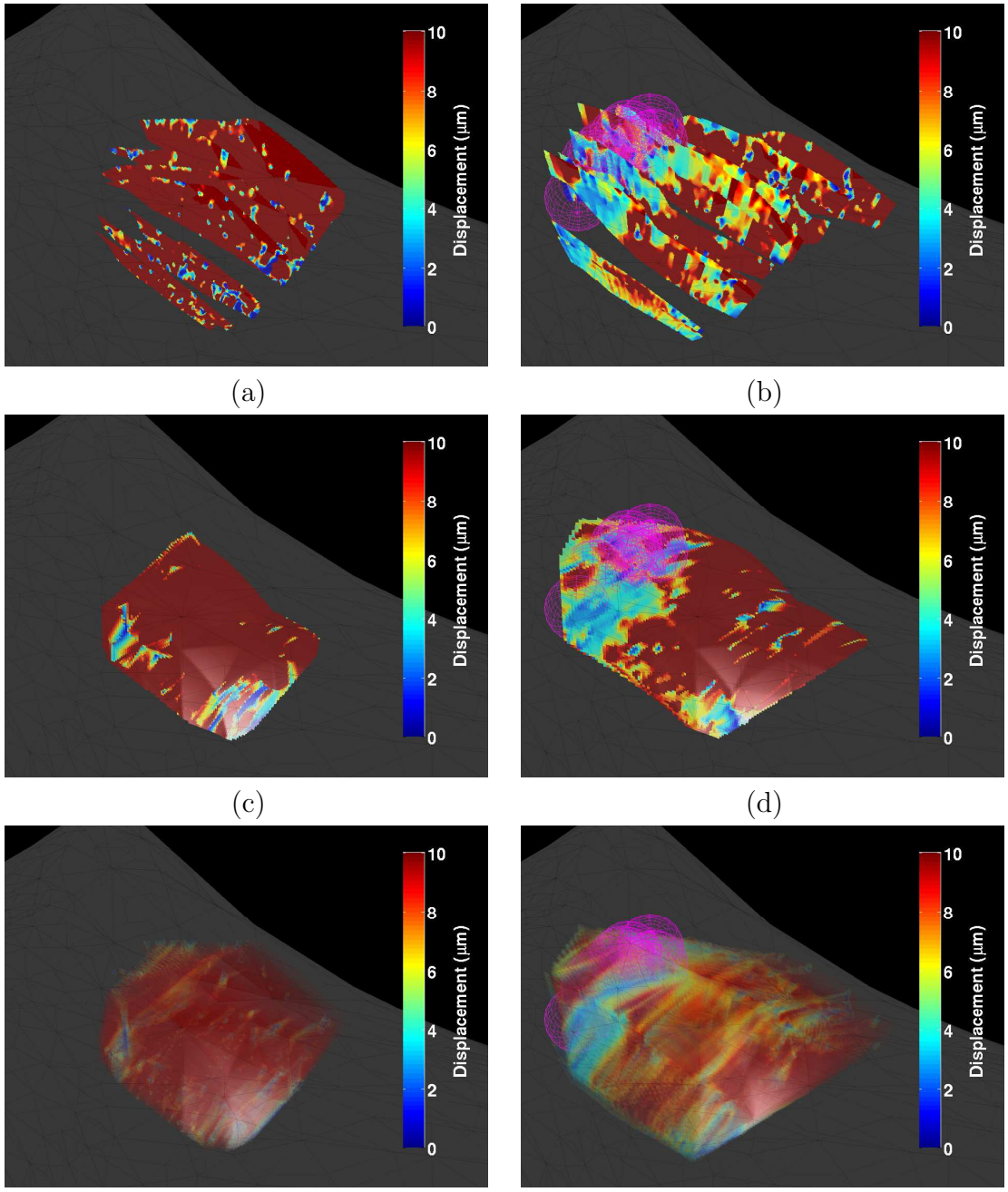

FIGURE 7.3: (a,b) Registered 3-D ARFI images, masked by the myocardium, before and after ablation. (c,d) ARFI interpolated onto the endocardial surface, before and after ablation. (e,f) Interpolated myocardial volume, before and after ablation. The ablation sites are marked by magenta spheres.

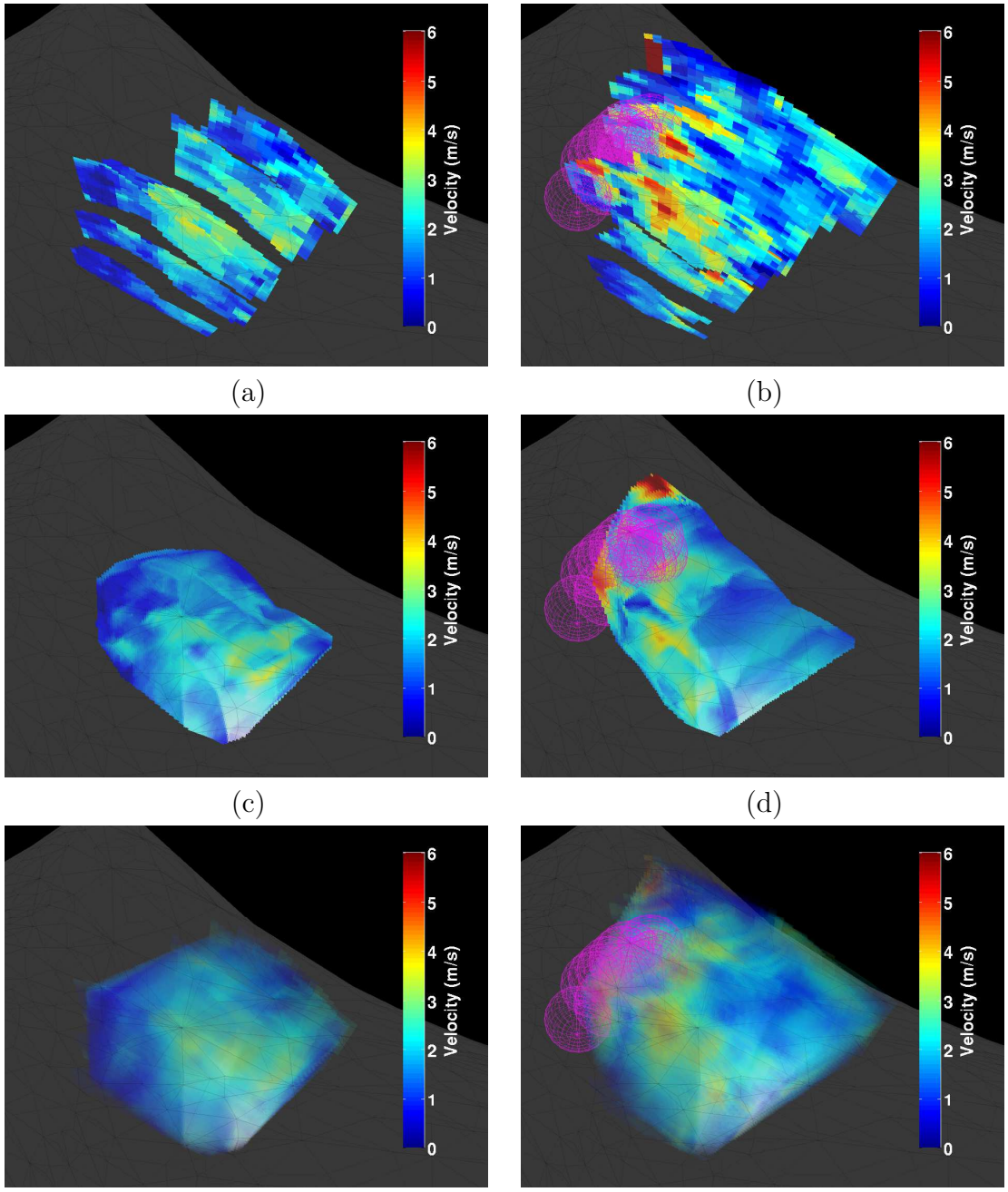

FIGURE 7.4: (a,b) Registered 3-D SWEI images, masked by the myocardium, before and after ablation. (c,d) SWEI interpolated onto the endocardial surface, before and after ablation. (e,f) Interpolated myocardial volume, before and after ablation. The ablation sites are marked by magenta spheres.

7.4.2 Control Right Atrial Wall

Figure 7.5 shows the B-Mode, ARFI, MTL-SWEI and STL-SWEI images from the new imaging, from the second animal. The frames shown were used to make the volume reconstruction shown in figure 7.7. Each column shows a different mode and each row shows a different data set. The myocardium retains a uniform appearance across the 56° elevational field of view, with B-Mode brightness being on average 0.31±0.16, ARFI displacements 4.07±3.60 μm, MTL-SWEI 2.90±1.16 m/s and STL-SWEI 2.86±1.17 m/s. ARFI images have the greatest heterogeneity in these scans, and STL-SWEI and MTL-SWEI agree almost perfectly.

Figure 7.6 shows the images from figure 7.5, mapped onto the anatomical mesh from the CARTO data. Each column shows different camera positions in 60° increments. The small B-Mode images at the top serve a visual aid for following the camera's orbit. Figure 7.7 shows the same data, rendered as a semitransparent volume at the endocardial surface, extending 3 mm through the myocardium. The tissue appears homogeneous in ARFI, STL-SWEI and MTL-SWEI images and volumes.

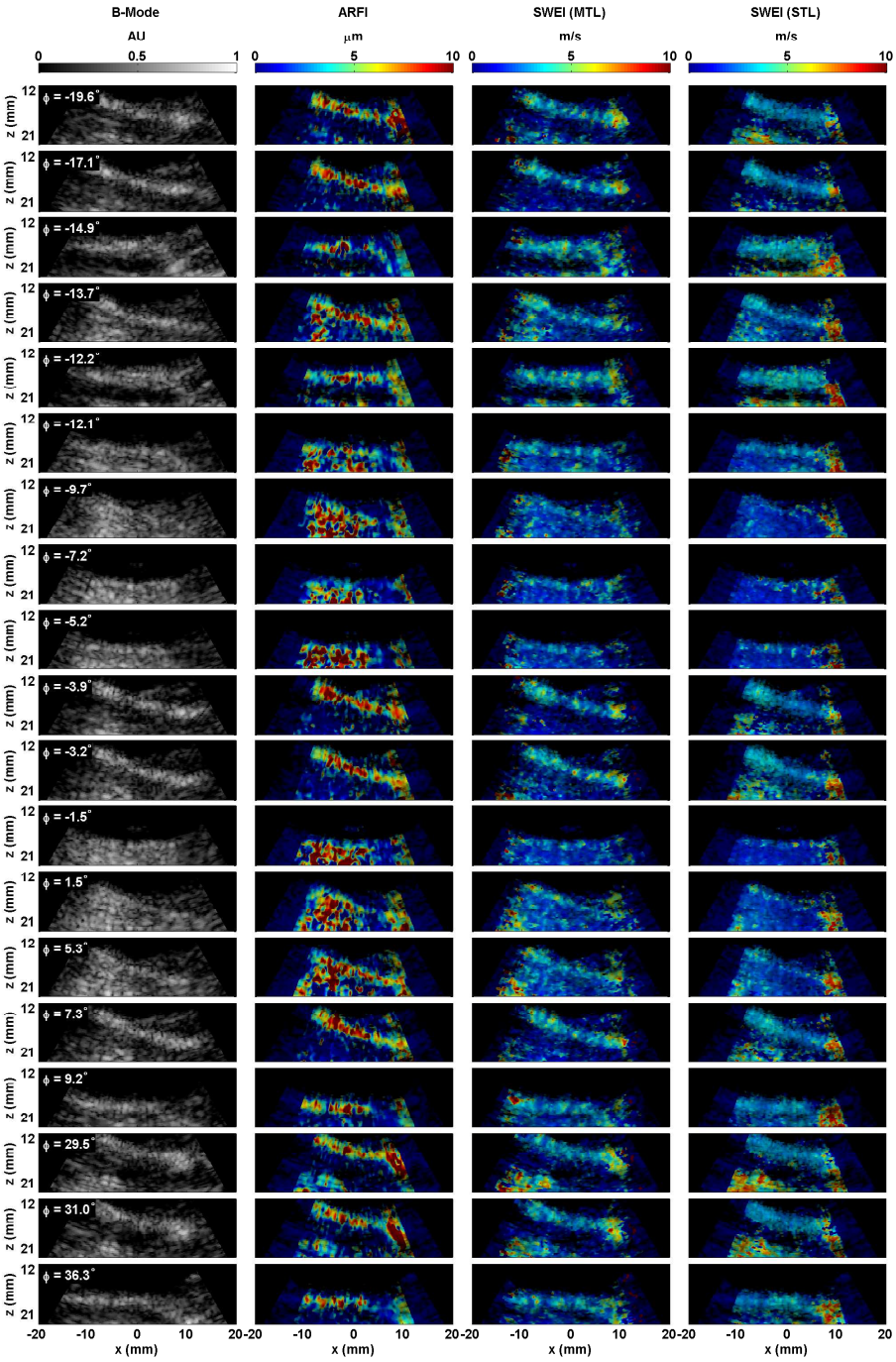

FIGURE 7.5: All of the B-Mode, ARFI, MTL-SWEI and STL-SWEI image slices used for volume reconstruction from the second animal. The square root of the B-Mode brightness is used as the transparency map for the elasticity images.

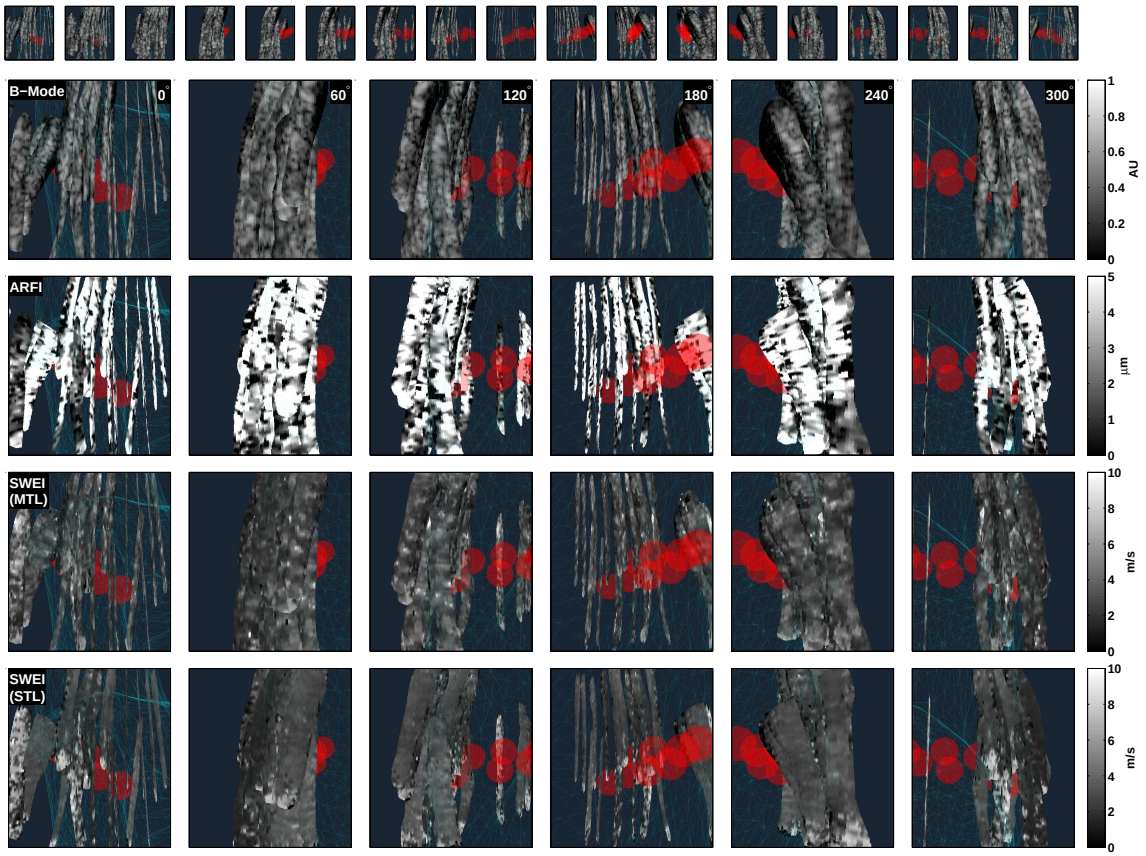

FIGURE 7.6: Rendered B-Mode, ARFI, MTL-SWEI and STL-SWEI slices in a section of myocardium prior to ablation in the second animal. There are gaps in the data, especially visible in the last column. Little variation in the signal or shear wave speeds is seen across the scanned region. This region of tissue was identified as a good target for ablation imaging. The ablations were supposed to be placed at the red dots, but a malfunction of the ablation equipment caused no RF energy to be delivered, despite the 3-D anatomical markers being placed by the CARTO.

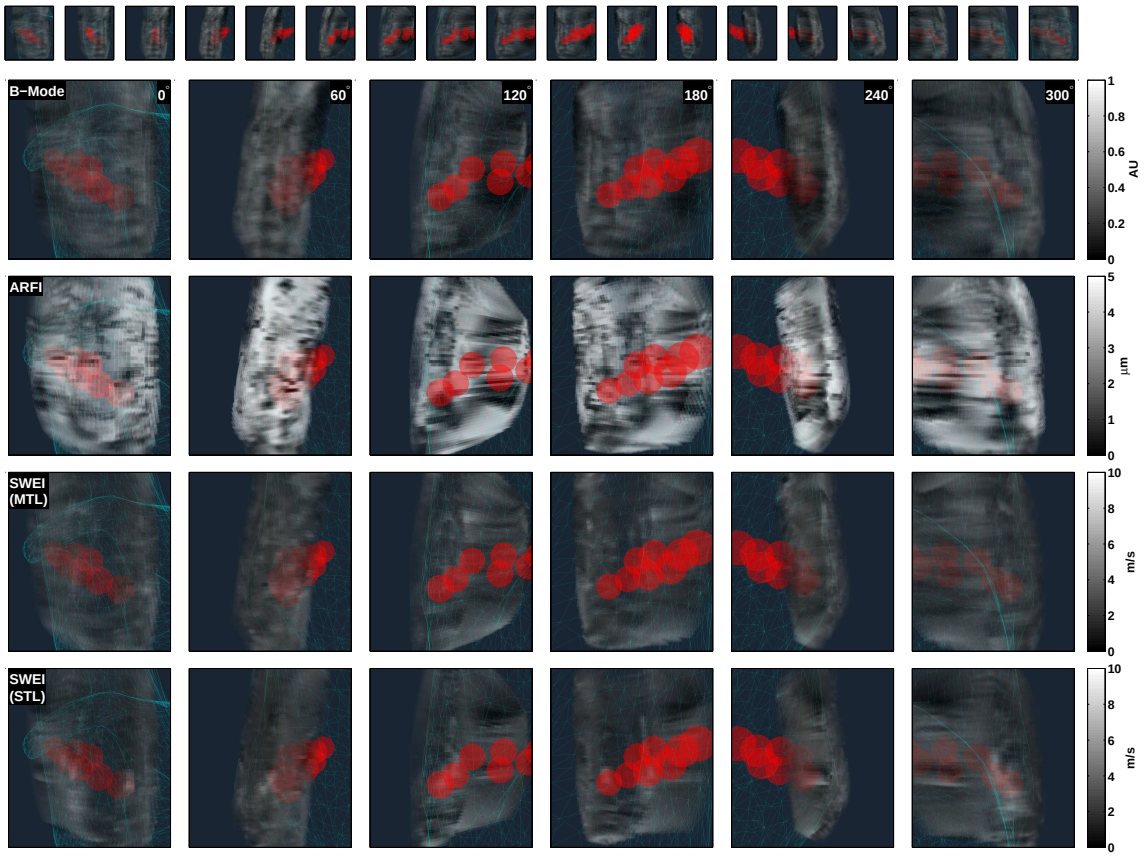

FIGURE 7.7: Rendered volumes made from the data in figure 7.6, extending 3 mm into the myocardium. Smearing is seen where there is a gap in the elevational field of view, particularly visible in the third, fourth, and last columns. Otherwise,

7.4.3 Distributed Ablation

Figures 7.8 and 7.9 show the data from the third animal, from different camera positions in 60° increments, before and after ablation. Again, the small B-modes at the top are a visual aid for following the camera's orbit. Figure 7.8 shows the baseline images, and figure 7.9 shows the post-ablation images. From these renders, it can be seen that the displacements in the center of the imaging field are reduced following ablation, and that the overall brightness of the SWEI images increases with ablation, indicating increased shear wave speed.

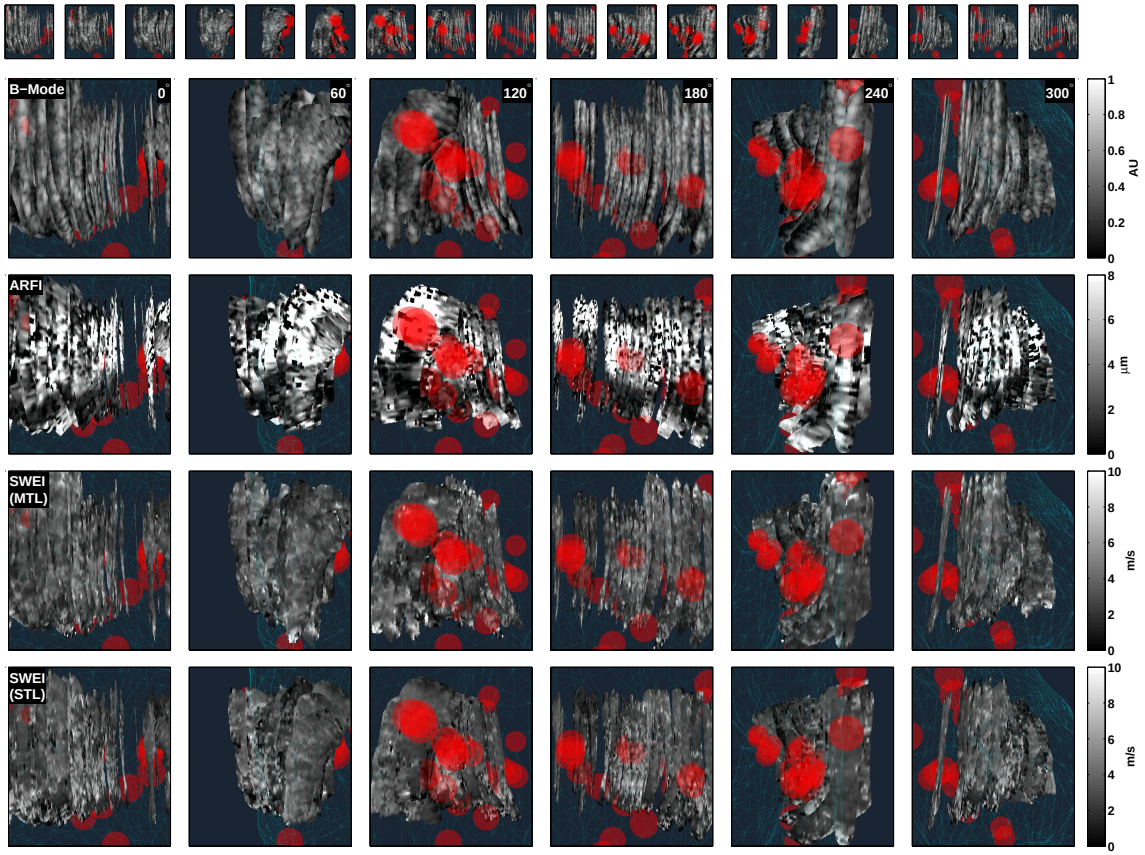

FIGURE 7.8: Rendered slices in the right atrium prior to ablation in the third animal, at 60° camera angles.

Figures 7.8 and 7.11 show the same data as figures 7.8 and 7.9, but interpolated into a semitransparent volume. Significant smearing is seen between the elevational

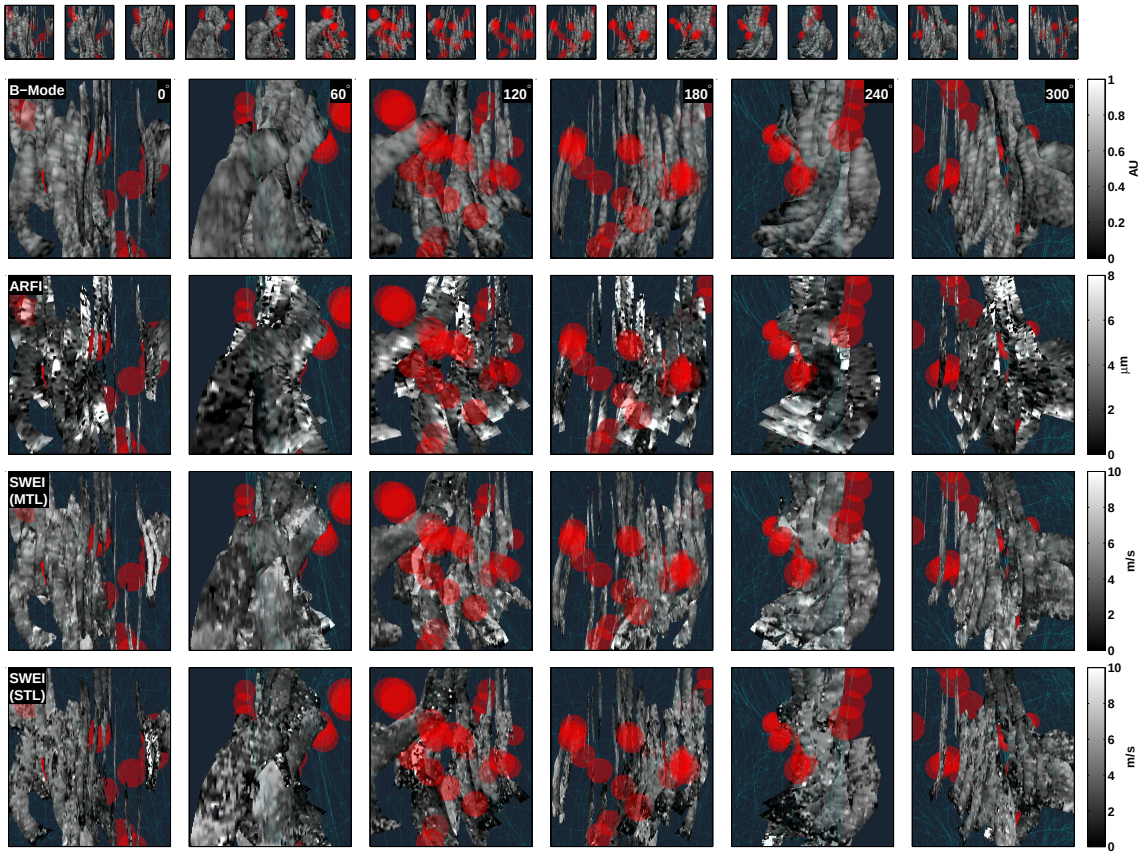

FIGURE 7.9: Rendered slices in the right atrium after ablation in the third animal, at 60° camera angles.

slices, and defined ablation structures are not visible within each volume.

Figure 7.12 shows a set of images with the position of the ablation site reverse transformed into the imaging plane. Red regions indicate intersection with the 2 mm radius sphere, and the color gradient beyond indicates proximity up to 4 mm from the edge of the sphere.

Figure 7.13 shows the same set of images, but following ablation. A region of suppressed ARFI displacement and elevated shear wave speed is seen in the area around the ablation site.

Figure 7.14 shows a photograph taken after *ex vivo* TTC staining of the right atrial wall. The ablation pattern is not a single line, but rather a series of spots

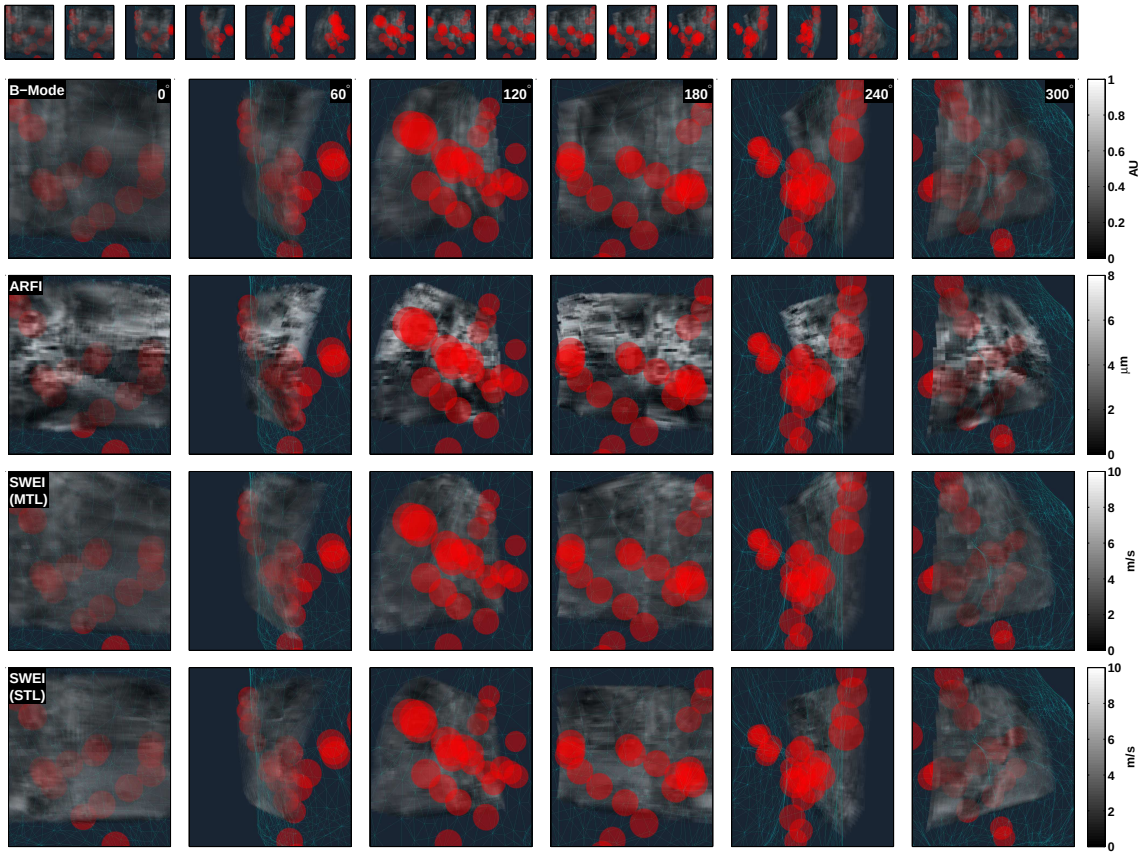

FIGURE 7.10: Rendered volume in the right atrium prior to ablation, at 60° camera angles. Heterogeneity is seen in the ARFI volumes, while the MTL- and STL-SWEI volumes show uniform stiffness over the imaging field of view.

distributed over a large section of the wall. This corresponds to the pattern of markers recorded in the CARTO.

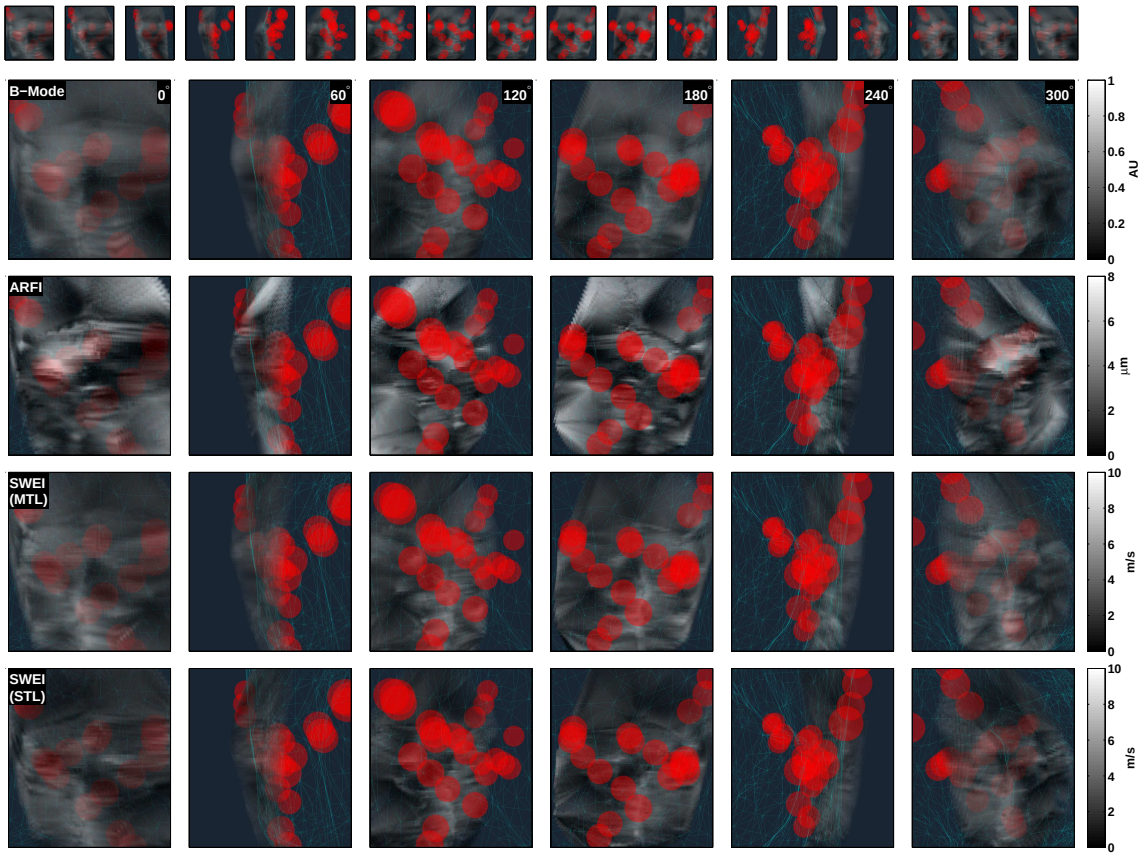

FIGURE 7.11: Rendered volume in the right atrium following ablation, at 60° camera angles.The ARFI image appears more heterogeneous, although identification of the darkened region in the center is obscured by inter-frame smearing. The MTL- and STL-SWEI images show a moderate increase in stiffness distributed throughout the field of view.

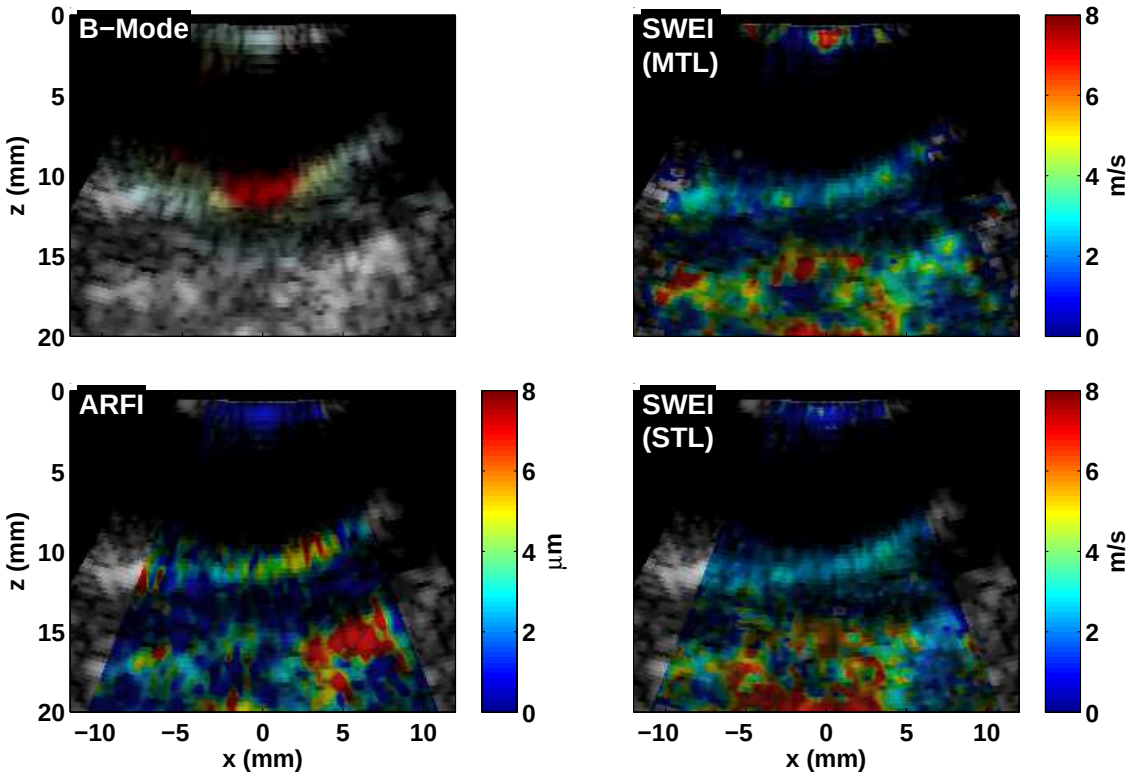

FIGURE 7.12: B-Mode, ARFI, MTL-SWEI and STL-SWEI images of the right atrium in the third animal prior to ablation. The red dot on the B-Mode indicates where the ablation was placed after these images were taken. The shear wave speeds appear uniform, but the ARFI image shows heterogeneity.

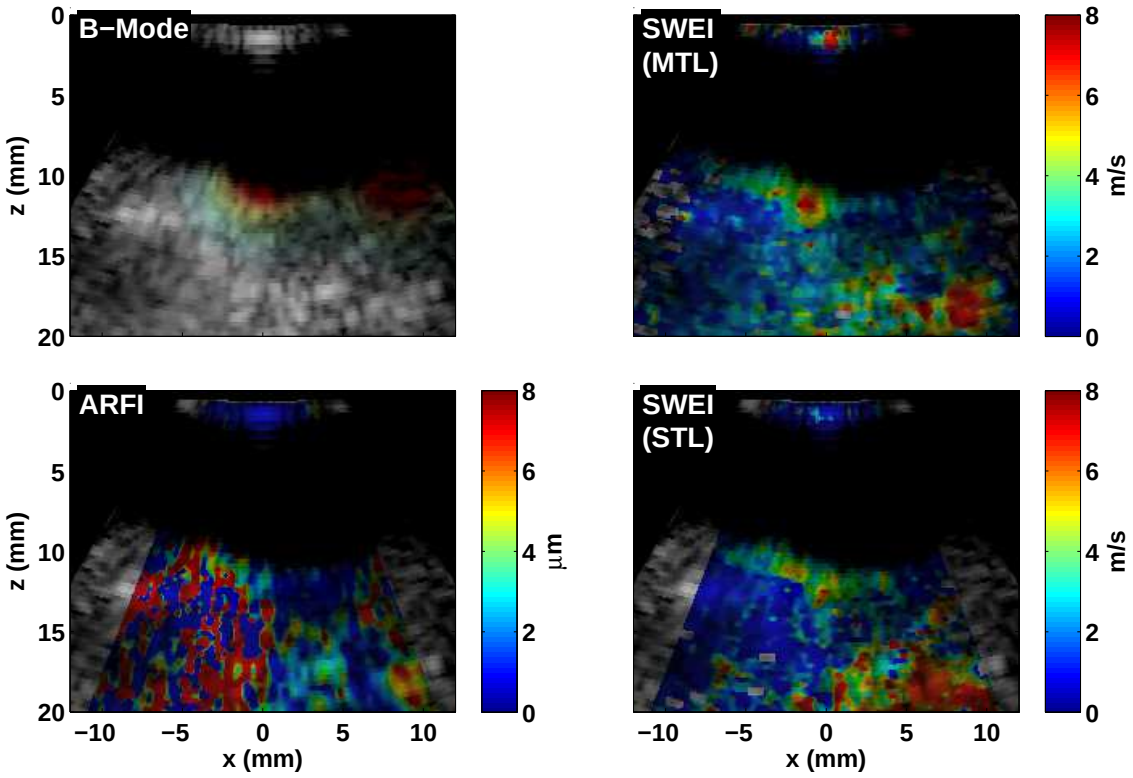

FIGURE 7.13: B-Mode, ARFI, MTL-SWEI and STL-SWEI images of the right atrium in the third animal after ablation. The red mark on the B-mode indicates the ablation site, transformed from the 3-D data. Lowered displacements are seen close to the lesion location, between -3 mm and 6 mm laterally. ARFI and SWEI disagree on the right boundary of the lesion. This set of images shows the same location as the set shown in figure 7.12

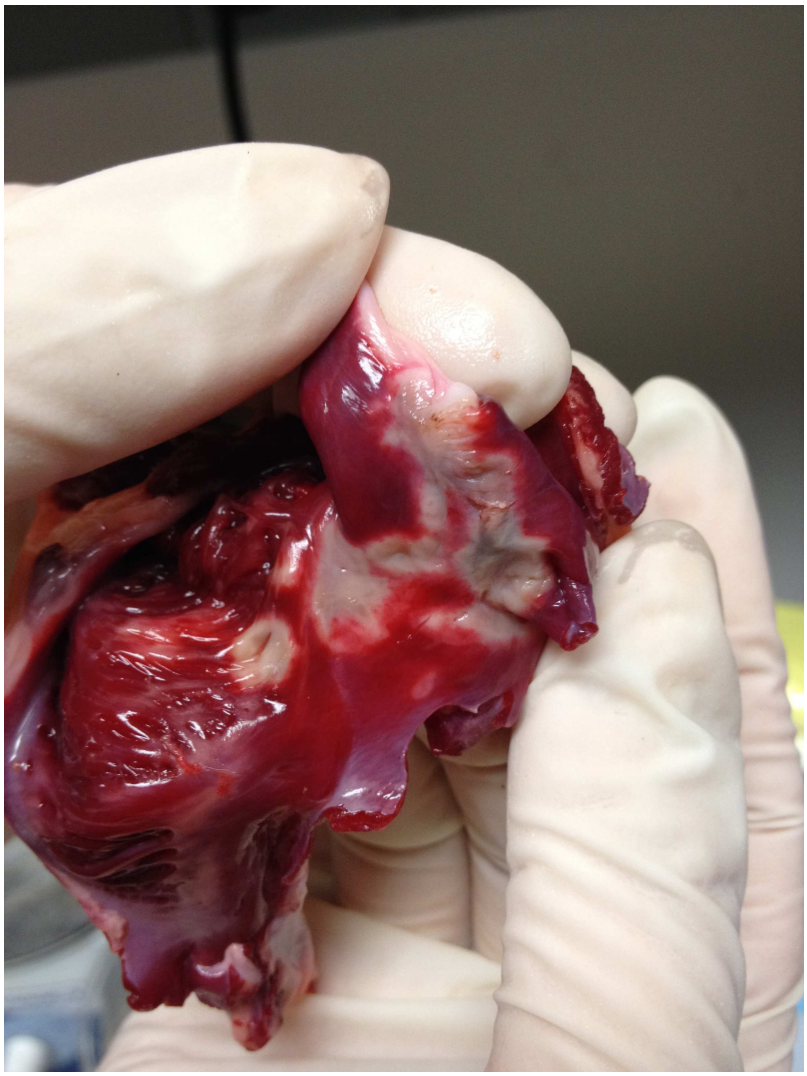

FIGURE 7.14: Photograph of TTC-Stained ablated myocardium from the third animal. The ablations do not form a single contiguous line.

7.4.4 Focal Ablation

Figures 7.15 and 7.16 show the B-Mode, ARFI, MTL-SWEI and STL-SWEI images from the fourth animal, segmented to match the tissue region in each image, and registered to the 3-D anatomical mesh. Figure 7.15 shows mis-registration between the position of the myocardium in the images and the endocardial surface on the EAM. Otherwise, the baseline images show uniform, though noisy, ARFI displacements. The MTL-SWEI images indicate low shear wave speeds though the regions intersecting the tissue. The STL-images have more variance. Following ablation, a focal spot of reduced displacement is visible in the ARFI images (see the right side of the 0° ARFI figures). The same edge of the field of view was not covered by the baseline sweep, though, so confirmation of homogeneity prior to ablation in the baseline images is not possible. In the MTL- and STL-Images, a bright spot is seen in the same location, while the regions away from the ablations show smooth, characteristically low velocities.

Figures 7.15 and 7.18 show the same data as figures 7.15 and 7.16, but interpolated onto a semitransparent volume. The baseline volumes fail to render correctly because the registered images do not intersect the endocardium. Only a small region of the interpolated surfaces falls within the region covered by the data.

Figure 7.19 shows a set of images prior to ablation with a marker on the B-Mode indicating the location to be ablated, taken from the CARTO data. The tissue appears uniform in all imaging modes.

Figure 7.20 shows the set of images after ablation, taken at a similar view to those in figure 7.19. Decreased displacement magnitude and increased shear wave speeds are seen in the regions around the marked ablation site.

Figure 7.21 shows a photograph taken after *ex vivo* TTC staining of the right atrial wall. This time, the ablations form a line on the lateral wall of the RA,

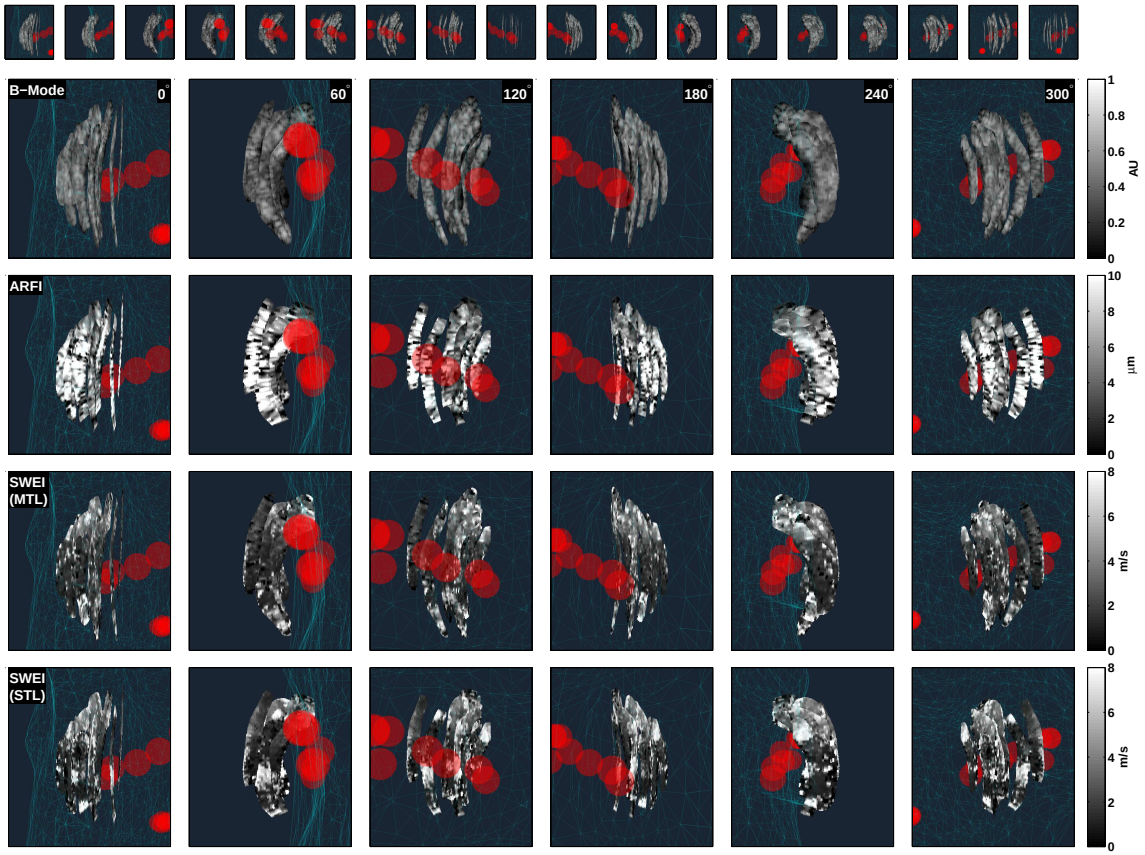

FIGURE 7.15: Rendered slices in the right atrium prior to ablation in the fourth animal, at 60° camera angles. Significant mis-registration between the registered slices and the endocardial surface is observed. Uniform displacement magnitude is seen across the myocardium along with low shear wave speeds in MTL-SWEI and STL-SWEI. The SWEI images show heterogeneity.

corresponding to the pattern of markers recorded in the CARTO.

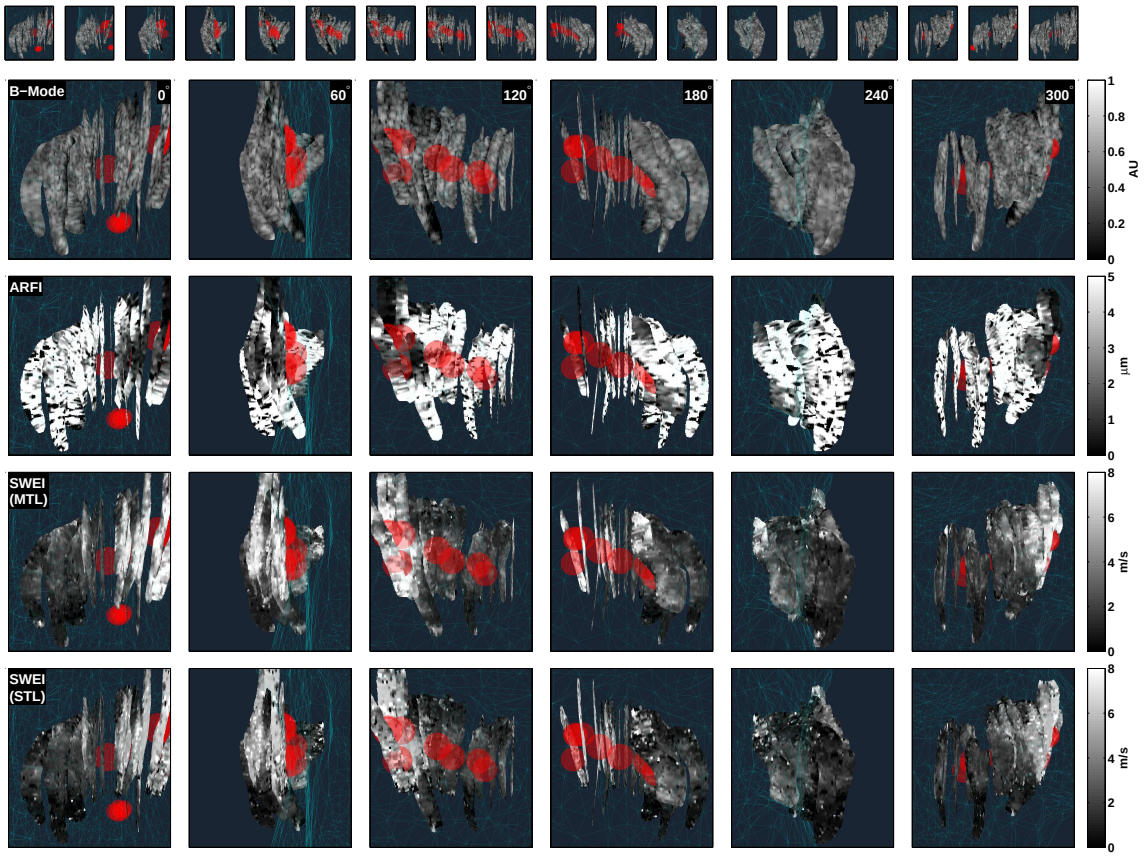

FIGURE 7.16: Rendered slices in the right atrium after ablation in the fourth animal, at 60° camera angles. A region of increased stiffness is clearly visible in the ARFI displacements and shear wave speeds, aligned with the expected ablation sites.

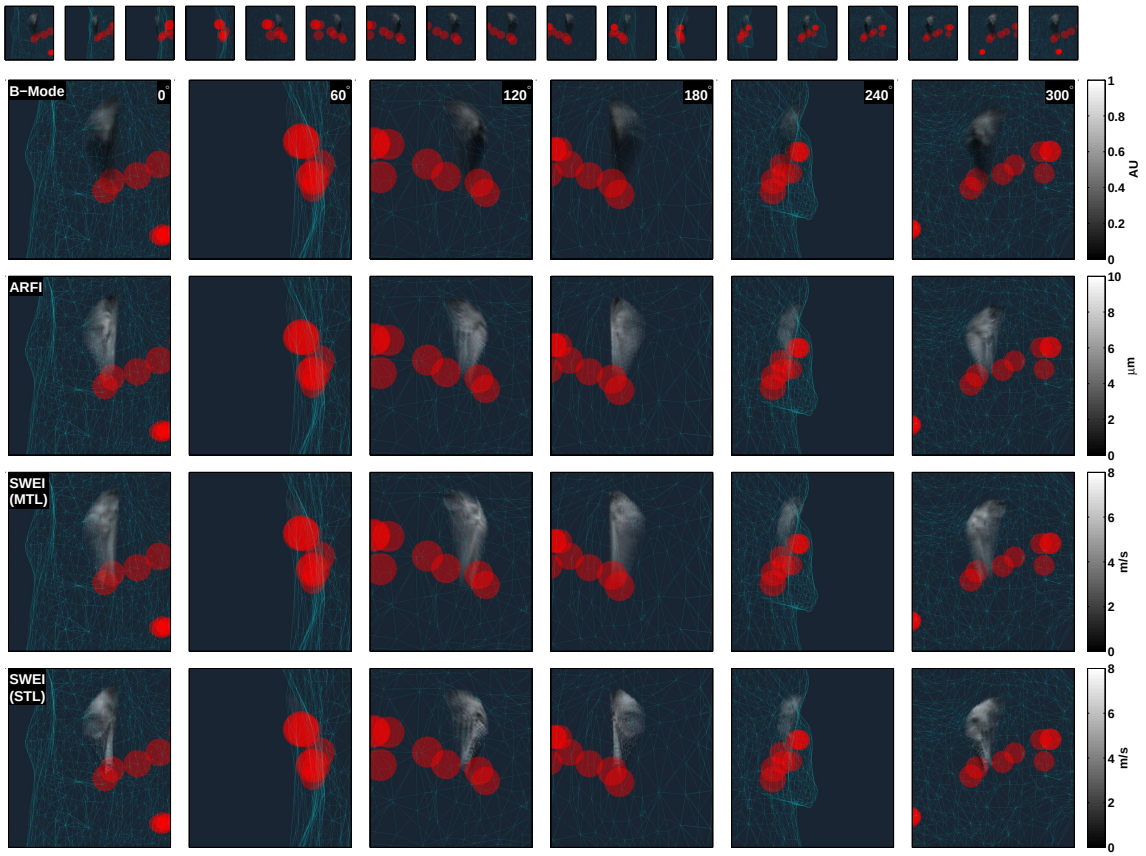

FIGURE 7.17: Rendered volume before ablation in the fourth animal. The misregistration between the images and the anatomical mesh limits the reconstructable region.

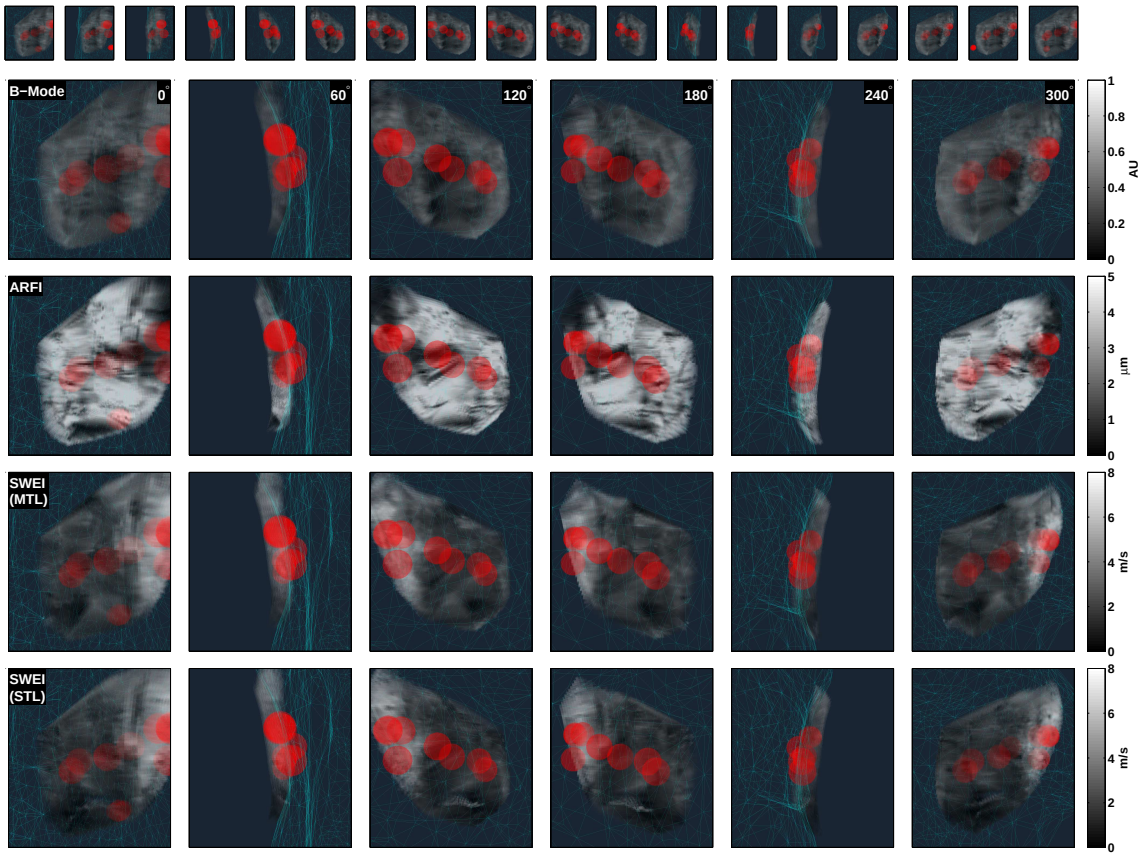

FIGURE 7.18: Rendered volume after ablation in the fourth animal. The ARFI volume shows a line of decreased displacement along the ablation lesion markers, and the MTL-SWEI and STL-SWEI images show increased shear velocities along the ablation. A large, stiff region is visible on the edge of the field of view.

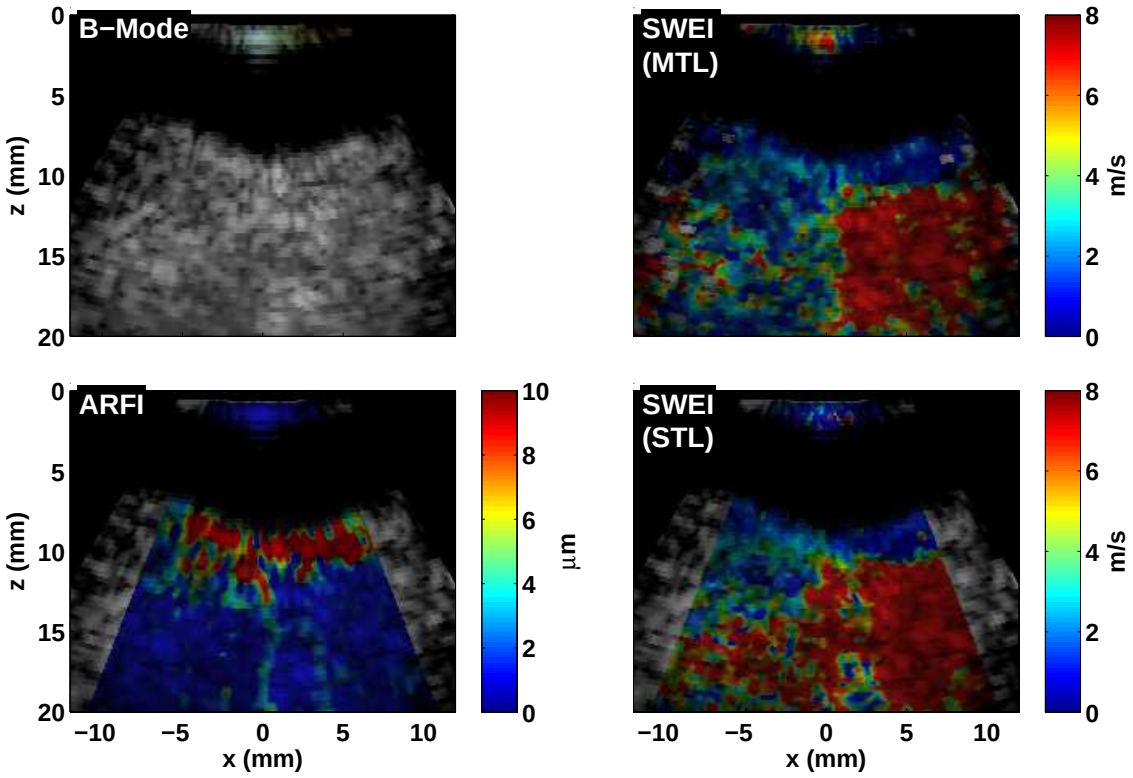

FIGURE 7.19: B-Mode, ARFI, MTL-SWEI and STL-SWEI images from the fourth animal, taken prior to ablation. The myocardium is only the first 1 mm of tissue beyond the endocardial border. The red mark on the B-Mode indicates where a lesion was later placed. The myocardium is uniform in all modalities. Signals beyond the first millimeter through the tissue are noise associated with reflections.

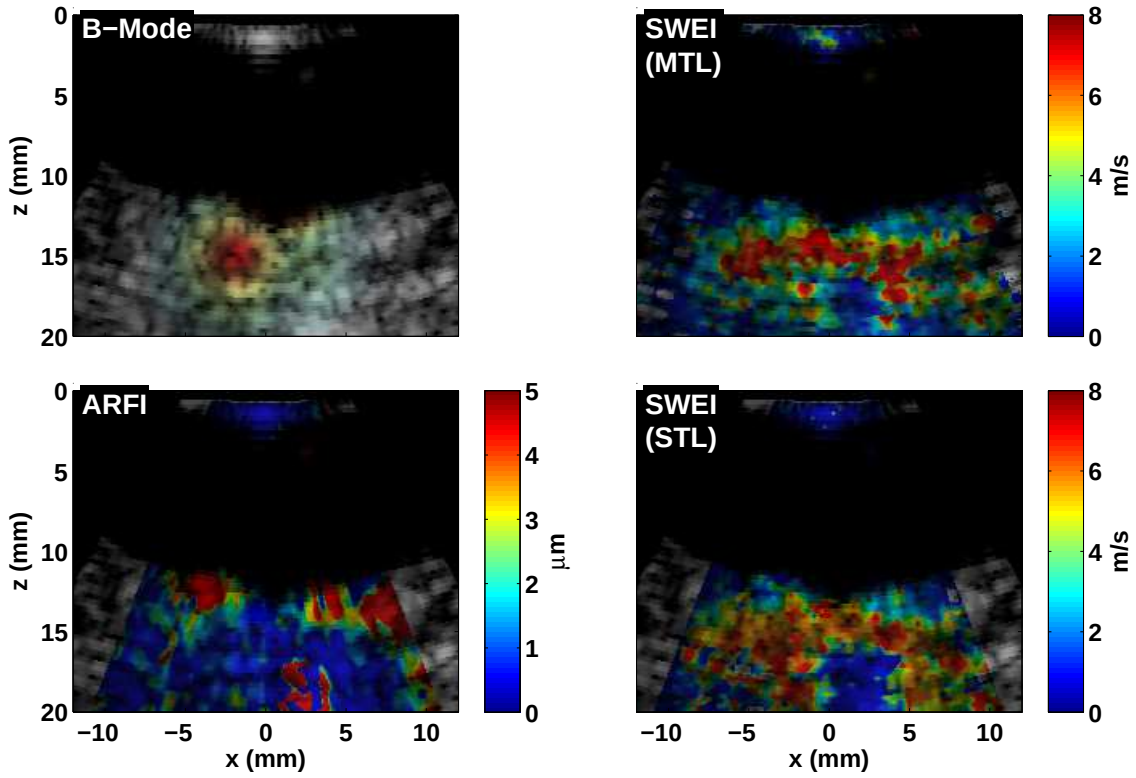

FIGURE 7.20: B-Mode, ARFI, MTL-SWEI and STL-SWEI images from the fourth animal, taken after ablation in approximately the same location as figure 7.19. The myocardium is only the first 1 mm of tissue beyond the endocardial border, and signals beyond that depth are outside of the tissue and associated with reflections. The lesion is visible in the ARFI as reduced displacement, and in the MTL-SWEI and STL-SWEI as increased shear wave speed.

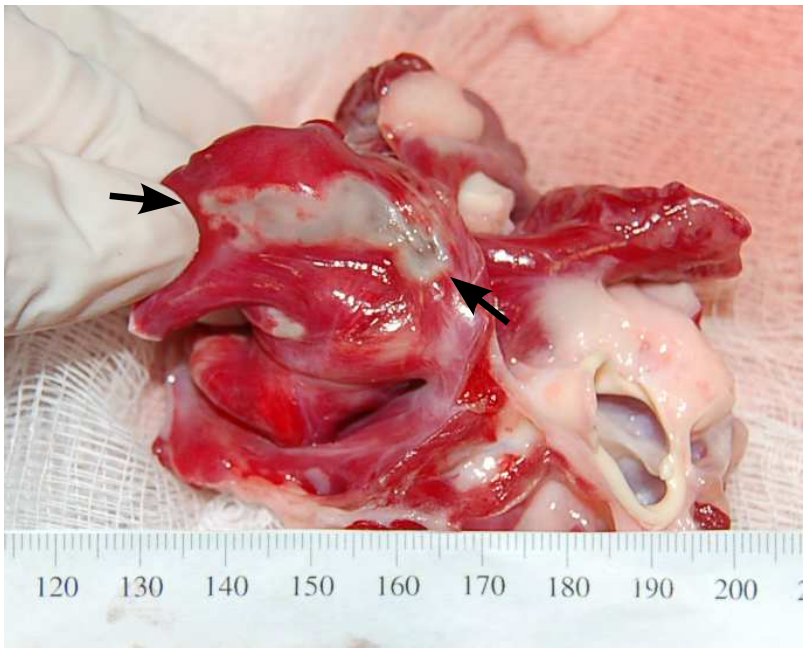

FIGURE 7.21: Photograph of TTC-Stained ablated myocardium from the fourth animal. The ablations form a single, contiguous line.

7.5 Discussion

The 3-D registration of the ARFI and SWEI images was readily performed with the saved transformations for the matched B-Mode frames. A number of factors prevented these 3-D reconstruction from achieving the image quality obtained in the *ex vivo* scans, despite using the same imaging sequences. Primarily, these were due to transducer and tissue motion, though each of the four studies discussed here faced unique challenges.

7.5.1 Initial In Vivo Results

On the first experiment, the CARTO was dialed only to the matching part of the cardiac cycle as the acquisition was triggered to, but not necessarily the same beat. Respiration was held during acquisition so gross motion from beat to beat was expected to be minimal, but misregistration was unable to be controlled for. The ARFI images were of much higher quality that the MTL-SWEI images, and as a result, the interpolated surface and volume show much greater contrast and contiguity that than the SWEI counterparts, clearly showing the 5-7 mm-wide ablation line. The SWEI sequences were able to generate shear waves in the unablated myocardium, but within the ablation, the shear waves were difficult to distinguish from background noise, which made the MTL-SWEI images correspondingly noisy. The cross correlation coefficients of the aligned slow-time displacement traces could be used to exclude these velocity estimates, but this would have completely excluded the lesion area. The first study thus favored ARFI over MTL-SWEI for imaging RFA lesions.

7.5.2 Control Right Atrial Wall

The images reconstructed of the right atrial wall (figure 7.5) show good consistency across a variety of steering angles. The shear wave velocities in both STL-SWEI and MTL-SWEI remain low across the field of view 2.86 and 2.9 m/s, respectively,

and the ARFI displacements are around 4 μm, but with much greater variability, likely due to the previously discussed effects of transducer kickback. The right side of all images shows a characteristic kickback artifact, with erroneously elevated displacements and velocities. This artifact appears on the right side of images since images are acquired left-to-right, and the most kickback has accrued at the end of the scan. Unfortunately, the red markers in figures 7.6 and 7.7, which were the sites where ablations were supposed to be applied, were not ablated due to an equipment malfunction. This failure was observed *in vivo* by our imaging system and by other researchers using different ARFI sequences, and was confirmed following the study with *ex vivo* TTC staining of the chamber of interest. This is especially unfortunate since the reconstructed slices and volumes show excellent uniformity in all of the imaging modalities, and are sampled finely in elevation. There are still gaps in elevation due to rejected frames corrupted by kickback, but overall this was the most uniform scan we were able to record.

7.5.3 Distributed Ablation

In the third animal, we also were able to create smooth pre-ablation scans, with fine sampling in elevation. The ARFI images show angular sensitivity effect, but otherwise, the images agreed across of a variety of steering angles (figures 7.8 and 7.10). Looking at the red dots, however, we were unsuccessful in creating a focal ablation line. Correspondingly, the suppression of ARFI displacements and elevation of shear wave speeds occurs heterogeneously, and without clear structure. The distributed shape of the ablation was also confirmed with *ex vivo* TTC staining (figure 7.14). It is difficult to say whether or not the imaging system accurately characterized the ablation distribution with the ablation point markers spread all over the place, but the images did show spots of varied stiffness, which is what was actually ablated, even if a matched comparison was not possible.

7.5.4 Focal Ablation

In the fourth animal, we finally were able to both create and image a focal ablation line. The post-ablation images and volume (figures 7.16 and 7.18) show a darkened region in the ARFI images and a bright region in the SWEI images that correspond to the markers for ablation placement. The reverse transformation images (figures 7.19 and 7.20) show in more detail that the ablation line ran down the center of the imaging plane. However, the pre-ablation scans (figure 7.16) did not spatially register to the myocardial surface indicated by the CARTO, possibly due to an offset in ECG triggering between data acquisition and the trigger that the CARTO system uses to build it's maps (it shows a static triggered volume, though the heart is in constant, repetitive motion). This affected the reconstructed volume, which was defined relative to the CARTO's endocardial mesh surface, and resulted in the cropped volume shown in figure 7.18. *Ex vivo* TTC-staining confirmed the creation of the focal ablation (figure 7.21), although the ARFI methods showed preferential contrast at one end of the line. It is unclear if this was an imaging angle effect, or an actual area of especially stiff tissue, though we are inclined to lean towards the latter.

7.6 Conclusion

Using the 3-D positioning data saved in the CARTO3 EAM system, we were able to register the ARFI and SWEI images in 3-D relative to the electroanatomical map, as well as transform 3-D markers from the CARTO system back into the individual images. Using 3-D linear interpolation, we combined series of planar images into volumes that show the distribution of elasticity throughout the myocardium. Although hindered by sampling, motion, and challenging ablations, the reconstructed volumes showed elasticity maps that agreed with eithe

8

Conclusions and Outlook

8.1 System and Experimental Limitations

Two primary limitations prevented the *in vivo* 3-D images in chapter 7 from obtaining the image quality seen in the *ex vivo* preparations of chapter 6.

Cardiac motion and Transducer Kickback

The first limiting factor is related to the motion of the heart and SoundStar relative to one another. Cardiac motion is large, but relatively low frequency on the time scale of an ARFI push-track ensemble. As such, it can generally be removed by the use of an extrapolation or interpolation motion filter, using data from before the push, or long after the push. A first order extrapolation filter or second order interpolation filter are often sufficient, depending on the amount of tissue acceleration. Motion filtering enables improved detection of arrival times and benefits SWEI images, but also is critical to separate the induced ARFI displacement from background motion. Residual or incompletely filtered motion creates errors in ARFI displacement estimates, which can be large for motion profiles that poorly fit the chosen filter model. A more challenging source or noise specific to the SoundStar and AcuNav is the

problem of transducer kickback. When an ARFI push is delivered by the transducer to the tissue, the transducer itself experiences radiation force and recoils away from the tissue. This is suppressed when the catheter tip is fixed, such as in the *ex vivo* scans, but *in vivo*, depending on the curvature of the catheter or the presence of a sheath, the kickback may be very small or very large. The kickback manifests as both a transient displacement after each push that lasts only a few milliseconds (like an ARFI displacement) as well as a slower build-up over multiple pushes that creates large, slow motion of the catheter. The second type behaves like tissue motion and can be filtered, but the transient kickback is linked to the radiation force push, and cannot be filtered by extrapolation or interpolation. Instead, because the kickback is the motion of the transducer, it can be estimated from the motion common to all lateral positions and depth. However, subtracting the kickback motion adds a second source of residual error to ARFI estimates. Furthermore, when imaging the atria, there is often little tissue area in the image that isn't being excited from which to make the estimate.

Acquisition Time and Data Volume

The other challenge unique to the *in vivo* experiments is the interface with the CARTO system. Because the system only saves clips on demand, we could not automatically trigger the CARTO system to record the position of the SoundStar. As a result, one of the operators had to dial in the CARTO to the correct frame in each three second clip before the next point could be acquired. The operator of the catheter could begin steering as soon as the first dataset was acquired, but the CARTO system does not show live positioning while the frame was being adjusted and saved, so acquisition of the next point had to wait for the CARTO operator. Because each acquisition was done with respiration held, only one or two points could be taken per breath hold. While respiration motion is cyclic and repeatable, on the

scale over which we want to reconstruct volumes, this can create misregistration artifacts. Furthermore, because the CARTO could only save 100 clips, and clips could not be deleted, there was a hard limit on elevational sampling.

8.2 The Importance of 3-D Position Tracking

Chapters 3 and 4, although they demonstrated that cardiac elasticity dynamics could be imaged with ARFI methods, also highlighted the need for 3-D position tracking. Even if ARFI and SWEI images were processed in real-time, the acquisition time to build each type of image would limit the frame rate. Future scanners may be able to continuously acquire ARFI data and beamform both live B-mode and elasticity information, perhaps displaying a B-Mode image colored by elasticity estimates, but such technology is beyond the capabilities as well as safety limits of our current technology. Without high framerate, real-time imaging, registration to anatomical landmarks of interest is necessary, since the field of view for the intracardiac array is so small. More advanced transducers may have better fields of view, but the 3-D tracking afforded by the system described in chapter 7 allowed us to stitch many small field-of-view images into a larger volume, as well as register our images to the ablation sites. While a more streamlined process of recording the 3-D data would enable wider field-of-view and more densely sampled volumes,

8.3 STL-SWEI: Speckle-free SWEI

Perhaps the greatest contribution to the field of acoustic radiation force impulse elasticity imaging in this work is the description and analysis of Single-Track-Location Shear Wave Elasticity Imaging (STL-SWEI). This variant of SWEI has the potential to break the speckle resolution limit of MTL-SWEI, and enable micro-elasticity (μ-E) imaging. The speckle-bias cancellation of using push beam separation instead of track beam separation for shear wave estimation is not new, but understanding

the reciprocity between MTL-SWEI and STL-SWEI imaging allowed us to apply our state of the art processing (direction filters, arrival time estimators, moving linear regressions etc.) to the STL-SWEI data. The sequences were carefully designed so that we could obtain precisely-matched MTL-SWEI data, which allowed for direct comparison and observation of just how "speckle-free" STL-SWEI is. Furthermore, the corrections outlined in appendix B allow us to eliminate what had been seen previously as a push beamwidth limitation. Precise border definition was shown possible even with 75% overlapping push beams and 0.15 mm beam spacing, although more work will be required to determine what the ultimate limit of resolution is, and what effects frequency and focusing have on STL-SWEI image metrics. The next step for this work and for μ-E in general will be to construct sequences that can acquire very tightly-sampled STL-SWEI images within whatever acquisition time is acceptable for *in vivo* use. This was already done in the context of ICE ARFI in chapters 6-7, under the constraints of diastolic imaging and scanner digitization limits, although the sequences ultimately couldn't have the push beam density to realize the potential resolution gains. More creative approaches, such as multiple, simultaneous pushes may enable the sort of framerates necessary for significantly improving ICE SWEI, but even in its current realization, STL-SWEI provides an often-less-noisy alternative to conventional MTL-SWEI, and was able to make some excellent 3-D reconstructions, particularly figure 6.15, which really shows what sort of imaging is possible with and ICE ARFI and STL-SWEI.

8.4 Electrical Activity and Elasticity: The Next Critical Component

While the results presented here provide convincing evidence that ARFI and SWEI methods can be successfully implemented on an ICE transducer to characterize myocardial elasticity, a key connection between the heart's mechanical and electrical properties remains relatively unknown. We hypothesize that some border tissue

around RFA lesions becomes transiently stunned, and that although the ablation may appear initially effective by ECG and EAM, that the stunned tissues will recover over time and restore the aberrant electrical pathways, and that these stunned tissues will have a different appearance in ARFI and/or SWEI from fully-ablated tissue. However, we are yet to prove that this is the case, largely because the experimental setup would be quite complicated, involving long-term animal studies, since we would have to wait for the arrhythmia to reoccur. We are not, at the time of this thesis, equipped to do those studies technically, and before entering into such a costly study, need to know that we have reliable tools for mapping elasticity. Such work, though very important, may need to wait until ICE technology is better equipped for reliable *in vivo* ARFI and SWEI, or find a way to do the study somewhat retrospectively from clinical data once enough patients have been scanned that some start to return.

8.5 Implications for the Future of ICE ARFI

For the system described here to be useful in the clinic, a few key improvements could be made by the system manufacturers, or else alternatives developed in a research environment. Firstly, better communication is necessary between the ultrasound scanner's data acquisition, and the EAM system's 3-D mapping. The ability to insert the ARFI and SWEI images into the CARTO system, such that they could be displayed in 3-D during the procedure would be beneficial. Also, on demand, triggered saving of the ICE transducer's 3-D position (as the transformation matrix) would allow the scanner to fire many more images, each triggered off of the ECG, and the system could digitize the 3-D position of each, allowing for dozens of images to be acquired in each breath hold. With more data, volumes could be more fully sampled, a few lost frames wouldn't be as big of a problem, and overlapping images could be averaged in 3-D to remove noise and/or explore anisotropic shear wave

propagation. Even if each image only maps a small segment of the myocardium, the chamber could be mapped mechanically in the same way that it is currently mapped electrically, point-by-point, using greater image density (and thus greater voxel density in the reconstructed volumes) to adaptively image ablated areas for small gaps in the ablation lines. The other technological development that would enable this system to reach its potential would be in the design of ARFI-specific ICE transducers. There are two directions in which catheter design could proceed. With a larger aperture and a heavier or more rigid transducer tip, the ICE array could have a larger field of view, generate larger, more tightly focused displacements, and be more resistant to kickback. This would allow the left side of the heart to be imaged from the right side, alleviating the need to take the catheter across the septum. Alternatively, because of the stringent requirements on imaging angles for ARFI methods, an ARFI-specific ICE transducer may benefit from an alternate shape or steering configuration that would enable a smaller catheter to more readily obtain the necessary imaging angles and distances. We were able to achieve success with careful positioning and near-real time processing to check image quality, but to make a clinically accepted tool, the reliability of obtaining quality images will need to be improved through transducer and system design, and continued development of advanced algorithms to analyze and model the observed motion.

Appendix A

Demonstration of Very High Frame-rate SWEI Imaging in an Ex Vivo Langendorff Heart Model

This work represents the evolution of the tools used in chapters 3 and 4, which was not published elsewhere. These results are intended to demonstrate that significant improvements to the repeated SWEI sequences are made possible with improved hardware capabilities.

A.1 Abstract

Rapid, repeated estimation of tissue elasticity may be useful for characterizing dynamic myocardial stiffness, as highlighted in chapters 3 and 4. Shear Wave Elasticity Imaging (SWEI) uses ultrasound to both excite tissue and track the motional response to characterize elasticity, and can be implemented on commercial intracardiac echocardiography (ICE) systems. With the availability of increased parallel beamforming on newer ultrasound scanners, shear wave propagation to the left and right of a push can be imaged simultaneously, allowing for increased frame rates. This work demonstrates "M-Mode" SWEI imaging at 180 pushes per second, with

continuous, 10,000 fps tracking. An *ex vivo* Langendorff-perfused rabbit heart is used as a target, and the dynamics of contraction and relaxation are imaged.

A.2 Methods

An Siemens AcuNav Intracardiac Echocardiography (ICE) transducer, connected to a Siemens Acuson SC2000 ultrasound scanner (Siemens Medical Systems, Mountain View, CA), was used to acquire all data. The *ex vivo* Langendorff-perfused isolated rabbit heart was suspended in a saline bath, with the AcuNav positioned to have a short axes view of the left ventricle. The sequences used 192 6 MHz, 90 Vpp, 300-cycle push pulses every 5.6 ms, focused at 12.5 mm to excite the myocardium. The motion was tracked at a frame rate of 10,000 fps continuously for 1075 ms, with 32 parallel receive beams placed over a 22° lateral field of view surrounding the push. Axial motion was estimated with a phase-root seeking algorithm, (Pesavento et al., 1999) with a 5λ axial kernel, between each successive tracking frame. Each ensemble was motion-filtered with a 2nd-order interpolation filter, using motion before the push and greater 2.25 ms after the push as the background estimate. Velocities were averaged over around the focus (11 - 14 mm), and the shear wave speed was found by normalized cross correlation of the average of the center two track lines (those within 0.4° of the push) with each laterally-offset track line. The estimation was repeated for each of the 192 ensembles.

A.3 Results

Figure A.1 shows the effect of using a motion filter to separate the background tissue motion from the ARFI-induced motion. The arrival times in the right frame are fit to a shear wave speed model, shown in white.

Figure A.2 summarizes the results of the scan. The top row shows the center line of the B-Mode through the 192 acquisitions, as an M-Mode. The yellow line indicates

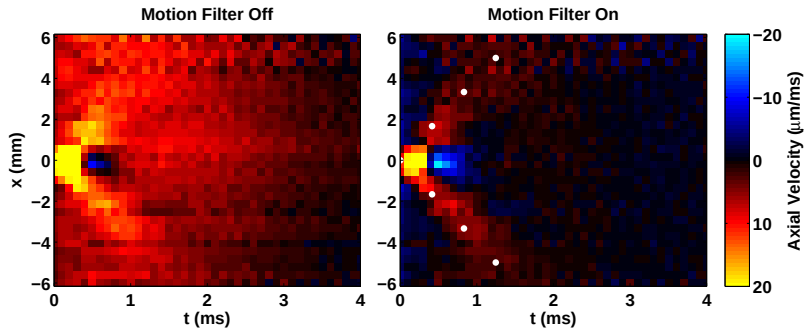

FIGURE A.1: Axial tissue displacements around the focus for a single shear wave excitation, before (left) and after (right) interpolation motion filtering. The peak of the shear wave becomes more conspicous, and can be fit to the shear wave model (white).

the focal depth, about which displacements are averaged for the rest of the figure. The second row shows the axial tissue motion, averaged over the timesteps prior to each push. Red is motion away from the transducer, and blue is motion toward the transducer. The pattern of motion is consistent with the motion in the first row, and shows gradients across the lateral field of view. The third row shows excerpted shear wave profiles, displaying the first millisecond after the push. The background motion is visible, as are the induced shear waves. The fourth row shows the results of motion filtering, with the shear wave speed fit superimposed in white. The frames with large upward motion fail to filter correctly, and correspond to outliers in the estimates. The fifth row shows the shear wave speed estimates for all 192 pushes. The final row shows the correlation coefficients associated with each estimate.

A.4 Discussion

With 32:1 parallel beamforming and very high frame-rate tracking, these sequences can obtain high quality shear wave estimates at a very high frame rate. These results are similar to those published by Pernot et al. (2011), but performed on an ICE catheter and at 35% higher framerate. Although a few frames are dropped due

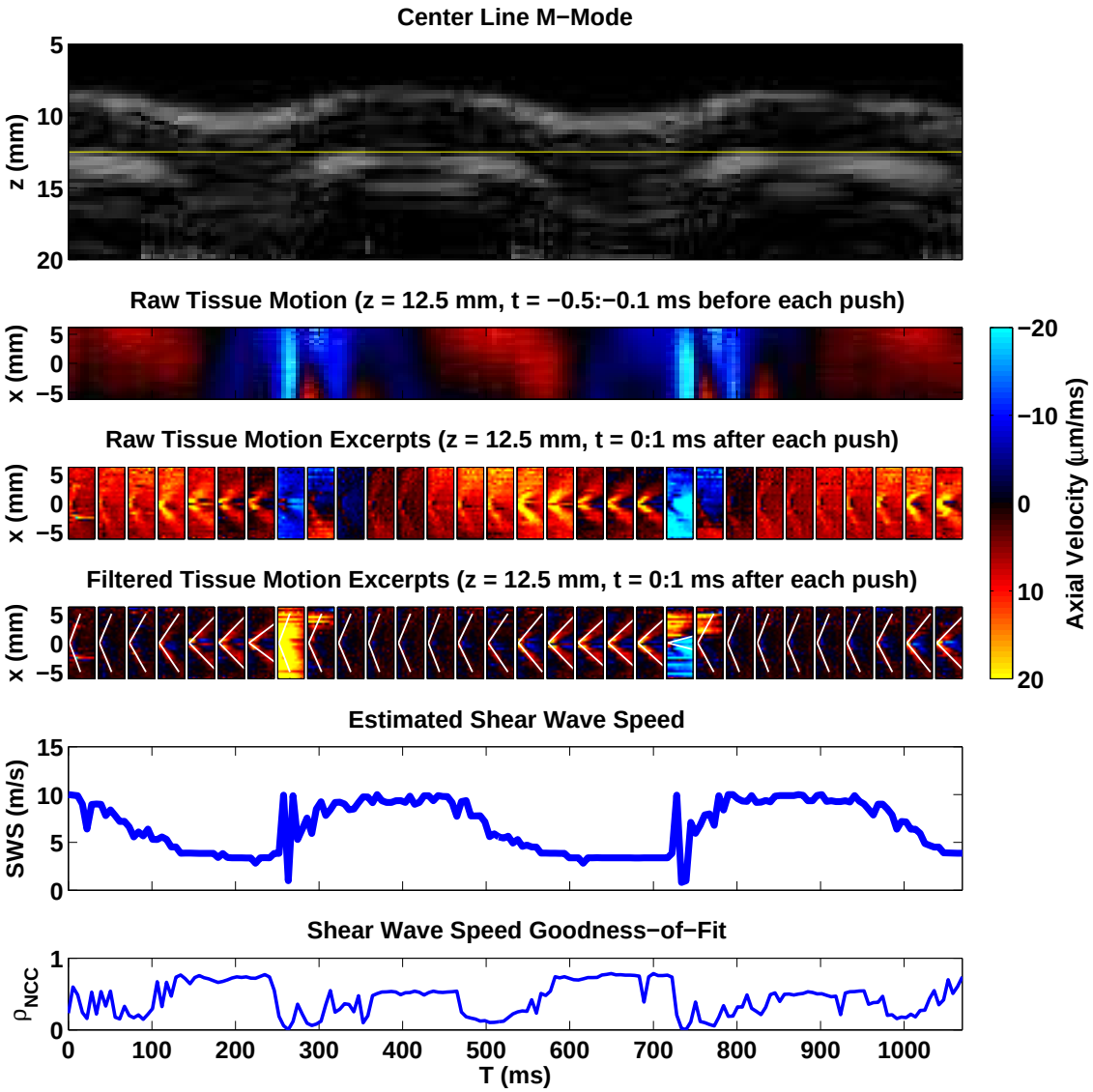

FIGURE A.2: Top row: The center line of the tracking data, for each of the 192 push locations. Second Row: The axial tissue motion, averaged prior to each push. Lateral gradients of motion are visible. Third row: Axial tissue motion after each push (30/192 pushes are shown). Both the background motion and ARFI motion are visible. Fourth row: Axial tissue motion after each push with motion filters applied, and the shear wave speed fit overlaid in white. Fifth row: Shear wave speed estimates for each frame. Speeds correspond with contraction and relaxation. Sixth row: Normalized cross correlation coefficient fit for each shear wave speed estimate. Outlier speed estimates are associated with low correlation coefficients.

to excessive motion, enough frames are acquired that the contraction and relaxation properties are still visible through the periods of elevated motion. Because of the way that the heart was suspended, the upward motion corresponded to contraction, as sides pulled in. The increase in stiffness is seen concurrent with the upward motion, but not leading it, as might be expected. This phenomenon warrants further inspection, but is beyond the scope of this work, which is only intended as a demonstration of this tool.

A.5 Conclusion

The imaging sequences demonstrate here represent a significant improvement over those presented in chapters 3 and 4, enabled by the additional hardware capabilities of the newer scanner. The elevated framerate and quality of visualized shear waves could allow a more detailed analysis, were those studies to be repeated. Parallel beamforming is critical for shear wave imaging in the presence of motion, and enables imaging of complex dynamics with very high framerates.

Appendix B

Beamforming Bias Compensation in Single Track Location Shear Wave Elasticity Imaging

This chapter is currently in review for publication and is presented in its entirety. This work explores an aspect of STL-SWEI that had been casually observed in great detail through simulation. As we developed STL-SWEI and started thinking about what meant for the estimated shear wave speeds to represent the area "between the push beams", we noticed an offset between the images made with the left- and right-going waves. This work identifies the source of that offset and proposed a technique for correcting it to improve lateral resolution and extend the axial field of view. This correction is applied to all STL-SWEI images we present.

B.1 Abstract

Shear wave elasticity imaging (SWEI) uses the local propagation velocity of mechanical shear waves, generated and tracked with ultrasound, to build images of the local elastic properties of tissue. In conventional SWEI, the local scatterer distribution of the high frame rate ultrasonic tracking used to estimate tissue motion creates uncertainty in the tracking beam's effective location and results in biased errors in shear wave arrival times, limiting the resolution and SNR of the system. Single tracking location SWEI offers a solution to this limitation by using the wave arrival times measured sequentially from multiple laterally offset excitations at a single tracking location to estimate local velocity, thereby negating the effects of the speckle bias. This work demonstrates that single tracking location arrival time estimates are biased by the geometry of the pushing beams such that they sample the area between the edges (as opposed to the centers) of the push beams. Knowledge of the shape of the push beam allows for correct mapping of the estimates onto the image. The use of both *a priori* knowledge of the push beam geometry and the initial displacement field to determine the appropriate correction term are shown. Finite element method simulation results are presented showing successful compensation for the offset in multiple push beam focusing scenarios, resulting in an extended usable depth of field and improved resolution when combining images from multiple tracking locations.

B.2 Background

B.2.1 Shear Wave Imaging

Sarvazyan *et al.* proposed estimating the elastic properties of tissue from the group velocity of transverse wave propagating through linear, isotropic media, known as shear wave elasticity imaging (SWEI)Sarvazyan et al. (1998). Estimating tissue properties in this way has in recent years become increasingly promising for the purposes of diagnosis, staging, and treatment guidance, among others Bercoff et al. (2004); Huwart et al. (2006); Palmeri et al. (2008); Bouchard et al. (2009b); Muller et al. (2009); Hollender et al. (2010); Nenadic et al. (2011); Arnal et al. (2011); Couade et al. (2011); Hollender et al. (2012); Rotemberg et al. (2012). As new applications continue to be developed, the accuracy and resolution of SWEI images becomes paramount to acceptance into a clinical setting. Both Rouze *et al.* Rouze et al. (2012) and Deffieux *et al.* Deffieux et al. (2012) have analyzed factors that cause degradation of conventional shear wave images, and the reader is referred to those papers for topics not addressed here. Rouze *et al.* discussed parameters including kernel size, shear wavelength, and arrival time estimation method, while Deffieux *et al.* addressed sources of noise, including electronic noise, speckle decorrelation, and shear waveform decorrelation. Rouze *et al.* found that linearly regressing arrival times estimated from the first derivative of tissue displacement ("time-to-peak-slope", or TTPS) was more resistant to reflection artifacts than regressing the peak displacement directly ("time-to-peak", or TTP). Rouze *et al* also pointed out that larger regression kernels reduced variation in shear wave velocity estimates at the expense of resolution. Deffieux *et al.* also acknowledged the trade-off with regression kernel size between noise suppression and resolution, noting that there is a limit on how close two tracking lines can be before the time delay is so noisy that the velocity image is rendered useless.

B.2.2 Spatially Modulated Ultrasonic Radiation Force

McAleavey *et al.* proposed the use of a Spatially Modulated Ultrasonic Radiation Force (SMURF) excitation to simultaneously excite two lateral locations in tissue. This imaging method estimated the elasticity of the tissue from the motion signal recorded at a single tracking location offset from the modulated excitation. In the initial work, the temporal wavelength of the recorded motion was compared to the spatial wavelength of the modulated push to build a velocity estimate in a homogeneous medium with reduced variation through depthMcAleavey et al. (2007, 2009b). Elegbe *et al.* proved that the depth-dependent variation in SWEI images (the limiting factor Deffieux *et al.* had noted) was not random noise, but rather correlated speckle bias resulting in a lateral offset in the effective location of the beam at each depth relative to the beam axis. For shear wave imaging methods that fix the tracking location and use offset excitations to compute the time delay (like SMURF), the speckle bias cancels itself, providing potentially speckle-free shear wave imagesElegbe and McAleavey (2013). The same group also published images made with pairs of sequentially-excited push locations as a comparison to SMURF images (called SMURF-mod in that work), using cross-correlation of the signals measured at an offset location between each pair of pair of pushes to build each lateral line in the image McAleavey et al. (2009a), asserting that the estimates mapped the elasticity between the push beam excitation axes. In that work, images were limited to the depth of field, where the shear wave had a vertical front edge and a beam width of 0.65 mm. The structures imaged were on the order of 1.5 mm to 1 cm. The push beam spacing was set to 2.48 mm in that work, limiting the resolution of the system such that the artifact presented here would not have been obvious.

B.2.3 Single Track Location Shear Wave Elasticity Imaging

The preliminary SMURF work has paved the way for the development of single track location SWEI (STL-SWEI), a variant of traditional SWEI, which will be distinguished from STL-SWEI hereafter as multiple track location SWEI (MTL-SWEI). For both modalities, the velocity of a transverse shear wave is estimated over some spatial region, and local estimates of velocity determine the pixel values in an image of elasticity. MTL-SWEI estimates the local velocity from the arrival times measured at multiple offset spatial locations from a single push. STL-SWEI conversely uses the arrival times measured at a fixed location but generated at different locations to build its shear wave movies. While MTL-SWEI can build an image from a single excitation using parallel receive beamforming, STL-SWEI requires successive excitation of each location between which one wants to estimate elasticity, a spatial sampling requirement similar to acoustic radiation force impulse (ARFI) imaging. At the same time, however, parallel receive tracking allows for multiple independent STL-SWEI images to be generated together, which can be averaged together in the same way as MTL-SWEI images from multiple push locations can be. In the case of using a push beam spacing exactly equal to the parallel receive track beam spacing, MTL-SWEI and STL-SWEI acquisition sequences converge, such that equivalently sampled and processed MTL-SWEI and STL-SWEI images can be generated from the same data set with very minor changes to post-processing. The advantage that STL-SWEI has for high-resolution shear wave imaging is that its time delay estimates are degraded not by the uncertainty in the track beams. They are, however, degraded by uncertainty in the acoustic radiation force push beams, but these beams are formed primarily through absorption rather than scattering. The uncertainty in the push beams is therefore much lower due to the absence of a strong speckle bias. This permits STL-SWEI images to use more closely spaced beams (or similarly, smaller

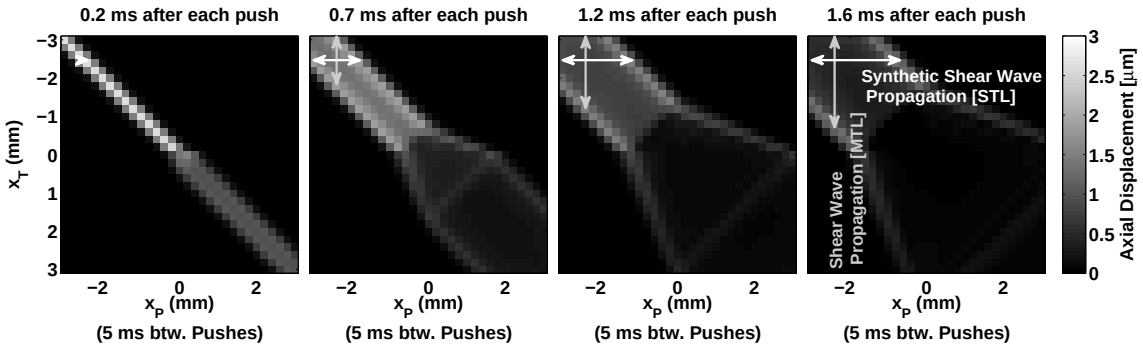

FIGURE B.1: Images of propagating shear wave displacement from a simulated dataset (31 push and track beam locations, each spaced 0.2 mm apart with a vertical boundary in shear modulus at $x = 0$). The y-axis portrays track beam locations, which are monitored at the same time using parallel beamforming methods. The x-axis represents push beam locations, which must be interrogated sequentially. Displacement through time is monitored for each push at all track beam locations. MTL-SWEI employs linear regression along the vertical axis x_T (i.e., between the wave arrival times and the track beam locations, shown as the gray vertical arrows), whereas STL-SWEI employs linear regression along the horizontal axis x_P (i.e., between the wave arrival times and the push beam locations, shown as the white horizontal arrows).

regression kernels) than MTL-SWEI, resulting in either higher resolution, improved CNR, or both. This work demonstrates that although STL-SWEI images are free from the speckle bias, the beamforming of the excitations creates spatial distortions in the images. These distortions can be corrected with knowledge of the push beam geometry.

B.3 Methods

B.3.1 STL-SWEI Acquisition Sequence

The STL-SWEI acquisition sequences used here are identical to the MTL-SWEI sequences that would be used to sample the same area with the same spacing of push and track beams. The difference is that in MTL, the wave is considered to propagating laterally from each push across the tracking locations, whereas in STL, the wave "propagates" laterally from each track location across push locations. Figure

B.1 shows both the physical propagation of the MTL wave and the synthetic propagation of the STL wave. For this work, we selected a set of 31 tracking beams that remained consistent across all 31 excitations, such that the push and track locations were the same. In MTL, each push beam forms an entire SWEI image, estimating velocity across track beams. In STL, each *track* beam forms an entire SWEI image, estimating the velocity between the push beams. In MTL-SWEI, additional excitations provide overlapping images that can be averaged together, whereas in STL the additional tracking lines perform the same function. In this way, the spatial sampling and amount of averaging possible for the STL-SWEI images is the same as it would be for MTL-SWEI. In Figure B.1, MTL-SWEI can be thought of as finding the local slope of arrival times along x_T and averaging across the x_P, and finding the local slope along x_P and averaging across the x_T for STL-SWEI.

B.3.2 Finite Element Models

Finite element methods were used to simulate radiation force excitations in tissue and the resulting shear wave responses using previously validated modelsPalmeri et al. (2005). Simulations consisted of mesh generation, radiation force excitation calculation and finite element simulation.

Three-dimensional finite element models were generated using LS-PrePost (Livermore Software Technology Corporation) for four different target structures. All materials were modeled as linear, elastic, isotropic solids with a Poisson's ratio of $\nu = 0.499$ and a density of $\rho = 1.0$ g/cm^3. The total mesh size was 7.2 mm x 5 mm x 35 mm with cubic elements of size 0.1 mm x 0.1 mm x 0.1 mm. Half-symmetry with non-reflecting boundaries was used to mirror the simulated structure in elevation. The top and bottom boundaries were fully constrained. In all targets, the background material was given a Young's modulus of $E = 4.5$ kPa. A vertical layer target divided the model in half in the lateral dimension, extending fully in

the axial and elevation dimensions, and had a Young's modulus of $E = 24$ kPa. A spherical inclusion was created centered at a depth of 15 mm with a radius of 1.5 mm and a Young's modulus of $E = 24$ kPa. Horizontal layer phantoms with moduli of $E = 24$ kPa and $E = 4.5$ kPa were also simulated with a boundary at 15 mm, with the stiffer region alternately on the bottom and top. Diagrams of the simulated phantom structures and the expected shear wave velocities are shown in Figure B.2.

Several focal geometries were used to simulate radiation force excitations. In all cases, the Acuson ER7B transducer was simulated with a pitch of 0.4 mm and center frequency of 5 MHz. Previously measured experimental impulse responses for this transducer were used. FIELD II Jensen and Svendsen (1992); Jensen (1996) was used to generate an acoustic intensity profile for each focal configuration, which were converted into acoustic radiation force point loads using an attenuation value of 0.5 dB/cm/MHz. Push beam geometry is described by focal depth and F-number (F/#). For each target geometry, an F/3 push beam was simulated with a focal depth of 15 mm. An F/1 push beam was also simulated with focal depths of 12.5 mm, 15 mm and 17.5 mm. A "supersonic shear imaging" (SSI) sourceBercoff et al. (2004) was simulated by combining these three focal depth configurations in post-processing with varying time delays. The shape of the SSI source is described by the Mach number, the ratio of the axial speed of the excitation beam (push spacing divided by excitation delay) to the lateral shear wave speed. Similarly, a simultaneously "multifocal" excitation was created by exciting all three depths with F/1 beams simultaneously (an SSI source with an infinite Mach number). An excitation duration of 60 μs was used in all cases.

LS-Dyna (Livermore Software Technology Corporation) was used to explicitly solve for node displacements recorded at 10 frames/ms. The total duration simulated was 5 ms to allow propagation of the shear wave from one end of the mesh to the other. Separate simulations were performed for push beams spaced 0.2 mm apart

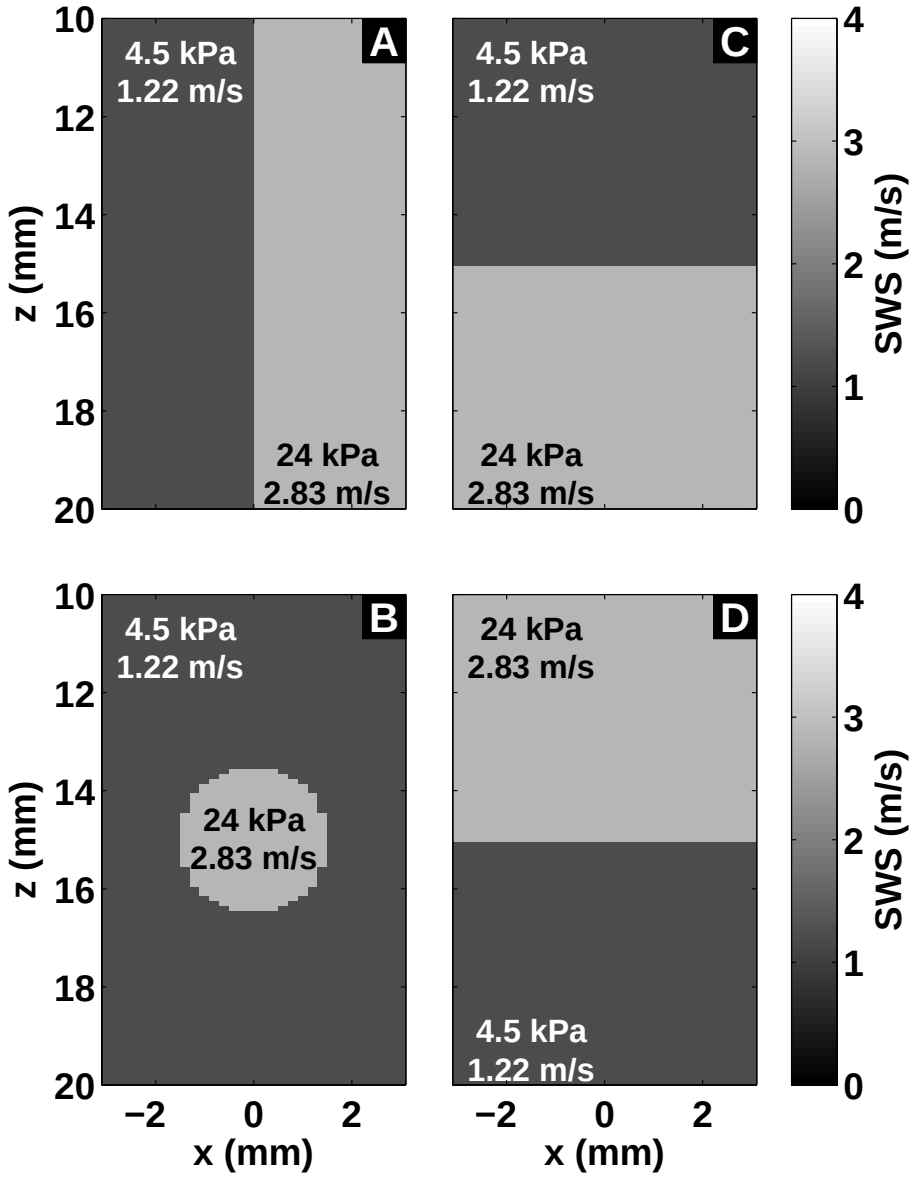

FIGURE B.2: Simulated geometries: (A) vertical layer, (B) 3 mm diameter sphere, (C) horizontal layer (stiff bottom), (D) horizontal layer (stiff top). Young's modulus and the expected shear wave velocity are labeled for each component.

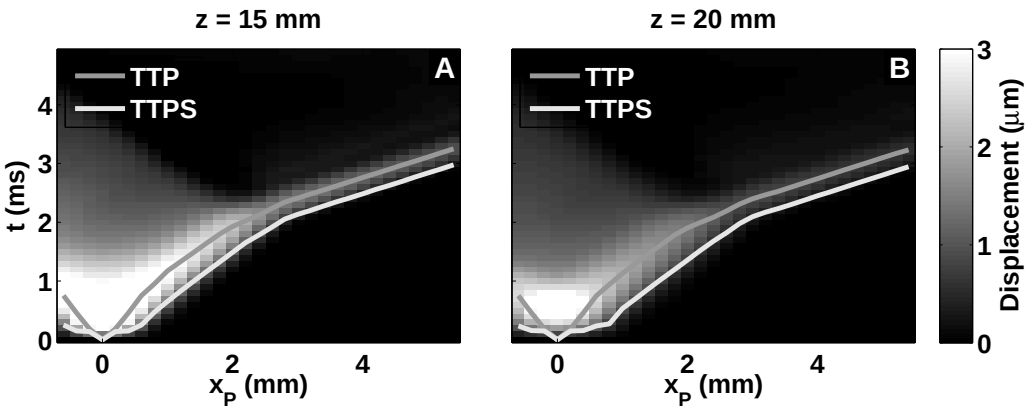

FIGURE B.3: (A) Shear wave displacements at the focus (15 mm). (B) Shear wave displacements deep to the focus (20 mm). Time-to-peak-displacement (TTP) and time-to-peak-slope (TTPS) are shown. For TTPS, the arrival time is driven by the leading edge of the wave, which starts spatially offset from the beam push axis.

across the mesh, producing 31 simulations per focal configuration and target. Axial displacements in the lateral-axial center plane were extracted and saved for post-processing.

B.3.3 Arrival Time Estimation

Arrival times can be estimated in multiple ways, though here we only consider two. "Time-to-peak" (TTP) estimates the arrival time as the time of maximum axial displacement for each lateral location. "Time-to-peak-slope" (TTPS) uses the maximum of the first derivative of displacement with respect to time of displacement signal. TTPS has a sharper peak (differentiation is a high-pass filter), and is more resistant to background noise (linear motion becomes constant, quadratic becomes linear, etc.) Rouze et al. (2012). Figure B.3 shows two shear wave displacement profiles at different depths. The left panel (A) shows the displacements at the focus, with an overlay for the calculated arrival times by each method. It can seen that TTPS estimates the wave arrival time before the TTP estimator. Both methods rely on identification of a particular feature of the wave that is offset from the center

of the original excitation, TTPS further than TTP, and whose offset varies through depth, as shown by the profile in Figure B.3 from 5 mm below the focus.

In STL-SWEI, a single sub-image is produced from each tracking line with the region of direct excitation masked off as undefined. The sub-images can be combined into a single composite image by taking the median at each axial and lateral pixel across all sub-images, ignoring any undefined pixels. These composite images have no undefined areas, and suppress any noise present in the individual sub-images. This performs the same function as averaging MTL-SWEI images from multiple push locations, but is achieved through parallel receive tracking. For the simulations presented here, the same spacing and sampling is used for the push and track beams, providing equivalence between STL-SWEI and MTL-SWEI.

B.4 Observation of Spatial Bias

B.4.1 Dependence of Lateral Bias on Arrival Time Estimation

Using an F/1 excitation beam focused at 15 mm axially, an STL-SWEI image was created of the vertical layer target shown in Figure B.2(A). A single receive line centered at $x = -2.4$ mm was used to create the images shown in Figure B.4. The FIELD II-simulated beam intensity on the $x_T = -2.4$ mm receive line is shown in panel A, numerically equivalent to the intensity that would be seen at all receive lines for a push at $x_P = -2.4$ mm in MTL-SWEI. TTP and TTPS images were created from this data set and the initial push beam has been masked off to remove estimates at locations under direct excitation.

The results show that both TTP and TTPS arrival time estimators suffer from geometric error due to the shape of the beam profile. The true vertical boundary location is shown by a dashed white line. Both show reasonable reconstruction of the boundary layer within the depth of field of the excitation, but with a fixed lateral offset in each case. Outside the depth of field, the TTP image shows corruption

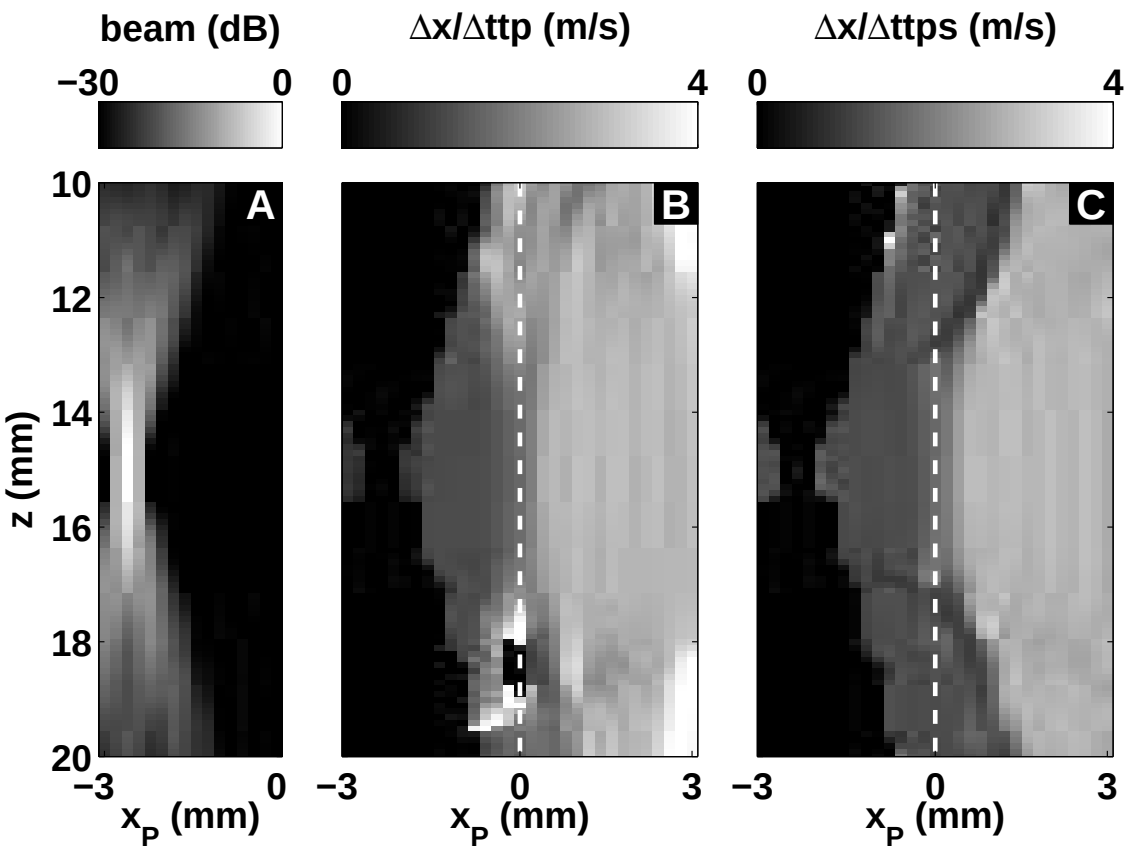

FIGURE B.4: (A) The FIELD II-simulated push beam intensity on a single receive line located at $x = -2.4$ mm for all excitations across the field of view. (B) STL-SWEI image created from the tracking line in panel A, using the time-to-peak displacement (TTP) as arrival time. (C) STL-SWEI image created from the tracking line in panel A, using the time-to-peak-slope (TTPS) as arrival time. Away from the focus, the boundary is blurred in panel B, and appears offset in panel C.

and ringing artifacts that do not indicate a clear method for correction. The TTPS image, on the other hand, shows a smoothly-varying lateral shift through depth that seems to follow the shape of the push beam.

The STL-SWEI images in panel B show a shift of the boundary to the right of its true location, corresponding to the tracking line being located to the left of the boundary. A tracking line on the right side of the structure produces an equivalent shift to the left, creating a left/right bias between images from different locations. When tracking lines from both sides are combined into a single image, as is commonly

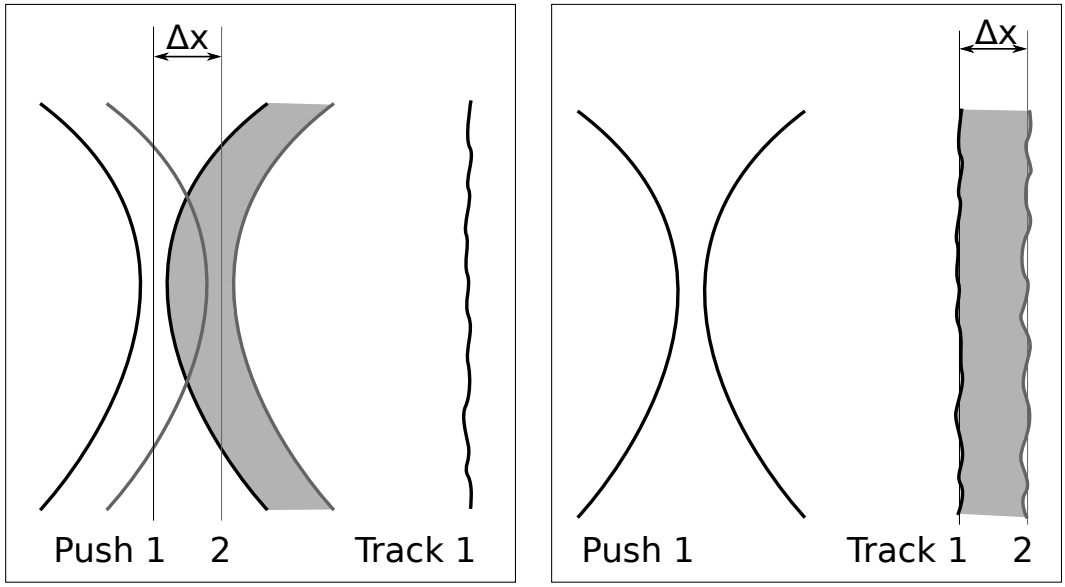

STL-SWEI (A) MTL-SWEI (B)

FIGURE B.5: In both STL-SWEI and MTL-SWEI, the wave speed at each depth is calculated by dividing the known distance Δx by the difference in shear wave arrival time. The tracking beam is illustrates random speckle bias through depth. The interrogated region is shaded. (A) STL-SWEI configuration. Two push beams separated by Δx produce shear waves recorded at a single tracking location. (B) MTL-SWEI configuration. A single shear wave is tracked at multiple locations spaced laterally Δx apart.

done in a manner similar to MTL-SWEI combining sub-images from multiple pushes, a blurring of the edge will occur. This will reduce resolution around the focus by an amount on the order of a beamwidth, and by an even greater amount away from the focus, based on the hourglass geometry.

B.4.2 Hypothesized Source of Lateral Bias

For STL-SWEI, the difference in arrival times has been previously defined as the wave propagation between the excitations. We propose here a more rigorous definition of that region. With tightly spaced, overlapping push beams, there will be no propagation between the push beam axes since that region between will be under direct excitation for both pushes. We hypothesize that the region whose elasticity

would determine the time delay at some distant track line would not lie between the centers of the beams, but rather between the *edges* of the beams closest to the track line, since this is the region which supports a shear wave for one excitation and is under direct excitation for the other. Outside of both beams, the propagation of both waves should be the same, and not influence the arrival time difference calculation.

Figure B.5 shows the interrogated region for both STL and MTL and the cause of the geometric artifact in STL-SWEI. When the wave speed measured is assigned to the lateral location between the centers of the two push beams rather than the depth-varying location between the wavefronts, there is a lateral distortion of the image determined by the shape of the excitation. While the true separation between the track beams in MTL-SWEI varies through depth due to speckle bias, the push beam shape has little effect on the resulting wave speed estimates. The track beam geometry may create some small bias in MTL-SWEI, but dynamic receive focusing with receive aperture growth make the transmit-receive beam geometry of the tracking lines much tighter and more uniform through depth, and thus the size of the offset is likely to be small relative to the resolution of these systems.

B.4.3 Axial Bias

Figure B.6 shows the results for the STL-SWEI simulations of the horizontal layer phantoms. In both cases, the size of the stiff region is overestimated. For the simulated focal configurations and stiffness contrast, the size of the offset was approximately 0.7 mm. To examine this more closely, Figure B.7 shows depth slices close to the boundary. A pair of apparent shear waves associated with the propagation in both media are visible at the displayed depths with varying amplitudes. The apparent presence of each wave in the opposite medium is likely due to the displacement continuity across the boundary needed to enforce boundary conditions. In the top and bottom rows, the correct wave front (the one associated with the material

properties at that depth) is tracked by TTPS. In panels B and I, the faster moving apparent wave is assigned the arrival time, even though the material properties at that location are that of the slower wave. At the boundary (panels C and H), the faster wave clearly dominates the signal. This bias is not the result of STL-SWEI beamforming; it is also present in the equivalent MTL-SWEI images, which, though not shown, appear indistinguishable from those shown in Figure B.6. This is hypothesized to be the result of arrival time being representative of the leading edge of the displacements when multiple shear waves are apparent, as is indicated in Figure B.7. For low contrast boundaries, this can be expected to be an axial blurring, as the fast and slow wavefronts are continuous across the boundary. For higher contrast media, a sharper boundary indicates that the two waves have separated, with the leading edge of the each wave generating motion in the opposite medium due to the boundary conditions of the interface. A correction factor for this bias is not proposed here, since the bias is dependent on the target's geometry and elasticity.

B.5 Lateral Bias Compensation

B.5.1 Empirical Determination of Correction Factor

The lateral offset observed in Figure B.4(C) appears to at least coarsely follow the hourglass shape of the transmit intensity, but what constitutes the "edge" of the beam must be more precisely defined. To determine what correction factor should be applied to optimally align the vertical boundary at each depth, all possible integer-sample shifts were applied to each row, and compared to the simulated lateral velocity profile from Figure B.2(A) with normalized cross correlation. Using the STL-SWEI image from panel A of Figure B.8, the normalized cross correlation coefficient was calculated for each depth and at each candidate shift with respect to the target geometry. The peak of the correlation function in panel B is shown as a solid black line, and in panel C this "ideal" shift is used to adjust the STL-SWEI image. Panel

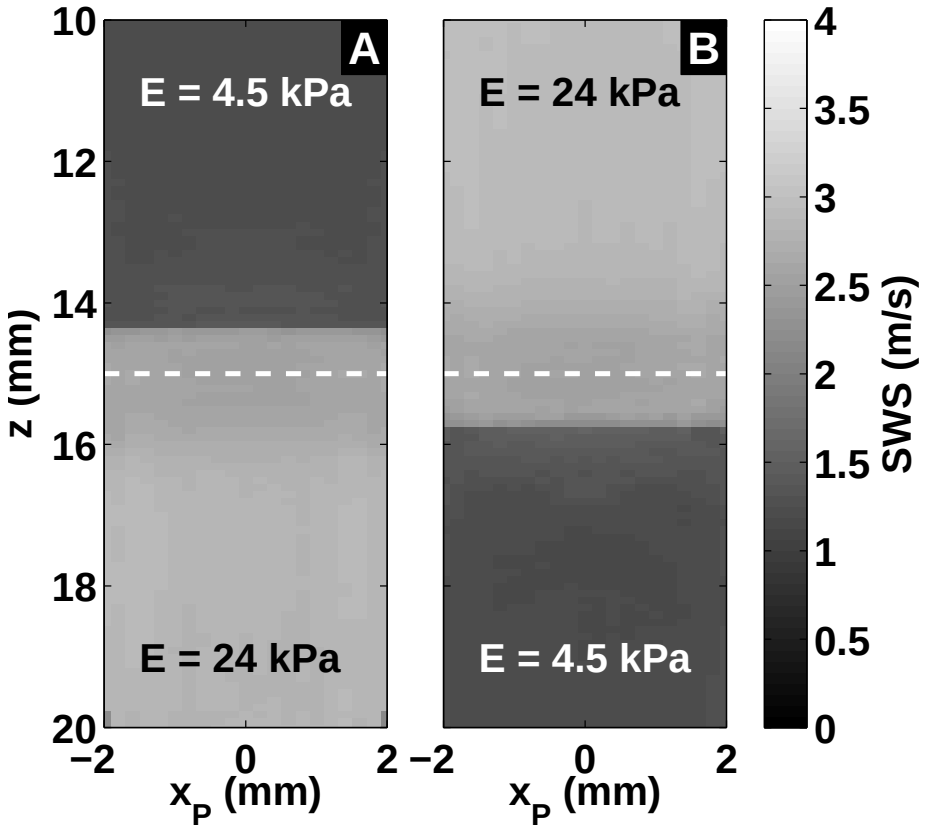

FIGURE B.6: (A) STL-SWEI image of the horizontal layer phantom in Figure B.2(C). The simulated boundary at 15 mm is drawn as a dotted white line. (B) STL-SWEI image of the horizontal layer phantom in Figure B.2(D). The axial region in the softer material that is within 0.7 mm of the boundary shows the higher wave velocity from the other side of the boundary.

D overlays the same shift from panel B onto a beamplot of the excitation normalized through depth, with filled contours showing the the -3, -9, -15 and -21 dB levels.

Panel C shows improved boundary definition and successful removal of the offset. The corrected image has a reduced lateral field of view in the shallow and deep regions of the image, showing undefined values (black pixels) at the right of the image where the correction has pulled estimates to the left and no more data is available. Conversely, the correction reduces the extent of the masking seen around the receive beam, leaving only a narrow undefined region to be masked off. The total area imaged has remained the same, only having changed shape with the correction.

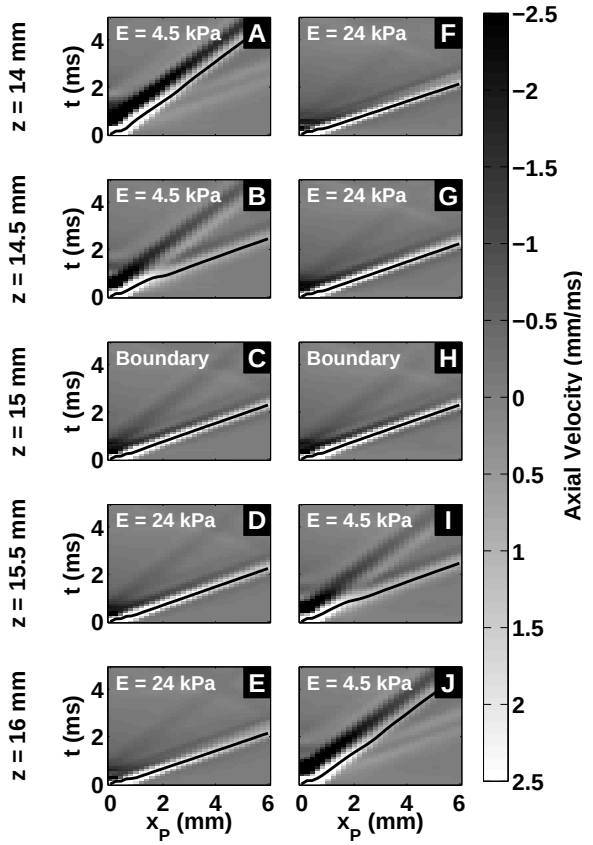

FIGURE B.7: Axial slices of shear wave propagation from the horizontal layer simulations. The left column shows slices from the stiff-bottom phantom (Figure B.2(C)) and the right column shows slices from the stiff-top phantom (Figure B.2(D)). The rows show different depths, above, below, and within the problematic region near the boundary. The TTPS arrival time is indicated by the black line in each panel.

With additional tracking locations (as are readily acquired through parallel receive tracking), sub-images are created with different undefined regions such that all of the gaps can be filled in by averaging.

The empirically determined shift matches well with between the -3 and -9 dB contour lines of the excitation beam, suggesting that *a priori* knowledge of the excitation beam geometry can be used to estimate the necessary shift. We further hypothesize that the correction factor should be selected from the pattern of not just transmit intensity, but the induced acoustic radiation force $F(\vec{x}) = 2\alpha I(\vec{x})/c$, where

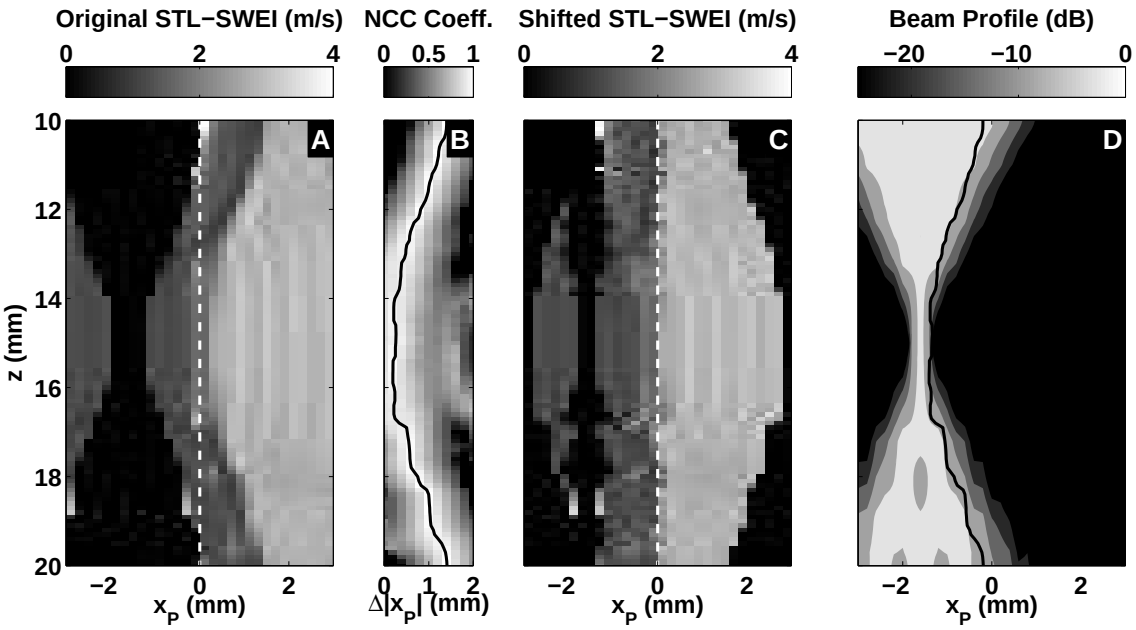

FIGURE B.8: (A) STL-SWEI image generated for tracking line located at $x = -2.4$ mm, using TTPS for arrival times. (B) Normalized cross correlation coefficient as a function of correction shift as a function of depth between versions of panel A with shifted rows, and the simulated truth in Figure B.2(A) The location of the peak coefficient is drawn as a black line. (C) The "ideal" corrected STL-SWEI image, with each row shifted according to the peak coefficients identified in panel B. (D) The simulated beam intensity, normalized to each depth, with the peak shift from panel B superimposed. The best correction factor at each depth follows the beam's hourglass shape.

$I(\vec{x})$ is the spatial intensity distribution, α is the absorption coefficient and c is the speed of sound.

B.5.2 Bias Correction Schema

Without *a priori* knowledge of the push beam geometry (due to unknown absorption, for example), the initial displacement profile measured immediately after excitation may provide a sufficient approximation for the push beam geometry, from which an appropriate lateral correction profile can be estimated. Figure B.9 shows both the FIELD II simulated beam profile (panel A) and corresponding FEM-simulated initial displacement, estimated 0.1 ms after excitation (panel B) for the F/1 push beam

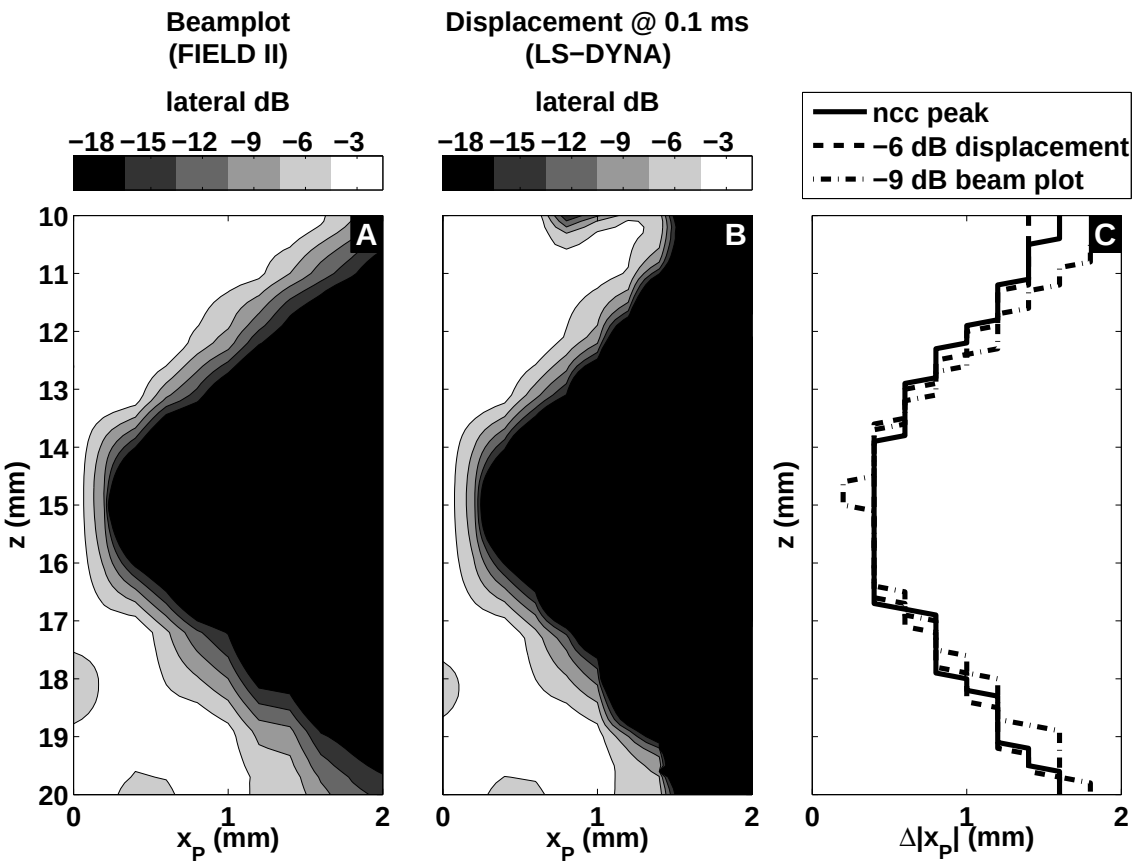

FIGURE B.9: (A) Filled contours of FIELD II-simulated beam intensity at a single tracking location, normalized to the maximum at each depth. (B) Filled contours of the displacements measured at a single tracking location 0.1 ms after excitation of each push location, normalized to the maximum at each depth. (C) Correction factors selected from panels A and B, along with the correction factor indicated by the peak of the cross correlation function in figure B.8

shown above, with each depth self-normalized to the peak displacement. The shapes of the two beams are very similar, suggesting that the initial displacement provides a good estimate of the geometry. To compare the two methods more closely, panel C compares the correction factor found in Figure B.8 with the correction factors found from the -6 dB initial displacement contour and the -9 dB beamplot contour. Good agreement between the three correction factors is seen, and the initial displacement correction appears to be slightly more accurate compared to the estimated "ideal" correction factor, as the beamplot shows a slightly more aggressively focused beam

edge. The discretization of these estimates is due to the spacing of the sampling beams (0.2 mm), though subsample estimation and shifting are possible. Distortions in the beam due to elastic inhomogeneity may influence the approximation of the beam shape, as might imaging very stiff materials, for whom the first image timestep may represent significant shear wave propagation.

B.5.3 Validation for Different Geometries

Using this approach, the simulated initial displacement profiles and shear wave velocity images for the vertical layer are compiled in Figure B.10. The left column of images shows the excitation beam profile for the first tracking location ($x_T = -3.1$ mm). The x-axis shows excitation beam location, and the y-axis shows depth. The brightness is mapped to the tissue displacement 0.1 ms after excitation. The drawn line indicates the edge of the beam, the distance from the center at which the initial displacement drops below 50% of its maximum. The second and third columns show the shear wave velocity maps recovered from the synthetic waves initiated by the beam in the leftmost panels, without and with the lateral correction, respectively. The rightmost two columns show the median shear wave images across all 31 tracking locations without and with the correction term. For the uncorrected images, the region around the beam has been excluded from each frame. Each row of Figure B.10 indicates a different excitation beam configuration, resulting in a different beam profile and different correction terms. The beam shape in the left column is clearly visible as a lateral bias in the second column, and results in a blur in the fourth column. For excitations without a depth-dependent beam width, the vertical layer is laterally offset initially, but corrected by the lateral shift.

All cases demonstrate improved imaging of the vertical layer, giving nearly identical results after correction despite different distortions in the original images. The corrected images demonstrate expanded depth of field compared to the original im-

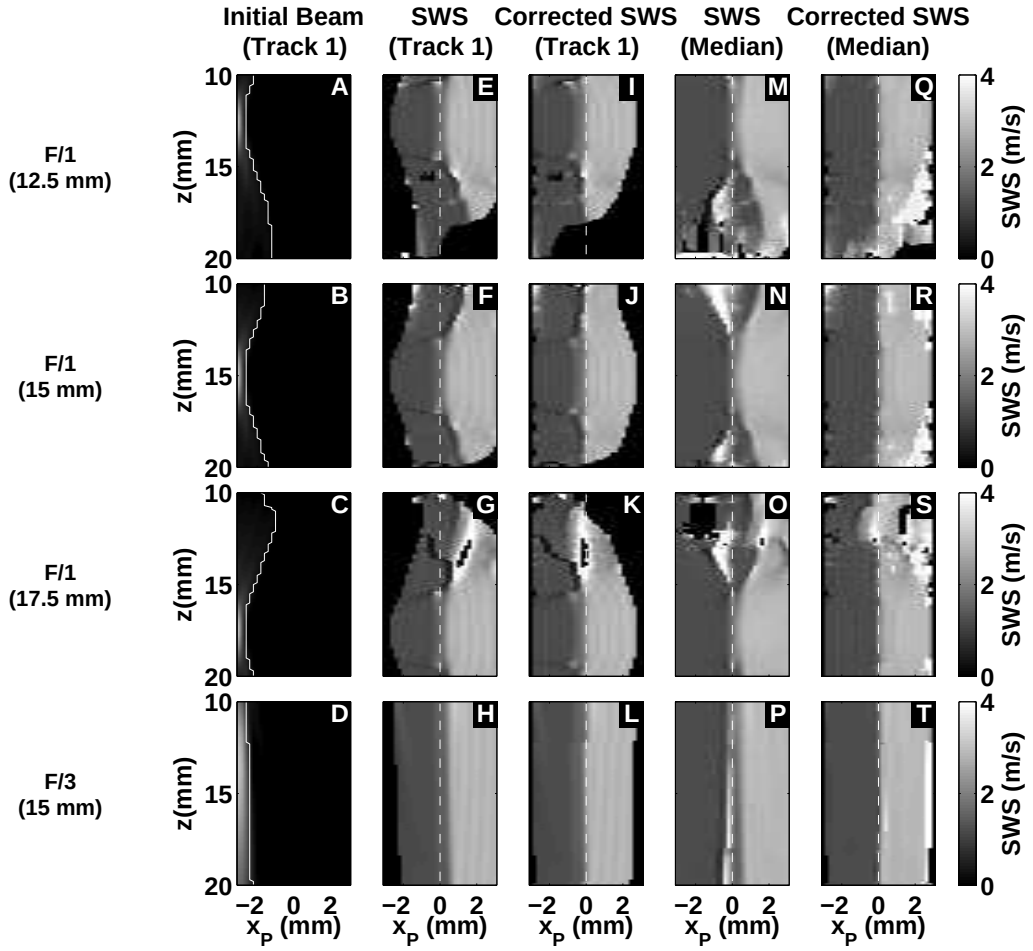

FIGURE B.10: Column 1 (A-D): Excitation beam profiles for each of the focal configurations. The edge of the beam, used as the correction factor, is indicated by the white line. Column 2 (E-H): STL-SWEI images from the synthetic excitation beams shown in the leftmost frames. The vertical layer is shown at $x_P = 0$ mm with a dotted vertical white line. Column 3 (I-L): The shifted STL-SWEI images after application of the correction factor. Column 4 (M-P): The median STL-SWEI image across all tracking locations. Column 5 (Q-T): the same images as column 4, but shifted by the correction factor prior to taking the median. The transition between the left and right halves of the STL-SWEI images aligns more closely with the expected boundary after the correction has been applied.

ages, but panels I and K show artifacts in regions where extreme correction was needed, meaning that it is still important to choose a focal zone appropriate for the desired target.

The F/3 push in panel D shows a more subtle geometric artifact due to the extended depth of field, but panel T demonstrates correction that results in an image similar the other focal cases, although with lower resolution due to the beam width. Panel H also demonstrates that even within the depth of field, the estimates are incorrectly assigned when they are based on the centers of the beam locations rather than the edges of the excited waves. After compensation, the offset is removed and the vertical boundary is correctly shown at the center of the image. In the combined (median) images, this beam-dependent offset in the layer causes blurring that is removed in the corrected images, producing a sharp boundary.

B.5.4 Correcting Multifocal Excitation Images

The results for using simulated supersonic shear imaging (SSI)Bercoff et al. (2004) excitations are shown in Figure B.11. The top and bottom row have 0.4 ms between each excitation, resulting in a disjointed wavefront, which is apparent in the "tearing" artifact visible in the corresponding STL-SWEI images.

The intuitive correction for an SSI excitation that produces an angled shear wave that travels laterally might be to correct by the angle of the produced wave seen in the initial displacement profile. However, panels K-O show that this approach, using the correction measured in gray in panels A-E, incorrectly adjusts the estimates for all but the simultaneous multifocal excitation. This is because the edge of the initial displacement beam around the first excitation is given some time to propagate while the other locations are excited. Since the propagation is determined by the shear wave velocity, the ROI interrogated between two adjacent multifocal pushes is that between the beam edges during each focal zone's excitation, not after all focal zones

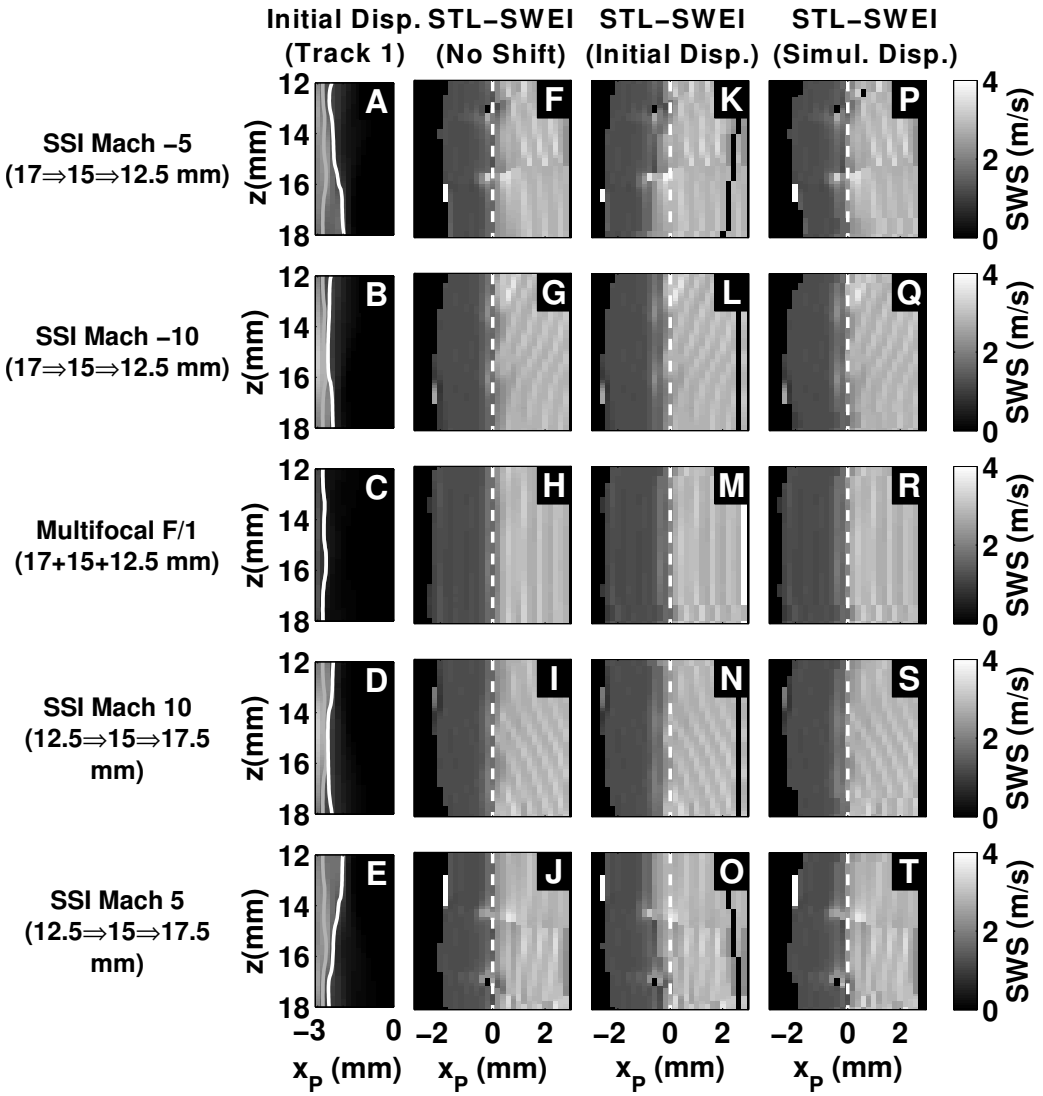

FIGURE B.11: Comparison of correction strategies for multiple focal zone SSI-style excitations. Column 1 (A-E): Initial displacement profiles. The edge of the displacement profile is marked with a white line, and the beam edge from the simultaneous multifocal beam (panel C) is shown in gray. Column 2 (F-J): The original STL-SWEI images. The vertical boundary is indicated with a dotted white line. The boundary appears slightly offset to the right of the line in the STL-SWEI images. Column 3 (K-O): The shifted STL-SWEI images, using the initial displacements from each configuration to determine the shift. Except for (M), the boundary has been over-corrected above or below the focus, and moved to the left of the dotted line. Column 4 (P-T): Corrected STL-SWEI images using the simultaneous multifocal beam profile from panel C. The boundary is shifted correctly.

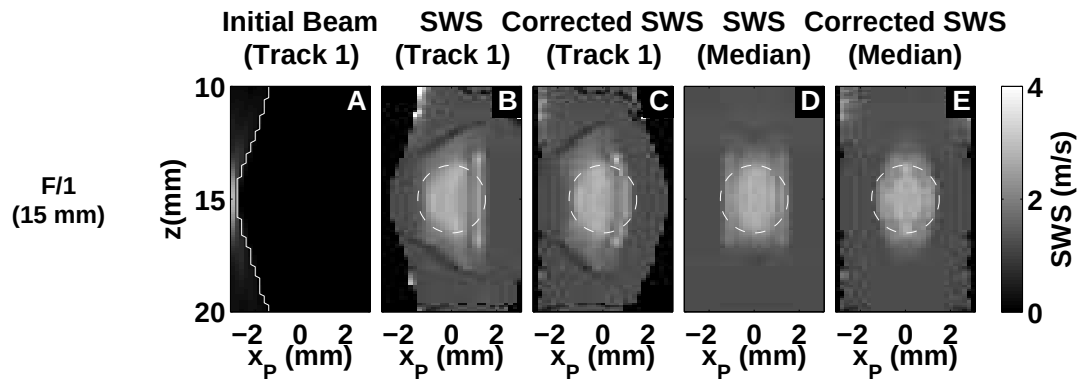

FIGURE B.12: (A) Excitation beam geometry for the F/1 excitation, taken as the displacements detected by the tracking beam at $x = -3.1$ mm from each push 0.1 ms after excitation. The beam edge is shown as a white line. (B) The STL-SWEI image created from the same tracking line as (A), with estimates from within the excitation beam blacked out. (B) The shifted STL-SWEI image from the same tracking line as (A). (C) The median STL-SWEI image from all tracking lines. (D) The median STL-SWEI image from all tracking lines with the shifts applied.

have been excited. The correct compensation is the same as the simultaneously excited multifocal zone case, where there has been no shear wave propagation when the initial displacement is measured. Because these excitations are created from a series of F/1 excitations, the initial excitation beam (the one we want to use regardless of the timing of the pushes) is tightly focused through depth, so the corrections within the excitation region are small and do not vary much with depth.

B.5.5 Spherical Lesion Target

To test the performance of the correction term on a more realistic target, the spherical target from Figure B.2(B) was used. The simulated beam profiles and shear wave velocity images for an F/1 excitation at 15 mm are shown in Figure B.12. The edges at the center of the sphere are improved in the corrected images, but the top and bottom of the sphere are blurred into the background. This vertical bias towards the stiffer medium is consistent with the results in Figure B.6 and not compensated for by the proposed correction factor.

B.6 Conclusion

We have demonstrated a geometric compensation necessary to correct for the observed bias in STL-SWEI imaging. The time delay measured at an offset tracking location is demonstrated to represent the local elasticity between the leading edges of the two push beams, and not the area between the center of the beams. When using the TTPS estimator, we have shown through simulations that an appropriate correction profile can be measured experimentally from the observed initial displacements or based on *a priori* knowledge of the focal geometry and tissue properties. The corrected images show improved localization of the target and extend the useful depth of field. For multiple focal zones, such as with SSI excitations, the initial beam profile of each excitation is more appropriate than the initial shape of the compound shear wave.

STL-SWEI and MTL-SWEI images both have spatial bias in the interrogation dimension, between pairs of push beams and track beams, respectively. As demonstrated here, the bias in STL-SWEI is a result of the geometry of the radiation force excitation and is more readily corrected for than the bias in MTL-SWEI, which is dependent on the specific 3-D scatterer distribution within the tracking beam's PSF. Because the radiation force pattern can be estimated with more certainty than the local scatterer distribution, STL-SWEI images can be constructed to compensate for thie spatial bias, allowing for high resolution imagingof small targets.

Appendix C

A Multiresolution Approach to Shear Wave Image Reconstruction

This chapter is in review for publication with IEEE TUFFC, and is presented in its entirety. It is also the basis of a patent application that was submitted in 2014. This work represents the application of classical inverse problem methods to the task of shear wave speed estimation, and moreover presents a way of thinking about shear wave speed estimation more abstractly. Because it addresses only random errors and not speckle bias, it doesn't solve the first-order noise problem in MTL-SWEI (chapter 5), and wound up being more computationally expensive than we cared to implement, especially considering the volume of data we would be getting in vivo (chapter 7). As computation power increases and we continue to develop micro-elasticity STL-SWEI systems, we can expect this algorithm to make a return.

C.1 Abstract

The group velocity of a propagating shear wave can be estimated by comparing the motion of the medium in which the wave is traveling at two or more points along the path of propagation. In a non-dispersive medium, the motion signals recorded at each pair of points will be time-delayed, scaled versions of each other, with the ratio of spatial separation of the points Δx to the arrival time difference Δt being equal to the group velocity c that, in linear elastic materials, is proportional to the square root of the shear modulus G. Because the time delay between any pair of locations is proportional to the distance between them, there is an inherent trade-off between robustness to noise and resolution based on the number and spacing of the receive points used for each estimate. This work proposes a method of using the time delays measured between all combinations of receiver pairs to estimate a noise-robust, high-resolution image. The time-of-flight problem is presented as an overdetermined system of linear equations that can be directly solved with or without spatial regularization terms. Finite element method simulations of acoustic radiation force-induced shear waves are used to illustrate the method, demonstrating superior contrast-to-noise ratio and lateral edge resolution characteristics compared to linear regression of arrival times. The application and limitations of this method are discussed.

C.2 Introduction

Measuring the group or phase velocity of an induced transverse mechanical wave propagating through a region of interest (ROI) has become an increasingly popular way to characterize tissue elastic properties for the purposes of diagnosis, staging,

and treatment guidance, among others (Bercoff et al., 2004; Kanai, 2005; Huwart et al., 2006; Palmeri et al., 2008; Bouchard et al., 2009b; Muller et al., 2009; Hollender et al., 2010; Nenadic et al., 2011; Arnal et al., 2011; Couade et al., 2011; Hollender et al., 2012; Rotemberg et al., 2012). Ultrasound has provided a convenient means of both generating and tracking mechanical waves, using high-intensity ultrasonic pulses to deliver momentum to the tissue through the effect of acoustic radiation force (Nightingale et al., 2003), and high-framerate ultrasonic imaging to image the propagation of the induced vibrations. This modality is known as "shear wave elasticity imaging" (SWEI). Magnetic resonance imaging (MRI) has also been used to track vibrations induced by an external mechanical vibrator in a modality called "magnetic resonance elastography" (MRE)(Manduca et al., 2001).

It is important to make the distinction between using the *averaged* velocity of a transverse wave to characterize the modulus of an entire region of tissue, such as in fibrosis staging, from the task of using the *local* velocity of the wave to generate images of elasticity, such as for lesion visualization. In the former task, it is of interest to use as large of an ROI as possible both to average out local variations in imaged wave propagation and to feed as much data into the model as possible. For the task of imaging local propagation velocity, though, it is of interest to use the smallest possible ROI to maximize resolution while maintaining accuracy. This trade-off makes the optimization problem more challenging and interesting. While moving linear regression with a kernel size selected to balance stability and accuracy with resolution has been commonly used, the algorithm presented here seeks to maximize the data fed into our model prior to the specification of spatial regularization and thus minimize the effect of time-delay jitter while maintaining high resolution.

C.3 Background

Sarvazyan *et al.* Sarvazyan et al. (1998) proposed the idea of using an ultrasonically-induced mechanical shear wave to measure material properties by characterizing the propagation velocity of the wave, demonstrating that in a semi-infinite, linear elastic medium, the shear velocity c would be proportional to the square root of Young's modulus E:

$$c = \sqrt{\frac{E}{2\rho(1+\nu)}} = \sqrt{\frac{G}{\rho}}, \tag{C.1}$$

where ρ is the density, ν is Poisson's ratio, and G is the shear modulus. Under assumptions of incompressibility ($\nu \approx 0.5$) and a density close to water ($\rho \approx 1.0 g/ml$), one must only measure the shear velocity to estimate Young's modulus. To estimate shear velocity, Sarvazyan *et al.* proposed finding the time of peak displacement at a number of receive locations along the path of the wave's propagation and fitting the arrival times by linear regression, assuming homogeneity within the ROI. In the subsequent 15 years, researchers have used a variety of techniques to convert imaged tissue motion into an estimate of wave velocity. Nightingale *et al.* Nightingale et al. (2003) used pseudo-direct inversion of the Helmholtz equation to reconstruct shear velocity images from a single excitation, noting the noisiness of the estimates. Rouze *et al.* Rouze et al. (2010) and Wang *et al.* Wang et al. (2010) developed model-based approaches to better estimate shear velocities within homogeneous regions, while Palmeri *et al.* Palmeri et al. (2010) characterized heterogeneous tissues with local linear regressions of the arrival time differences. Rouze *et al.* Rouze et al. (2012) analyzed various time-of-flight (TOF) methods, looking for the ideal kernel size for local reconstructions. Meanwhile, McAleavey *et al.* McAleavey et al. (2007) used a spatially-modulated source function to estimate shear velocity from a single recording location, and extended the method to create images using a fixed spa-

tial distance between the source functions and the receive location McAleavey et al. (2009a); Elegbe and McAleavey (2013), trading tracking waves from a single excitation at multiple track locations for tracking a single location, and using a synthetic shear wave generated from multiple offset excitations. Bercoff *et al.* Bercoff et al. (2004) proposed Helmholtz inversion in the Fourier domain, as well as estimation by cross correlation of pairs of receive lines to create images. McLaughlin *et al.* used level set inversion of arrival times relative to a single point and the Eikonal equation for shear wave speed estimation (McLaughlin and Renzi, 2006b,a), and Oberai *et al.* used the adjoint method (Oberai et al., 2003).

C.4 Time of Flight Estimation

In accordance with the wave equation for a propagating cylindrical wave, for any pair of recording locations located along the axis of propagation away from a shear wave source in a linear elastic homogeneous medium, the signals of tissue motion at each location $u(x,t)$ will be scaled, time-delayed versions of the each other. The time delay reflects the shear wave velocity between the recording locations, and the amplitude decreases with distance from the source of the induced wave:

$$u(x_j,t) = \left(\frac{x_i}{x_j}\right) u\left(x_i, t - \left(\frac{x_j - x_i}{c}\right)\right), \tag{C.2}$$

where u is the axial displacement, x is the distance from the excitation, t is the time after excitation, and c is the shear velocity. In a heterogeneous medium, the propagation of the wave is affected by the local stiffness, so c becomes $c(x)$ and Equation C.2 becomes:

$$u(x_j,t) = \left(\frac{x_i}{x_j}\right) u\left(x_i, t - \left(\int_{x_i}^{x_j} \frac{1}{c(x)} dx\right)\right). \tag{C.3}$$

Now the time delay is dependent on the *averaged* compliance between the recorded locations. This assumes that the derivative of $c(x)$ is small relative to the wavelength

such that there is negligible reflection. In the case of a single, significant reflection, we can readily split $u(x,t)$ into its transmitted and reflected components $u_T(x,t)$ and $u_R(x,t)$, which are scaled by transmission and reflection coefficients, respectively. For multiple reflections, additional wave components must be added. In practice, a directional filter can be used to suppress the reflected wave components in post-processing Deffieux et al. (2011), and time delay estimators can be made robust to variations in signal amplitude through normalization. There are a number of existing methods to estimate the time delay between the two signals, including sum-of-absolute differences, normalized cross-correlation, and phase-based methods. The "arrival time" of the wave at each particular point can also be estimated directly from some feature of the recorded signal, such as the sample with the greatest displacement from the reference ("time-to-peak" (TTP)), or the greatest velocity (the derivative of displacement through tracking time, "time-to-peak-slope" (TTPS)). When directly estimating arrival time, the velocity can be found from the difference in arrival times between two points or from a set of arrival times such as with a moving linear regression. The algorithm proposed here uses independently-estimated relative time delay estimates, whereas the linear regression method provided for comparison uses directly-estimated arrival times via TTPS.

C.5 Algorithm

For N discrete receiver locations, there are N^2 possible sets of time delay pairs. We assume that all N receivers are located colinearly along the direction of wave propagation, and that the source of the wave is outside of the receiver positions. To form a consistent set, the delays must obey a set of rules:

1. $\Delta t_{ii} = 0$. A signal compared with itself will indicate no time delay,

2. $\Delta t_{ij} = -\Delta t_{ji}$. The delay is the same regardless of which signal is the reference,

3. $\Delta t_{ij} + \Delta t_{jk} = \Delta t_{ik}$. The delay between two points is the sum of delays along any path that connects the points.

By this formulation, we have N-1 degrees of freedom, the time delays $\Delta T_{i(i+1)}$, which are each the denominator term for the corresponding local shear wave velocity:

$$c_{i(i+1)} = \frac{x_{i+1} - x_i}{\Delta T_{i(i+1)}} = \frac{1}{\int_{x_i}^{x_{i+1}} \frac{1}{c(x)} dx}. \tag{C.4}$$

To take advantage of multiple estimates, each of the observations Δt_{ij} is expressed as the linear combination of the parameters $\Delta T_{i(i+1)}$, that is:

$$\Delta t_{ij} = \sum_{k=i}^{j-1} \Delta T_{k(k+1)}, \text{for } j > i, \text{ and} \tag{C.5}$$

$$\Delta t_{ij} = -\sum_{k=j}^{i-1} \Delta T_{k(k+1)} \text{for } j < i. \tag{C.6}$$

Expressed in matrix form $\mathbf{A}\vec{b} = \vec{y}$, with $\vec{b} = \Delta\vec{T}$ and $\vec{y} = \vec{\Delta t}$:

$$\begin{bmatrix} 1 & 0 & 0 & \cdots & 0 \\ 1 & 1 & 0 & & 0 \\ 1 & 1 & 1 & & 0 \\ & \vdots & & \ddots & \\ 1 & 1 & 1 & & 1 \\ 0 & 1 & 0 & \cdots & 0 \\ 0 & 1 & 1 & & 0 \\ & & & \ddots & \\ 0 & 0 & 0 & & 1 \end{bmatrix} \begin{bmatrix} \Delta T_{12} \\ \Delta T_{23} \\ \Delta T_{34} \\ \vdots \\ \Delta T_{(N-1)N} \end{bmatrix} = \begin{bmatrix} \Delta t_{12} \\ \Delta t_{13} \\ \Delta t_{14} \\ \vdots \\ \Delta t_{1N} \\ \Delta t_{23} \\ \Delta t_{24} \\ \vdots \\ \Delta t_{(N-1)N} \end{bmatrix}. \tag{C.7}$$

The problem has been turned into a classical inverse problem, and to recover $\vec{\Delta T}$, we can invoke the linear least-squares solution:

$$\vec{\Delta T} = \left(\mathbf{A}^T\mathbf{A}\right)^{-1}\mathbf{A}^T\vec{\Delta t}. \tag{C.8}$$

Notably, the least-squares solution can be expressed as a linear transformation of the observations, and the matrix inversion step can be performed *a priori* on our condition matrix $\mathbf{A}$. Because $\mathbf{A}$ has such a simple structure, we can look at $\left(\mathbf{A}^T\mathbf{A}\right)^{-1}\mathbf{A}^T$ explicitly to build an intuition about the solution. As an example, we consider the case where we have three receive locations, giving us three observations Δt_{12}, Δt_{23}, and Δt_{13}:

$$\begin{bmatrix} 1 & 0 \\ 0 & 1 \\ 1 & 1 \end{bmatrix} \begin{bmatrix} \Delta T_{12} \\ \Delta T_{23} \end{bmatrix} = \begin{bmatrix} \Delta t_{12} \\ \Delta t_{23} \\ \Delta t_{13} \end{bmatrix}. \tag{C.9}$$

The solution for the high-resolution estimates ΔT_{12} and ΔT_{23} takes the following form:

$$\Delta T_{12} = \frac{2}{3}\left(\Delta t_{12}\right) + \frac{1}{3}\left(\Delta t_{13} - \Delta t_{23}\right) \tag{C.10}$$

$$\Delta T_{23} = \frac{2}{3}\left(\Delta t_{23}\right) + \frac{1}{3}\left(\Delta t_{13} - \Delta t_{12}\right). \tag{C.11}$$

Intuitively, this makes sense. We have the direct observation of our estimate, and the two others whose difference must be equal to the first. The direct observation is preferentially weighted. Expanding this notion to find a high-resolution estimate from all multiresolution estimates within n samples of the estimate, a pattern emerges in the linear combination applied to the nearby observations (the row of $\left(\mathbf{A}^T\mathbf{A}\right)^{-1}\mathbf{A}^T$ corresponding to the estimate). Figure C.1 shows the coefficients as a filter that can

be applied to the main diagonal of the matrix containing all observations Δt_{ij} for varying neighborhood sizes to estimate ΔT_{ij}.

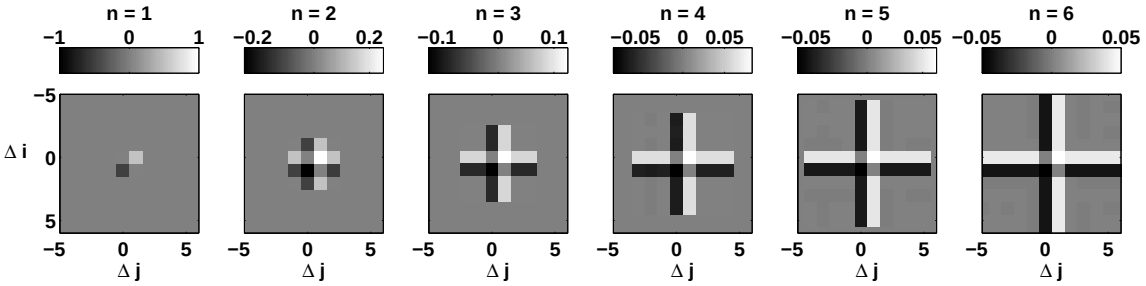

FIGURE C.1: The least-squares multiresolution solution for a high-resolution estimate ΔT_{ij}, expressed as a filter applied to a localized set of time delays with kernel size n. The upper-right half of the matrix is the forward observations $\Delta t_{ij}, (j > i)$, and the lower-left half is the reverse observations $\Delta t_{ij}, (j < i)$, which are negatively symmetric.

With no multiresolution kernel ($n = 1$), the estimate $\Delta T_{i(i+1)}$ is simply the average of the forward and reverse estimates $\Delta t_{i(i+1)}$ and $-1 * \Delta t_{(i+1)i}$, which, for cross-correlation, are identical. For larger multiresolution kernels, the solutions include all of the two-observation multipath combinations that yield the estimate with $|i - j| \leq n$ samples. From this formulation, we can also introduce the idea of spatial regularization, to favor solutions that are more smooth. Using Tikhonov regularization (Golub et al., 1999), the solution becomes:

$$\Delta\vec{T} = \left(\mathbf{A}^T\mathbf{A} + \lambda\mathbf{\Gamma}^T\mathbf{\Gamma}\right)^{-1}\mathbf{A}^T\Delta\vec{t} \tag{C.12}$$

where $\mathbf{\Gamma}$ is a regularization matrix, scaled by the regularization factor λ. To favor solutions with small first derivatives, we choose the difference operator for $\mathbf{\Gamma}$. As we increase λ, we favor solutions that are increasingly smooth. This can be seen in the filter metaphor, shown in Figure C.2.

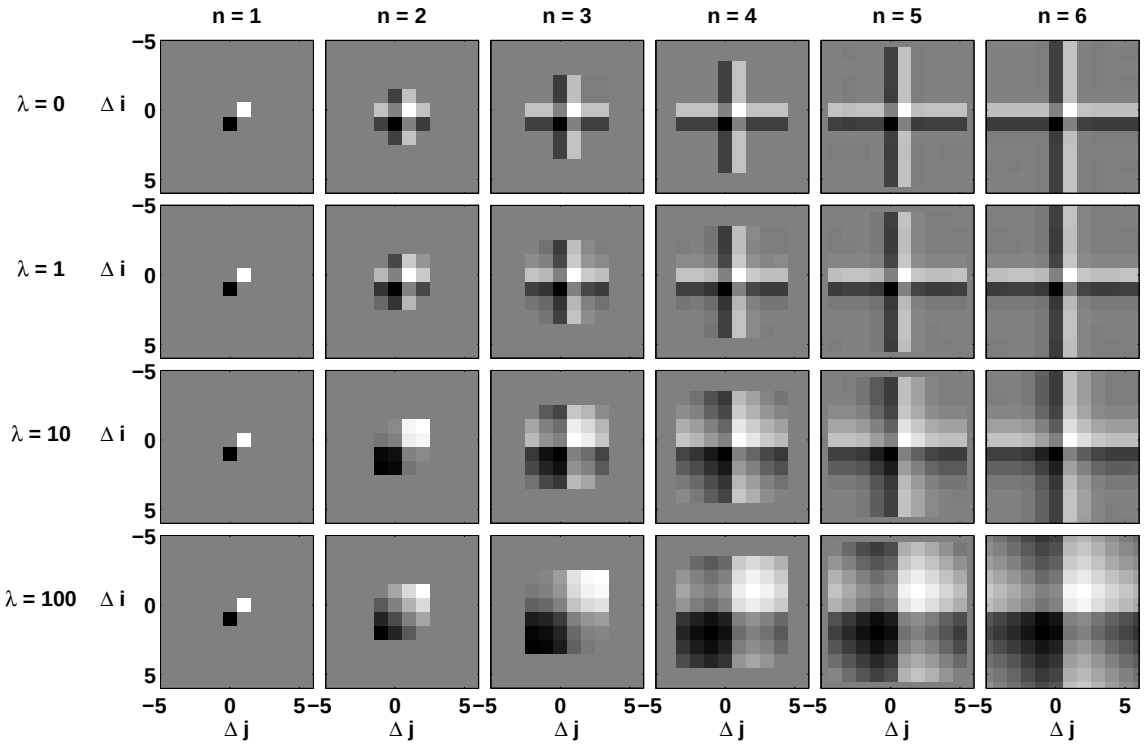

FIGURE C.2: The least-squares solution for a high-resolution estimate ΔT_{ij}, expressed as a filter applied to neighboring multiresolution observations with kernel size n and including varying degrees of first-order difference Tikhonov regularization λ. As λ increases, the solution looks increasingly like a low-resolution version of the no-multiresolution filter.

C.6 Finite Element Method Simulation

To demonstrate the performance of the algorithm, a finite element method (FEM) simulation of a shear wave generated by acoustic radiation force was created using LS-DYNA. The simulated radiation force excitation and shear wave response in tissue have been previously validatedPalmeri et al. (2005). A Siemens Acuson ER7B linear array transducer was simulated for a 6 MHz excitation, with a transmit focus of 15 mm at F/3. The induced shear wave was recorded at 1,000 fps with lateral spacing of 0.2 mm over 6 mm to the right of the excitation. The elastic material was simulated with a Young's modulus of 4.5 kPa on the left side and 24 kPa on the right side with a vertical layer boundary 3 mm to the right of the excitation. The axial displacements

calculated from the FEM simulation were used without simulated ultrasonic tracking.

A directional filter was applied to the displacements to remove reflected componentsDeffieux et al. (2011). The time delays between each lateral pair of tracking locations was computed via normalized cross-correlation of the tissue velocity signals at each pixel with the same depth for the multiresolution algorithm, and the arrival times were estimated directly from the peak of same signals with parabolic subsample peak interpolation. For linear regression, kernels between 2 points (0.2 mm) and 18 points (3.4 mm) were used and the same kernels were used for the multiresolution extent. Normally distributed random noise was applied to the time delays with standard deviations σ_e between 0 and 0.1 ms applied to each time delay or arrival time. Sixteen noise realizations were used for each experiment. For regularization of the multiresolution scheme, Tikhonov regularization was applied to the first difference of $\Delta T_{i(i+1)}$, with λ values between 0 and 100:

$$\mathbf{\Gamma} = \frac{1}{2}\begin{bmatrix} 1 & -1 & 0 & & \cdots & & 0 \\ 0 & 1 & -1 & 0 & \cdots & & 0 \\ & & & \ddots & & & \\ 0 & & \cdots & & 0 & -1 & 1 \end{bmatrix}. \tag{C.13}$$

To calculate CNR, the average velocity on each side of the vertical boundary was used, bounded axially about the focus between 10 and 20 mm, and laterally between 1.5 and 2.5 mm to the side of the boundary. CNR was computed as:

$$CNR = \frac{|\mu_L - \mu_R|}{\sqrt{\sigma_L^2 + \sigma_R^2}}, \tag{C.14}$$

where μ_L and μ_R are the means of $c(z, x)$ to the left and right of the boundary, and σ_L and σ_R are the respective standard deviations. Edge resolution was calculated as the 20–80% rise distance w for a piecewise linear function fit to $c(x)$ averaged

between 10 and 20 mm axially:

$$c(x) = \begin{cases} \mu_L & \text{if } x < -w/2 \\ \dfrac{\mu_R - \mu_L}{w} x + \dfrac{\mu_R + \mu_L}{2} & \text{if } |x| \leq w/2 \\ \mu_R & \text{if } x > w/2 \end{cases} . \tag{C.15}$$

C.7 Results

Figure C.3 shows the axial tissue velocity at the focal depth for a wave generated on the left side of the ROI ($x = -3$ mm) and propagating to the right, encountering a boundary at $x = 0$ mm. A directional filter has been applied to the data to remove the reflected wave. The change in shear wave velocity is apparent in the slope of the directly estimated arrival time, drawn as a black line.

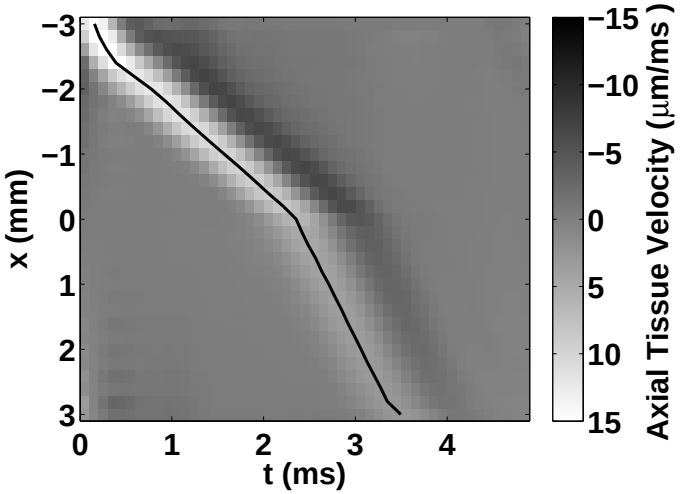

FIGURE C.3: Axial tissue velocity as a function of lateral position and time for a wave generated at $x = -3$ mm and tracked as it propagates to the right, encountering a boundary at $x = 0$ mm. A directional filter has been used to remove the reflected wave. The directly-estimated arrival time is shown as a black line.

Figure C.4 shows estimated time delays for every pair of receive locations at the focal depth. There is a vertical boundary at $x = 0$ mm. The main diagonal ($x_i = x_j$) has time delays that are identically zero while those in the upper-right ($x_j > x_i$) are

positive and those in the lower-left ($x_j < x_i$) are negative. In both directions, the time delay scales with $|x_i - x_j|$ such that estimates closer to the main diagonal are higher-resolution than those in the upper-right and lower-left corners.

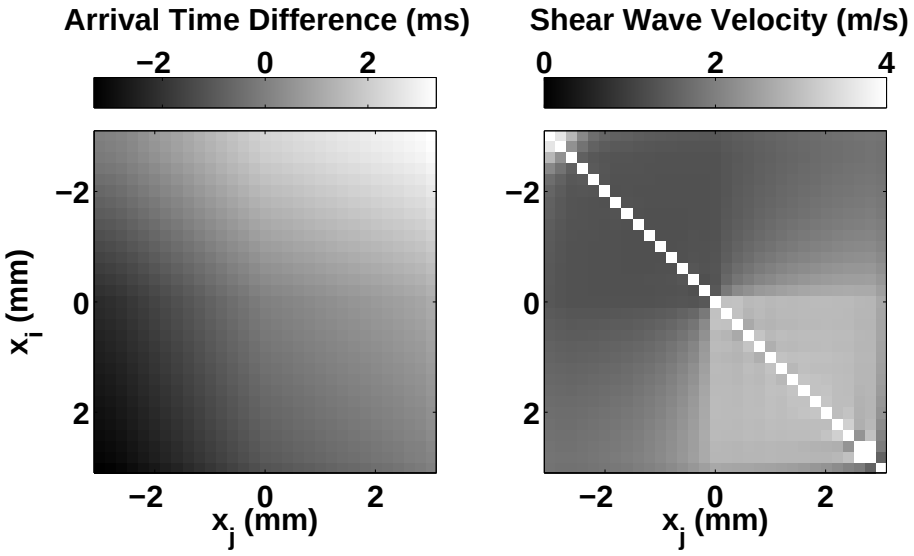

FIGURE C.4: (left) All combinations of time delay estimates for a wave excited at $x = -3$ mm, propagating across a boundary at $x = 0$ mm. As the pair of tracking locations gets farther apart ($|x_i - x_j|$ gets larger, so does the measured time delay. (right) The time delays, converted to velocity estimates. The degradation is resolution is apparent away from the main diagonal, as the layer boundary becomes blurred.

Each time delay pair Δt_{ij} in the left panel of Figure C.4 corresponds to a shear velocity estimate, and those estimates are shown in the right panel. The boundary is apparent, as is the degradation in resolution associated with using estimates with greater spacing.

The directly-estimated arrival times from Figure C.3, with varying degrees of additive noise, were fed through moving linear regression filters, while the relative time delay pairs were given the same additive noise and fed through the multiresolution filters. Figure C.5 shows shear wave images of a simulated phantom, using a moving linear regression of size K to estimate the shear wave velocity from the arrival times. Each column shows an increasing amount of jitter on the arrival time

estimates, and each row shows an increasing filter size. In the presence of noise, the boundary becomes clearer as the filter increases, but edge resolution gets worse.

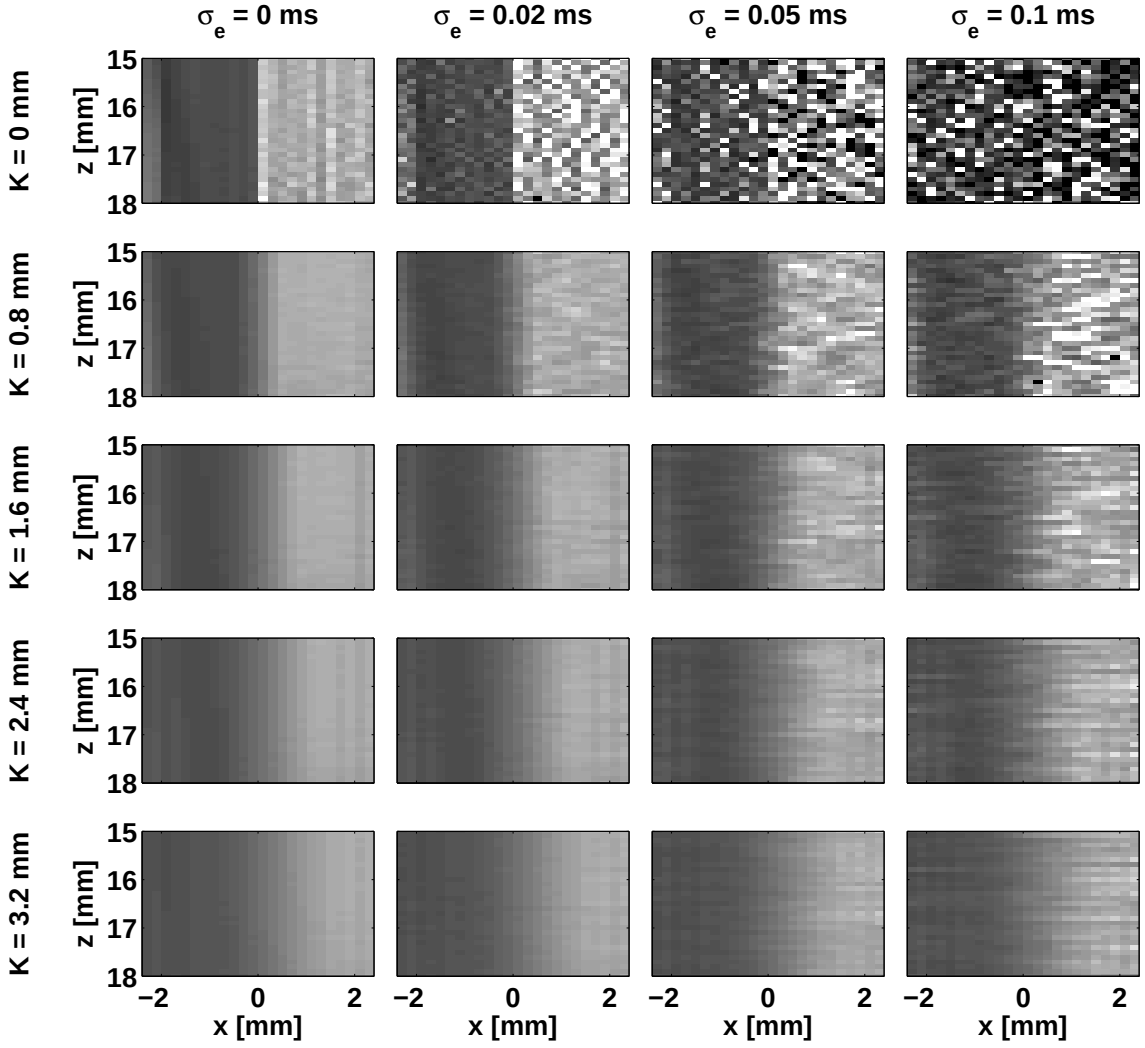

FIGURE C.5: Shear wave images of a simulated phantom using moving linear regression kernels of size K on the high-resolution arrival time differences. Noise is reduced for larger kernels, but so is resolution.

Figure C.6 shows the equivalent shear wave images as Figure C.5, but uses the multiresolution filter instead of the linear regression filter, combining all combinations of arrival time differences within the kernel. Noise is reduced as the filter size is increased, but without an apparent corresponding loss in resolution.

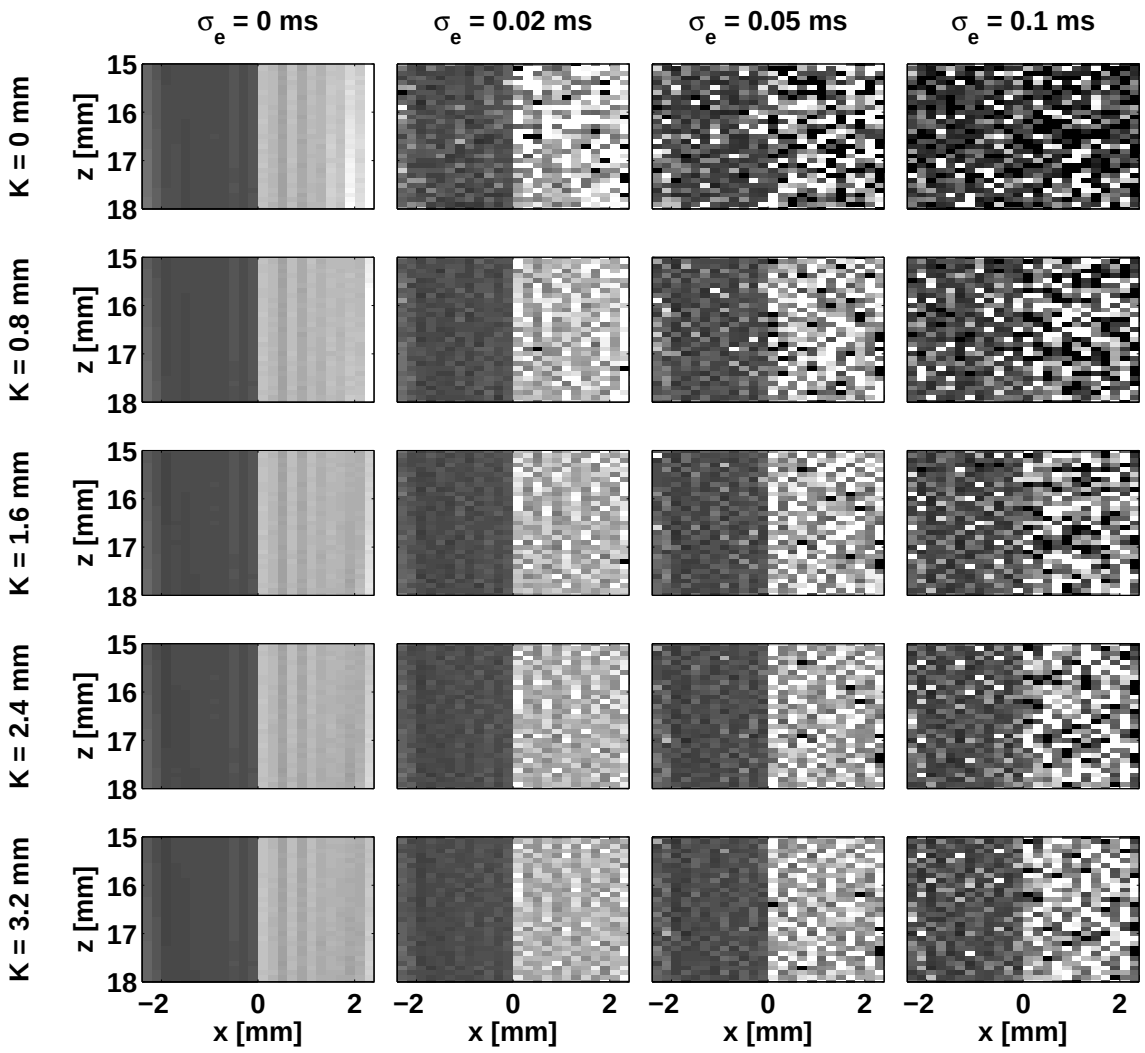

FIGURE C.6: Shear wave images of a simulated phantom using multiresolution kernels of increasing size K. Noise is reduced for larger kernels, while maintaining edge resolution.

Lateral variation near the boundary in Figure C.6 is not reduced by the multiresolution filter alone. Figure C.7 shows the effect of regularization for a 1.6 mm multiresolution kernel size. Increasing the regularization scaling λ suppresses noise at the expense of resolution.

To quantify the observations about noise suppression and resolution, Figure C.8 shows contrast-to-noise ratio (CNR) as a function of kernel length for a moving linear regression filter of arrival times, on the upper-left, and multiresolution filter

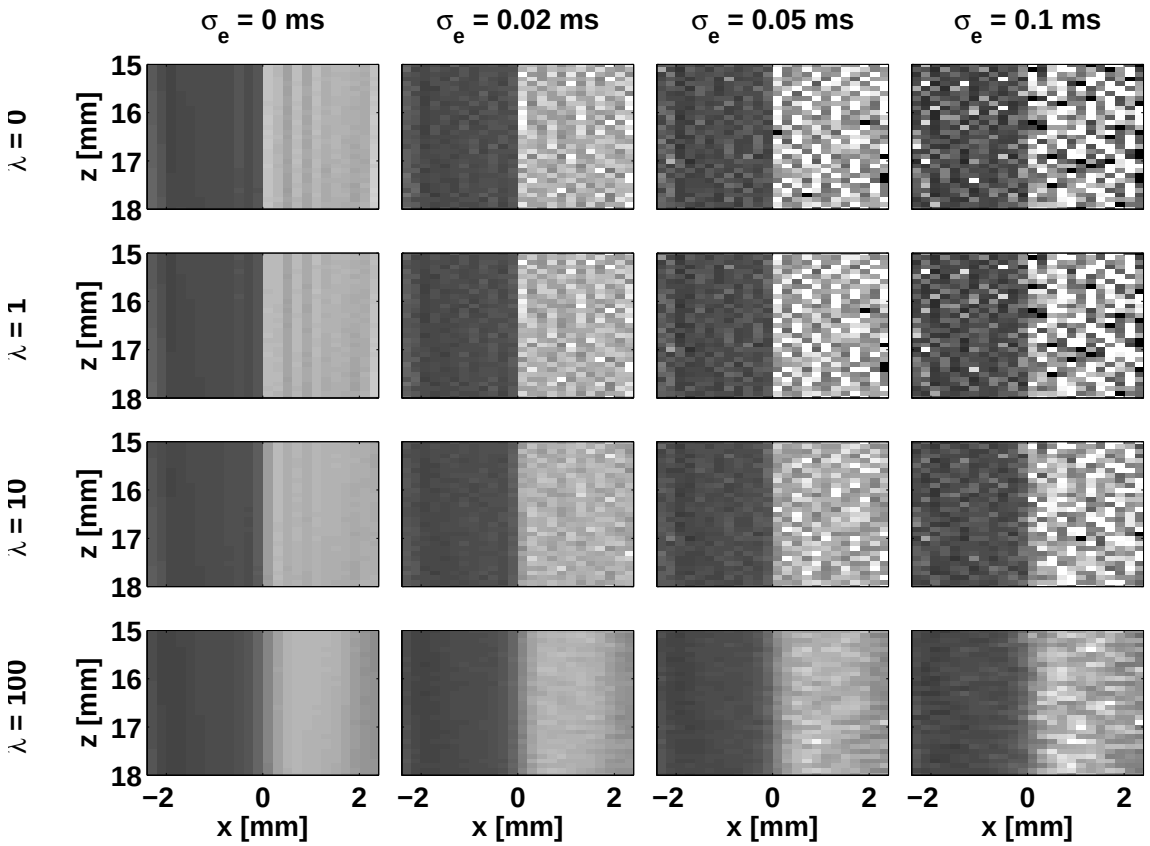

FIGURE C.7: Shear wave images for the simulated phantom using a 1.6 mm multiresolution kernel for different levels of noise and regularization. Higher vales of λ reduce the noise at the expense of resolution.

length, on the upper-right, at different arrival time noise levels. Error bars represent the standard deviation over sixteen noise realizations. As noise increases, larger kernels are needed to achieve a given CNR. With no regularization, linear regression shows higher CNR. The lower-right panel shows that increasing the scaling of the Tikhonov regularization term λ causes significant increases in CNR, surpassing the linear regression CNR values.

To illustrate how the increase in CNR afforded by Tikhonov regularization is accompanied by a corresponding decrease in edge resolution, Figure C.9 shows the matched CNR and resolution (20–80% edge width) values for each value of λ, and at each noise level. For higher-resolution images, a lower value of λ is shown to be

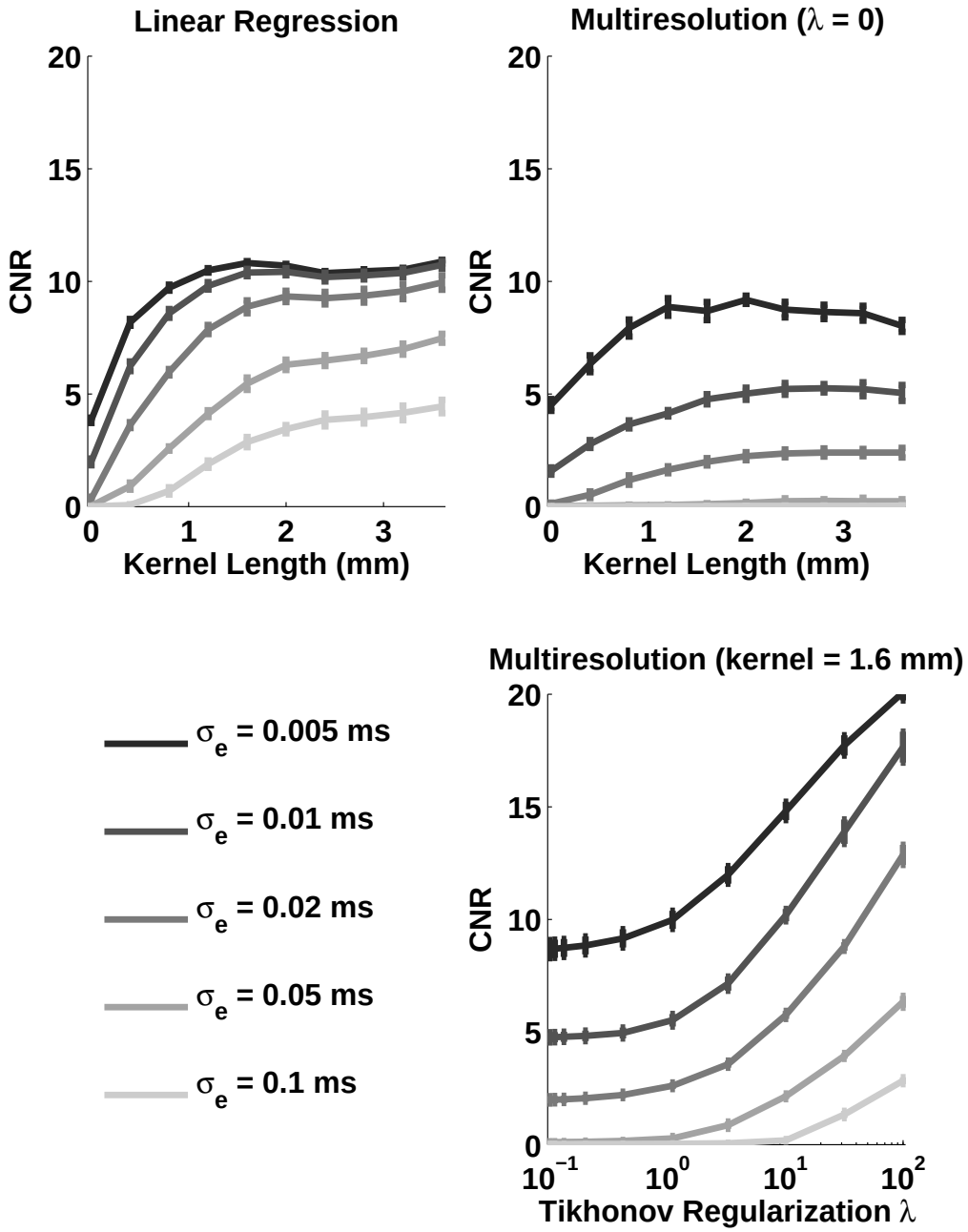

FIGURE C.8: CNR for different levels of noise, as a function of multiresolution kernel size for linear regression (left), multiresolution kernel size with no regularization (center), and regularization parameter λ with a 1.6 mm multiresolution kernel (right).

desirable, while for greater noise suppression, higher λ is preferred.

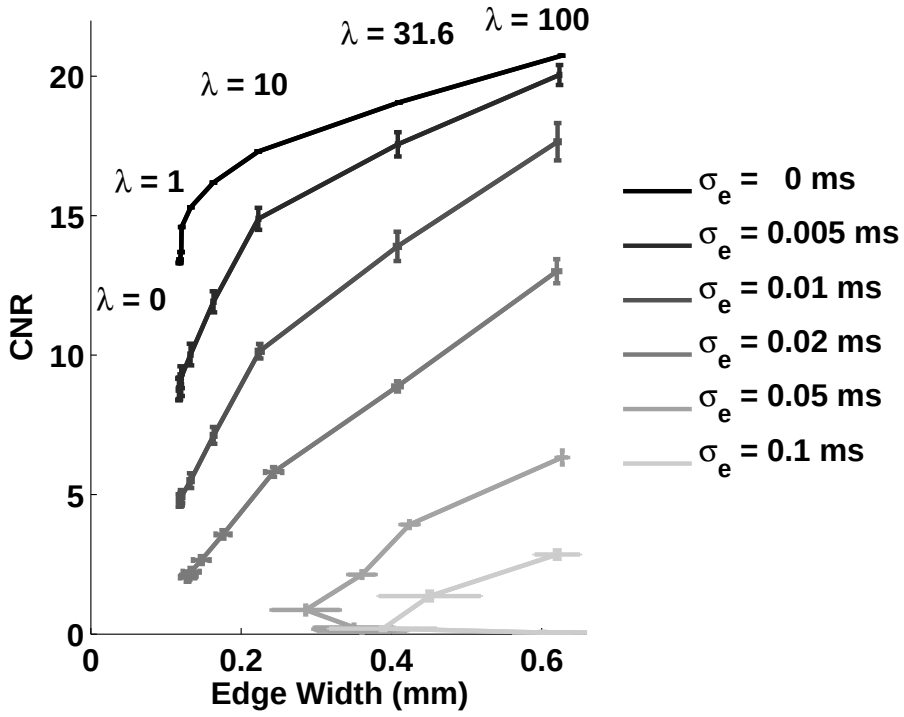

FIGURE C.9: CNR-resolution regularization trade-off curve for 1.6 mm multiresolution kernel. The lower-left point of each curve (highest resolution, lowest CNR) is $\lambda = 0$, and the upper-right point (lowest resolution, highest CNR) is $\lambda = 100$.

To compare the trade-off of CNR and resolution in the multiresolution scheme against the same trade-off for linear regression, Figure C.10 shows both trade-off curves, using a kernel of 1.6 mm and varying λ for the multiresolution scheme, and varying kernel length for linear regression. The noise level was set to 5 μs. With no regularization ($\lambda = 0$), multiresolution filtering has slightly lower CNR than linear regression using the same 1.6 mm kernel, but for any given CNR value achieved by linear regression, the multiresolution scheme can achieve the same CNR through regularization with significantly better resolution.

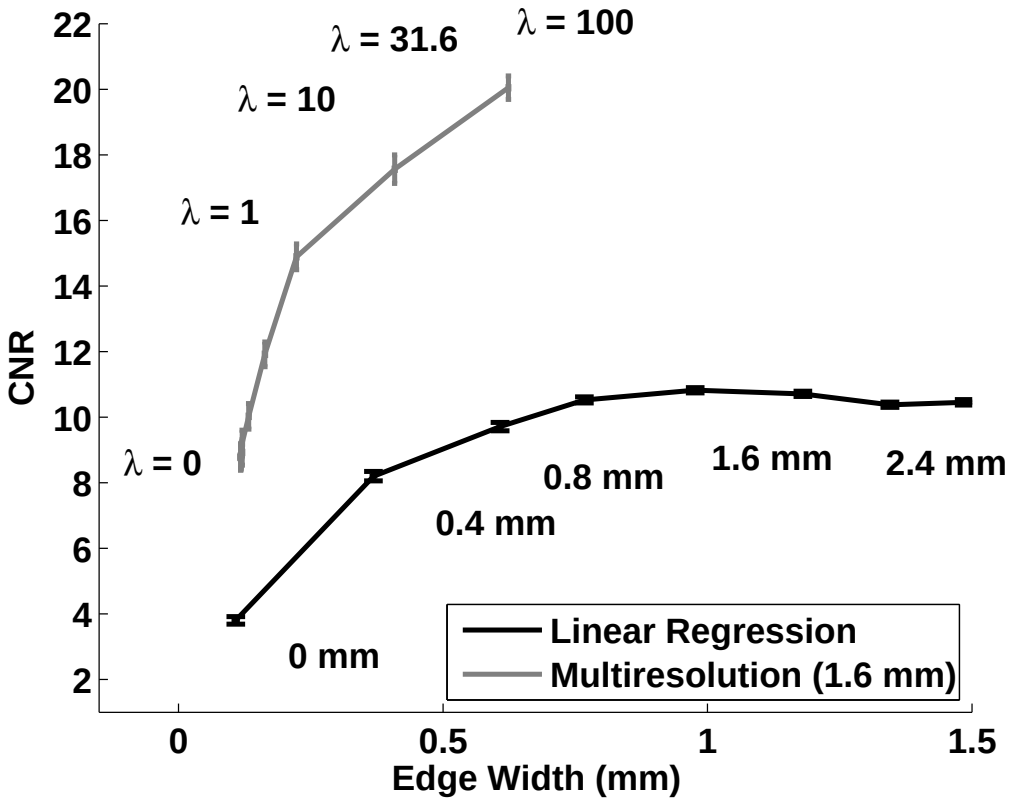

FIGURE C.10: CNR-resolution trade-off curves for multiresolution (circles) and linear regression (squares) at the $\sigma_e = 5$ μs noise level. Multiresolution uses a 1.6 mm kernel and varies the regularization term λ, while linear regression directly varies filter size.

C.8 Discussion

C.8.1 Comparison to Linear Regression

The multiresolution approach to time-of-flight estimation central to shear wave image reconstruction presented here provides better suppression of uncorrelated time-delay jitter than linear regression with less loss in spatial resolution. Because the quantity of data fed into the model is maximized prior to any spatial regularization, the CNR-resolution tradeoff curve (Figure C.10) can maintain higher CNR at a given resolution or better resolution at a given CNR compared to linear regression by appropriate selection of regularization parameter λ. Linear regression can successfully

suppress jitter (Figure C.5), but does so at the expense of lateral resolution, seen as a blurring of the boundary. For very noisy arrival time estimates, the visual conspicuity of small structures would be lost either in the noise or in the regression. The multiresolution approach without regularization is equivalent to a weighted average of all combinations of time delays that sum to give the high-resolution time delays (Figure C.1). This serves to maximally reduce jitter (Figure C.6) while preserving the spatial independence of the estimates. For additional noise suppression or for dealing with correlated noise, the use of regularization allows controlled used of neighboring information to influence each estimate. Figure C.2 demonstrates this performance explicitly. As the regularization term λ increases, estimates between points outside of the high-resolution pair Δt_{ij} are given increasing weight. For large λ, the filter starts to look like a large version of the $n = 0$, $\lambda = 0$ case, which is just a lower-resolution estimate, more resistant to a given jitter level, since the size of the actual time delay is larger compared to the error. Figure C.7 demonstrates the use of regularization, suppressing even high levels of jitter in exchange for a relatively small reduction in resolution. Tikhonov regularization of the slope is comparable to linear regression in terms of the noise-reduction/resolution trade-off, but the multiresolution form already has the redundant-estimate averaging in place, so starts at a relatively higher CNR. The other advantage of using Tikhonov regularization is that λ can take on any value, while linear regression must be specified in terms of samples, providing more precise control of the CNR-resolution trade-off.

C.8.2 Limitations

The first limitation of the multiresolution approach to shear wave speed estimation is added computational complexity. For N receive locations, N^2 cross-correlations can be performed, compared to the N arrival time estimates that must be performed to linear regression. The total number of cross-correlations can be reduced, however,

by only finding time delays Δt_{ij} for $j > i$, using the first two continuity constraints ($\Delta t_{ii} = 0$ and $\Delta t_{ij} = -1 * \Delta t_{ji}$, respectively) to fill in the rest of the estimates. This reduces the number of cross-correlations to $N(N-1)/2$, but the multiresolution approach is still $\mathbf{O}(N^2)$, compared to $\mathbf{O}(N)$ for linear regression. Further reductions are possible by only considering estimates up to $|j-i| = n$ (Figure C.1). This reduces the number of correlations to $n(N-(n+1)/2)$, which brings the order down to $\mathbf{O}(N * n)$, but still requires more correlations than linear regression. Choosing a large n could provide greater noise reduction but requires more computation, and estimates with very large Δx_{ij} may have low correlation coefficients and be less useful when estimating $\Delta t_{ij} = \Delta t_{ik} - \Delta t_{jk}$ for $k \gg j$. A trade-off between noise reduction gains and computational complexity therefore exists, and in practice is addressed by selecting an appropriate value of n. This could be addressed more rigorously, however, by introducing weighting to the least-squares solution:

$$\Delta\vec{T} = \left(\mathbf{A}^T\mathbf{W}\mathbf{A}\right)^{-1}\mathbf{A}^T\mathbf{W}\Delta\vec{t} \tag{C.16}$$

The weights can be chosen based on peak cross-correlation coefficient and/or *a priori* knowledge (de-weighting estimates with $j \gg i$, for example). If the weighting is based on the data, however, the least-squares solution cannot be precomputed and must be calculated for each estimate. This requires matrix inversion for every sample, further increasing the computational load. Future work will explore the use of weighting to improve the estimates.

The second limitation of the multiresolution approach is that it primarily reduces uncorrelated jitter on the time-delay cross-correlations. It may also reduce reflection artifacts, since errors due to the reflected wave change for different receiver pairs, but it does not assist with the reduction of biased time delay data. An error in receiver position due to the local scattering random walk will be consistent across all estimates, and all multiresolution paths to the estimate will yield the same biased

result. The speckle bias is likely to be the dominant source of noise when using multiple tightly-spaced tracking locations, so this algorithm may provide the most benefit to single tracking location (STL) SWEI, which is theoretically free of speckle bias Elegbe and McAleavey (2013). However, even if the multiresolution estimation does not address the speckle bias in multiple-track location (MTL) SWEI imaging, phrasing the problem in this way still provides access to the suite of tools for solving and regularizing inverse problems and opens may possibilities beyond simple linear regression.

C.9 Conclusion

This work poses the shear wave time-of-flight estimation problem for multiple tracking locations as a classic overdetermined linear systems inverse problem and examines the performance of some basic solution strategies, demonstrating improved CNR and resolution compared to simple linear regression in the presence of jitter on the time-delay estimates. The averaging of noisy data using multiple estimates and the reduction in resolution are separated in the multiresolution approach, compared to linear regression where they are tied to the integer-sample-limited kernel size. Spatial constraints on the multiresolution solution are imposed by Tikhonov regularization for additional noise suppression at the expense of resolution. This work motivates further exploration of the inverse problem approach to shear wave velocity estimation, as it opens the field to a wide array of research, algorithms, and techniques that have been used for years in other applications. As computational power increases and the number of tracking locations imaged for a shear wave rises, new opportunities for leveraging the volume of data arise to improve the quality and diagnostic usefulness of shear wave images.

Bibliography

Abramoff, M., Magalhaes, P., and Ram, S. (2004), "Image Processing with ImageJ," *Biophotonics International*, 11, 36–42.

Adams, J., Trent, R., and Rawles, J. (1993), "Earliest electrocardiographic evidence of myocardial infarction: implications for thrombolytic treatment. The GREAT Group." *British Medical Journal*, 307, 409–413.

Arentz, T., Macle, L., Kalusche, D., Hocini, M., Jais, P., Shah, D., and Haissaguerre, M. (2004), "Dormant pulmonary vein conduction revealed by adenosine after ostial radiofrequency catheter ablation," *Journal of cardiovascular electrophysiology*, 15, 1041–1047.

Arnal, B., Pernot, M., and Tanter, M. (2011), "Monitoring of thermal therapy based on shear modulus changes: II. Shear wave imaging of thermal lesions," *Ultrasonics, Ferroelectrics and Frequency Control, IEEE Transactions on*, 58, 1603–1611.

Bercoff, J., Tanter, M., and Fink, M. (2004), "Supersonic shear imaging: a new technique for soft tissue elasticity mapping," *Ultrasonics, Ferroelectrics and Frequency Control, IEEE Transactions on*, 51, 396–409.

Berruezo, A., Tamborero, D., Mont, L., Benito, B., Tolosana, J. M., Sitges, M., Vidal, B., Arriagada, G., Méndez, F., Matiello, M., et al. (2007), "Pre-procedural predictors of atrial fibrillation recurrence after circumferential pulmonary vein ablation," *European Heart Journal*, 28, 836–841.

Bleeker, G., Steendijk, P., Holman, E., Yu, C.-M., Breithardt, O., Kaandorp, T., Schalij, M., van der Wall, E., Nihoyannopoulos, P., and Bax, J. (2006), "Assessing right ventricular function: the role of echocardiography and complementary technologies," *Heart*, 92, 19 – 26.

Bogen, D. K., Rabinowitz, S. A., Needleman, A., McMahon, T. A., and Abelmann, W. H. (1980), "An analysis of the mechanical disadvantage of myocardial infarction in the canine left ventricle." *Circulation Research*, 47, 728–41.

Bolli, R. (1990), "Mechanism of myocardial "stunning"." *Circulation*, 82, 723–38.

Bonow, R. O., Mann, D. L., Zipes, D. P., Libbey, P., and Braunwald, E. (2011), *Braunwald's Heart Disease - A Textbook of Cardiovascular Medicine*, vol. 1, Saunders, an Imprint of Elsevier, 9 edn.

Bouchard, R., Dahl, J., Hsu, S., Palmeri, M., and Trahey, G. (2009a), "Image quality, Tissue heating, and Frame Rate Trade-offs in Acoustic Radiation Force Impulse Imaging," *Ultrasonics, Ferroelectrics and Frequency Control, IEEE Transactions on*, 56, 63–76.

Bouchard, R., Hsu, S., Wolf, P., and Trahey, G. (2009b), "In Vivo Cardiac, Acoustic-Radiation-Force-Driven, Shear Wave Velocimetry," *Ultrasound Imaging*, 31, 201–213.

Bouchard, R., Hsu, S., Palmeri, M., Rouze, N., Nightingale, K., and Trahey, G. (2011), "Acoustic Radiation Force-Driven Assessment of Myocardial Elasticity Using the Displacement Ratio Rate (DRR) Method," *Ultrasound Med Biol.*, 37, 1087–1100.

Braunwald, E. and Kloner, R. A. (1982), "The stunned myocardium: prolonged, postischemic ventricular dysfunction." *Circulation*, 66, 1146–9.

Burkhardt, J. D. and Natale, A. (2009), "New technologies in atrial fibrillation ablation," *Circulation*, 120, 1533–1541.

Calkins, H., Brugada, J., and Packer, D. L. e. a. (2007), "HRS/EHRA/ECAS Expert Consensus Statement on Catheter and Surgical Ablation of Atrial Fibrillation: Recommendations for Personnel, Policy, Procedures and Follow-Up," *Europace*, 9, 335–379.

Calkins, H., Kuck, K. H., Cappato, R., Brugada, J., Camm, A. J., Chen, S.-A., Crijns, H. J., Damiano, R. J., Davies, D. W., DiMarco, J., et al. (2012), "2012 HRS/EHRA/ECAS Expert Consensus Statement on Catheter and Surgical Ablation of Atrial Fibrillation: Recommendations for Patient Selection, Procedural Techniques, Patient Management and Follow-up, Definitions, Endpoints, and Research Trial Design," *Europace*, 14, 528–606.

Chen, S., Fatemi, M., and Greenleaf, J. (2004), "Quantifying elasticity and viscosity from measurement of shear wave speed dispersion," *J. Acoust. Soc. Am.*, 116, 2781–2785.

Chen, S., Urban, M., Pislaru, C., Kinnick, R., Zheng, Y., Yao, A., and Greenleaf, J. (2009), "Shearwave Dispersion Ultrasound Vibrometry (SDUV) for Measuring Tissue Elasticity and Viscosity," *IEEE Trans Ultrason*, 56, 55–62.

Chu, E., Fitzpatrick, A., Chin, M., Sudhir, K., Yock, P., and Lesh, M. (1994), "Radiofrequency Catheter Ablation Guided by Intracardiac Echocardiography," *Circulation*, 89, 1301–1305.

Couade, M., Pernot, M., Messas, E., Bel, A., Ba, M., Hagege, A., Fink, M., and Tanter, M. (2011), "In Vivo Quantitative Mapping of Myocardial Stiffening and Transmural Anisotropy During the Cardiac Cycle," *IEEE Trans Med Imag*, 30, 295–305.

Dahl, J., Pinton, G., Palmeri, M., Agrawal, V., Nightingale, K., and Trahey, G. (2007), "A parallel tracking method for acoustic radiation force impulse imaging," *Ultrasonics, Ferroelectrics and Frequency Control, IEEE Transactions on*, 54, 301 –312.

Daoud, E. G., Kalbfletsch, S. J., and Hummel, J. D. (1999), "Intracardiac Echocardiography to Guide Transseptal Left Heart Catheterization for Radiofrequency Catheter Ablation," *Journal of Cardiovascular Electrophysiology*, 10, 358–363.

Deffieux, T., Gennisson, J.-L., Bercoff, J., and Tanter, M. (2011), "On the effects of reflected waves in transient shear wave elastography," *Ultrasonics, Ferroelectrics and Frequency Control, IEEE Transactions on*, 58, 2032–2035.

Deffieux, T., Gennisson, J.-L., Larrat, B., Fink, M., and Tanter, M. (2012), "The variance of quantitative estimates in shear wave imaging: Theory and experiments," *Ultrasonics, Ferroelectrics and Frequency Control, IEEE Transactions on*, 59, –.

D'Hooge, J., Heimdal, A., Jamal, F., Kukulski, T., Bijnens, B., Rademarers, F., Hatle, L., Suetens, P., and Sutherland, G. (2000), "Regional Strain and Strain Rate Measurements by Cardiac Ultrasound: Principles, Implementation and Limitations," *Eur. J. Echocardiogr*, 1, 154.

Diamond, G. and Forrester, J. S. (1972), "Effect of Coronary Artery Disease and Acute Myocardial Infarction on Left Ventricular Compliance in Man," *Circulation*, 45, 11–19.

Elegbe, E. C. and McAleavey, S. A. (2013), "Single Tracking Location Methods Suppress Speckle Noise in Shear Wave Velocity Estimation," *Ultrasonic imaging*, 35, 109–125.

Elen, A., Loeckx, D., Gao, H., Claus, P., Suetens, P., Maes, F., and D'hooge, J. (2008), "Three-Dimensional Cardiac Strain Estimation using Spatio-Temporal Elastic Registration of Ultrasound Images: A Feasibility Study," *IEEE Trans. Med. Imag.*, 27, 1580–1591.

Eyerly, S., Hsu, S., Agashe, S., Trahey, G., Li, Y., and Wolf, P. (2010), "An In Vitro Assessment of Acoustic Radiation Force Impulse Imaging for Visualizing Cardiac Radiofrequency Ablation Lesions," *Journal of Cardiovascular Electrophysiology*, 21, 557–563.

Eyerly, S. A., Bahnson, T. D., Koontz, J. I., Bradway, D. P., Dumont, D. M., Trahey, G. E., and Wolf, P. D. (2012), "Intracardiac acoustic radiation force impulse imaging: A novel imaging method for intraprocedural evaluation of radiofrequency ablation lesions," *Heart Rhythm*, 9, 1855–1862.

Fisher, W. G., Pelini, M. A., and Bacon, M. E. (1997), "Adjunctive Intracardiac Echocardiography to Guide Slow Pathway Ablation in Human Atrioventricular Nodal Reentrant Tachycardia Anatomic Insights," *Circulation*, 96, 3021–3029.

Giannantonio, D., Dumont, D., Trahey, G., and Byram, B. (2011), "Comparison of Physiological Motion Filters for In Vivo Cardiac ARFI," *Ultrasonic Imaging*, 33, 89–108.

Golub, G. H., Hansen, P. C., and O'Leary, D. P. (1999), "Tikhonov regularization and total least squares," *SIAM Journal on Matrix Analysis and Applications*, 21, 185–194.

Gruseels, E. W. M., Deckers, J. W., Hoes, A. W., Hartman, J. A. M., Van Does, E. D., Loenen, E. V., and Simoons, M. L. (1995), "Pre-hospital triage of patients with suspected myocardial infarction," *European Heart Journal*, 16, 325–332.

Haas, F., Haehnel, C., Picker, W., Nekolla, S., Martinoff, S., Meisner, H., and Schwaiger, M. (1997), "Preoperative positron emission tomographic viability assessment and perioperative and postoperative risk in patients with advanced ischemic heart disease." *J Am Coll Cardiol.*, 30, 1693–1700.

Haddad, F., Hunt, S., Rosenthal, D., and Murphy, D. (2008), "Right Ventricular Function in Cardiovascular Disease, Part I: Anatomy, Physiology, Aging and Functional Assessment of the Right Ventricle," *Circulation*, 117, 1436–1448.

Haissaguerre, M., Hocini, M., Sanders, P., Sacher, F., Rotter, M., Takahashi, Y., Rostock, T., HSU, L.-F., Bordachar, P., Reuter, S., et al. (2005), "Catheter ablation of long-lasting persistent atrial fibrillation: Clinical outcome and mechanisms of subsequent arrhythmias," *Journal of cardiovascular electrophysiology*, 16, 1138–1147.

Hare, J. (2007), "The Etiologic Basis of Congestive Heart Failure," in *Atlas of Heart Failure*, ed. W. Colucci, chap. 3, pp. 29–56, Springer, 5 edn.

Hauser, A. M., Gangadharan, V., Ramos, R. G., Gordon, S., Timmis, G. C., and Dudlets, P. (1985), "Sequence of mechanical, electrocardiographic and clinical effects of repeated coronary artery occlusion in human beings: Echocardiographic observations during coronary angioplasty," *Journal of the American College of Cardiology*, 5, 193 – 197.

Heger, J. J., Weyman, A. E., Wann, L. S., Dillon, J. C., and Feigenbaum, H. (1979), "Cross-sectional echocardiography in acute myocardial infarction: detection and localization of regional left ventricular asynergy." *Circulation*, 60, 531–8.

Hollender, P., Bouchard, R., Hsu, S., Bradway, D., Wolf, P., and Trahey, G. (2010), "Intracardiac Measurements of Elasticity using Acoustic Radiation Force Impulse (ARFI) methods: Temporal and Spatial Stability of Shear Wave Velocimetry," *IUS, 2010 IEEE*, pp. 682–685.

Hollender, P., Wolf, P., and Trahey, G. (2011), "Intracardiac shear wave velocimetry using Acoustic Radiation Force (ARF) excitations: In vivo results," in *Ultrasonics Symposium (IUS), 2011 IEEE International*, pp. 21–24, IEEE.

Hollender, P., Bradway, D., Wolf, P., Goswami, R., and Trahey, G. (2013), "Intracardiac acoustic radiation force impulse (ARFI) and shear wave imaging in pigs with focal infarctions," *Ultrasonics, Ferroelectrics and Frequency Control, IEEE Transactions on*, 60.

Hollender, P. J., Wolf, P. D., Goswami, R., and Trahey, G. E. (2012), "Intracardiac Echocardiography Measurement of Dynamic Myocardial Stiffness with Shear Wave Velocimetry," *Ultrasound in Medicine and Biology*, 38, 1271 – 1283.

Hsu, S., Fahey, B., Dumont, D., Wolf, P., and Trahey, G. (2007a), "Challenges and Implementation of Radiation-Force Imaging with an Intracardiac Ultrasound Transducer," *Ultrasonics, Ferroelectrics and Frequency Control, IEEE Transactions on*, 54, 996–1009.

Hsu, S., Bouchard, R., Dumont, D., Wolf, P., and Trahey, G. (2007b), "In Vivo Assessment of Myocardial Stiffness with Acoustic Radiation Force Impulse Imaging," *Ultrasound Med Biol.*, 33, 1706–1719.

Hsu, S. J., Fahey, B. J., Dumont, D. M., and Trahey, G. E. (2005), "Acoustic radiation force impulse imaging with an intra-cardiac probe," in *Medical Imaging*, pp. 196–204, International Society for Optics and Photonics.

Huwart, L., Peeters, F., Sinkus, R., Annet, L., Salameh, N., ter Beek, L. C., Horsmans, Y., and Van Beers, B. E. (2006), "Liver fibrosis: non-invasive assessment with MR elastography," *NMR in Biomedicine*, 19, 173–179.

Jensen, J. A. (1996), "Field: A program for simulating ultrasound systems," in *10th Nordbaltic Conference on Biomedical Imaging*, vol. 4, Supplement 1, Part 1, pp. 351–353.

Jensen, J. A. and Svendsen, N. B. (1992), "Calculation of pressure fields from arbitrarily shaped, apodized, and excited ultrasound transducers," *Ultrasonics, Ferroelectrics and Frequency Control, IEEE Transactions on*, 39, 262–267.

Kanai, H. (2005), "Propagation of Spontaneously Actuated Pulsive Vibration in Human Heart Wall and In Vivo Vescoelasticity Estimation," *Ultrasonics, Ferroelectrics and Frequency Control, IEEE Transactions on*, 52, 1931–1942.

Karolle, B. L., Carlson, R. E., Aisen, A. M., and Buda, A. J. (1991), "Transmural distribution of myocardial edema by NMR relaxometry following myocardial ischemia and reperfusion," *American Heart Journal*, 122, 655 – 664.

Kasai, C., Namekawa, K., Koyano, A., and Omoto, R. (1985), "Real-time Two-dimensional Blood Flow Imaging using Autocorrelation Technique," *Ultrasonics, Ferroelectrics and Frequency Control, IEEE Transactions on*, 32, 458–463.

Khaykin, Y., Skanes, A., Whaley, B., Hill, C., Beardsall, M., Seabrook, C., Wulffhart, Z., Oosthuizen, R., Gula, L., and Verma, A. (2008), "Real-time integration of 2D intracardiac echocardiography and 3D electroanatomical mapping to guide ventricular tachycardia ablation," *Heart Rhythm*, 5, 1396 – 1402.

Kim, R. J., Fieno, D. S., Parrish, T. B., Harris, K., Chen, E.-L., Simonetti, O., Bundy, J., Finn, J. P., Klocke, F. J., and Judd, R. M. (1999), "Relationship of MRI Delayed Contrast Enhancement to Irreversible Injury, Infarct Age, and Contractile Function," *Circulation*, 100, 1992–2002.

Kim, R. J., Wu, E., Rafael, A., Chen, E.-L., Parker, M. A., Simonetti, O., Klocke, F. J., Bonow, R. O., and Judd, R. M. (2000), "The Use of Contrast-Enhanced Magnetic Resonance Imaging to Identify Reversible Myocardial Dysfunction," *New England Journal of Medicine*, 343, 1445–1453.

Kolipaka, A., Araoz, P. A., McGee, K. P., Manduca, A., and Ehman, R. L. (2010), "Magnetic resonance elastography as a method for the assessment of effective myocardial stiffness throughout the cardiac cycle," *Magnetic Resonance in Medicine*, 64, 862–870.

Kowalski, M., Grimes, M. M., Perez, F. J., Kenigsberg, D. N., Koneru, J., Kasirajan, V., Wood, M. A., and Ellenbogen, K. A. (2012), "Histopathologic Characterization of Chronic Radiofrequency Ablation Lesions for Pulmonary Vein Isolation," *Journal of the American College of Cardiology*, 59, 930 – 938.

Krijnen, P. A. J., Nijmeijer, R., Meijer, C. J. L. M., Visser, C. A., Hack, C. E., and Niessen, H. W. M. (2002), "Apoptosis in myocardial ischaemia and infarction," *Journal of Clinical Pathology*, 55, 801–811.

Kybic, J. and Unser, M. (2003), "Fast Parametric Elastic Image Registration," *IEEE Trans. Image Proc.*, 12, 1427–1442.

Laine, G. A. and Allen, S. J. (1991), "Left ventricular myocardial edema. Lymph flow, interstitial fibrosis, and cardiac function." *Circulation Research*, 68, 1713–21.

Langeland, S., D'hooge, J., Wouters, P., Leather, H., Claus, P., Bijnens, B., and Sutherland, G. (2005), "Experimental Validation of a New Ultrasound Method for the Simultaneous Assessment of Radial and Longitudinal Myocardial Deformation Independent of Insonation Angle," *Circulation*, 112, 2157–2162.

Lardo, A. C., McVeigh, E. R., Jumrussirikul, P., Berger, R. D., Calkins, H., Lima, J., and Halperin, H. R. (2000), "Visualization and Temporal/Spatial Characterization of Cardiac Radiofrequency Ablation Lesions Using Magnetic Resonance Imaging," *Circulation*, 102, 698–705.

Ledesma-Carbayo, M., Kybic, J., Desco, M., Santos, A., Sühling, M., Hunziker, P., and Unser, M. (2005), "Spatio-Temporal Nonrigid Registration for Ultrasound Cardiac Motion," *IEEE Trans. Med. Imag.*, 24, 1113–1126.

Lee, T. H., Rouan, G. W., Weisberg, M. C., Brand, D. A., Cook, E. F., Acampora, D., and Goldman, L. (1987), "Sensitivity of Routine Clinical Criteria for Diagnosing Myocardial Infarction Within 24 Hours of Hospitalization," *Annals of Internal Medicine*, 106, 181–186.

Lima, J. A. C., Judd, R. M., Bazille, A., Schulman, S. P., Atalar, E., and Zerhouni, E. A. (1995), "Regional Heterogeneity of Human Myocardial Infarcts Demonstrated by Contrast-Enhanced MRI," *Circulation*, 92, 1117–1125.

Loupas, T., Peterson, R., and Gill, R. (1995), "Experimental evaluation of velocity and power estimation for ultrasound blood flow imaging, by means of a two-dimensional autocorrelation approach," *IEEE Trans. Ultrason.*, 42, 672–688.

Mahnken, A. H., Koos, R., Katoh, M., Wildberger, J. E., Spuentrup, E., Buecker, A., Gnther, R. W., and Khl, H. P. (2005), "Assessment of Myocardial Viability in Reperfused Acute Myocardial Infarction Using 16-Slice Computed Tomography in Comparison to Magnetic Resonance Imaging," *Journal of the American College of Cardiology*, 45, 2042 – 2047.

Manduca, A., Oliphant, T. E., Dresner, M., Mahowald, J., Kruse, S., Amromin, E., Felmlee, J. P., Greenleaf, J. F., and Ehman, R. L. (2001), "Magnetic resonance elastography: non-invasive mapping of tissue elasticity," *Medical image analysis*, 5, 237–254.

Marrouche, N. F., Martin, D. O., Wazni, O., Gillinov, A. M., Klein, A., Bhargava, M., Saad, E., Bash, D., Yamada, H., Jaber, W., Schweikert, R., Tchou, P., Abdul-Karim, A., Saliba, W., and Natale, A. (2003), "Phased-Array Intracardiac Echocardiography Monitoring During Pulmonary Vein Isolation in Patients With Atrial Fibrillation," *Circulation*, 107, 2710–2716.

Matsunari, I., Taki, J., Nakajima, K., Tonami, N., and Hisada, K. (2003), "Myocardial viability assessment using nuclear imaging," *Annals of Nuclear Medicine*, 17, 169–179.

McAleavey, S., Menon, M., and Elegbe, E. (2009a), "Shear modulus imaging with spatially-modulated ultrasound radiation force," *Ultrasonic imaging*, 31, 217–234.

McAleavey, S., Collins, E., Kelly, J., Elegbe, E., and Menon, M. (2009b), "Validation of SMURF estimation of shear modulus in hydrogels," *Ultrasonic imaging*, 31, 131–150.

McAleavey, S. A., Nightingale, K. R., and Trahey, G. E. (2003), "Estimates of echo correlation and measurement bias in acoustic radiation force impulse imaging," *Ultrasonics, Ferroelectrics and Frequency Control, IEEE Transactions on*, 50, 631–641.

McAleavey, S. A., Menon, M., and Orszulak, J. (2007), "Shear-modulus estimation by application of spatially-modulated impulsive acoustic radiation force," *Ultrasonic imaging*, 29, 87–104.

McKay, R. G., Pfeffer, M. A., Pasternak, R. C., Markis, J. E., Come, P. C., Nakao, S., Alderman, J. D., Ferguson, J. J., Safian, R. D., and Grossman, W. (1986), "Left ventricular remodeling after myocardial infarction: a corollary to infarct expansion." *Circulation*, 74, 693–702.

McLaughlin, J. and Renzi, D. (2006a), "Shear wave speed recovery in transient elastography and supersonic imaging using propagating fronts," *Inverse Problems*, 22, 681.

McLaughlin, J. and Renzi, D. (2006b), "Using level set based inversion of arrival times to recover shear wave speed in transient elastography and supersonic imaging," *Inverse Problems*, 22, 707.

Mebazaa, A., Karpati, P., Renaud, E., and Algotsson, L. (2004), "Acute Right Ventricular Failure – from Pathophysiology to New Treatments," *Intensive Care Med*, 30, 185–196.

Melby, S. J., Lee, A. M., Zierer, A., Kaiser, S. P., Livhits, M. J., Boineau, J. P., Schuessler, R. B., and Jr., R. J. D. (2008), "Atrial fibrillation propagates through gaps in ablation lines: Implications for ablative treatment of atrial fibrillation," *Heart Rhythm*, 5, 1296 – 1301.

Montaldo, G., Tanter, M., Bercoff, J., Benech, N., and Fink, M. (2009), "Coherent plane-wave compounding for very high frame rate ultrasonography and transient elastography," *Ultrasonics, Ferroelectrics and Frequency Control, IEEE Transactions on*, 56, 489 –506.

Morales, C., Gonzlez, G. E., Rodriguez, M., Bertolasi, C. A., and Gelpi, R. J. (2002), "Histopathologic time course of myocardial infarct in rabbit hearts," *Cardiovascular Pathology*, 11, 339 – 345.

Mullen, M., Dias, B., Walker, F., Siu, S., Benson, L., and McLaughlin, P. (2003), "Intracardiac Echocardiography Guided Device Closure of Atrial Septal Defects," *J Am Coll Cardiol*, 41, 285–292.

Muller, M., Gennisson, J.-L., Deffieux, T., Tanter, M., and Fink, M. (2009), "Quantitative Viscoelasticity Mapping of Human Liver Using Supersonic Shear Imaging: Preliminary In Vivo Feasability Study," *Ultrasound in medicine & biology*, 35, 219–229.

Myronenko, A., Song, X., and Sahn, D. (2007), "LV Motion Tracking from 3d Echocardiography using Textural and Structural Information," *MICCAI*, 4792, 428–435.

Nenadic, I., Urban, M., Mitchell, S., and Greenleaf, J. (2011), "Lamb Wave Dispersions Ultrasound Vibrometry (LDUV) method for quantifying mechanical properties of viscoelastic solids," *Phys. Med. Biol.*, 56, 2245–2264.

Nightingale, K., Soo, M. S., Nightingale, R., and Trahey, G. (2002), "Acoustic radiation force impulse imaging: in vivo demonstration of clinical feasibility," *Ultrasound in Medicine and Biology*, 28, 227 – 235.

Nightingale, K., McAleavey, S., and Trahey, G. (2003), "Shear-wave Generation using Acoustic Radiation Force: In Vivo and Ex Vivo Results," *Ultrasound Med Biol.*, 29, 1715–1723.

Nightingale, K., Palmeri, M., and Trahey, G. (2006), "Analysis of contrast in images generated with transient acoustic radiation force," *Ultrasound in medicine & biology*, 32, 61–72.

Nyborg, W. (1965), "Acoustic Streaming," in *Physical Acoustics*, ed. W. Mason, vol. IIB, chap. 11, p. 1965, New York: Academic Press Inc.

Oberai, A. A., Gokhale, N. H., and Feijoo, G. R. (2003), "Solution of inverse problems in elasticity imaging using the adjoint method," *Inverse Problems*, 19, 297.

Pagley, P. R., Beller, G. A., Watson, D. D., Gimple, L. W., and Ragosta, M. (1997), "Improved Outcome After Coronary Bypass Surgery in Patients With Ischemic Cardiomyopathy and Residual Myocardial Viability," *Circulation*, 96, 793–800.

Palmeri, M., Sharma, A., Bouchard, R., Nightingale, R., and Nightingale, K. (2005), "A Finite-Element Method Model of Soft Tissue Response to Impulsive Acoustic Radiation Force," *Ultrasonics, Ferroelectrics and Frequency Control, IEEE Transactions on*, 52, 1699–1712.

Palmeri, M., McAleavey, S., Fong, K., and Trahey, G. (2006a), "Dynamic Mechanical Response of Elastic Spherical Inclusions of Impulsive Acoustic Radiation Force

Excitation," *Ultrasonics, Ferroelectrics and Frequency Control, IEEE Transactions on*, 53, 2065–2079.

Palmeri, M., McAleavey, S., Trahey, G., and Nightingale, K. (2006b), "Ultrasonic Tracking of Acoustic Radiation Force-Induced Displacements in Homogenous Media," *Ultrasonics, Ferroelectrics and Frequency Control, IEEE Transactions on*, 53, 1300–1313.

Palmeri, M., Wang, M., Dahl, J., Frinkley, K., and Nightingale, K. (2008), "Quantifying Hepatic Shear Modulus In vivo using Acoustic Radiation Force," *Ultrasound Med Biol*, 34, 546–558.

Palmeri, M. L. and Nightingale, K. R. (2004), "On the thermal effects associated with radiation force imaging of soft tissue," *Ultrasonics, Ferroelectrics and Frequency Control, IEEE Transactions on*, 51, 551–565.

Palmeri, M. L., Rouze, N. C., Wang, M. H., Ding, X., and Nightingale, K. R. (2010), "Quantifying the impact of shear wavelength and kernel size on shear wave speed estimation," in *Ultrasonics Symposium (IUS), 2010 IEEE*, pp. 13–16, IEEE.

Pernot, M., Mace, E., Dubois, R., Couade, M., Fink, M., and Tanter, M. (2009), "Mapping myocardial elasticity changes after RF-ablation using supersonic shear imaging," in *Computers in Cardiology, 2009*, pp. 793 –796.

Pernot, M., Couade, M., Mateo, P., Crozatier, B., Fischmeister, R., and Tanter, M. (2011), "Real-Time Assessment of Myocardial Contractility Using Shear Wave Imaging," *J. American College of Cardiology*, 5, 65–72.

Pesavento, A., Perrey, C., Krueger, M., and Ermert, H. (1999), "A time-efficient and accurate strain estimation concept for ultrasonic elastography using iterative phase zero estimation," *Ultrasonics, Ferroelectrics and Frequency Control, IEEE Transactions on*, 46, 1057–1067.

PG, M. and J, B. (2012), "Post myocardial infarction of the left ventricle: The course ahead seen by cardiac MRI." *Cardiovasc Diagn Ther*, 2, 113–127.

Pinton, G., Dahl, J., and Trahey, G. (2006), "Rapid Tracking of Small Displacements with Ultrasound," *IEEE Trans. Ultrason.*, 53, 1103–1117.

Pislaru, C., Urban, M., Nenadic, I., and Greenleaf, J. (2009), "Shearwave Dispersion Ultrasound Vibrometry Applied to In Vivo Myocardium," *EMBC 2009*, pp. 2891–2894.

Ren, J.-F., Marchilinksi, F. E., Callans, D. J., and Zado, E. S. (2001), "Echocardiographic Lesion Characteristics Associated with Successful Ablation of Inappropriate Sinus Tachycardia," *Journal of Cardiovascular Electrophysiology*, 12, 814–818.

Rosenzweig, S. J., Palmeri, M. L., and Nightingale, K. R. (2014), "Analysis of Rapid Multi-Focal Zone ARFI Imaging," *Ultrasonics, Ferroelectrics and Frequency Control, IEEE Transactions on, in Review*.

Rotemberg, V., Palmeri, M., Nightingale, R., Rouze, N., and Nightingale, K. (2012), "The impact of hepatic pressurization on liver shear wave speed estimates in constrained versus unconstrained conditions," *Physics in medicine and biology*, 57, 329.

Rouze, N., Wang, M., Palmeri, M., and Nightingale, K. (2010), "Robust Estimation of the Time-of-Flight Shear Wave Speed using a Radon Sum Transformation." *Ultrasonics, Ferroelectrics and Frequency Control, IEEE Transactions on*, 57, 2662–2670.

Rouze, N. C., Wang, M. H., Palmeri, M. L., and Nightingale, K. R. (2012), "Parameters affecting the resolution and accuracy of 2-D quantitative shear wave images," *Ultrasonics, Ferroelectrics and Frequency Control, IEEE Transactions on*, 59, 1729–1740.

Saraste, A., Pulkki, K., Kallajoki, M., Henriksen, K., Parvinen, M., and Voipio-Pulkki, L.-M. (1997), "Apoptosis in Human Acute Myocardial Infarction," *Circulation*, 95, 320–323.

Sarvazyan, A., Rudenko, O., Swanson, S., Fowlkes, J., and Emelianov, S. (1998), "Shear Wave Elasticity Imaging; A New Ultrasonic Technology of Medical Diagnostics," *Ultrasound Med Biol.*, 24, 1419:1436.

Serri, K., Reant, P., Lafitte, M., Berhouet, M., Bouffos, V. L., Roudaut, R., and Lafitte, S. (2006), "Global and Regional Myocardial Function Quantification by Two-Dimensional Strain: Application in Hypertrophic Cardiomyopathy," *J. American College of Cardiography*, 6, 1175–1181.

Shah, R. U., Freeman, J. V., Shilane, D., Wang, P. J., Go, A. S., and Hlatky, M. A. (2012), "Procedural complications, rehospitalizations, and repeat procedures after catheter ablation for atrial fibrillation," *Journal of the American College of Cardiology*, 59, 143–149.

Sharma, A. C., Soo, M. S., Trahey, G. E., and Nightingale, K. R. (2004), "Acoustic radiation force impulse imaging of in vivo breast masses," in *Ultrasonics Symposium, 2004 IEEE*, vol. 1, pp. 728–731, IEEE.

Solomon, S. and Pfeffer, M. (2007), "Cardiac Remodeling and Its Prevention," in *Atlas of Heart Failure*, ed. W. Colucci, chap. 4, pp. 57–75, Springer, 5 edn.

Sorzano, C., Thévenaz, P., and Unser, M. (2005), "Elastic Registration of Biological Images Using Vector-Spline Regularization," *IEEE Trans Biomed. Eng.*, 42, 652–663.

Sparks, P. B., Jayaprakash, S., Vohra, J. K., Mond, H. G., Yapanis, A. G., Grigg, L. E., and Kalman, J. M. (1998), "Left atrial ?stunning? following radiofrequency catheter ablation of chronic atrial flutter," *Journal of the American College of Cardiology*, 32, 468–475.

Szili-Torok, T., Kimman, G., Theuns, D., Res, J., Roelandt, J., and Jordaens, L. (2003), "Visualisation of Intra-cardiac Structures and Radiofrequency Lesions Using Intracardiac Echocardiography," *European Journal of Echocardiography*, 4, 17–22.

Tanter, M., Bercoff, J., Athanasiou, A., Deffieux, T., Gennisson, J.-L., Montaldo, G., Muller, M., Tardivon, A., and Fink, M. (2008), "Quantitative assessment of breast lesion viscoelasticity: initial clinical results using supersonic shear imaging." *Ultrasound Med Biol*, 34, 1373–1386.

Thuny, F., Lairez, O., Roubille, F., Mewton, N., Rioufol, G., Sportouch, C., Sanchez, I., Bergerot, C., Thibault, H., Cung, T. T., Finet, G., Argaud, L., Revel, D., Derumeaux, G., Bonnefoy-Cudraz, E., Elbaz, M., Piot, C., Ovize, M., and Croisille, P. (2012), "Post-Conditioning Reduces Infarct Size and Edema in Patients With ST-Segment Elevation Myocardial Infarction," *Journal of the American College of Cardiology*, 59, 2175 – 2181.

Torr, G. R. (1984), "The acoustic radiation force," *American Journal of Physics*, 52, 402–408.

Uusimaa, P., Risteli, J., Niemel, M., Lumme, J., Ikheimo, M., Jounela, A., and Peuhkurinen, K. (1997), "Collagen Scar Formation After Acute Myocardial Infarction," *Circulation*, 96, 2565–2572.

Vaina, S., Ligthart, J., Vijayakumar, M., Cate, F. T., Witsenburg, M., Jordaens, L., Sianos, G., Thornton, A., Scholten, M., de Jaegere, P., and Serruys, P. (2006), "Intracardiac echocardiography during interventional procedures," *EuroIntervention*, 1, 454–64.

Van de Werf, F., Ardissino, D., Betriu, A., Cokkinos, D. V., Falk, E., Fox, K. A., Julian, D., Lengyel, M., Neumann, F.-J., Ruzyllo, W., Thygesen, C., Underwood, S. R., Vahanian, A., Verheugt, F. W., and Wijns, W. (2003), "Management of acute myocardial infarction in patients presenting with ST-segment elevation," *European Heart Journal*, 24, 28–66.

Wagner, R. F., Smith, S. W., Sandrik, J. M., and Lopez, H. (1983), "Statistics of speckle in ultrasound B-scans." *IEEE TRANS. SONICS ULTRASONICS.*, 30, 156–163.

Wagner, R. F., Insana, M. F., and Smith, S. W. (1988), "Fundamental correlation lengths of coherent speckle in medical ultrasonic images," *Ultrasonics, Ferroelectrics and Frequency Control, IEEE Transactions on*, 35, 34–44.

Walker, W. and Trahey, G. (1995), "A fundamental limit on delay estimation using partially correlated speckle signals," *Ultrasonics, Ferroelectrics and Frequency Control, IEEE Transactions on*, 42, 301 –308.

Walker, W. F. and Trahey, G. E. (1998), "The application of k-space in pulse echo ultrasound," *Ultrasonics, Ferroelectrics and Frequency Control, IEEE Transactions on*, 45, 541–558.

Wang, M. H., Palmeri, M. L., Rotemberg, V. M., Rouze, N. C., and Nightingale, K. R. (2010), "Improving the robustness of time-of-flight based shear wave speed reconstruction methods using RANSAC in human liver in vivo," *Ultrasound in Medicine & Biology*, 36, 802.

Westermann, D., Kasner, M., Steendijk, P., Spillmann, F., Riad, A., Weitmann, K., Hoffman, W., Poller, W., Pauschinger, M., Schultheiss, H., and Tschöpe, C. (2008), "Role of Left Ventricular Stiffness in Heart Failure with Normal Ejection Fraction," *Circulation*, 117.

Wittkampf, F. H., Vonken, E.-J., Derksen, R., Loh, P., Velthuis, B., Wever, E. F., Boersma, L. V., Rensing, B. J., and Cramer, M.-J. (2003), "Pulmonary vein ostium geometry analysis by magnetic resonance angiography," *Circulation*, 107, 21–23.

Wolf, P., Eyerly, S., Bradway, D., Dumont, D., Bahnson, T., Nightingale, K., and Trahey, G. (2011), "Near Real Time Evaluation of Cardiac Radiofrequency Ablation Lesions with Intracardiac Echocardiography Based Acoustic Radiation Force Impulse Imaging," *Presented at 161st meeting of the Acoust. Soc. Amer., J. Acoust. Soc. Amer.*, 129, 2438–2438.

Zile, C., Baicu, F., and Gaasch, W. (2004), "Diastolic Heart Failure- Abnormalities in Active Relaxation and Passive Stiffness of the Left Ventricle," *N. Engl. J. Med.*, 350, 1953–1959.

Biography

Peter J. Hollender was born March 1st, 1987 in Iowa City, Iowa. He grew up in Cleveland, Ohio, where he had his first engineering job as a high school intern at NASA's Glenn Research Center. He completed his B.S.E. in both Electrical & Computer Engineering and Biomedical Engineering at Duke University in 2009. Upon graduation, he was convinced to remain at Duke for his Ph.D. in Biomedical Engineering, which he hereupon completes in 2014. As an NIH MITP scholar, his graduate career was enhanced by attending a variety of prestigious conferences and working closely with doctors to understand the clinical side of his research. He also served as President of the Engineering Graduate Student Council for two years, increasing collaboration with other groups and providing quality programming for his peers. During this time he also founded Duke's PhD Plus program to aid Duke Engineering Ph.D.'s with career planning and preparation. He also served as the IEEE Ultrasonics, Ferroelectrics and Frequency Control Society's Student Representative for Ultrasonics from 2011-2013, where he advised leaders in the field from across the globe on student membership and engagement strategies. He served as Duke's University Innovations Fellow for the eponymous program sponsored by the National Collegiate Inventors and Innovators Alliance (NCIIA) from 2013-2014, working with students at other universities on strategies and programs to promote entrepreneurship at Duke.

Selected Publications

Hollender, P., Wolf, P., and Trahey, G. (2011), "Intracardiac Shear Wave Velocimetry using Acoustic Radiation Force (ARF) Excitations: In Vivo Results," *Presented at the IUS in Orlando, Florida*.

Hollender, P., Bradway, D., Wolf, P., Goswami, R., and Trahey, G. (2013), "Intracardiac acoustic radiation force impulse (ARFI) and shear wave imaging in pigs with focal infarctions," *Ultrasonics, Ferroelectrics and Frequency Control, IEEE Transactions on*, 60.

Hollender, P., Bottenus, N., Nightingale, K., and Trahey, G. (2014a), "Beamforming Bias Compensation in Single Track Location Shear Wave Elasticity Imaging," *In Review*.

Hollender, P., Rosenzweig, S., Nightingale, K., and Trahey, G. (2014b), "Matched Single- and Multiple- Track Location Shear Wave and Acoustic Radiation Force Impulse Imaging: Comparison of Suitability for Micro-Elasticity Imaging," *In Review*.

Hollender, P., Bottenus, N., and Trahey, G. (2014c), "A Multiresolution Approach to Shear Wave Image Reconstruction," *In Review*.

Hollender, P. J., Wolf, P. D., Goswami, R., and Trahey, G. E. (2012), "Intracardiac Echocardiography Measurement of Dynamic Myocardial Stiffness with Shear Wave Velocimetry," *Ultrasound in Medicine and Biology*, 38, 1271 – 1283.